



CORONAL DIMMINGS ASSOCIATED WITH  
CORONAL MASS EJECTIONS: EVOLUTION,  
LIFETIME, AND RELATION TO THE  
DIRECTIVITY

*Doctoral Thesis*

by

GALINA CHIKUNOVA

DOCTORAL PROGRAM IN ENGINEERING SYSTEMS

Supervisor

Associate Professor, Tatiana Podladchikova

Moscow, 2023

© Galina Chikunova, 2023.

I hereby declare that the work presented in this thesis was carried out by myself at Skolkovo Institute of Science and Technology, Moscow, except where due acknowledgement is made, and has not been submitted for any other degree.

Galina Chikunova (Candidate)

Associate Prof. Tatiana Podladchikova (Supervisor)

## Abstract

Coronal mass ejections (CMEs) are the most powerful eruptive events in the solar system. These massive magnetized plasma structures, which arise from instabilities in the solar magnetic field, are expelled from the Sun to interplanetary space with speeds in the range of some  $100 \text{ km s}^{-1}$  up to  $> 3000 \text{ km s}^{-1}$ . Their ability to trigger strong geomagnetic storms underscores their importance as main sources of disturbances in space weather.

Coronal dimmings are the most distinct phenomena related to CMEs. They manifest as regions of reduced extreme ultraviolet (EUV) or soft X-ray (SXR) emission and occur during the early eruptive phase of a CME, indicating a decrease in density due to mass loss or rapid coronal expansion. Historically, coronal dimmings have been recognized as indicators for Earth-directed CMEs. However, their enormous diagnostic potential has yet to be adequately explored.

We develop a comprehensive methodology for dimming analysis, from the first steps of data preprocessing to advanced methods that relate dimming evolution to the properties of CMEs. We apply these methods to highlight the potential of using dimmings observations to improve the estimations of the mass, speed, trajectory of CMEs, as well as to track the recovery of the solar corona after eruption.

We study coronal dimmings that were observed above the limb by STEREO/EUVI and compared their properties with the mass and speed of the associated CMEs. The unique position of satellites allowed us to compare our findings with the results from [Dissauer et al. \[2018b, 2019\]](#), who studied the same events observed against the solar disk by SDO/AIA. Such statistics is done for the first time and confirms the relation of coronal dimmings and CME parameters for the off-limb viewpoint.

Coronal dimmings remain evident throughout the entire lifecycle of a CME, providing insights into the post-eruption recovery of the corona and the permanent connection of magnetic structures to the Sun. We propose two advanced methods for detailed analysis of the dimming recovery time, allowing tracking both the recovery time of the total dimming region and differentiation between core and secondary components. We demonstrated that dimmings in general recover within 1 day, showing 2-step trends. Some parts of the dimming regions (probably, core dimmings) do not recover within 3 days, whereas the outer regions (secondary dimmings) show a full recovery.

As markers of CMEs in the lower corona, coronal dimmings not only indicate the onset of eruptions but also provide insights on their initial trajectory. We have introduced a method to determine the dominant direction of dimming based on its area evolution. For the event under study, 28 October 2021, the dominant propagation of the dimming growth reflects the direction of the erupting magnetic structure (filament) low in the solar atmosphere. At the same time, the overall dimming morphology closely resembles the inner part of the CME reconstruction, validating the use of dimming observations to obtain insight into the CME direction.

In summary, coronal dimmings provide valuable insights into the dynamics and the early evolution of CMEs. Solar observations with EUV imagers promise to refine the characterization of CMEs directed toward Earth, a critical component in improving space weather forecasting.

# Publications

## Main author

1. G. Chikunova, T. Podladchikova, K. Dissauer, A. M. Veronig, M. Dumbović, M. Temmer, and E. Dickson. Three-dimensional relation between coronal dimming, filament eruption, and CME - a case study of the 28 October 2021 X1.0 event. *Astron. Astrophys.*, 678:A166, October 2023. doi:[10.1051/0004-6361/202347011](https://doi.org/10.1051/0004-6361/202347011)
2. G. Chikunova, K. Dissauer, T. Podladchikova, and A. M. Veronig. Coronal Dimmings Associated with Coronal Mass Ejections on the Solar Limb. *Astrophys. J.*, 896(1):17, June 2020. doi:[10.3847/1538-4357/ab9105](https://doi.org/10.3847/1538-4357/ab9105)

## Co-author

3. J. K. Thalmann, M. Dumbović, K. Dissauer, T. Podladchikova, G. Chikunova, M. Temmer, E. Dickson, and A. M. Veronig. Tracking magnetic flux and helicity from the Sun to Earth. Multi-spacecraft analysis of a magnetic cloud and its solar source. *Astron. Astrophys.*, 669:A72, January 2023. doi:[10.1051/0004-6361/202244248](https://doi.org/10.1051/0004-6361/202244248)
4. M. Dumbović, A. M. Veronig, T. Podladchikova, J. K. Thalmann, G. Chikunova, K. Dissauer, J. Magdalenić, M. Temmer, J. Guo, and E. Samara. 2019 International Women's Day event. Two-step solar flare with multiple eruptive signatures and low Earth impact. *Astron. Astrophys.*, 652:A159, August 2021. doi:[10.1051/0004-6361/202140752](https://doi.org/10.1051/0004-6361/202140752)
5. S. Jain, T. Podladchikova, G. Chikunova, K. Dissauer, and A. M. Veronig. Coronal dimmings as indicators of early CME propagation direction. *Astron. Astrophys.*, 2023. doi:[10.48550/arXiv.2311.13942](https://doi.org/10.48550/arXiv.2311.13942)
6. G. Ronca, G. Chikunova, T. Podladchikova, K. Dissauer, and A. Veronig. Recovery of the coronal dimmings. *Astron. Astrophys.*, 2023, under review

# Acknowledgments

I want to express my deep gratitude to Tatiana Podladchikova, my advisor, for her incredible support and guidance throughout my academic journey. I was extremely lucky to meet you on my academic path, which led me to discover a research area I'm excited about. You've become my guiding star through all these challenging times - close, incredibly bright, and a constant source of inspiration and brave ideas.

Furthermore, I am very grateful to Astrid Veronig and Karin Dissauer, a bit more distant but brightly shining stars. I always learn so much from you. Thank you for being always present, it is remarkable how we maintain our effective teamwork, despite the physical distance between us.

I owe a lot to Shantanu and Giulia, without whom this work also wouldn't be possible. Shantanu, thank you for always being there for me and for joining this mission to explore the coronal dimmings. Thank you for all our endless conversations in Skoltech and Indian chocolates. Giulia, you were the best student to mentor, it was a pleasure to work and chat with you online, in Moscow and in Milan.

I thank Skoltech for my academic life, for all the opportunities and connections with exceptional people and community. I am always very proud to tell about our unique university.

To my parents, thanks for your enormous love and all the chances that allowed me to pursue my dreams and yours. My friends, I am so lucky to have so many of you. Now we are living all over the world, but we are always connected.

Finally, a heartfelt thanks to my partner, Kirill. You had the hardest task to support me and bear all my hardships on yourself. In this vast universe, home could be just one person.

# Coronal dimming

evolution



lifetime



directivity



# Contents

<b>Glossary</b>	<b>11</b>
<b>Introduction</b>	<b>15</b>
Overview . . . . .	15
Thesis Outline . . . . .	17
<b>1 Basics of Heliophysics</b>	<b>20</b>
1.1 An Overview of the Sun . . . . .	20
1.1.1 Sun as a star . . . . .	20
1.1.2 Solar interior . . . . .	21
1.1.3 Atmosphere of the Sun . . . . .	22
1.1.4 Solar cycle . . . . .	27
1.1.5 Magnetic field of the Sun . . . . .	29
1.2 Space Weather and its effects . . . . .	32
<b>2 Coronal Mass Ejections</b>	<b>35</b>
2.1 Overview of CMEs . . . . .	35
2.2 Properties of CMEs . . . . .	37
2.2.1 Morphology . . . . .	38
2.2.2 Occurrence rate . . . . .	39
2.2.3 Angular width . . . . .	41
2.2.4 Mass . . . . .	43
2.2.5 Speed and energy . . . . .	43
2.2.6 Acceleration . . . . .	43
2.3 Initiation mechanisms . . . . .	44

2.4	CME modeling with GCS . . . . .	45
2.5	Associated Phenomena . . . . .	46
2.5.1	Flares . . . . .	48
2.5.2	Filaments and Prominences . . . . .	49
2.5.3	EUV waves . . . . .	51
2.5.4	Coronal dimmings . . . . .	52
<b>3</b>	<b>Coronal Dimmings</b>	<b>53</b>
3.1	Nature of appearance . . . . .	53
3.2	Formation of Coronal Dimmings . . . . .	54
3.3	Historical Overview . . . . .	56
3.4	Relations to the CME parameters . . . . .	56
3.5	Detection Algorithms and Dimming Analysis . . . . .	57
<b>4</b>	<b>Methodology of the dimming analysis</b>	<b>66</b>
4.1	Data and instruments . . . . .	66
4.1.1	SDO mission . . . . .	66
4.1.2	STEREO mission . . . . .	69
4.2	Dimming detection . . . . .	71
4.2.1	From SolarSoft IDL to Python and Sunpy . . . . .	71
4.2.2	Loading and calibration . . . . .	72
4.2.3	Differential rotation . . . . .	74
4.2.4	Data preprocessing . . . . .	76
4.2.5	On-disk dimming detection . . . . .	77
4.2.6	Off-limb dimmings detection . . . . .	79
4.3	Characteristic dimming parameters . . . . .	82
4.3.1	Dimming area . . . . .	84
4.3.2	Dimming brightness . . . . .	85
4.3.3	Impulsive phase of the dimming . . . . .	87
4.3.4	Magnetic flux . . . . .	87
4.3.5	Recovery time . . . . .	88
4.4	Area correction . . . . .	89

4.5	Examples of dimming analysis . . . . .	94
4.5.1	International Women Day event - 8 March 2019 . . . . .	94
4.5.2	2 November 2021 . . . . .	97
<b>5</b>	<b>Relation to the CME speed and mass</b>	<b>103</b>
5.1	Project summary . . . . .	103
5.2	Literature review . . . . .	104
5.3	Methodology . . . . .	104
5.3.1	Data and Data preprocessing . . . . .	105
5.3.2	Characteristic dimming parameters . . . . .	106
5.4	Results . . . . .	107
5.4.1	Evolution and distribution of the dimming parameters . . . . .	108
5.4.2	Relation between off-limb and on-disk dimmings . . . . .	114
5.4.3	Relation between off-limb dimming and CME parameters . . . . .	117
5.5	Summary and Discussion . . . . .	119
5.6	Conclusion . . . . .	123
<b>6</b>	<b>Dimming lifetime</b>	<b>125</b>
6.1	Project summary . . . . .	125
6.2	Literature review . . . . .	126
6.3	Statistical study . . . . .	128
6.4	Methodology . . . . .	129
6.4.1	Event selection . . . . .	130
6.4.2	Data preprocessing . . . . .	133
6.4.3	Dimming detection . . . . .	134
6.4.4	Calculation of coronal dimming parameters . . . . .	134
6.5	Results . . . . .	143
6.5.1	2011 September 6 . . . . .	144
6.5.2	2012 March 7 . . . . .	149
6.5.3	2012 June 14 . . . . .	152
6.5.4	2019 March 8 . . . . .	154
6.5.5	Comparison of the events . . . . .	156

---

6.6	Discussion . . . . .	158
6.7	Conclusions . . . . .	160
<b>7</b>	<b>Relation to the CME direction</b>	<b>161</b>
7.1	Project summary . . . . .	161
7.2	Literature review . . . . .	162
7.3	Data and event observation . . . . .	163
7.4	Methods and results . . . . .	169
7.4.1	Coronal dimming . . . . .	169
7.4.2	Eruptive filament . . . . .	172
7.4.3	GCS reconstruction of the CME . . . . .	180
7.4.4	Relationship between dimming, filament, and CME directivity	180
7.5	Discussion and conclusions . . . . .	186
7.6	Development of DIRECD method . . . . .	190
7.6.1	Project summary . . . . .	190
7.6.2	Methods and Analysis . . . . .	190
7.6.3	Resulted CME cone . . . . .	192
7.6.4	Validation . . . . .	195
7.6.5	Summary . . . . .	195
7.7	Conclusion . . . . .	195
<b>8</b>	<b>Conclusions and future work</b>	<b>197</b>
	<b>Bibliography</b>	<b>205</b>

# Glossary

- AIA** Atmospheric Imaging Assembly. 30, 47, 56, 59, 60, 62–68, 72–75, 77, 79, 82, 83, 95, 96, 99, 100, 103–105, 107, 114, 115, 119, 121, 123, 133–135, 137, 139, 143–145, 147, 149, 150, 152, 154–156, 164, 167–169, 173–176, 178, 182, 183, 198
- APL** Applied Physics Laboratory. 70
- AR** Active region. 99, 130, 131, 149, 152, 156, 159, 164
- AURA** Association of Universities for Research in Astronomy. 24
- BD** Base Difference. 58, 76, 77, 79–82, 106, 107, 134, 137, 143, 145
- CACTus** Computer Aided CME Tracking. 37, 40, 58
- CDAW** Coordinated Data Analysis Workshop. 37, 39, 58
- CDS** Coronal Diagnostic Spectrometer. 56
- CH** Coronal hole. 56, 152
- CHEVOL** Coronal Hole Evolution detection algorithm. 62
- CMD** Central meridian distance. 115
- CME** Coronal Mass Ejection. 32
- CoDit** Coronal Dimming Tracker. 62
- CORIMP** Coronal image processing. 37
- DEM** Differential Emission Measure. 127
- DIRECD** Dimming InfeRred Estimate of CME Direction. 161, 190, 195, 196, 199, 201, 202
- DKIST** D. Inouye Solar Telescope. 23, 24
- EIT** Extreme ultraviolet Imaging Telescope. 48, 56, 58, 126
- ESA** European Space Agency. 31, 34, 39, 42, 48, 198, 203

- ESCAPE** Extreme-ultraviolet Stellar Characterization for Atmospheric Physics and Evolution. 204
- EUI** Extreme Ultraviolet Imager. 47, 48, 198
- EUV** Extreme Ultraviolet. 15, 32
- EUVI** Extreme-Ultraviolet Imaging Telescope. 46, 48, 64, 66, 70, 71, 73, 74, 79, 81–85, 103–107, 114, 115, 119, 120, 133–135, 144, 147, 149, 151, 152, 154, 164, 173–176, 195, 198
- EVE** EUV Variability Experiment. 61, 62, 67, 131
- FITS** Flexible Image Transport System. 72
- FOV** Field of View. 48, 50, 120, 180
- FSI** Full Sun Imager. 48, 50
- GCS** Graduated Cylindrical Shell. 45, 46, 161, 162, 169, 180–186, 188, 195, 198, 200
- GLE** Ground level enhancement. 32
- GOES** Geostationary Operational Environmental Satellites. 25, 26, 47, 48, 72, 95, 97, 98, 102, 131, 133, 144, 147, 154, 157, 177–179, 187, 198
- GPS** Global Positioning Satellite. 33
- HEEQ** Heliocentric Earth Equatorial. 74, 75, 173
- HF** High frequency. 33
- HI** Heliospheric Imager. 70
- HMI** Helioseismic and Magnetic Imager. 23, 62–64, 67, 68, 88, 99, 104
- HXR** Hard X-rays. 166, 179, 187
- IDL** Interactive Data Language. 68, 71–74, 78
- IMF** Interplanetary Magnetic Field. 25
- IMPACT** In-situ measurements of particles and CME transients. 70
- ISES** International Space Environmental Services. 29
- LASCO** Large Angle and Spectrometric COronagraph. 24–26, 37–39, 42, 46, 48, 133, 164, 165, 175, 176, 180, 181, 183, 184
- LBR** Logarithmic Base Ratio. 76–78, 80–82, 84, 85, 106, 107, 109, 111, 113, 118–121, 134–137, 139, 143, 145, 148, 155, 156

- LWS** Living With a Star. 34
- MC** Magnetic cloud. 57, 127
- MHD** Magnetohydrodynamics. 30, 146
- NASA** National Aeronautics and Space Administration. 29, 31, 34, 39, 42, 66, 68–71, 105, 203
- NEMO** Novel EIT wave Machine Observing. 58
- NOAA** National Oceanic and Atmospheric Administration. 29, 130, 131, 133
- NSF** National Science Foundation. 24
- NSO** National Solar Observatory. 24
- PIL** Polarity inversion line. 44
- PLASTIC** PLAsma and supraThermal ion composition. 71
- PSP** Parker Solar Probe. 26
- RD** Running Difference. 58
- SDO** Solar Dynamics Observatory. 16, 18, 23, 30, 31, 47, 49, 51, 56, 59–62, 64–68, 72–75, 77, 79, 82, 83, 88, 93, 95, 96, 103–105, 107, 114, 115, 119, 121, 123, 125, 131, 133–135, 139, 143–145, 147, 149, 152, 161, 164, 168, 172–176, 184, 185, 187, 198, 199, 201
- SECCHI** Sun Earth Connection Coronal and Heliospheric Investigation. 70, 73
- SEEDS** Solar Eruptive Event Detection System. 37
- SEP** Solar energetic particle. 32
- SO** Solar Orbiter. 31
- SOHO** Solar and Heliospheric Observatory. 24, 37–39, 42, 45, 46, 48, 51, 56, 58, 126, 161, 162, 164, 165, 175, 176, 180, 181, 183, 184
- SSA** Space Situational Awareness. 34
- SSN** Sunspot Number. 41
- STEREO** Solar TERrestrial RELations Observatory. 16, 24, 37, 39, 40, 42, 45, 46, 48, 51, 52, 64, 66, 69–71, 73, 74, 79, 81–85, 103–107, 110, 113–116, 119, 121–123, 125, 133–135, 144, 147, 149, 151, 152, 154, 161–166, 172–176, 180, 181, 184, 185, 187, 195, 198, 199
- STIX** Spectrometer/Telescope for Imaging X-rays. 102, 166, 168, 170, 177–179

- 
- STP** Solar Terrestrial Probes. 69
- SUIT** Solar Ultra-Violet Imaging Telescope. 203
- SunCET** Sun Coronal Ejection Tracker. 203
- SUVI** Solar Ultraviolet Imager. 25, 26, 47, 48, 198
- SWAP** Sun Watcher using Active Pixel System detector and Image Processing. 47, 48, 198
- SXR** Soft X-ray. 15, 47, 177–179, 187
- SXT** Soft X-ray Telescope. 56, 126
- TMF** Total Magnetic Field. 41

# Introduction

## Overview

Earth-directed CMEs are one of the main drivers of space weather effects, which can trigger a range of effects in geospace, including power network knockouts, disturbances of the radio signal, and various anomalies in the functionality of satellites [e.g., reviews by [Pulkkinen, 2007](#), [Koskinen et al., 2017](#), [Temmer, 2021](#)]. However, Earth-directed CMEs are the most difficult to measure through observations from instruments along the Sun-Earth line, due to strong projection effects [[Burkepile et al., 2004](#), [Gopalswamy et al., 2000](#)]. In addition, their initiation and early acceleration are also difficult to observe as these regions are blocked by the coronagraph’s occulter disk. The analysis of CME manifestations in the low corona is therefore important for our understanding of the initiation mechanism and the early evolution of CMEs.

Coronal dimmings are transient regions of strongly reduced emission in soft X-rays (SXR) [[Hudson et al., 1996](#), [Sterling and Hudson, 1997](#)] and extreme-ultraviolet (EUV) [[Thompson et al., 1998](#), [Zarro et al., 1999a](#)] wavelengths that occur in association with CMEs. In general, they are interpreted as density depletion caused by mass loss during the CME eruption [[Webb et al., 2000](#)]. During the history of their observations, coronal dimmings were widely acknowledged as reliable indicators of front-side CMEs [[Thompson et al., 2000](#)], as they appear on the visible part of the solar disk. More detailed monitoring [[Mandrini et al., 2007](#), [Wills-Davey and Attrill, 2009](#), [Temmer et al., 2011](#), [Dissauer et al., 2018b](#)] and simulations [[Downs et al., 2012](#), [Prasad et al., 2020](#)] show that the locations of the so-called “core” dimmings map the footpoints of the erupting structure, while the spatial growth of the more

wide-spread secondary dimmings indicates the expansion of the overlying magnetic field of the CME expansion in the low corona.

Existing research has already established correlations between various aspects of coronal dimmings (such as intensity, area, and magnetic flux) and key characteristics of the accompanying CMEs, including their mass and speed [Harrison and Lyons, 2000, Harrison et al., 2003, Zhukov and Auchère, 2004, Mason et al., 2016, Krista and Reinard, 2017, Dissauer et al., 2019]. However, despite these established connections, the absence of a unified theoretical structure underscores the need to incorporate additional data and conduct further research to achieve a comprehensive understanding of the intricate relationships between these phenomena.

Therefore, the primary objective of our project is to develop further and refine our understanding of the connections between CMEs and coronal dimmings and to develop a framework for the coronal dimming analysis using multi-viewpoint observations of the solar corona.

This dissertation addresses the following research question:

***How can we use coronal dimmings to estimate properties of the coronal mass ejections (CMEs)?***

- **Relation to CME mass and speed (q1):** How can we use dimmings to estimate the mass and speed of CMEs?
- **Dimming lifetime (q2):** How and when does the solar corona recover after a CME eruption?
- **Relation to CME direction (q3):** How is the evolution and morphology of dimmings connected to the early propagation direction of CMEs?

In this study, we use data from cutting-edge solar missions, including [SDO](#), [STEREO](#), Solar Orbiter, to investigate coronal dimmings and their associated CMEs from different perspectives. A particular focus is made on analyzing off-limb dimmings observed by STEREO satellites—an aspect important for forthcoming L5 missions and early space weather predictions. Based on regression analysis, we con-

firm the relation of coronal dimmings and CME parameters for the off-limb viewpoint, for certain parameters obtaining even higher correlation coefficients than were reported before for dimmings observed on-disk.

Furthermore, we introduce effective methods for studying dimming lifetimes. Our approach considers the evolution of both total dimming regions and their individual components, enabling the independent tracking of core and secondary dimmings evolution. The outcomes provide valuable insights into the processes of coronal recovery after a CME eruption, helping to study how long CMEs are connected to the Sun.

Multi-viewpoint observations of the events also allowed us for the first time to relate the morphology of dimmings to the 3D reconstruction of CME/filament directions. Additionally, we pioneer methods proposing the use of dimmings as an early indicators of the initial CME direction.

These novel contributions advance our understanding of coronal dimmings and their relation to CMEs. Furthermore, they carry substantial implications for the field of space weather forecasting and modeling.

## Thesis Outline

**Chapter 1** is a comprehensive examination of the Sun, addressing its characteristic features and structural composition. In addition, this section serves as a starting point for the discussion of Space Weather research and highlights present-day open questions in solar physics. We also spotlight the ongoing missions specifically designed to investigate these questions.

**Chapter 2** introduces the Coronal Mass Ejections (CMEs), one of the most energetic and disruptive phenomena on the Sun. We will take an in-depth look at the key parameters of CMEs that are critical for their accurate predictions and explore the subtleties that make such predictions a complex endeavor.

**Chapter 3** provides an overview of coronal dimming phenomena, including their nature, formation processes, the historical evolution of observations, and the various detection algorithms used for their analysis. It also highlights the importance of

coronal dimmings for understanding and characterizing the associated coronal mass ejections, which provides a foundation for the subsequent chapters of this thesis.

In **Chapter 4**, we establish a comprehensive framework for coronal dimming analysis dimmings data acquisition, calibration, preprocessing, and implementation of our dimming detection algorithm. We emphasize the versatility of this methodology, which considers both on-disk and off-limb data sources and ensures the reliability and consistency of our analyses. The chapter serves as an essential reference point for further research on coronal dimmings and a detailed roadmap for handling and processing the data. We illustrate the application of these basic techniques with practical examples and show how effective they are in identifying and characterizing coronal dimmings. This methodology forms the basis for the in-depth investigations and findings presented in the following chapters.

**Chapter 5** addresses research question **q1** and aims to statistically correlate the properties of dimmings detected on the solar limb with key CME attributes such as mass and speed. This chapter embarks on a detailed statistical analysis of dimming events associated with CMEs directed toward Earth. By focusing on the coronal dimming events observed by STEREO /EUVI above the limb, we compare their properties and the mass and velocity of the associated CMEs and match our results with those of [Dissauer et al. \[2018b, 2019\]](#), who investigated the same events on the solar disk from the viewpoint of SDO/AIA. The content of this chapter is based on publication in the *Astrophysical Journal* [[Chikunova et al., 2020](#)].

**Chapter 6** delves into the study of dimming recovery time (**q2**). We track four coronal dimming events and introduce two new methods to investigate the recovery process and discuss the possible limitations. The study aims to investigate how long we can reliably track coronal dimmings using single-point observations (both for on-disk and off-limb). We present our results in the collaborative study in *Astronomy & Astrophysics* [[Ronca et al., under review](#)].

In **Chapter 7** we examine the intricate relationship between the evolution of the dimming region, the direction of the filament eruption, and the CME propagation for the X1.0 flare/CME event of October 28, 2021. To establish relationships between the coronal dimming, eruptive filament, and CME, we present a method for deriving

the dominant direction of dimming, 3D reconstructions of the low-lying eruptive filament, and a developed CME at heights of 6 solar radii. This approach allowed the first investigation of the relationship between the direction of dimming, the trajectory of the filament eruption, and the motion of the CME (**q3**). The results are presented in *Astronomy & Astrophysics* [Chikunova et al., 2023].

In answering the various research questions, we consistently interweave the study of **dimming with other signatures of CMEs**. This integrated approach ensures that as we explore specific aspects of CMEs in each project, we simultaneously expand our understanding of how dimmings relate to and are influenced by other eruptive signatures of a CME. This symbiotic exploration provides a comprehensive perspective on the multi-faceted nature of solar events.

Finally, in **Chapter 8**, we provide a general discussion of the findings, and highlight the potential implications and future directions.

"I'll stare directly at the Sun, but  
never in the mirror"

Taylor Swift, 2022

# Chapter 1

## Basics of Heliophysics

The Sun, an irreplaceable source of life-sustaining energy for our planet, also holds the potential for unprecedented violence and disruption. As inhabitants of the Earth, understanding the intricate workings of the Sun and its processes is not only a scientific goal but a critical undertaking to protect our technological infrastructure and our way of life. By unraveling the questions of solar activity, identifying its risks, and attempting to predict its behavior, we embark on a mission of great importance.

To understand the nuances of Space Weather, we must begin with a comprehensive understanding of Heliophysics — a discipline that is the cornerstone of our quest.

### 1.1 An Overview of the Sun

#### 1.1.1 Sun as a star

The Sun, a star of spectral type G2V, is at the center of the solar system and triggers local space weather phenomena. Its gravitational dominance comprises 99.86% of the Solar System's mass and controls the motions of celestial bodies such as planets, asteroids, and comets. The fusion of hydrogen and helium powers the Sun. Each second, the Sun fuses approximately 600 million tons of hydrogen to helium, converting about 4 million tons of matter to energy.

According to [Burgess et al. \[1995\]](#), the elemental composition of the Sun is 74%

hydrogen, 24% helium, and trace amounts of oxygen (0.77%), carbon (0.29%), iron (0.16%), neon (0.12%), nitrogen (0.09%), silicon (0.07%), magnesium (0.05%) and sulfur (0.04%). Positioned at about 25,000 light years from the galactic center, the Sun follows an orbit of  $220 \text{ km s}^{-1}$  around the core of the Milky Way.

The main characteristics of the Sun:

Solar Parameter	Value
Radius	696000 km
Mass	$1.989 \cdot 10^{30} \text{ kg}$
Luminosity	$3.86 \cdot 10^{26} \text{ W}$
Solar age	$4.57 \cdot 10^9 \text{ yr}$
<i>At the surface of the Sun</i>	
Blackbody temperature	5770 K
Gravitational acceleration	$274 \text{ m s}^{-2}$
Density	$2.07 \cdot 10^{-7} \text{ g cm}^{-3}$
Composition	70% H, 28% He, 2% (C, N, O, ...)
Escape velocity	$618 \text{ km s}^{-1}$
<i>At the center of the Sun (modeled)</i>	
Central temperature	$15.6 \cdot 10^6 \text{ K}$
Central density	$150 \text{ g cm}^{-3}$
Central pressure	$2.477 \cdot 10^{11} \text{ bar}$

Table 1.1: Relevant Solar parameters.

Apart from its astrophysical properties, the central role of the Sun in sustaining life and creating space weather effects underlines its exceptional status from a human perspective. Understanding the properties and behavior of solar-type stars, especially our own Sun, provides astronomers with valuable insights into the broader universe. By studying our nearest star, we gain insights into the fundamental processes that govern stellar life cycles, energy production, and the potential habitability of planets, allowing us to appreciate our place in the universe better.

### 1.1.2 Solar interior

The interior of the Sun consists of the core, the radiation zone, the convection zone, and a transition layer known as the tachocline [Vita-Finzi, 2008].

At the heart of the Sun lies the **core**, a region about 200 000 km wide [Moldwin, 2008], where the superior process of nuclear fusion generates the star's primary energy production. In this zone, hydrogen nuclei fuse to form helium, releasing immense energy.

The **radiation zone** extends from about 0.3 to 0.7  $R_{\odot}$  and serves as a channel for transferring the energy produced in the core. Electromagnetic photons play a dominant role in the transfer of this energy through radiative processes. Remarkably, the radiation zone exhibits a unique behaviour: It rotates like a coherent solid body, as shown by helioseismology [Gizon, 2004].

As the energy moves outward, it enters the **convection zone**, where heat is transported mainly by convective motion. This region extends from the radiative zone's outer boundary to the Sun's surface. Convection involves hot plasma rising and cooler plasma sinking, facilitating the movement of energy.

The **tachocline** is a transition layer between the radiative and convective zones characterized by differential rotation. This means that its rotation rate varies with depth, making it different from the solid rotation of the radiation zone and the differential rotation of the convection zone. This layer is believed to be a component of the solar dynamo, which is connected with the solar cycle [Spiegel and Weiss, 1980, Gilman, 2000].

### 1.1.3 Atmosphere of the Sun

The solar atmosphere is defined as the layers from which radiation can escape directly into space. The atmosphere of the Sun consists of three main layers: **photosphere**, **chromosphere**, **corona**, and a **transition region** between the chromosphere and the corona.

The lowest layer, **photosphere**, is about 500 km thick. High-resolution close-up images of the photosphere show its "granulation structure" (see Fig.1-1). Shadowed lanes of cooler, downward-flowing solar plasma encircle upward-moving plasma (granules). The granules are about 1000 km in size and live  $\approx$  5-10 minutes. The bright regions are typically 500 K hotter than the dark regions [Moldwin, 2008].

The images for Figure 1-1 were produced by the largest ground-based telescope,

**D. Inouye Solar Telescope** [DKIST, Rimmele et al., 2020], and released in May 2023, previewing solar data taken during the telescope's first year of operations during its commissioning phase. The exceptional ability of the DKIST telescope to acquire data in unprecedented detail is poised to significantly enhance the comprehension of solar scientists regarding a better understanding of the Sun's magnetic field and the drivers of solar activity.

Closely examining the photosphere, we can unveil prominent dark structures, such as sunspots, that originate within it. The sunspots are cooler and darker than the quiet-sun regions because of the strong concentrations of magnetic field, which prevents convection. The lifetime of individual sunspots or their groups can vary from a few days to months. Usually, they occur in pairs with opposite magnetic polarity [Hoyt and Schatten, 1998]. Sunspots have two parts: the central umbra, which is dark and where the magnetic field is approximately perpendicular to the solar surface, and the surrounding penumbra, which is brighter and where the magnetic field is more inclined [Beckers and Tallant, 1969].

For most of the solar photosphere, the average intensity of the magnetic field is a few Gauss, increasing to a few thousand Gauss for the active regions around the sunspots. Today, we can measure the intensity of the magnetic field on the surface of the Sun with space-based instruments such as the Helioseismic and Magnetic Imager (HMI) [Scherrer et al., 2012] at the **Solar Dynamics Observatory** [SDO; Pesnell et al., 2011].

The next layer, the **chromosphere** (literally, "color sphere"), emits the rosy red color that we can observe only during solar eclipses. The density of the chromosphere is only  $10^{-4}$  times that of the photosphere, making it nearly invisible without special equipment (normally the chromosphere is observed in the  $H\alpha$  and Ca II wavelengths). The chromosphere may play a role in conducting heat from the interior of the Sun to its outermost layer, the corona. It ranges from about 4100 K in the region of temperature minimum at an altitude of 500 km (the boundary with the photosphere) to about 10000 K at an altitude of 2000 km [Avrett, 2003].

Different complex and dynamic phenomena can be observed in the chromosphere: solar flares, prominence and filament eruptions. We will describe them in the next

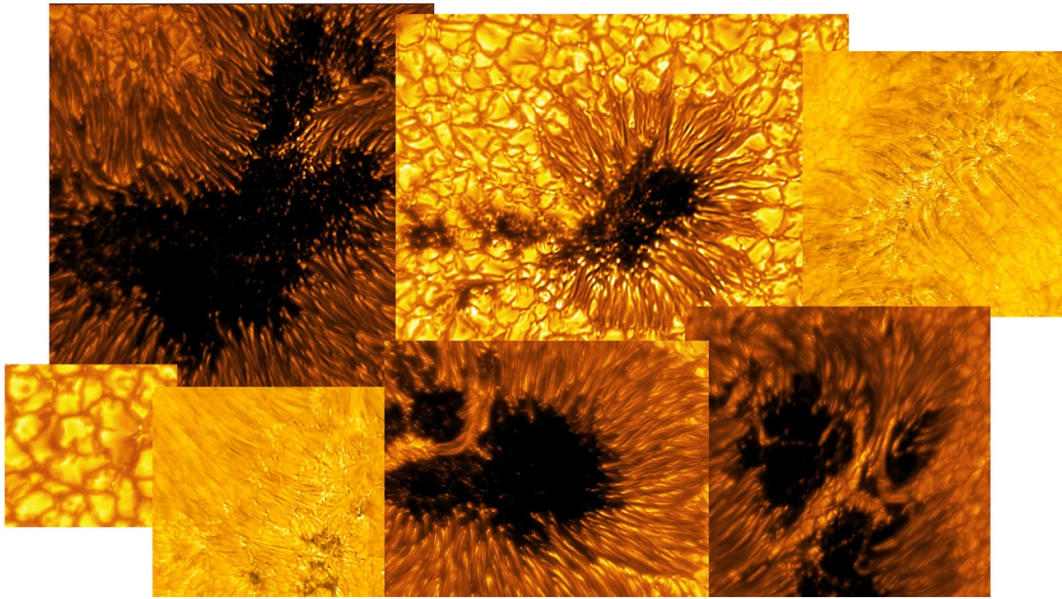


Figure 1-1: A mosaic of solar images in visible light produced by [DKIST](#), showing sunspots and quiet-sun regions of the solar photosphere. Credit: [NSF/AURA/NSO](#).

chapters.

Between the chromosphere with a temperature of about  $10^4$  K and the extremely hot corona with temperatures of about  $10^6$  K lies a crucial region known as the **transition region**. This region, which spans only a few hundred kilometers, exhibits a remarkably rapid change in temperature and density. Across this thin layer, as seen in Fig. 1-3, temperature values increase by two orders of magnitude while density decreases by nearly four orders of magnitude [[Peter, 2002](#)].

The outermost atmospheric layer of the Sun, the **corona**, forms the final stage. At temperatures as high as  $10^6$  K, even hydrogen and helium, the predominant elements, are stripped of electrons and completely ionized. Heavier elements such as iron and calcium can retain only a fraction of their electrons at this extreme heat.

Due to very low density, the corona is much less bright than the photosphere. That is why it is being studied by special instruments, coronagraphs, which cover the disk and filter all the bright light coming from the photosphere. Nowadays, scientists obtain data from the Large Angle and Spectrometric COronagraph [[LASCO](#); [Brueckner et al., 1995](#)] onboard the **Solar and Heliospheric Observatory** [[SOHO](#); [Domingo et al., 1995](#)] satellite and COR1/COR2 coronagraphs [[Thompson et al., 2003](#)] onboard the **Solar TERrestrial RELations Observatory** [[STEREO-A](#);

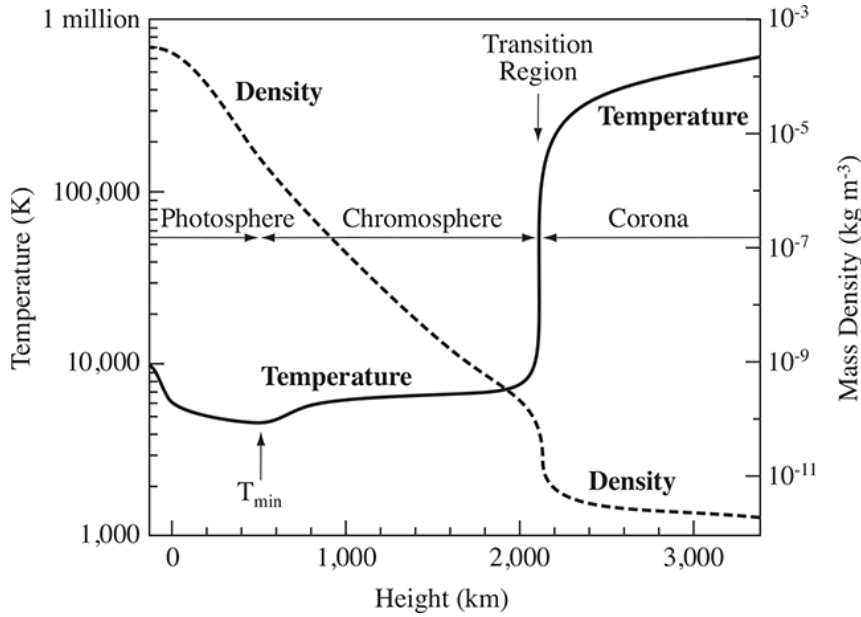


Figure 1-2: Profiles of the mean value of temperature and density as a function of height in the solar atmosphere according to the VAL model (courtesy Eugene Avrett, Smithsonian Astrophysical Observatory).

[Kaiser et al., 2008](#)] satellite.

Figure 1-3 depicts an assembly comprising the coronagraphic observation via [LASCO](#), the EUV imagery from Solar Ultraviolet Imager [[SUVI](#); [Darnel et al., 2022](#)] onboard **Geostationary Operational Environmental Satellites (GOES-16)**, and the processed ground-based image of the August 21, 2017 solar eclipse. This arrangement elucidates the interrelation between the configurations within the extensive corona and their corresponding source regions on the solar disk. This composition shows the connections between coronal structures and the source regions on the solar disk and effectively bridges the informational void typically encountered in coronagraphic observations.

The solar corona extends very far into space. Because of the high temperature, the particles of the corona move at very high speed, large enough to escape the gravity of the Sun (the escape velocity is  $618 \text{ km s}^{-1}$  for the low corona). These particles generate a stream - the solar wind. The solar wind pulls the coronal magnetic field out into the heliosphere, forming the Interplanetary Magnetic Field (IMF), the crucial link between the solar atmosphere and the Earth system [[Owens and Forsyth, 2013](#)]. Eugene Parker, a physicist from the University of Chicago,

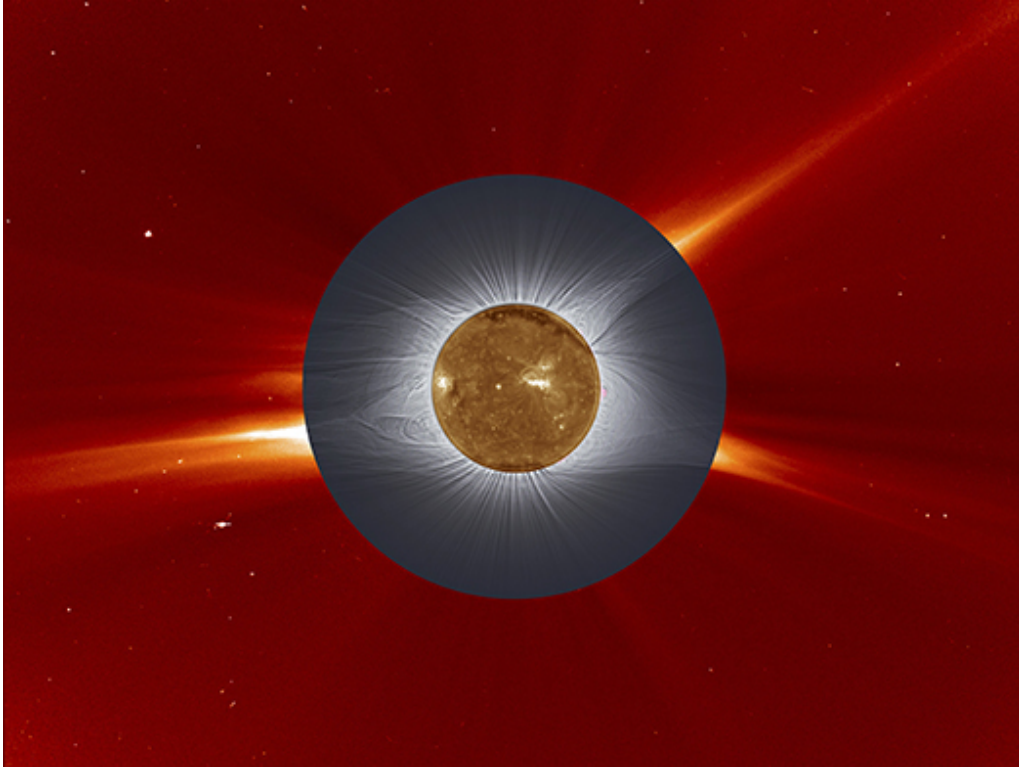


Figure 1-3: A combination of the August 21, 2017 solar eclipse image between an EUV image from [GOES-16/SUVI](#) at  $195 \text{ \AA}$  and an image from the [LASCO C2](#) coronagraph, occulting up to  $2.5 R_{\odot}$  from [Pasachoff et al. \[2018\]](#).

was the first to develop the solar wind concept. Today, we have the **Parker Solar Probe** [[PSP](#); [Raouafi et al., 2023](#)] mission, traveling through the solar corona since 2018 to explore the fundamental origins of this phenomenon.

Why the corona is so hot is still an open question. Energy cannot move from the cooler photosphere to the hotter corona through regular heat transfer because that would break the rules of thermodynamics. Among the numerous proposed theories, two prominent mechanisms have been considered for the transmission of heat from lower regions to the corona: 1) wave heating, in which different types of waves create turbulence in the convection zone; 2) magnetic heating, in which energy is released by magnetic reconnection in the form of solar flares of different sizes [[Erdélyi and Ballai, 2007](#)]. Scientific discourse goes around the observation that, with the exception of Alfvén waves, most waves dissipate or refract before reaching the corona. Alfvén waves, in contrast, demonstrate resilience within the corona. Consequently, the efficacy of the first theory becomes apparent only when

considering a non-uniform corona characterized by density fluctuations. Meanwhile, the development of the second theory requires an approach, separating the magnetically closed corona (encompassing the quiet Sun and active regions) from the open corona (encompassing coronal holes and the solar wind) [Klimchuk, 2015]. However, the microflare heating may not offer sufficient power, which introduces a layer of complexity to the ongoing scientific inquiry. Consequently, additional research efforts and new missions are imperative to address these outstanding questions to advance our understanding of the coronal heating.

### 1.1.4 Solar cycle

There is a periodic 11-year change in the Sun's activity and appearance, which can be noticed by the observations of sunspots. Theoretically, the average period of the solar cycle is 11.2 years, but its duration can vary between 8 and 15 years. For the first time, the solar cycle was determined by Heinrich Schwabe in 1843 [Khazanov, 2016]. His discovery initiated the work of Johann Rudolf Wolf to conduct daily observations of the Sun and extend the works of previous years [Wolf, 1861]. He invented a method for the calculation of the solar activity cycle based on counting the number of sunspots  $R$ :

$$R = k \cdot (10G_n + S_n), \quad (1.1)$$

Here,  $G_n$  is the number of sunspot groups (regions),  $S_n$  is the total number of individual spots in all the groups, and  $k$  is a scaling factor that corrects for seeing conditions.

The formula  $R$  is still being used in solar cycle predictions and analysis (detailed report about solar cycle studies with the history perspective in Clette et al. [2014]). This choice isn't necessarily due to the agreement on its superiority but rather stems from the extensive historical data it offers. Increasing efforts are being made in solar physics to reconcile the differences in sunspot numbers and provide a reliable record from 1610 to the present. The cyclical behavior of the number of sunspots and differences in calculation can be seen in Fig.1-4.

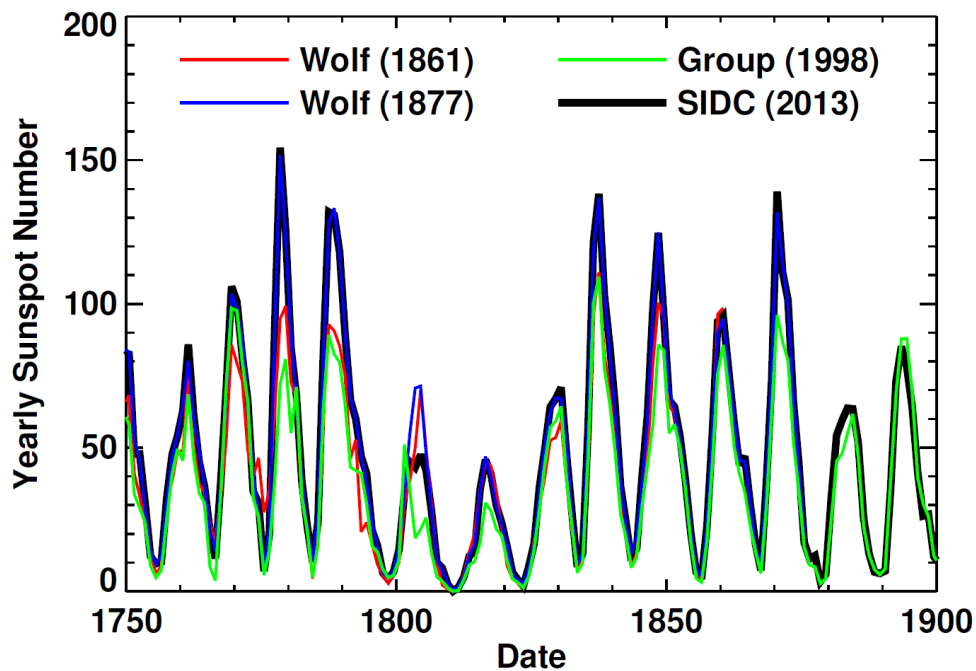


Figure 1-4: Sunspot number revisions. Yearly sunspot numbers as reported by Wolf [1861] (red line), Wolf [1877] (blue), Hoyt and Schatten [1998] (green), and by SILSO in 2013 (black). These sunspot numbers have disagreements as late as 1900. The plot from Hathaway [2015].

Solar cycles have been designated with numbers since 1761, and presently, we are at the inception of the 25th cycle that started in December 2019. The peak point of sunspot counts is termed solar maximum. During this phase, sunspots mark zones with robust magnetic fields, which lead to occurrences like solar flares and coronal mass ejections, thereby releasing heightened radiation and energy from the Sun. Conversely, the period when only a limited number of sunspots emerge is called solar minimum.

At the beginning of the solar cycle, sunspots are usually at mid-latitudes in both hemispheres (opposite polarities in the hemispheres), and as the cycle progresses, they appear increasingly at lower latitudes until there are no sunspots at the end of the cycle. In the next cycle, the process repeats, but the orientation of the sunspots reverses. Therefore, the magnetic sunspot cycle is 22 years.

Forecasting the solar activity behavior became the subject of many scientific papers to predict the solar cycle 25 behavior [Li et al., 2015, 2021, Yan et al., 2021, Benson et al., 2020]. Cycle 25 comes after the weak Cycle 24 (low number

of sunspots), which came after the deep minimum [Russell et al., 2010]. Mostly, the scientists expected a similarly underwhelming performance for the current cycle. Surprisingly, it gained momentum in 2022, steadily outpacing the official predictions (see Fig.1-5). Figure 1-5 shows daily observational sunspot number, monthly mean sunspot number, and its prediction for Cycle 25: official by NOAA/NASA/ISES predicted in 2019 and the current updated method by McIntosh et al. [2023], based on defining the solar cycle not by peaks, but by so-called terminator event. Various reviews of methods of predicting solar activity have been published for the last solar cycles [e.g., Hathaway, 2010, Pesnell, 2012, 2020, Petrovay, 2020].

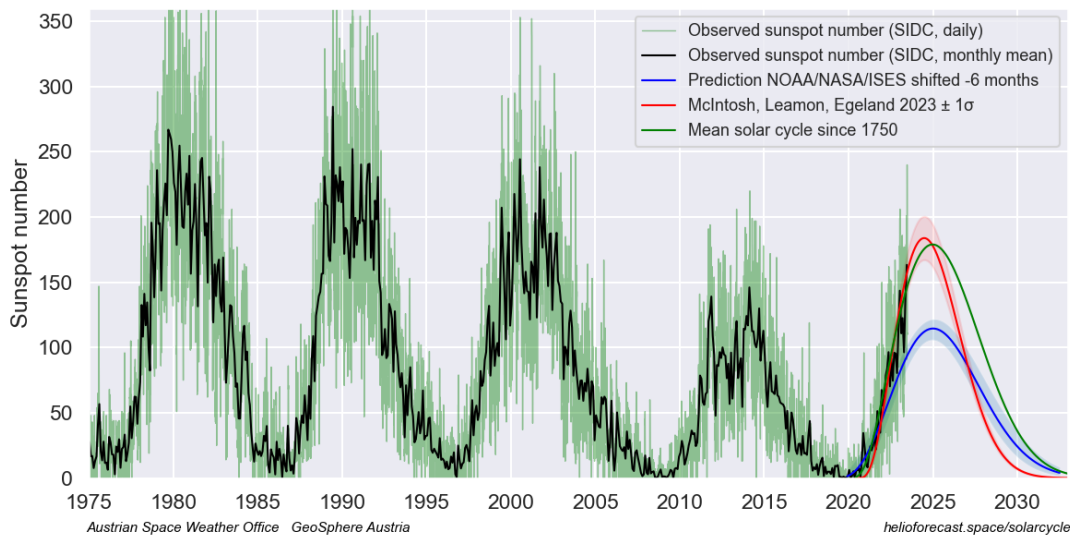


Figure 1-5: Daily updated predictions for the sunspot numbers for solar cycle 25, by the NOAA/NASA/ISES panel (from 2019) and from a prediction by McIntosh et al. [2023]. The plot is from Helio4cast.

### 1.1.5 Magnetic field of the Sun

The average magnetic field strength on the solar surface is about 1 Gauss. However, the strongest magnetic fields occur near sunspots and reach about  $\approx 3000$  G. The sunspots result from the pairing of opposite magnetic polarities [Hale, 1908] and serve as markers for the solar cycle. The solar wind carries charged particles beyond the solar surface, interacting with the Earth’s magnetosphere and causing magnetic disturbances.

The current explanation for the nature of the solar cycle comes from the field of

magnetohydrodynamic (MHD) dynamo theory. This theory deals with the complicated nonlinear process that governs the generation and transformation of magnetic fields. It involves a complicated interplay between the plasma currents in the solar interior and the magnetic field itself. The solar cycle arises from the generation and cyclic replenishment (fed by the energy in the plasma motions) of two magnetic field components: the toroidal and poloidal components [Muñoz-Jaramillo et al., 2009]. The first component arises from the stretching of an originally poloidal field due to the differential rotation of the Sun, a phenomenon known as the dynamo  $\Omega$ -effect [Parker, 1955]. The sunspots that appear on the poloidal field (whose radial component is observed as a vertical field on the solar surface) must be regenerated from this toroidal field in a process traditionally called the dynamo  $\alpha$ -effect.

Typical magnetic field strengths, as detected by HMI, for various parts of the Sun are:

<b>Part of the Sun</b>	<b>Magnetic Field Value</b>
Polar Field	1 – 2 G
Sunspots	3000 G
Prominences	10 – 100 G
Chromospheric plages	200 G
Bright chromospheric network	25 G

Table 1.2: Magnetic field strengths for different parts of the Sun.

Figure 1-6 shows the magnetic field lines overplotted on the SDO AIA 193 Å image on August 26, 2017. The highest density of magnetic fields is concentrated around the prominent bright areas observable on the Sun, known as magnetically strong active regions. Many of these magnetic field lines establish connections between different active regions. Spacious dark regions, coronal holes, represent the regions of open magnetic fields where the solar wind escapes the Sun into space at high speeds. The location and population of coronal holes also change with the solar cycle. During the solar maximum phase, a reversal of magnetic fields occurs on the Sun, leading to the formation of new coronal holes near the poles with opposite magnetic orientations. These coronal holes subsequently expand in both size and quantity, moving farther and farther away from the poles as the Sun again

approaches the solar minimum phase [Harvey and Recely, 2002].

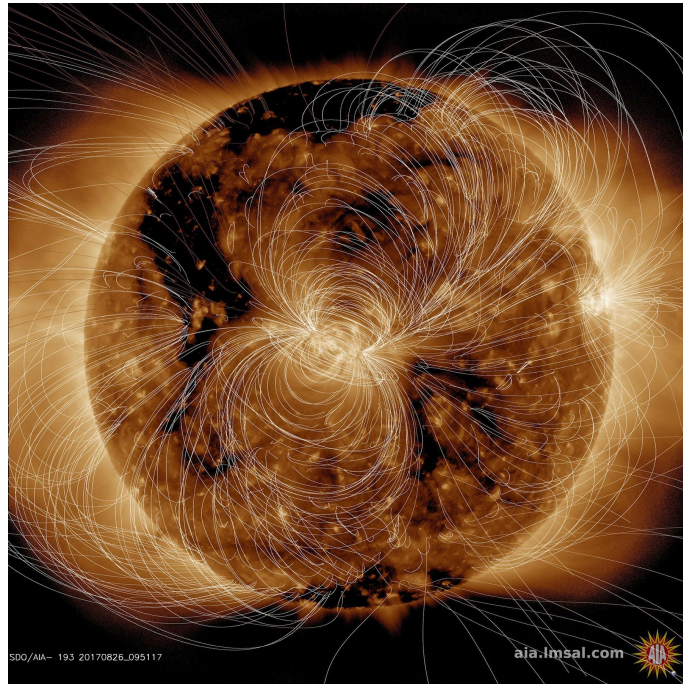


Figure 1-6: The illustration of the magnetic field lines of the Sun overplotted the 193 Å image from SDO on August 26, 2017. Imagery provided courtesy of NASA.

The goal of the international collaborative mission between ESA and NASA, **Solar Orbiter** [SO; Müller et al., 2020], launched in 2020, is to take unprecedented close-up images of the Sun, including for the first time its polar regions, analyzing the composition of the solar wind and establishing a link between its origin on the solar surface and its properties. Solar Orbiter’s magnificent high-resolution data have already contributed to a significant discovery: scientists have identified numerous tiny jets of material emerging near the coronal hole [Chitta et al., 2023]. These jets have a relatively short duration, between 20 and 100 seconds, and eject plasma at a speed of about  $100 \text{ km s}^{-1}$ . The researchers found that these jets provide enough energy and plasma to potentially drive a significant portion of the solar wind, at least during quiet periods, challenging previous assumptions that the solar wind forms only in a steady, continuous flow. As the mission progresses, the spacecraft will gradually incline its orbit toward the polar regions, giving us an entirely new perspective.

## 1.2 Space Weather and its effects

The term Space Weather generally refers to conditions on the Sun, in the solar wind, and within Earth's magnetosphere, ionosphere, and thermosphere that can influence the performance and reliability of space-borne and ground-based technological systems and can endanger human life or health [Schwenn, 2006].

The activity of the Sun results in cyclic variations that cause more to less frequent active events on the observable solar surface. These high-energy events, resulting from shifts in the Sun's magnetic field, travel through our solar system and interact with the atmospheres of the planets. These interactions can cause geomagnetic disturbances with modern societal impacts.

Short bursts of extreme ultraviolet (EUV) rays and X-rays from the Sun reach Earth within 8 minutes. These rays heat and ionize the upper layers of the atmosphere, triggering disturbances that affect the propagation of radio signals. Such changes can disrupt shortwave signals, and even strong radio bursts associated with solar flares can introduce interference into wireless communications systems [Lanzetta, 1999].

Solar energetic particles (SEPs) can be rapidly ejected from the Sun, accelerating in the corona and reaching Earth with significant energies within 1-2 hours. These particles, often produced by shock waves associated with CMEs or solar flares [Cliver, 2008], pose a threat to astronauts, spacecraft integrity, and computer systems. Recent research has identified widespread SEP events that have the potential to fill the entire heliosphere [Dresing et al., 2012, Gómez-Herrero et al., 2015, Lario et al., 2016, Dresing et al., 2023]. Specifically, 10 October 2017 documented as a widespread event that marked the first ground level enhancement (GLE) observed simultaneously on the surface of two planets, Earth and Mars [Guo et al., 2018]. Moreover, on 28 October 2021, a rare GLE event was recorded simultaneously on Earth, the Moon, and Mars [Guo et al., 2023].

Occasionally, the Sun's surface erupts a large part of the solar atmosphere, containing magnetized plasma. These eruptive events, called coronal mass ejections (CMEs, we fully introduce them in Section 2), contain large amounts of material

and move it away from the Sun at velocities up to  $3000 \text{ km s}^{-1}$  [Vršnak and Žic, 2007, Gopalswamy et al., 2009] and can reach Earth even within 15-18 hours. This entire study is devoted to gaining a deeper understanding of their initial evolution to improve the accuracy of space weather predictions. Earth-directed CMEs can create severe magnetic storms that lead to a multitude of space weather effects in geospace, including power network knockout, disruption of the Earth's navigation systems, and various anomalies of satellites [e.g., reviews by Pulkkinen, 2007, Koskinen et al., 2017, Temmer, 2021].

During the declining phase of the solar cycle in October 2003, a complex group of sunspots caused an unexpected increase in solar activity, resulting in several CMEs and solar flares [Pulkkinen et al., 2005]. These events triggered geomagnetic storms that disrupted radio frequency communication systems (HF) causing multiple flights rerouting, induced fluctuations in the power grid, and affected satellite networks [Xue et al., 2023]. In total, 47 satellites experienced service disruptions, while Global Positioning Satellite (GPS) users experienced failures that resulted in service outages.

An accidental reentry of 38 Starlink satellites occurred in early February 2022 during not severe but moderate geomagnetic storms. The unresolved complex structures of coming CMEs caused the magnetic disturbances at unexpected timing. This loss underscores the importance of better understanding the minor CME structures to improve current space weather prediction capabilities. During this event, an increase in drag of about 50% was detected at an altitude of about 200 km, which affected the normal safety operation of the satellites [Kataoka et al., 2022].

At the same time, solar storms play the role of Earth's shield by Forbush decreases, diminishing the intensity of energetic particles streaming in from the Galaxy [Forbush, 1946]. During the maximum of the solar cycle, the Earth is affected by strong and intense space weather disturbances while experiencing enhanced protection from cosmic rays. The enhanced solar magnetism plays a crucial role in protecting our planet.

Human technologies have advanced considerably in the last century, making society more sensitive to solar activity. We live in the era of satellites and global



# Chapter 2

## Coronal Mass Ejections

### 2.1 Overview of CMEs

Coronal Mass Ejections (CMEs) are one of the most violent and dangerous eruptive phenomena on the Sun and are also considered the main drivers of space weather effects. CMEs are huge masses of magnetized plasma that are ejected from the Sun into interplanetary space at velocities ranging from a few  $100 \text{ km s}^{-1}$  to  $> 3000 \text{ km s}^{-1}$  [Gopalswamy et al., 2009, Webb and Howard, 2012]. They can eject  $\approx 10^{15} \text{ g}$  of coronal material and have an embedded magnetic field (frozen in flux) stronger than the usual interplanetary magnetic field ejected by the Sun. CMEs are formed by the large release of magnetic energy in a coronal loop ( $\sim 10^4 \text{ km}$ ), expand to cover a significant portion of the solar surface, and then enlarge from the lower corona into interplanetary space, becoming the largest eruptive phenomenon in the solar system.

Coronagraphs are used in the study of CMEs. These instruments are designed to obstruct the intense direct white light emanating from the photosphere as it passes through the solar disk.

The first CME was discovered by the coronagraph aboard the Orbiting Solar Observatory, OSO-7 [Koomen et al., 1975], in 1971, 112 years after solar flares were first observed. This delay resulted from many conflicting theories identifying the source of various shock wave-related phenomena (EIT waves, Moreton waves, type II radio bursts, and other space weather disturbances) [Gosling, 1993].

The white light emissions from the solar corona result from Thomson scattering of photospheric radiation by the free electrons in the corona. Increased brightness values indicate a localized increase in coronal electron density along the observer's line of sight. It is worth noting that the intensity of Thomson scattered radiation depends on two key factors: the incident photospheric radiation interacting with the electrons and the angle formed between the direction of incidence and the observer's line of sight. Therefore, CMEs are preferentially observed when they are closer to the plane of the sky.

Continuous observation of CMEs by a variety of ground- and space-based coronagraphs has enabled the compilation of an extensive database of thousands of recorded CME events, which has paved the way for comprehensive statistical analyses of the properties of CMEs, as shown in [Chen \[2011\]](#).

Also, other observations indicate that CMEs can be observed in different wavelengths, such as soft X-rays, extreme ultraviolet, radio, and others [[Hudson and Cliver, 2001](#)] (see Section 2.5 for more details).

The importance of CME research transcends the boundaries of solar physics for several reasons. First and foremost, these eruptions are linked to disturbances of the solar wind, which subsequently have noticeable effects on planetary magnetospheres, comets, and cosmic rays. This connection not only improves our understanding of the Sun's influence on the heliosphere more broadly but also highlights the importance of CMEs in the context of space weather and its potential impact on various space-based systems and the terrestrial environment.

The possibility of analogous mass ejections occurring on other stars stimulates thought about their potential impact on exoplanetary environments. These considerations extend beyond the boundaries of the solar system and stimulate interest in their applicability in a broader astrophysical context.

Thus, studying the CMEs represents an important area of research, not only because of their profound implications for solar physics but also because of their far-reaching consequences in the field of space weather and astrophysics, which ultimately shed light on the dynamic interplay between stars and their environments.



Figure 2-1: A rare observation of the coronal mass ejection during the natural total solar eclipse on 14 December 2020 from Argentina. The image is a processed composite of 55 calibrated exposures ranging from 1/640 to 3 seconds. Credit: Miloslav Druckmuller, Andreas Moller, published in [NASA's Astronomy Picture of the Day](#).

## 2.2 Properties of CMEs

Scientists measure various properties of CMEs, including their occurring rates, location, angular width, velocity and acceleration, energy, and mass ([Webb et al. \[2004\]](#), [Vourlidas et al. \[2011a\]](#)). For over 25 years, [LASCO](#) coronagraph [[Brueckner et al., 1995](#)] onboard [SOHO](#) has been diligently observing the Sun. Its continuous observations initiated the development of five catalogs of CMEs, including manual [CDAW](#) [[Yashiro et al., 2004](#)], and automatic [CACTus](#) [[Robbrecht et al., 2009](#)], [SEEDS](#) [[Olmedo et al., 2008](#)], [ARTEMIS](#) [[Boursier et al., 2009](#)], and [CORIMP](#) [[Byrne, 2015](#)]. This marked the beginning of studying the dependence of CME properties on the solar cycle [[Gopalswamy et al., 2004](#)]. Furthermore, coronagraphs [COR2 A](#) and [B](#), located on the twin probe [STEREO](#), conducted synchronized dual-point stereoscopic observations of CMEs from 2007 to 2014 until the loss of the [STEREO-B](#).

CME observations suffer strongly from projection effects, i.e., they are 3D structures projected in two dimensions in an optically thin medium [Burkepile et al., 2004]. This leads to distortions in their appearance and complicates the theoretical interpretation and determination of their properties.

### 2.2.1 Morphology

One of the fundamental properties of CMEs is their morphology close to the Sun, as interpreted from direct observations in white light by coronagraphs.

Although the term "mass ejection" suggests that a CME's primary and critical component is matter, the CME is a magnetic structure. There is a standard three-part model of their appearance, identified before the SOHO coronagraph observations era: a bright front, a dark cavity, and a bright core [Illing and Hundhausen, 1985, Harrison et al., 1990]. This structure is interpreted as a flux rope, i.e., a magnetic configuration of twisted field lines that fill the dark cavity region.

- The **bright front** moving away from the Sun is interpreted as outward moving structures with densities higher than the surrounding medium.
- The **cavity** is dark, as inside the flux rope, the gas pressure and density are lower due to additional magnetic pressure  $B_m = B^2/8\pi$ .
- The **bright core** is the innermost part of the flux rope, often identified as an erupting filament material [Vourlidas et al., 2012], upheld against gravitational forces by the upward Lorentz force at the low points or dips.

Figure 2-2 shows a clear three-part CME structure for 27 February 2000 event, observed by LASCO C3 coronagraph.

This three-part structure is the standard model for morphology of CMEs. However, observations show that only  $\approx 30\%$  of CMEs have all three parts [Webb and Hundhausen, 1987]. Some events do not begin to form a filament in the structure before the event or are not even associated with the filament at all [Chen, 2011, Howard et al., 2017]. Recent studies [e.g., Howard et al., 2017, Veronig et al., 2018,

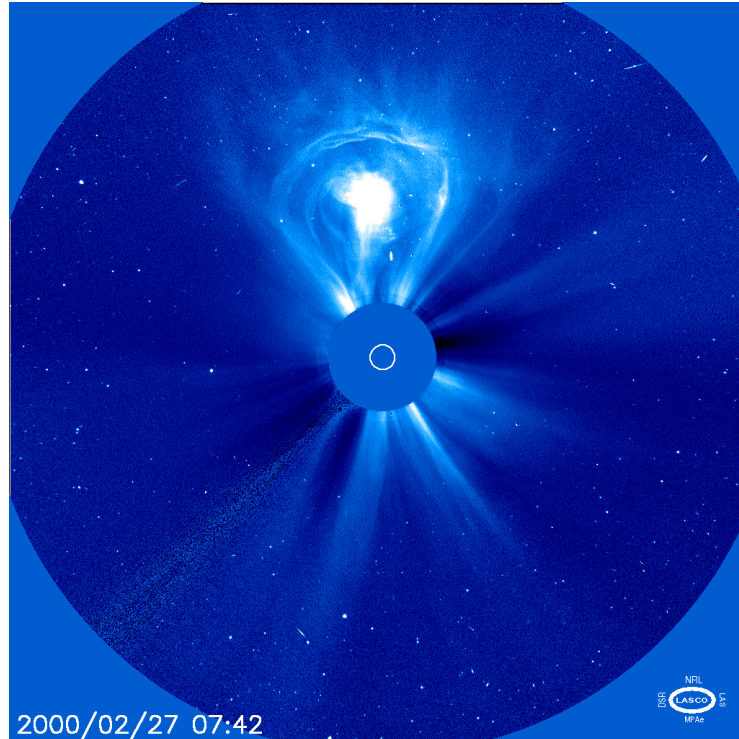


Figure 2-2: Looking like a light bulb, this classic image from LASCO coronagraph shows the core of the CME, surrounded by a cavity, and then bordered by the leading edge of the CME on 27 February 2000. The solid disk in the center is the occulting disk, and the white circle represents the solar disk. Credit: ESA/NASA/SOHO

Song et al., 2018] have also questioned the fundamental nature of the CME core and its connection to the filament, suggesting that the core is a rising flux rope.

Moreover, this traditional model does not include the **shock** (see Fig.2-3) later identified by sensitive observations of the solar corona from SOHO and STEREO [Ontiveros and Vourlidis, 2009]. The shock front appears as a contour or boundary delineating a faintly illuminated region containing displaced or bent coronal streamers and rays [Gopalswamy et al., 2009], but as a faint structure, it can easily be lost in the background corona. A shock forms when the speed of the CME ejecta relative to the surrounding solar wind exceeds the velocity of the fast-mode wave.

### 2.2.2 Occurrence rate

The CME catalog in the NASA CDAW data center shows that the occurrence of CMEs near the solar minimum is  $\approx 0.5$  per day and near the solar maximum is  $\approx 6$  per day (the result for more than 13000 CMEs during solar cycle 23). In parallel, for

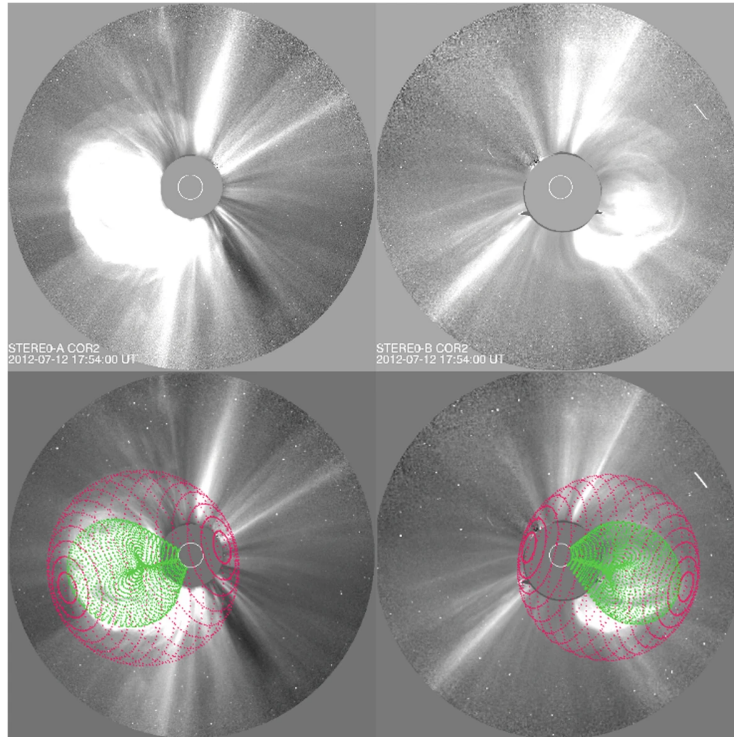


Figure 2-3: Forward model fitting of CME ejecta front and CME-driven shock front of July 12, 2012 event based on [STEREO-A COR2](#) (left) and [STEREO-B COR2](#) (right) images, along with (bottom) and without the raytrace mesh. The green mesh shows the GCS fitting to the eject front, whereas the red mesh shows the spheroid fitting to the shock front. Image from [Zhang et al. \[2021\]](#).

the same observation period with the automated software [CACTus](#), the rate values are about 2 per day during solar minimum and increase to about 8 per day near solar maximum ([Robbrecht et al. \[2009\]](#)).

The collective evidence from observations over complete solar cycles consistently confirms that the occurrence of CMEs is closely related to the solar activity cycle [[Webb and Howard, 1994](#), [Robbrecht et al., 2009](#), [Lamy et al., 2019](#)]. This correlation is shown in the middle panel of [Figure 2-4](#), as well as the correlation of CME occurrence with the total magnetic field and the radio flux at 10.7 cm.

It is also worth noting that CMEs vary in their occurrence rate as well as their characteristics over different solar cycles. In contrast to flare rates and their associated properties, which have remained relatively stable throughout previous solar cycles, CME characteristics during Solar Cycle 24 have shown significant differences, as illustrated by recent statistical findings presented by [Lamy et al. \[2019\]](#). For the

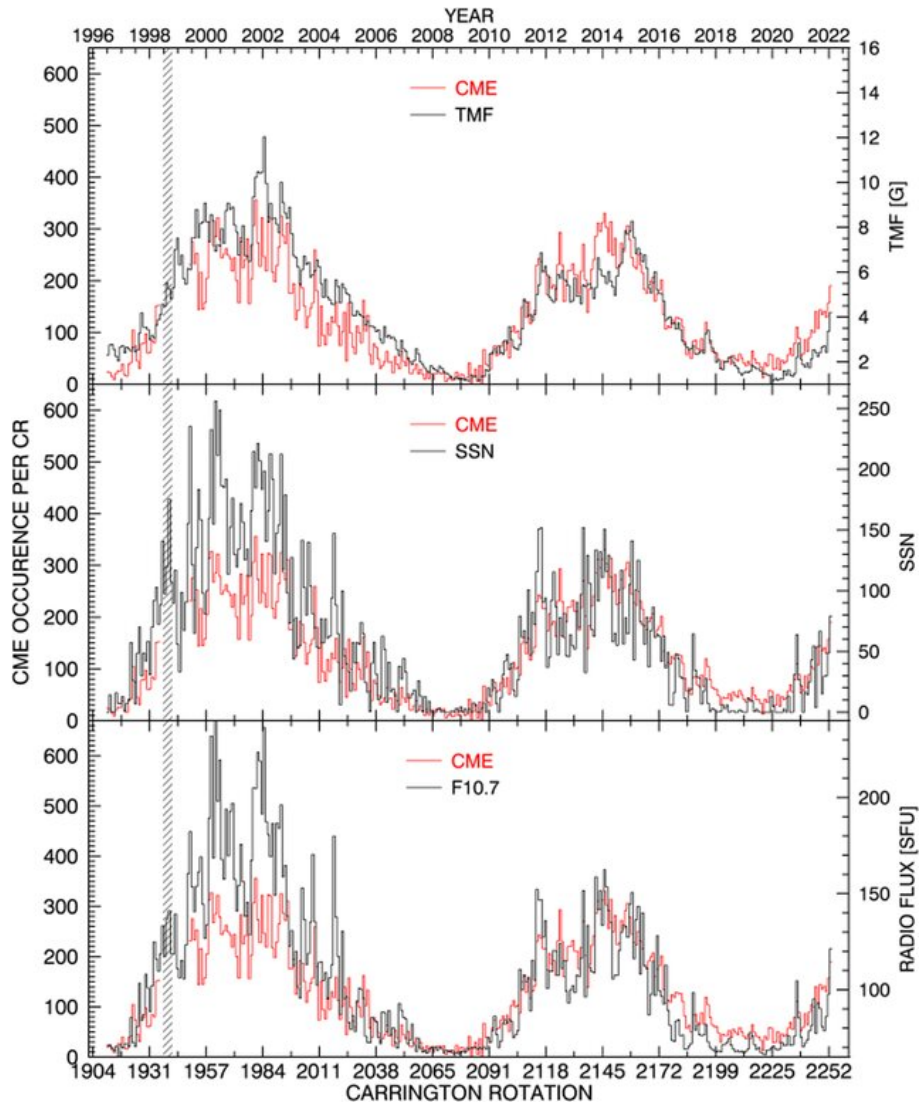


Figure 2-4: Temporal variation of the CME occurrence rate from 1996 to 2022 per Carrington rotation compared with those of the total magnetic field (TMF), the sunspot number (SSN), and the radio flux at 10.7 cm (F10.7) expressed in Solar Flux Unit ( $10^{22} \text{ W m}^{-2} \text{ Hz}^{-1}$ ). Credit: [Lamy and Gilardy \[2022\]](#)

solar minimum of Solar Cycle 25 the base level of the occurrence rate of CMEs was significantly larger than during the two previous minima [[Lamy and Gilardy, 2022](#)].

### 2.2.3 Angular width

Categorically, two types of CMEs can be distinguished based on their angular width: narrow CMEs with an angular span of less than  $20^\circ$  [[Bronarska et al., 2018](#)] and normal CMEs exceeding this threshold, i.e., very narrow CMEs have an elongated jet-like shape, whereas normal CMEs resemble closed loops. Through statistical

analysis, it was found that during solar maximum, narrow CMEs tend to have higher velocities compared to normal CMEs. However, it is noteworthy that their maximum velocity remains lower. This observation suggests that there can be different acceleration mechanisms for these two CME categories [Yashiro et al., 2003].

On average, from the *LASCO* coronagraphs field of view, CME fronts reveal an angular width of about  $30^{\circ}$ - $65^{\circ}$ . For the last cycles, CMEs were found to be wider compared to solar cycle 23 [Lamy et al., 2019].

Halo CMEs, extending to nearly  $360^{\circ}$  for the view from *LASCO*, can propagate toward or away from the Sun-Earth line. When halo CMEs erupt from a direction aligned with the Earth, they pose a significant risk of forming geomagnetic storms [Cid et al., 2012]. These events, which are extremely important for space weather, are the most complicated to study with data from a single spacecraft because of strong projection effects. Previously, the halo appearance of CMEs was thought to be due to geometric projection effects, but Kwon et al. [2015] discovered that 66% of events are observed as halos from different angles in *SOHO*, *STEREO-A*, and *STEREO-B* when they occur in quadrature configuration from 2010 to 2012.

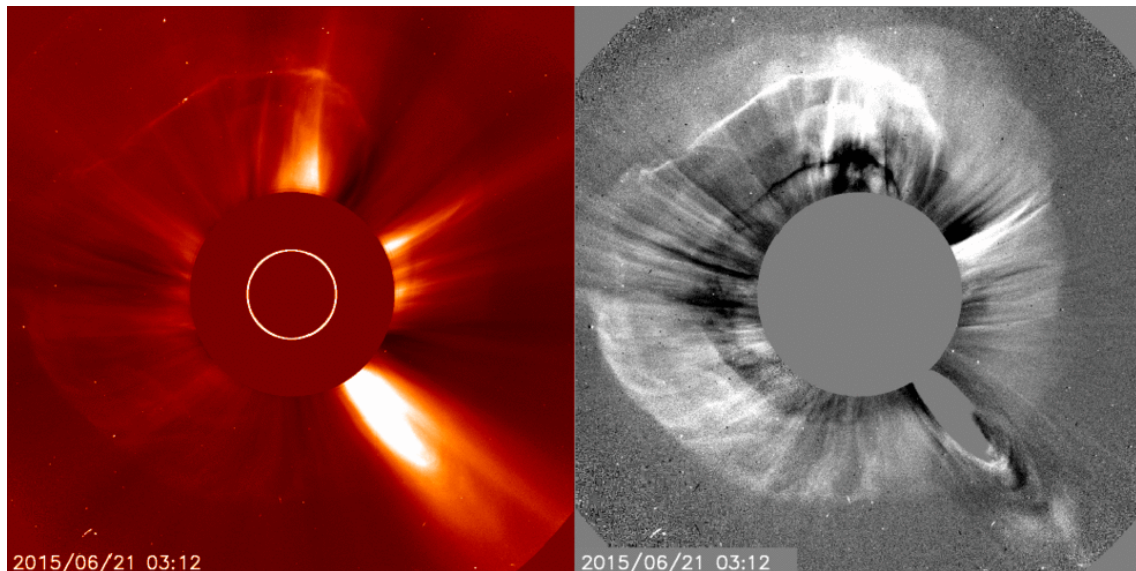


Figure 2-5: The example of full-halo CME on 21-Jun-2015 by *LASCO* coronagraph in white-light (left) and base difference (right) images. Credit: *ESA/NASA/SOHO*

### 2.2.4 Mass

Knowing the Thomson scattering nature of the intensity observed by the coronagraphs, the mass of the CME can be calculated (Billings [1966]), assuming that all CME parts are in the plane of the sky. Thus, if only the CME is located exactly on the solar limb, the CME mass can be estimated correctly. Otherwise, the method provides only an underestimation of mass (Chen [2011]).

In general, the average mass of a CME falls in the range of  $10^{14}$  -  $4 \times 10^{16}$  g, with an average of  $3 \times 10^{15}$  g [Hudson et al., 1996b, Vourlidas et al., 2010, 2011b, Lamy et al., 2019].

### 2.2.5 Speed and energy

On average, the CME velocity (projected in the plane of the sky) is  $300$ - $500$  km s<sup>-1</sup>, and some events can reach  $3500$  km s<sup>-1</sup> [Vourlidas et al., 2010, Lamy et al., 2019]. The kinetic and potential energies, in general, are  $10^{22}$ - $10^{25}$  J [Emslie et al., 2004]. Despite the Sun's escape speed of about  $618$  km s<sup>-1</sup>, many CMEs with lower speeds still escape into the space. The trajectory of these CMEs defies simple ballistic motion, as the interplay of various forces becomes evident. Close to the Sun the magnetic reconnection is believed to be dominant driver of the initial propagation of a CME, while aerodynamic drag takes over at larger heights [Michalek et al., 2015]. Notably, some studies [e.g., Lewis and Simnett, 2002] suggest that slow CMEs are primarily lifted by the surrounding solar wind, even independently of magnetic energy amount in the pre-event corona.

### 2.2.6 Acceleration

Statistical studies by Vršnak et al. [2007], Bein et al. [2011] obtained values for the maximal accelerations of CMEs of  $10$ - $1000$  m s<sup>-2</sup>, mean values of about  $800$  m s<sup>-2</sup>, respectively. The acceleration phase duration is proportional to the source region dimensions; i.e., compact CMEs are accelerated more impulsively [Vršnak et al., 2007]. The most powerful events reach accelerations  $\approx 5000$  m s<sup>-2</sup> [e.g., Bein et al., 2011, Vršnak et al., 2007, Temmer et al., 2008, Veronig et al., 2018].

## 2.3 Initiation mechanisms

For more than three decades, the quest to comprehend the mechanisms behind the rapid formation of CMEs has presented a challenge to solar physicists. These energetic eruptions consistently originate within filament channels, where essential free energy is stored, and are typically accompanied by multi-ribbon flares, prominence eruptions, interplanetary shocks, and the release of solar energetic particles. The distinct magnetic configuration of filament channels, characterized by intense magnetic nonpotentiality tightly aligned along a polarity inversion line (PIL) [Martin, 1998], plays a pivotal role in these events, yet the precise topology of this configuration remains a subject of controversy.

Eruption initiation is attributed to two principal mechanisms. On one hand, there is the notion of a loss of equilibrium or ideal instability, a concept put forth by Forbes and Isenberg [1991], Török and Kliem [2005] and extensively discussed by Démoulin et al. [2002], Kliem et al. [2014]. This instability arises from forces like the magnetic pressure force or Lorentz self-force, induced by the curvature of a flux rope [Titov and Démoulin, 1999]. Alternatively, the trigger for eruptions is attributed to the magnetic reconnection [Amari et al., 2000, Moore et al., 2001, Roussev et al., 2007, Titov et al., 2008]. While the ideal instability models necessitate the presence of a pre-existing twisted flux rope, the reconnection models can accommodate either a twisted flux rope or a sheared arcade [Forbes et al., 2006, Mackay et al., 2010]. The reconnection may involve the transformation of restraining overlying flux into the flux of the erupting sheared core or flux rope. Alternatively, it can generate highly bent magnetic field lines within a rope, resulting in high acceleration.

The implosion conjecture, as proposed in [Hudson, 2000], offers an alternative perspective on the release of magnetic energy. This proposed mechanism is characterized by a decrease in the coronal volume ( $V$ ) and the associated drop in magnetic pressure, with the released energy being proportional to  $\int B dV^2$ . The rate of coronal loop contraction, found to be closely correlated with emissions from flares [Simões and Kontar, 2013], supports this conjecture. This alternative viewpoint suggests that in understanding solar eruptions, one should not solely concentrate on

processes leading to outward expansion. Instead, it encourages consideration of the potentially significant role played by implosive forces.

Notably, two processes—instability and reconnection—often occur in tandem and exhibit close interplay. However, their distinct contributions to the acceleration of the eruption remain uncertain, likely contingent on various parameters and specific scenarios. Untangling their respective roles is a non-trivial challenge for modelers in the field [Gou et al., 2023].

## 2.4 CME modeling with GCS

Richardson et al. [2015] highlighted that even in the most reliable catalogs there are significant differences in CME parameters, with velocity differences reaching hundreds of  $\text{km s}^{-1}$ . The determination of CME widths is inconsistent across catalogs as it is affected by projection onto the plane of the sky and interpretation of coronagraph images. Higher accuracy of estimates can be achieved by aligning SOHO and STEREO observations with 3D CME models.

The Graduated Cylindrical Shell (GCS) model (see Fig. 2-6) is an empirical geometrical model of a flux rope defined by Thernisien et al. [2006b], Thernisien et al. [2009, 2011]. It has been widely used in the quantitative analysis of CMEs and allows precise characterization of their 3D features, including shape, size, location, and orientation [Dumbović et al., 2019]. This 3D geometric framework includes a central tubular section representing the core of the flux rope and two conical extensions symbolizing the "legs" connected to the solar surface. In this model, the bright front shell corresponds to the flux rope's surface, while the inner cavity represents the flux rope's body, consistent with the conventional view [Cremades et al., 2006]. A central axis of rotation passes through the curved tube and conical legs, imparting rotational symmetry to the flux rope's shell surface at each cross-section perpendicular to the axis, defining its geometric plane.

The GCS model includes six key parameters: (1) propagation longitude, (2) propagation latitude, (3) tilt angle of the curved central axis (which defines the plane of the flux rope), (4) height of the leading edge of the front, (5) half angle

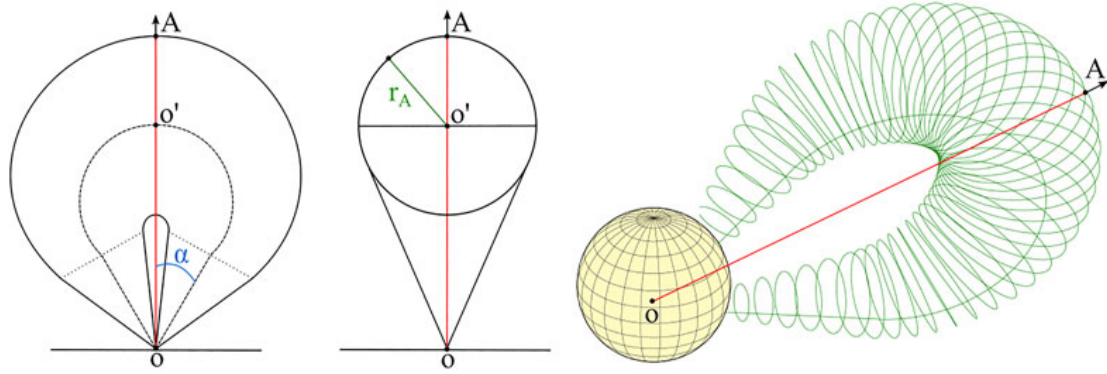


Figure 2-6: Plane sections of the GCS model (left and middle panels) showing the different parameters and a schematic of the model structure (right panel). From Kouloumvakos et al. [2022].

between the axes of the legs, and (6) aspect ratio, which is the ratio between the cross-sectional radius of the shell and the distance between the center of the sun and the outer edge. While the first three parameters characterize the geometry, the last three relate to the morphology and size of the CME.

It is noteworthy that the CME geometry changes significantly near the Sun while it remains relatively constant in interplanetary space. Conversely, the morphology of the CME remains self-similar in the corona but undergoes significant distortions as it propagates through the interplanetary medium.

Liu et al. [2010] compared the GCS modeling with the flux rope reconstruction using in situ measurements at 1 AU and showed that the model can be used to obtain estimations of CME position, direction, three-dimensional extent, and speed. A comprehensive review on the GCS and other CME reconstruction methods is published in Mierla et al. [2010].

## 2.5 Associated Phenomena

Coronagraphs have traditionally been an indispensable tool for the observations of CMEs, with modern instruments such as SOHO/ LASCO and STEREO-A/EUVI. However, a critical challenge is the limited lifetime of these instruments, as evidenced by the lack of data from the STEREO-B satellite.

Even with the help of coronagraphs, studying the early evolution of CMEs di-

rected toward Earth, which manifest as halo events when observed from our planet, remains a difficult endeavor. These events are of most importance in the context of space weather. However, halo CMEs suffer from substantial measurement inaccuracies due to severe projection effects. The occulting disk in coronagraphic observations obscures the lower corona, so we lack important information about the initial propagation and acceleration phases of CMEs.

Complementary to direct coronagraphic observations of CMEs is the opportunity to study associated activities in the lower solar atmosphere. These activities include filament eruptions, solar flares, posteruptive arcades, large-scale coronal EUV waves, and coronal dimmings as explained by [Hudson and Cliver \[2001\]](#). Observation of these solar disk phenomena is essential to identify whether a halo CME originates from the front or back of the Sun relative to the observer [[Shugay et al., 2022](#)]. Studying the evolution of these associated phenomena provides valuable insight into the early stages of CME development and contributes to improved estimation of their parameters.

In addition to using white-light imaging, detecting CMEs is possible by imaging their signatures in extreme ultraviolet (EUV) or soft X-ray (SXR) light. This capability likely results from the compression and heating processes that make CMEs detectable in filtergrams optimized for high-temperature phenomena, as discussed in [Glesener et al. \[2013\]](#).

Satellite missions equipped with EUV instruments that have a wide field of view provide a valuable opportunity to complement white light coronagraph data effectively. This approach allows for comprehensive tracking of CME structures and derivation of their kinematic profiles, especially during the primary acceleration phase of the CME evolution.

Nowadays we have regular high-cadence high-resolution imaging of the solar EUV corona by the Atmospheric Imaging Assembly [[AIA; Lemen et al., 2012](#)] onboard [SDO](#), the Extreme Ultraviolet Imager [[EUI; Rochus et al., 2020](#)] onboard Solar Orbiter, the Solar Ultraviolet Imager [[SUVI; Darnel et al., 2022](#)] onboard the Geostationary Operational Environmental Satellites (GOES), Sun Watcher using Active Pixel System detector and Image Processing [[SWAP; Berghmans et al., 2006](#)] on

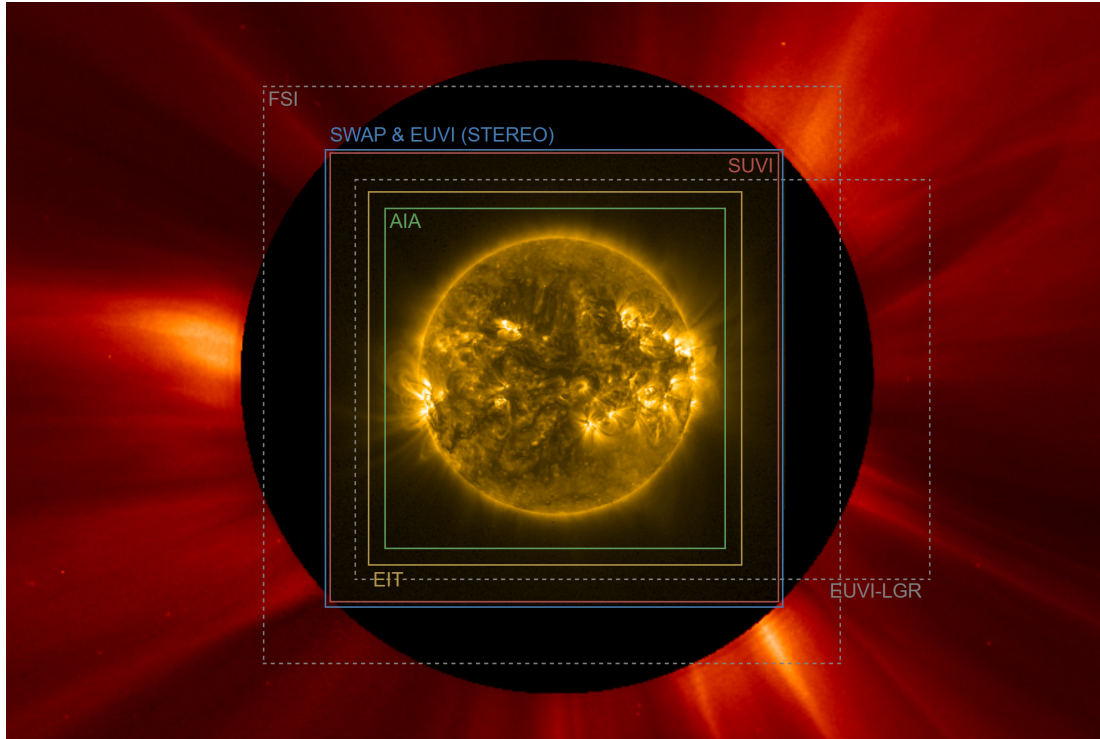


Figure 2-7: EUV image from Proba-2/SWAP combined with a LASCO/C2 coronagraph image covering a field of view up to around  $4 R_{\odot}$ , roughly covering the edge of the middle corona. The overlaid boxes show the relative nominal FOV of different EUV observing instruments: FSI (Full Sun Imager is part of the EUIS suite aboard Solar Orbiter), future EUVI-LGR, and SOHO/EIT. STEREO/EUVI, Proba-2/SWAP, GOES/SUVI are instruments with the largest field of view of about  $1.7 R_{\odot}$ . Image reproduced from <https://middlecorona.com/instruments>.

Proba-2 [Santandrea et al., 2013], as well as the STEREO-A Extreme-Ultraviolet Imaging Telescope [EUVI; Wuelser et al., 2004] (see Figure 2-7). ESA’s Lagrange L5 mission [Vigil; Palomba and Luntama, 2022] planned for 2028 will have the EUVI-LGR with an extended field of view (FOV) to the western limb of the Sun, tracking the evolution of the earth-directed events on the limb. These observations provide us with various possibilities to monitor the CME low coronal signatures, increasing the chances of detecting the potential geoeffective eruptions at a very early stage, i.e., even before their front reaches the field of view of coronagraphs.

### 2.5.1 Flares

Flares are abrupt bursts of electromagnetic radiation in the radio, visible, ultraviolet, and X-ray regions that occur in certain regions of the Sun. Flares usually accompany

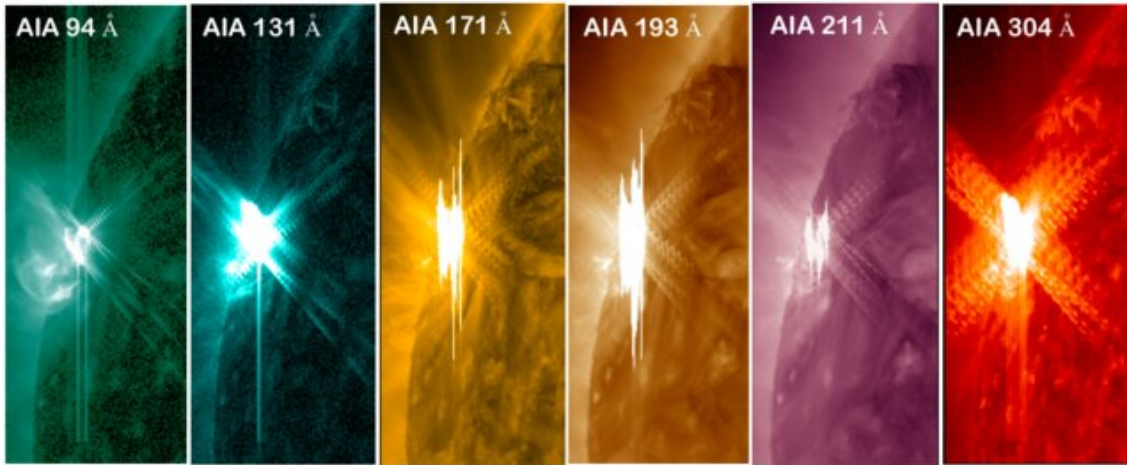


Figure 2-8: Multiwavelength observations of a solar flare observed in six EUV filters of SDO/AIA on the eastern limb on March 9, 2011. From Joshi [2022].

the CMEs as they are caused by the same magnetic processes in the Sun [Harrison, 1995]. It is important to note, however, that while CMEs and flares frequently occur together, they do not correspond one-to-one.

Evidence presented in several published studies suggests a strong correlation between the intensity of CMEs and the magnitude of accompanying flares. Powerful CMEs coincide statistically with strong flares, as evidenced by the studies of Aarnio et al. [2011] and Gopalswamy et al. [2009]. The observations also confirm the close association between the energy release in a flare and the dynamics of the associated CME [Temmer et al., 2008].

Moreover, several CME parameters, including velocity, acceleration, and kinetic energy, show robust correlations with indicators of flare strength, such as peak soft X-ray flux or integrated flux associated with the flare [Viřnak et al., 2005, Temmer et al., 2010, Bein et al., 2012].

Although there is a high probability of more than 80% that an X-class flare is associated with a CME [Yashiro et al., 2006], it is important to acknowledge the existence of exceptions in observed cases [Wang and Zhang, 2007].

## 2.5.2 Filaments and Prominences

Prominences and filaments consist of cooler material extending along magnetic field lines. This material becomes visible in EUV and  $H\alpha$  wavelengths when observed

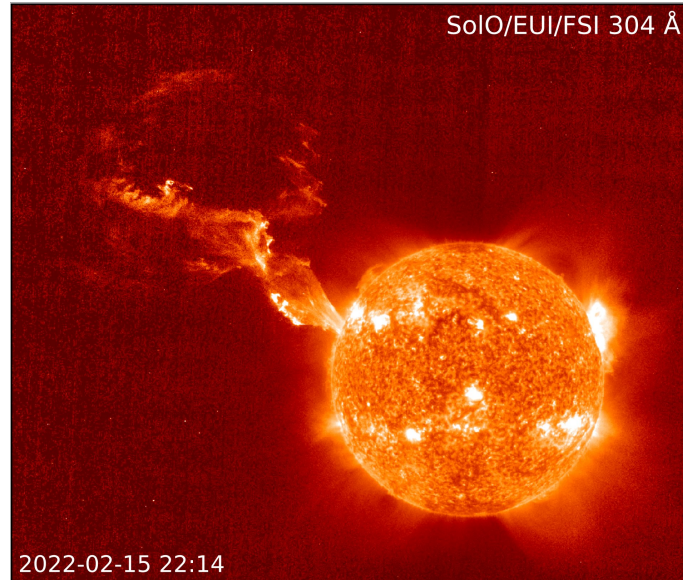


Figure 2-9: Erupting prominence observed by EUI/FSI aboard Solar Orbiter in the He II 304 Å passband on 15 February 2022, at 22:14 UT. The off-limb emission has been enhanced with a radial filter. From [Mierla et al., 2022]

near the solar limb, where it appears brighter compared to the surrounding corona (Fig. 2-9). When the perspective changes and these structures are viewed against the solar disk instead of against the background of space, they appear dimmer. In this context, they are called solar filaments, as described by Galsgaard and Longbottom [1999].

These structures mark the launch site of CMEs. It is noteworthy that the disappearance of a filament or the eruption of a prominence often occurs in association with CMEs [Hundhausen, 1999], and part of this material is thought to form the core of a "three-part" CME [Vourlidas et al., 2013].

EUV telescopes typically observe the early phases of prominence eruptions near the Sun, while white-light coronagraphs detect the subsequent propagation phase of CMEs [Mierla et al., 2013]. Efforts to combine low-corona EUV with high-corona white-light observations include studies by Byrne et al. [2014], O'Hara et al. [2019]. The cutting-edge Full Sun Imager (FSI) on Solar Orbiter boasts a unique, large field of view (FOV) of  $3.8^\circ \times 3.8^\circ$ , crucial for tracking prominences deep into the solar corona. Mierla et al. [2022] notably studied a remarkable solar prominence extending up to  $6 R_\odot$  (Fig. 2-9).

### 2.5.3 EUV waves

EUV waves are large-scale disturbances propagating in the corona and appear as moving fronts of enhanced EUV emission (Fig. 2-10). These waves typically have velocities of 200-400  $\text{km s}^{-1}$ , although velocities of up to 1000  $\text{km s}^{-1}$  have also been observed, as documented in studies [Nitta et al., 2013, Muhr et al., 2014, Thompson and Myers, 2009].

It is important to emphasize that EUV waves have often been misidentified as CMEs in the literature due to their strong association and similar expansion phenomena. Although both structures can manifest as wavefronts on images, their behavior and interpretation differ significantly. To account for this dual nature, the authors proposed specific definitions: EUV wave refers to a disturbance propagating along the EUV coronal surface at a considerable distance from an eruption, while a CME is a magnetic disturbance, often characterized as a magnetic flux rope, propagating outward from the solar corona [Patsourakos and Vourlidas, 2012].

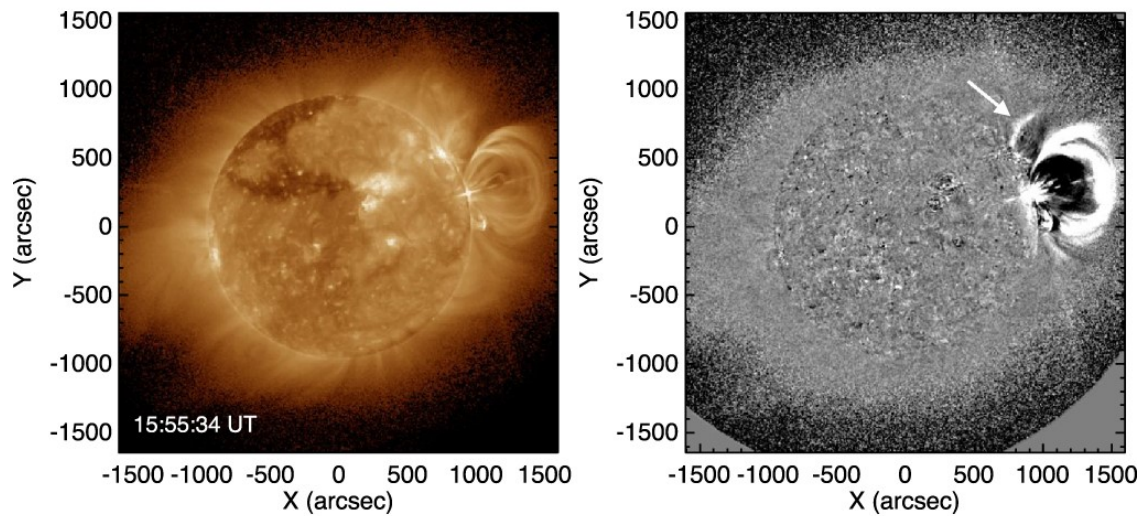


Figure 2-10: 10 September 2017 CME event observed by SUVI. Left: direct 195  $\text{\AA}$  image, right: base-difference image. The arrow indicate the EUV wave observed above the limb and on the disk. From [Veronig et al., 2018]

The use of multiple perspectives, by *STEREO* independently or in combination with *SOHO* or *SDO*, can provide crucial geometric details of EUV waves and their associated CMEs in three-dimensional space, including their lateral extents [Bemporad, 2009, Temmer et al., 2011, Podladchikova et al., 2019b]. As was mentioned

before, it has been observed that powerful events, characterized by significant compression, can be consistently detected as halo CMEs regardless of the observer's vantage point [Kwon and Vourlidas, 2018, Kwon et al., 2015]. In this context, data from STEREO have shown a strong agreement between the outermost shock component of CMEs and the solar surface structure of coronal EUV waves [Kienreich et al., 2009, Veronig et al., 2010, Kwon and Vourlidas, 2017, Veronig et al., 2018].

#### 2.5.4 Coronal dimmings

The most distinct phenomena associated with CMEs are coronal dimmings. These are localized regions in the low corona, characterized by reduced emission in the EUV [Thompson et al., 2000] and the soft X-ray [Jiang et al., 2007] wavelengths. They are typically interpreted as indicators of density loss due to either mass loss or the rapid expansion of the overlying corona during the initial phase of the CME lift [Cheng and Qiu, 2016].

In the coming chapters, we will fully explore the nature of coronal dimmings, explain the methods used for their detection and analysis, and highlight their close association with CMEs.

# Chapter 3

## Coronal Dimmings

Coronal dimmings are transient regions of strongly reduced emission in soft X-rays (SXR) [Hudson et al., 1996, Sterling and Hudson, 1997] and EUV [Thompson et al., 1998, Zarro et al., 1999a] wavelengths that occur in association with CMEs. In general, they are interpreted as density depletion caused by mass loss during the CME eruption [Webb et al., 2000].

Coronal dimmings can be observed both on the visible solar disk close to the eruption site (referred to as on-disk dimmings) and above the solar limb (off-limb dimmings) from lateral perspective. On-disk dimming observations involve integrating the emission along the line-of-sight of CME propagation, corresponding to a projection of the cross-section of the CME from a top view. Conversely, off-limb dimming observations offer a line-of-sight integration across the CME.

### 3.1 Nature of appearance

According to Attrill and Wills-Davey [2010], Mason et al. [2014] there are two generally accepted mechanisms of dimming formation:

- **Mass-loss dimming:** a density reduction due to plasma evacuation. It is caused by the eruption of the local magnetic field, which leads to a considerable expansion of the magnetic loops into the surrounding space. The larger the expansion volume, the more the plasma density is reduced. Such dimmings are observed as a decrease in several EUV emission lines simultaneously.

- **Temperature dimming:** The decrease in intensity can also be caused by temperature changes - the plasma is heated or cooled, the ionization fraction changes, and thus, the emission intensity changes. Such dimmings can be easily distinguished separately from mass loss dimmings by checking the emission of cospatial lines - thermal causes could be misidentified as mass loss if only one spectral line is observed. In addition, [Hudson et al. \[1996a\]](#) has shown that the time scale of the dimming observed in the Yohkoh/SXT data is much faster than the corresponding times of conductive and radiative cooling, suggesting that the dimmings are primarily a consequence of density depletion rather than a temperature effect.

Other physical processes can also cause the observation of dimmings [[Mason et al., 2014](#)]: some filaments moving between the bright material and the observer, the propagation of EUV waves (dimmings are observed far from the eruption site) [[Veronig et al., 2018](#), [Podladchikova et al., 2019a](#)], Doppler shift due to resonant fluorescence of a plasma cloud. Therefore, it is important to understand the initial process of the observed event and to find approaches to verify the results.

## 3.2 Formation of Coronal Dimmings

Coronal dimmings can be differentiated into two types: core [[Webb et al., 2000](#)] and secondary dimmings [[Mandrini et al., 2007](#)].

### Core dimmings

Core dimmings are characterized by localized regions of strongly reduced emission, which impulsively drops by up to 90% with respect to the pre-event emission on time scales of some 10 minutes [[Vanninathan et al.](#)] and are associated with the footpoints of the evacuated flux rope [[Sterling and Hudson, 1997](#)]. They are typically found close to the eruption site on the solar surface and occur in regions of opposite magnetic polarities.

One of the challenges in studying core dimmings is their limited extent. Because of their close proximity to the flare or CME source, it can be difficult to determine

their boundaries accurately. In some cases, core dimmings can manifest as distinct bipolar dimmings where both footpoints of the flux rope are clearly visible, but such cases are relatively rare [Dissauer et al., 2018a].

These dimmings are closely associated with the initiation and evolution of solar eruptions and provide valuable insight into the magnetic and dynamic processes occurring near the eruption site.

### Secondary dimmings

Secondary dimmings are more widespread regions of reduced emission in the solar corona. Unlike core dimmings, secondary dimmings result from expanding the CME body and associated overlying magnetic fields as the CME erupts and expands into the surrounding solar corona [Thompson et al., 2000, Attrill and Wills-Davey, 2009].

These dimmings are more diffuse and extended, encompassing a greater portion of the corona than core dimmings. Typically, they appear less intense, develop more gradually, and recover quicker than core dimmings [Vanninathan et al.]. Essentially, they reflect the CME expansion in the lower corona, offering valuable insights into the CME dynamics and its interactions with neighboring magnetic fields [Mandrini et al., 2007].

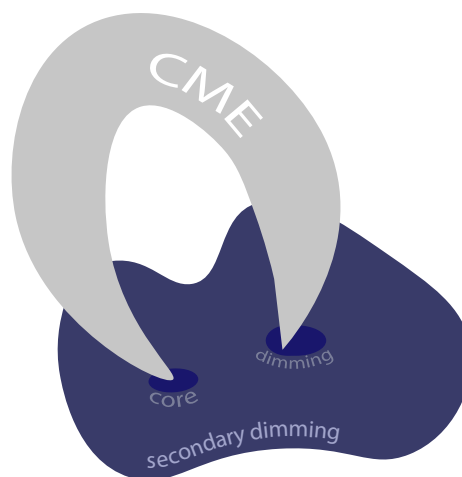


Figure 3-1: Cartoon depicting the process of mass-loss dimming. Core dimmings represent the footpoints of a flux rope. During and after the eruption the loops are brighter and reconfigured, a CME is ejected, and a void forms in the coronal plasma - a signature of a secondary dimming.

### 3.3 Historical Overview

Coronal dimmings, initially observed in the 1970s with data from Skylab, were initially referred to as "transient coronal holes" due to their reduced emission resembling CHs and their relatively short lifespans compared to typical CHs, as documented in Rust [1983]. Subsequent advancements in observations, such as those made possible by the Yohkoh Soft X-ray Telescope [SXT; Kosugi et al., 1992], provided a deeper understanding of dimming sources in the inner corona and their temporal characteristics.

Further insights into the nature of dimmings came from studies employing instruments onboard SOHO. Harrison and Lyons [2000] used the Coronal Diagnostic Spectrometer (CDS) to perform the first-ever spectroscopic observation of dimmings. They showed that a large portion of the CME mass could be originated from the dimmings. Harra and Sterling [2001] observed notable blueshifts in the coronal and transition region lines related to CME-associated dimmings, suggesting the presence of mass outflows. The Extreme-ultraviolet Imaging Telescope (EIT) on SOHO enabled consistent observations of dimmings associated with CMEs. These studies reinforced the link between dimmings and CMEs, emphasizing that coronal dimmings serve as reliable markers for the apparent footpoints of white-light CMEs, as detailed in Thompson et al. [2000].

The availability of high-resolution imaging data in seven different EUV filters from the SDO/AIA instrument enabled a deeper exploration of the plasma properties within the coronal dimming regions. This was achieved by applying differential emission measurement techniques as described in Vanninathan et al..

### 3.4 Relations to the CME parameters

Dimmings offer valuable insights into several characteristics linked to coronal mass ejections, as documented in the literature:

1. **Estimating CME mass:** Dimming volume and emission measure calculations can be used to estimate the amount of ejected plasma during the eruption

[López et al., 2017, 2019, Aschwanden et al., 2017].

2. **Analysis of angular extent:** Information on the spatial extent of coronal dimmings allows the study of the angular extent of associated CMEs [Thompson et al., 2000, Attrill and Wills-Davey, 2010]. There is also a correlation between the extension of the CME and the CME mass [Dissauer et al., 2019].
3. **Properties of the Magnetic Cloud:** The structure of the Magnetic Cloud (MC) at 1 AU can be associated with coronal dimmings, as they are thought to mark the footpoints of erupting flux ropes [Mandrini et al., 2007].
4. **Analysis of CMEs at onset and after eruption:** The study of coronal dimmings provides information on the early stages of CMEs [e.g., Qiu and Cheng, 2017] and their post-eruption evolution, including insights into the recovery phase [e.g., Attrill et al., 2008].
5. **Interactions of CMEs with surroundings:** The spatial distribution, emergence, and contribution of magnetic flux from dimmings to associated CMEs help to understand the interaction of CMEs with their environment during early development [Mandrini et al., 2007, Chertok et al., 2013, Jin et al., 2022].

The importance of coronal dimmings for the study of solar CME/flares, as well as the latest significant results in this area, are discussed in Kazachenko et al. [2022].

## 3.5 Detection Algorithms and Dimming Analysis

The analysis of coronal dimmings is challenging due to their diverse appearances and the potential for other physical processes that might resemble false dimmings. As a result, researchers continually develop new methods for detecting and extracting dimmings, with a particular focus on automated algorithms. Below, we will highlight some of these notable automated dimming detection methods.

**NEMO algorithm (Podladchikova and Berghmans [2005])**

**Data and Data Preprocessing:** SOHO/EIT data (on-disk measurements) are used. Running difference (RD) and base difference (EIT) images are computed. RD images represent the difference between consecutive images, while BD images subtract a fixed reference image from each subsequent image.

**Dimming Detection Method:** The Novel EIT wave Machine Observing (NEMO) algorithm detects coronal dimmings and EIT waves. It is based on the analysis of statistical properties and an understanding of the physics of eruptive events. Two masks are extracted: one consists of seed pixels, which represent the darkest pixels of the image, while the second mask is made of pixels that decreased in intensity and are detected using a certain thresholding level. The final dimming region is formed by using the seed pixels for a region-growing method in the second mask. The method works with the assumption that dimmings are connected areas, and their area is much larger than other areas of reduced intensity. The detection is hard to apply for the events without EUV waves.

**Main Results:** The NEMO algorithm successfully detects and extracts dimming regions in SOHO/EIT data. It provides information about dimming coordinates, area, and intensity changes, aiding in the study of eruptive solar events.

**Bewsher et al. [2008]**

**Data and Data Preprocessing:** The study involved the examination of dimmings occurring at the solar limb, specifically in the Fe XVI and Mg IX spectral lines, representing temperatures of  $2 \times 10^6$  K and  $1 \times 10^6$  K, respectively. To facilitate the tracking of dimmings, mosaic images were generated, and base-difference images were created by subtracting a pre-event frame from each event image. The selection of CMEs for analysis was based on the CDAW and CACTus CME lists.

**Dimming Detection Method:** Dimming detection involved limiting the spatial extent of the dimmings of interest using a minimum group size criterion equal to 1% of the mosaic area. Pixels were classified as dimming regions if their base-difference intensity value exceeded twice the error threshold. Subsequent analysis of neighboring pixels was conducted to establish the complete extent of a given

dimming event.

**Main Results:** A statistical association between dimmings and CMEs was established, affirming that a substantial percentage of dimming events are linked to CMEs. Specifically, the research indicates that up to 55% of dimming events were associated with CMEs. Furthermore, it was found that up to 84% of CMEs in their dataset could be traced back to dimmings, reinforcing the relationship between these two solar phenomena. The study also provided insights into the spatial extent and statistical properties of dimmings, contributing valuable information to our understanding of these solar events.

### **Reinard and Biesecker [2008]**

**Data and Data Preprocessing:** A statistical analysis of 96 CME-associated EUV coronal dimmings between 1998 and 2000. Base-difference images with selected subregions of dimming locations.

**Dimming Detection Method:** A thresholding algorithm is applied: pixels are flagged as dimmed if their intensity is below the chosen threshold of  $1\sigma$ . The detection method allows to derive dimming location and their area and brightness.

**Main Results:** The study reveals that coronal dimmings often occur near active regions and exhibit rapid intensity decrease followed by gradual recovery. All fast CMEs are observed with dimmings. The mean lifetime of the dimmings is around 8 hours (see Chapter 6 for more details).

### **Attrill et al. [2006], Attrill and Wills-Davey [2010]**

The detection part was developed with the NEMO algorithm as the base, where running-difference images were used for the detection; each of them was divided by 16 times for a fast real-time detection procedure. The segmentation part is based on the thresholding method.

**Data and Data Preprocessing:** Base-difference [SDO/AIA](#) images from seven EUV passbands, with a pre-event image selected 5 minutes before the detected dimming event.

**Dimming Detection Method:** BD images are subjected to a  $1\sigma$  threshold

based on the mean value of the pre-event image in each passband to identify dimmed pixels and a median filter is applied for smoothing. Dimming regions are defined by clustering pixels in a neighborhood, discarding any regions smaller than 1 arcmin<sup>2</sup> to ensure noise removal.

**Main Results:** The method can also be implemented for off-limb dimmings detection and even with original, non-difference data.

### **Kraaikamp and Verbeeck [2015b]**

Solar Demon is a software package that detects and characterizes flares, dimmings, and EUV waves in [SDO/AIA](#) images.

**Data and Data Preprocessing:** Running-difference and Percentage running-difference images from [SDO/AIA](#) 211 Å.

**Dimming Detection Method:** Dimming detection method uses a combination of high and low thresholding on running-difference and percentage running-difference images by only keeping clusters identified by both masks to identify coronal dimming regions. Each subsequent image is compared to the base image. A mask identifies pixels with intensity loss relative to the base image, extracting dimming attributes such as location and intensity changes over time. Tracking of dimming regions is limited to half an hour after the last detected brightness decrease, reducing noise-related false statistics. Tracking durations vary from 30 minutes for small events to several hours for larger ones due to the Sun's dynamic nature.

**Main Results:** *SolarDemon* algorithm stands as the only dimming detection method actively employed in operational mode for the real-time identification of solar dimmings. The dimming detector produces near real-time output with a 15-minute delay using synoptic quick-look data and synoptic science output with a longer delay of 7 days.

### **Mason et al. [2016]**

The study delves into various physical processes that can be interpreted as dimmings and provides a spectroscopic analysis of mass-loss coronal dimmings.

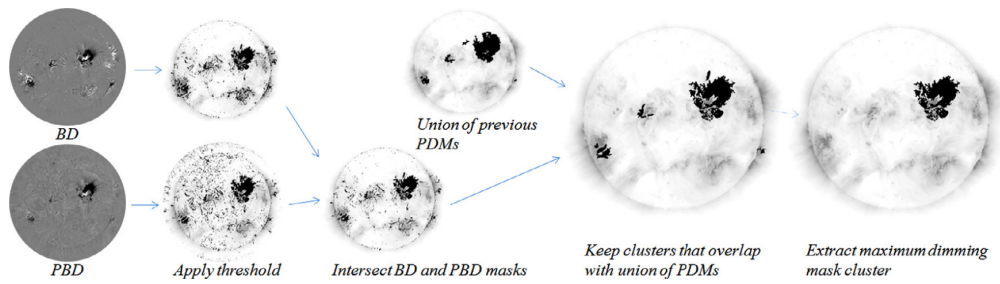


Figure 3-2: Creating a dimming characterization mask. From Kraaikamp and Verbeeck [2015b].

**Data and Data Preprocessing:** The analysis revolves around dimmings identified from spatially unresolved *SDO/EVE* full-disk irradiance light curves. This dataset encompasses 37 dimming events that occurred during two distinct two-week periods in the year 2011.

**Dimming Detection Method:** The method employed for dimming detection involves the removal of the gradual phase peak in the *EVE* dimming time series. This is achieved by temporally aligning the peak in the nondimming line with that in the dimming line. Subsequently, the nondimming peak is scaled down to match the intensity of the dimming peak, and the renormalized nondimming time series is subtracted from the dimming series. This approach offers the advantage of dealing solely with percentage changes, thus avoiding direct irradiance alterations. Consequently, it allows for the isolation and removal of the cooler coronal emission associated with dimmings, utilizing simultaneous measurements of warmer coronal lines. The authors emphasize that relying solely on a single dimming spectral line is insufficient for reliably predicting the occurrence of a CME. Instead, it is ideal to observe spectral lines spanning a wide range within an ionic sequence.

**Main Results:** The highest correlation was identified between the depth in the *SDO/EVE* light curve related to dimming and the CME mass. Furthermore, a correlation was established between the intensity drop rate in *SDO/EVE* profiles and the speed of the CME. The significance of observing dimmings in EUV light curves lies in their potential to establish connections between solar observations and their relevance in the context of stellar phenomena.

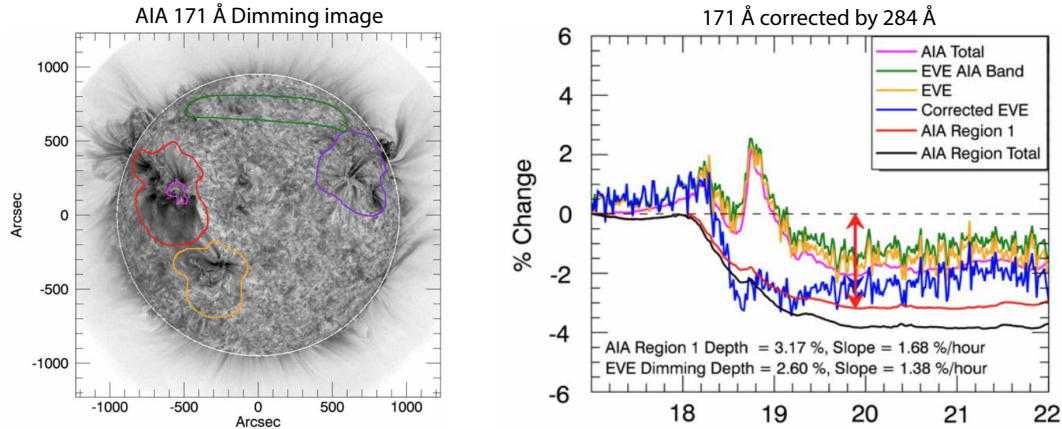


Figure 3-3: Comparisons of *EVE* and *AIA* light curves for M1.0 flare on 2010 August 7. Left panel: *SDO/AIA* EUV full disk images with coronal dimmings identified as regions of interest. Right panel: *SDO/EVE* spatially integrated irradiance measurements. The *EVE* corrections that make the light curves most closely match *AIA* mass-loss dimming are shown. The vertical arrows indicate the time where slope and depth are calculated in comparison to a time step prior to flare. Adapted from [Mason et al., 2014].

### CoDit (Krista and Reinard [2017])

The authors conducted a comprehensive statistical investigation of 154 dimmings, along with their associated flares and CMEs, spanning the entire year of 2013. Their focus was on exploring the physical and morphological characteristics of these solar phenomena.

**Data and Data Preprocessing:** The dataset consists of 154 dimming events observed in 2013. These observations were made using original non-difference *SDO AIA* 193 Å observations and *HMI* magnetograms, transformed to Lambert cylindrical equal-area projection maps.

**Dimming Detection Method:** The authors utilized a semi-automated tool called the Coronal Dimming Tracker (*CoDit*) for dimming detection. In a departure from the conventional use of base difference images, the authors adapted the Coronal Hole Evolution detection algorithm (*CHEVOL*, Krista et al. [2011]) to identify dimmings in original EUV images. This novel approach involved locating pixels with intensities lower than that of the quiet Sun. This method enabled the study of dimmings as the footpoints of CMEs, in contrast to the larger, diffuse dimmings typically observed in difference images, representing the projected view of the rising

and expanding plasma.

**Main Results:** The study revealed several significant relationships among the physical properties of dimmings, flares, and CMEs. Larger dimmings were found to have longer lifetimes, indicating that it takes more time for extensive open magnetic regions to "close down." During the growth phase, smaller dimmings tend to become more unipolar than larger dimmings, highlighting differences in their magnetic characteristics. The intensity of dimmings in EUV images was observed to correlate with the amount of plasma removed during the event and the energetic nature of the eruption.

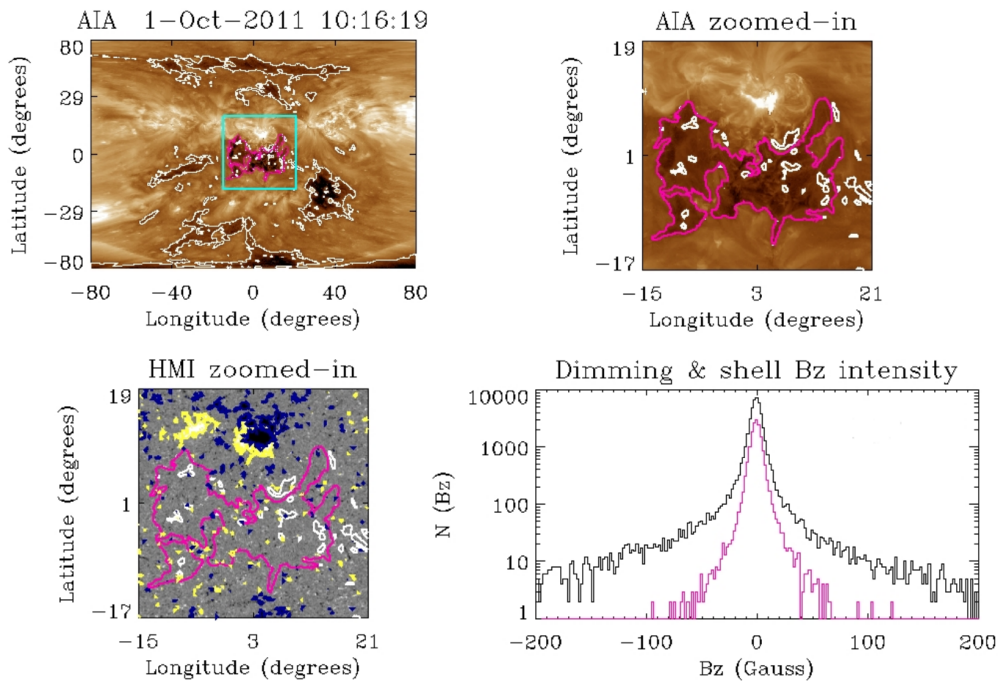


Figure 3-4: CODIT detection products example. Top left: [AIA](#) 193 Å Lambert map (1 Oct 2011, 10:16 UT) with dimming region (magenta) and intensity threshold regions (white). Top right: Close-up of [AIA](#) image with dimming. Bottom left: [HMI](#) magnetogram with dimming; yellow/blue contours show magnetic field strength  $>50$  G and  $<-50$  G. Bottom right: Histogram of a magnetic field in dimming (magenta) vs. surrounding regions (black). From [Krista and Reinard \[2017\]](#).

#### [Dissauer et al. \[2018a,b, 2019\]](#)

A thorough methodological approach and comprehensive statistical analysis of the characteristic properties of coronal dimmings, and their relation to the decisive parameters of the associated CMEs and flares has been presented in a series of papers.

**Data and Data Preprocessing:** The dataset encompasses 62 dimming events occurring between 2010 and 2012, where dimmings were observed on-disk by [SDO/AIA](#) and [HMI](#). To minimize projection effects, the kinematics of CMEs during the impulsive acceleration phase were studied near the limb using [STEREO/EUVI](#) and COR. Logarithmic base ratio images were constructed for dimming segmentation.

**Dimming Detection Method:** The dimming detection method employs a region-growing thresholding algorithm. A pixel is classified as a dimming pixel if its logarithmic base-ratio intensity decreases below a threshold of  $-0.19$  DN. Morphological operators are employed to smooth the extracted regions. This smoothing process helps eliminate small noise-induced features and fills minor gaps and holes. It subsequently facilitates the identification of seed pixels for a region-growing algorithm. The final dimming region is then extracted from the detected pixels that are connected neighbors to the seed pixels [[Dissauer et al., 2018a](#)]. With this method, the core dimming regions can be identified in the broader dimming region.

**Dimming parameters:** Characteristic dimming parameters are extracted through the cumulative summation of dimming pixels over time. This approach enables the comprehensive description of dimming regions, including their dynamics, morphology, magnetic properties, and brightness.

**Main Results:** The study's main outcomes reveal significant correlations between dimming properties and CME characteristics. Specifically, dimming area, total unsigned magnetic flux, and total brightness, which describe the dimming region in its final extent, exhibit the highest correlations with CME mass (correlation coefficients around 0.6-0.7). In summary, CME mass displays the most robust correlations with primary coronal dimming parameters, while the maximum velocity of the CME is strongly correlated with secondary dimming parameters. For events where a CME occurs concurrently with a flare, the statistical analysis demonstrates that coronal dimmings capture properties of both phenomena.

The methodology created in this dissertation was designed in accordance to this study, making it the most relevant to current research project.

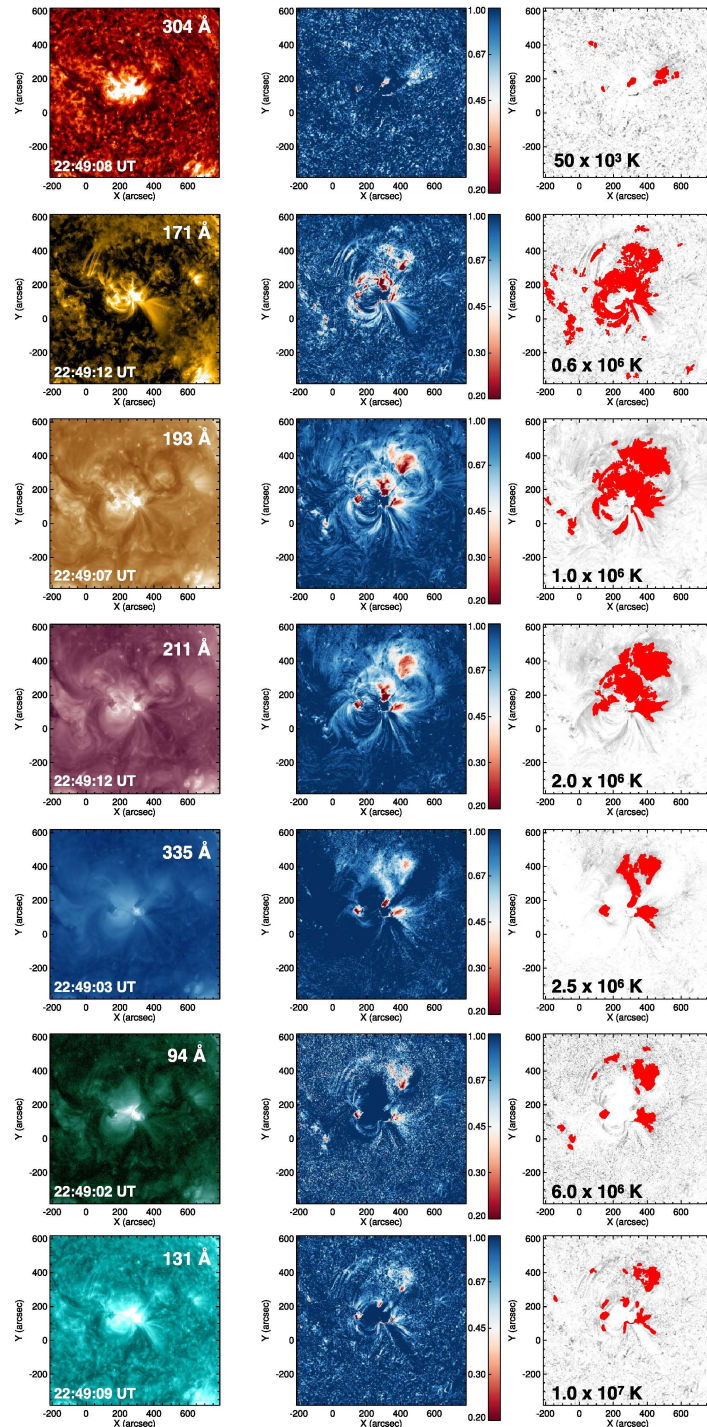


Figure 3-5: Detection of the coronal dimming regions around 22:49 UT on 2011 September 6 in seven EUV filters of [SDO/AIA](#) covering a temperature range from 0.5 to 10  $MK$  (top to bottom). The direct image (left) is plotted together with its corresponding logarithmic base-ratio image (middle) and the detected dimming pixels (indicated in red in the right panel). From [Dissauer et al. \[2018a\]](#).

# Chapter 4

## Methodology of the dimming analysis

### 4.1 Data and instruments

In this section, we provide an overview of the main instruments used in our study to analyze coronal dimming. Although our research includes several tools for each of the solar phenomena, the focus of this section is to present the data sources that have proven to be particularly valuable and informative for our study of coronal dimmings: [SDO/AIA](#) and [STEREO /EUVI](#) instruments for on-disk and off-limb dimming observations, respectively.

#### 4.1.1 SDO mission

The Solar Dynamics Observatory [[SDO](#); [Pesnell et al., 2011](#)] was launched on February 11, 2010, as part of the Living With a Star program from [NASA](#). The primary goal of the [SDO](#) mission is to deepen our understanding of the Sun's behavior, particularly for solar variability and its effects on Earth and near-Earth space. [SDO](#) has the unique capability to observe the solar atmosphere on small spatial and temporal scales at multiple wavelengths simultaneously. This allows scientists to study the generation and structure of the solar magnetic field, as well as the conversion and release of magnetic energy in the heliosphere, which takes the form of solar wind, energetic particles, and solar irradiance variations. The mission's focus on observing small-scale phenomena has great potential to improve our predictive capabilities

regarding solar activity.

Key features of the [SDO](#) mission are:

**Spacecraft and Orbit:** The [SDO](#) spacecraft is 4.5 m high and has dimensions of more than 2 m on each side. At launch, it weighed about 3100 kg, including propellant. The spacecraft operates in a semi-autonomous mode pointed at the Sun, providing nearly continuous observations of the Sun. It is in a 28° inclined geosynchronous orbit that provides a continuous data downlink to the [SDO](#) ground station in New Mexico. The data transmission rate reaches an impressive 130 Mb s<sup>-1</sup>.

**Science Instruments:** The [SDO](#) mission is equipped with three science instruments:

- **Atmospheric Imaging Assembly ([AIA](#)):** the [AIA](#) provides high-resolution images of the entire solar disk, including the corona and the transition region up to 0.5 R<sub>⊙</sub> above the solar limb. It achieves a spatial resolution of 1.5 arcsec and a temporal resolution of 12 seconds. [AIA](#) operates in ten different wavelength intervals that include a broadband white light channel, two UV channels, and seven EUV channels, centered on the following spectral lines: Fe XVIII (94 Å), Fe VIII, XXI (131 Å), Fe IX (171 Å), Fe XII, XXIV (193 Å), Fe XIV (211 Å), He II (304 Å), and Fe XVI (335 Å), providing a temperature diagnostics over the range from 6 · 10<sup>4</sup> K to 2 · 10<sup>7</sup> K [[Lemen et al., 2011](#)].
- **EUV Variability Experiment ([EVE](#)):** [EVE](#) measures the solar extreme ultraviolet spectral irradiance to understand time variations that influence Earth's climate and near-Earth space [[Woods et al., 2012](#)].
- **Helioseismic and Magnetic Imager ([HMI](#)):** [HMI](#) observes the full solar disk at 6173 Å with a resolution of 1 arcsecond to study oscillations and the magnetic field at the solar surface [[Scherrer et al., 2012](#)].

Figure 4-1 illustrates [SDO/AIA](#) observations at the different wavelengths, also highlighting which part of the atmosphere is better observed at each wavelength.

**Data Accessibility:** The [SDO](#) mission promotes open science by making its data products publicly available. [SDO](#) data can be obtained in either Level 1.5 or Level

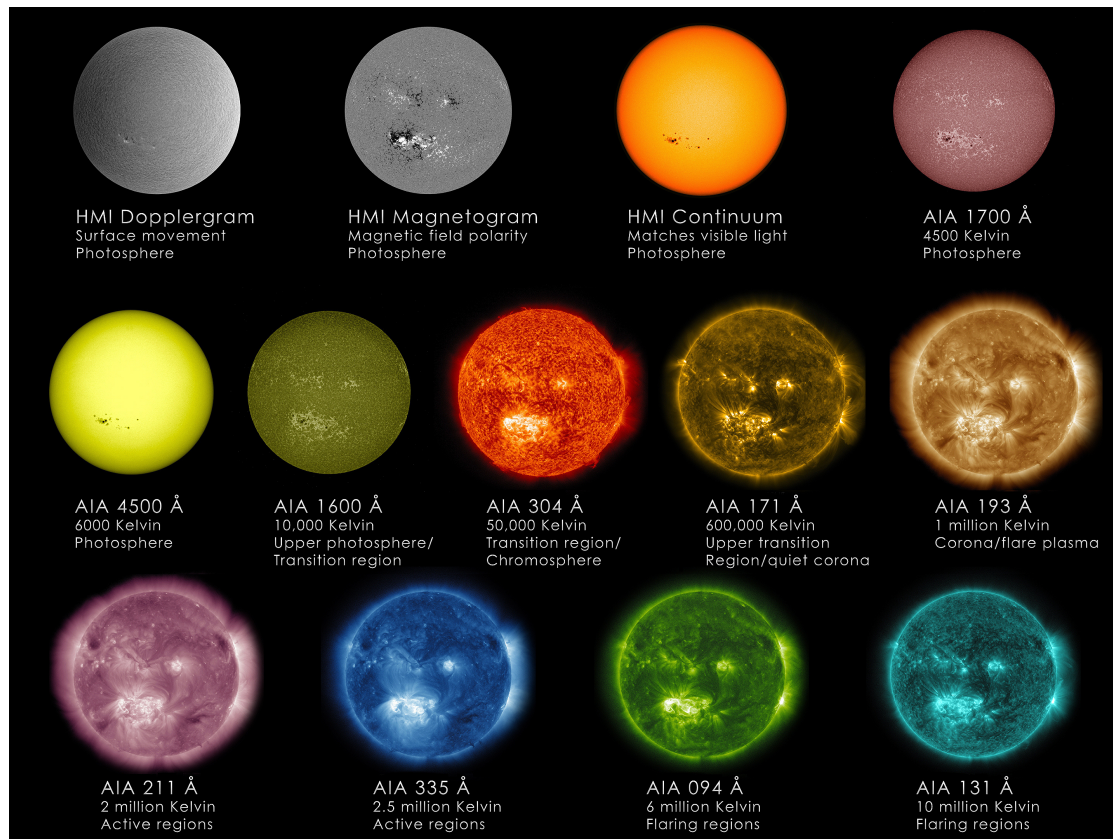


Figure 4-1: How SDO sees the Sun: each wavelength observed by AIA and HMI instruments onboard SDO. Courtesy of NASA/SDO/GSFC.

1.0 formats, with the ability to upgrade Level 1.0 data to Level 1.5 using user software. Several software packages, including SolarSoft (IDL) and SunPy (Python), provide routines for this purpose.

**AIA Data cadence:** SDO/AIA is characterized by its high temporal resolution. It can capture one frame per second, with a general temporal resolution of about 10 to 12 seconds. This frequent data acquisition allows scientists to observe rapid changes in solar activity.

**Data volume:** The SDO mission generates an astounding amount of scientific data, with over 1.5 terabytes of data collected daily, becoming one of the most informative projects in history. This huge data set provides researchers with an unparalleled resource for studying the Sun's dynamic behavior.

### 4.1.2 STEREO mission

The Solar TERrestrial RELations Observatory [STEREO; Kaiser et al., 2008] mission, consisting of two nearly identical spacecraft, was launched on October 25, 2006, as part of the Solar Terrestrial Probes (STP) program from NASA. This mission revolutionized our understanding of the Sun and its interactions with Earth by providing the first stereoscopic view of the Sun and its dynamic atmosphere. The two spacecraft STEREO, STEREO-A and STEREO-B (until 2014), located in heliocentric orbits, with one flying ahead of Earth and the other trailing behind, providing a unique 3D perspective of solar phenomena. The main scientific goals of the STEREO mission are to study the causes and mechanisms leading to the formation of CMEs, to understand how CMEs propagate in the heliosphere, to study the acceleration of energetic particles in the solar corona, and to improve our knowledge of the structure of the solar wind.

Key features of the STEREO mission:

**Stereoscopic observations:** STEREO-A and STEREO-B provide a stereoscopic view of the Sun and its atmosphere. Combined with data from ground-based observatories and observatories in low-Earth orbit, this dual perspective allows scientists to track the buildup and release of magnetic energy from the Sun. It also facilitates the construction of 3D trajectories for Earth-based CMEs, improving our understanding of their behavior.

**Communication and separation:** STEREO-A, which is in a faster and closer orbit around the Sun than STEREO-B, has gradually separated from its twin, moving  $44^\circ$  per year apart. Unfortunately, on October 1, 2014, communication with STEREO-B was lost due to hardware anomalies that affected the spacecraft's orientation control. Although contact was restored with STEREO-B in 2016, recovery efforts were unsuccessful, and the spacecraft has been out of contact. STEREO Ahead continues to operate nominally and currently provides our only images from the far side of the Sun.

**Technological Overview:** The two STEREO observatories are nearly identical in that each is a solar-powered satellite with 3-axis stabilization. They had a launch

mass of about 620 kg, including propellant. Communication with the spacecraft is via the Deep Space Network of [NASA](#), with mission operations based at the Applied Physics Laboratory ([APL](#)).

**Instrumentation:** Each [STEREO](#) satellite is equipped with four instrument packages:

- Sun Earth Connection Coronal and Heliospheric Investigation [[SECCHI](#); [Howard et al., 2008](#)]:
  - Inner Coronagraph (COR1) and Outer Coronagraph (COR2): two white-light coronagraphs to observe the inner ( $1.3-4 R_{\odot}$ ) and outer ( $2.5-15 R_{\odot}$ ) corona at high temporal and spatial resolution, and provide polarization information [[Thompson et al., 2003](#), [Howard et al., 2008](#)].
  - Heliospheric Imager (inner [HI1](#) and outer [HI2](#)): these are externally occulted coronagraphs that image the inner heliosphere between the Sun and the Earth between  $12-215 R_{\odot}$  [Eyles et al. \[2009\]](#).
  - Extreme UltraViolet Imager ([EUVI](#)): [EUVI](#) is of particular importance for studying coronal dimmings. [EUVI](#) observes the chromosphere and lower corona in several EUV emission lines, including He II  $304 \text{ \AA}$ , Fe IX  $171 \text{ \AA}$ , Fe XII  $195 \text{ \AA}$ , and provides high-resolution spatial and temporal data critical to understanding large-scale perturbations in the solar corona [[Wuelser et al., 2004](#)].
- [STEREO](#)/WAVES (SWAVES): SWAVES is designed for 3D localization and tracking of radio emissions associated with streams of energetic electrons and shock waves associated with CMEs [[Bougeret et al., 2008](#)].
- In-situ measurements of particles and CME transients ([IMPACT](#)): [IMPACT](#) contributes multipoint measurements of solar wind, suprathermal electrons, interplanetary magnetic fields, and solar energetic particles. It consists of seven individual sensors which are packaged into a boom suite, and a SEP suite [[Acuña et al., 2008](#)].

- PLAsma and supraThermal ion composition (**PLASTIC**): **PLASTIC** mass spectrometer is providing measurements of kinetic properties and composition for solar wind and suprathermal ions solar wind and suprathermal ions in the energy-per-charge range of  $\sim 0.3$  (0.2) up to  $\sim 80$  (100) keV/e [Galvin et al., 2008].

**Data Accessibility:** The **STEREO** mission data products are publicly available. SolarSoft **IDL** package can be used for calibration routines. Unfortunately, at this moment there are no calibration routines in Sunpy (Python).

**EUVI Data cadence:** From to 2.5 minutes in the 171 Å channel to 20 minutes in the 284 Å filter. Typical cadence of 195 Å is 5 minutes.

## 4.2 Dimming detection

For the dimming detection procedure, we start by loading and calibrating solar images, followed by differential rotation to match them with the pre-event image. Using an automatic thresholding algorithm based on region-growing, we segment the dimming regions. We adapted an algorithm from Dissauer et al. [2018a] The code was translated from SolarSoft **IDL** to Python and extended for off-limb detection, enabling comprehensive analysis of coronal dimming from multiple viewpoints.

### 4.2.1 From SolarSoft IDL to Python and Sunpy

For calibration, differential rotation, and visualization, we use the SunPy open-source software package The SunPy Community et al. [2020]. SunPy debuted in March 2011 and grew out of the collaborative efforts of a small group of scientists and developers at NASA’s Goddard Space Flight Center. Over time, SunPy has evolved into a Python package with a thriving and dedicated community that ensures continued development and frequent updates (including several version changes throughout this project).

While most scientists have traditionally relied on the **IDL** language’s SolarSoft (SSW) library, recent trends show a shift. A 2020 survey of solar physicists found

that 73% of respondents preferred [IDL](#) in their research, while 66% chose Python [Bobra et al. \[2020\]](#). Certainly, these tools are often used together: about 45% of respondents use Python and [IDL](#) in their work. SolarSoft remains essential for supporting cutting-edge Heliophysics System Observatory missions such as the Parker Solar Probe, Solar Orbiter, [SDO](#), [GOES 16](#), and [GOES 17](#).

Because of its versatility, flexibility, and open-source nature, SunPy has grown significantly over nearly a decade. This growth is further fueled by a robust community that actively shares insights and contributions. In addition, the popularity of Python in the broader computer science landscape, particularly in machine learning and computer vision, has fueled the adoption of SunPy.

Despite this change, the solar physics community continues to value SolarSoft. There is a growing trend toward creating a seamless interface combining SolarSoft and SunPy tools to facilitate research in a single environment. Efforts are underway to enable SSW support for execution in Jupyter notebooks and to develop Jupyter-based interactive tutorials [[Hurlburt et al., 2021](#)].

## 4.2.2 Loading and calibration

### Choice of wavelengths

The dimmings are seen in all coronal [AIA](#) filters, emphasizing the multithermal aspect of this phenomenon [[Vanninathan et al.](#)]. As recommended by [Dissauer et al. \[2018a\]](#) and [Kraaikamp and Verbeeck \[2015a\]](#), the most effective observation of coronal dimming occurs at wavelengths sensitive to the coronal temperatures of the quiet Sun, such as 195 Å, 171 Å, and 211 Å. We propose to use these wavelengths for dimming detection and analysis.

### Loading data

To search for and download data, we use the primary interface *sunpy.net.Fido*, which provides [SDO/AIA](#) data at Level 1.0. Obtained data can be conveniently stored in the [FITS](#) (Flexible Image Transport System) file format. [FITS](#) is an open standard that defines a digital file format widely utilized for storing, transmitting,

and processing data in the fields of astronomy and solar physics.

### Calibration of SDO/AIA images

Sunpy has an affiliated package *aiapy* for SDO/AIA data calibration. The preprocessing of the SunPy maps for the data analysis involves several methods from *aiapy.calibrate* (analog for SolarSoft `aia_prep.pro` routine):

1. Checking the exposure time metadata, discarding maps outside the selected threshold. We use images with exposure time ranging from 2.9 to 3 s.
2. Update pointing information in the header: `update_pointing` function.
3. Correct the metadata for heliographic longitude and latitude: `fix_observer_location` function.
4. Convert a full level 1 AIA map to a level 1.5 AIA map (rotating the North to align with the y-axis, adjust the resolution to 0.6 arcsec/pixel, correct the center of the solar disk, etc.): `register` function.
5. Normalize image to the exposure time such that the units of the image are [DN/pixel/s]: `normalize_exposure` function.
6. Resample from  $4096 \times 4096$  to  $2048 \times 2048$  pixels, adjusting metadata accordingly (resolution changes from 0.6 arcsec/pixel to 1.2 arcsec/pixel).

### Calibration of STEREO/EUVI images

Currently, there are no reliable functions for calibrating STEREO/EUVI data in Python. All calibration files are distributed as part of the SECCHI software package in IDL SolarSoft. Thus, we use standard SolarSoft routines for the preprocessing of this data:

1. Load EUVI data with `secchi_vso_ingest.pro` routine.

2. Check the exposure time of each image.
3. To ensure the accurate storage of **STEREO** coordinates, it is better to use the `register_stereo_spice_dlm.pro` routine (automatic handling of this process in **IDL** may not work reliably).
4. Convert from raw **EUVI** Level 0 images to calibrated Level 1 images, turning raw detector signals in data numbers (DN) into the number of photons per sec [ph/s] units: `secchi_prep.pro`.
5. Resample images if needed.

### 4.2.3 Differential rotation

The Sun is known to rotate differentially, meaning that its rotation rate varies across its surface. Near the poles, the rotation period is about 35 days, while near the equator, it is about 25 days. This phenomenon results from the fact that the Sun is not a solid body. Although the exact mechanisms behind it are not fully understood, the Sun's varying rotation is well documented [Howard et al., 1990] and must be taken into account for observations of solar features over time.

Figure 4-2 shows an **SDO/AIA** 171 Å image with overplotted lines of constant longitude (white) with their differentially rotated pairs (blue) in the Heliocentric Earth Equatorial (**HEEQ**) coordinate system. The period of rotation is 27 days. Note that the differentially rotated lines are plotted in the original coordinate frame, so it doesn't account for any motion of the observer over 27 days.

For tracking the evolution of coronal dimmings, we retrospectively rotate each image to a pre-event one, which is taken 30 minutes before the flare onset, the so-called "basemap".

**Sunpy:** `transform_with_sun_center` function. This function always removes the off-limb data.

**SolarSoft:** `drot_map.pro`. `KEEP_LIMB` keyword should be used not to remove the off-limb data after rotation.

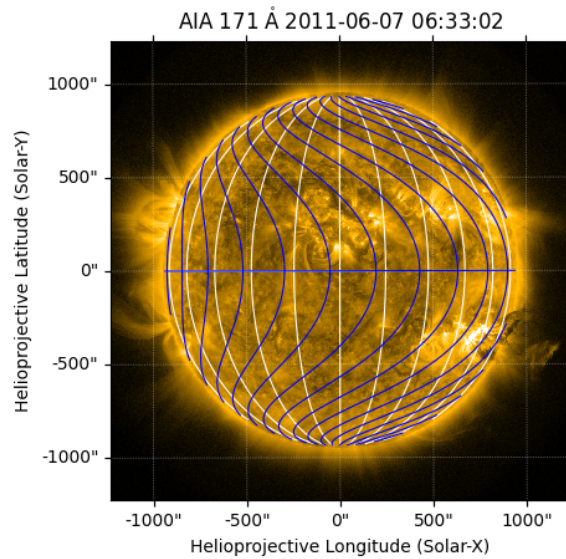


Figure 4-2: SDO/AIA 171 Å image with HEEQ constant longitudes before differential rotation (white) and after differential rotation for 27 days (blue).

An example of the map, differentially rotated on three days back is shown in Figure 4-3. From the central map, two observations are evident. First, the differential rotation process omits off-limb data, leaving only on-disk measurements. Second, there's a distortion on the solar disk's right side, causing it to lose its circular shape. This distortion arises because those pixels were located on the back side of the solar sphere, and their information is lost during rotation correction.

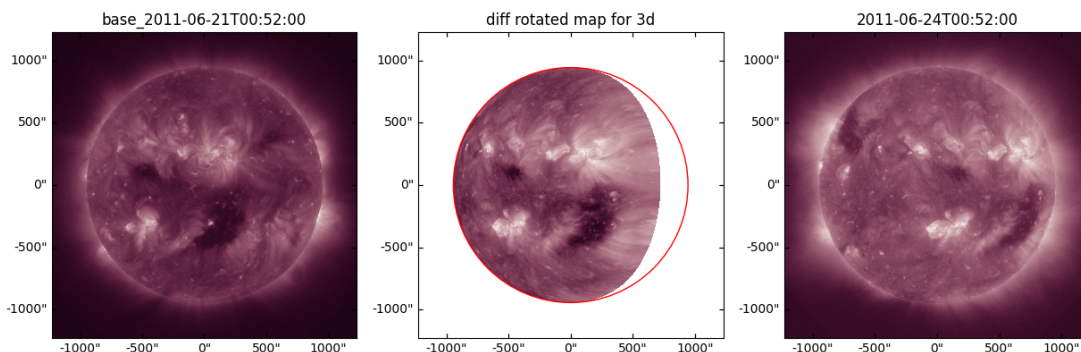


Figure 4-3: Left panel: base map on 6 June 2011 00:52. Middle panel: map on 9 June 2011 after it was differentially rotated to the time of the base map. The red contour indicates the solar limb of the base map. Right panel: original map on 9 June 2011 00:52.

## 4.2.4 Data preprocessing

Data preprocessing plays a crucial role in identifying the size and brightness of the dimming regions. To analyze dimming events, the initial step is to determine the dimming region. Typically, Base Difference (BD) images are used to detect coronal dimmings [Reinard and Biesecker, 2008, Attrill and Wills-Davey, 2010, Podladchikova and Berghmans, 2005]. These are created by subtracting the image before the event from the image at a given time:

$$BD = I_n - I_0, \quad (4.1)$$

where  $I_n$  and  $I_0$  are the intensity of the image at the time  $t_n$  and the base image at the time  $t_0$  respectively. BD images emphasize the absolute changes in intensity, facilitating the identification of regions with significant variations, such as active regions and coronal loops.

However, coronal dimmings, especially secondary dimmings, often occur in quiet solar regions characterized by low coronal intensity. Absolute intensity values alone cannot effectively detect such changes. For off-limb dimming detection, it is even more crucial, as in the upper corona, density is lower compared to regions closer to the solar surface. To address this problem, we use logarithmic base ratio (LBR) images, which form a ratio between the images and the base image (see comparison in Figure 4-4). This approach highlights relative changes and ensures that variations in both high-intensity regions (e.g., coronal loops) and low-intensity regions (e.g., quiet sun) are equally accounted. The logarithmic operation further enhances the visibility of these variations:

$$LBR = \log(I_n/I_0) = \log(I_n) - \log(I_0), \quad (4.2)$$

where  $I_n$  and  $I_0$  are the intensity of the image at the time  $t_n$  and the base image at the time  $t_0$  respectively.

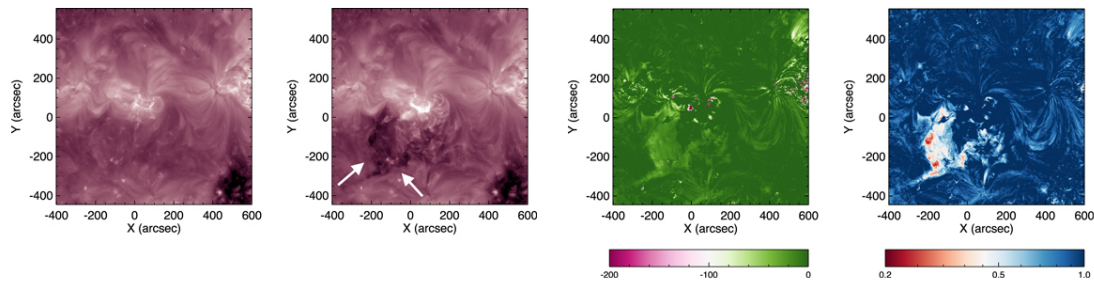


Figure 4-4: Advantages of using **LBR** images for detecting coronal dimming regions. From left to right: logarithmically scaled **SDO/AIA** 211 Å filtergrams before and during a coronal dimming event on 2011 October 1, the corresponding **BD** and **LBR** images. Image scaling is adjusted, with no-change levels set at 0.0 for base-difference and 1.0 for base-ratio images. Regions that increase in intensity over time are saturated, while dimming regions, where intensity decreases, are more distinct and visible. The white arrows point to a observed coronal dimming region. From [Dissauer et al. \[2018a\]](#).

#### 4.2.5 On-disk dimming detection

After the preprocessing steps, we crop the images for the region of interest to study a subfield of, e.g., around  $1000 \times 1000$  arcsecs around the center of the eruption to restrict the dimming detection.

We identify coronal dimming pixels by applying a thresholding algorithm to logarithmic base ratio images. A pixel is classified as a dimming pixel when its logarithmic ( $\log_{10}$ ) intensity ratio drops below -0.19, which corresponds to a decrease of about 35% in linear space. This threshold was determined empirically by comparing the intensity distributions of images before the dimming appearance and the maximum dimming extent for different events [see [Dissauer et al., 2018a](#)].

Seed pixels for the region-growing algorithm are the 30% of the darkest pixels in the **LBR** image. This percentage value is chosen after a trial and error procedure and is the percentage that guarantees that the extracted area is not very noisy (due to the presence of small areas) nor suffers the loss of significant areas, which may not be detected with a too small number of seeds. For more accurate dimming extraction, i.e., to remove small areas and fill gaps, median filtering can be applied to the obtained seed pixels. This filter functions optimally within a  $3 \times 3$  square window, evaluating the median pixel intensity in local neighborhoods.

The region growing method is easily available in `IDL` with the routine `region_grow`. `Sunpy` does not provide a built-in function for this particular task, and there are no documented procedures for implementing this method in Python. Therefore, we have developed a Python algorithm that follows the `IDL` routine to address this need.

Guided by the `IDL` routine `region_grow.pro`, the algorithm evaluates the four connected neighbors (left, top, right and bottom pixels) to grow from the seed points or, alternatively, the 8-connected neighborhood (which counts also the diagonal pixels), adding them to the dimming region if their intensity is lower than a predefined threshold of  $-0.19$ . This process iteratively expands the dimming region, creating a binary dimming map while preserving the original metadata. Ultimately, only contiguous neighboring pixels of these seed pixels are retained as final dimming regions, reducing the detection of small-scale fluctuations and removing misidentified pixels.

The resulting binary map serves as an instantaneous dimming pixel mask, denoted as  $S_m(p_i, t_m)$ , which we introduce in Section 4.3. This mask identifies dimming pixels, represented as  $p_i$ , at each time step  $t_m$ .

Finally, the suggested parameters for the algorithm are: thresholding level for logarithmic base ratio data ( $thr_{LBR}$ ), the amount of darkest pixels extracted from `LBR` data ( $dark\_pix$ ), the size of the square of median filtering for seed pixels ( $s_{LBR}$ ):

$$\begin{aligned} thr_{LBR} &= -0.19 \text{ DN}, \\ dark\_pix &= 30\%, \\ s_{LBR} &= [3, 3]. \end{aligned} \tag{4.3}$$

These parameters are recommended for extracting coronal dimmings and are suitable for statistical analysis, but they can be customized for each case study depending on the specific disturbances around the active region and the overall objectives of the dimming analysis.

### 4.2.6 Off-limb dimmings detection

We adapt the dimming segmentation approach also for dimmings detected off-limb with [STEREO/EUVI 195 Å](#) data.

The main difference of the algorithm is that the segmentation is based on both log base-ratio and base-difference data. This dual approach is necessary because ratio images can introduce significant noise, especially in the region outside the limb, which can hinder dimming extraction. By using base difference data alongside ratio images, we can effectively reduce this noise and improve the accuracy of our dimming analysis.

First, we threshold base-difference data by -1.0 DN and extract 30% of the darkest pixels from it. In this way, the number of pixels with an intensity drop of more than -1.0 DN form the array of seed pixels for the region-growing algorithm (see [Fig. 4-6d](#)). We use the darkest pixels in base-difference data because this criterion is independent of a fixed threshold and is therefore not affected by the changes in the mean intensity in the overall corona over time. In [BD](#) threshold optimization, it's more effective to increase the number of darker pixels rather than raising the threshold level for base-difference data. This approach minimizes the growth of misidentified noise in the lower corona without interfering with logarithmic base ratio data. Overly strict thresholding for base-difference data can lead to the loss of genuine dimming pixels in some instances.

In the next step, we select the thresholding level for logarithmic base ratio data: all pixels with a logarithmic base ratio intensity decrease below a value of -0.19 are identified as dimming pixels (cf. [Fig. 4-6e](#)). This threshold was also found empirically from the histograms by qualitatively checking different images during different development states of the dimming for several events. The thresholding level appeared to be the same as found in [Dissauer et al. \[2018a\]](#) for [SDO/AIA](#) data, as it performed well to separate the dimming pixel distribution from random noise within the majority of histograms investigated for the [STEREO/EUVI](#) data. In [Figure 4-5](#), we show for two sample events, the intensity distribution of the logarithmic base ratio images for two different time steps, one before and one during the dimming. The state before the dimming formation is presented as a black

histogram and shows a small variance in values; the dimming state at the time close to its maximal extent is presented as green histogram and reveals a systematic shift to negative intensity values, indicating the dimming pixels. The chosen thresholding level of -0.19 (blue vertical line) provides a basic, first-level separation of the non-dimming fluctuations in the image and the dimming pixels.

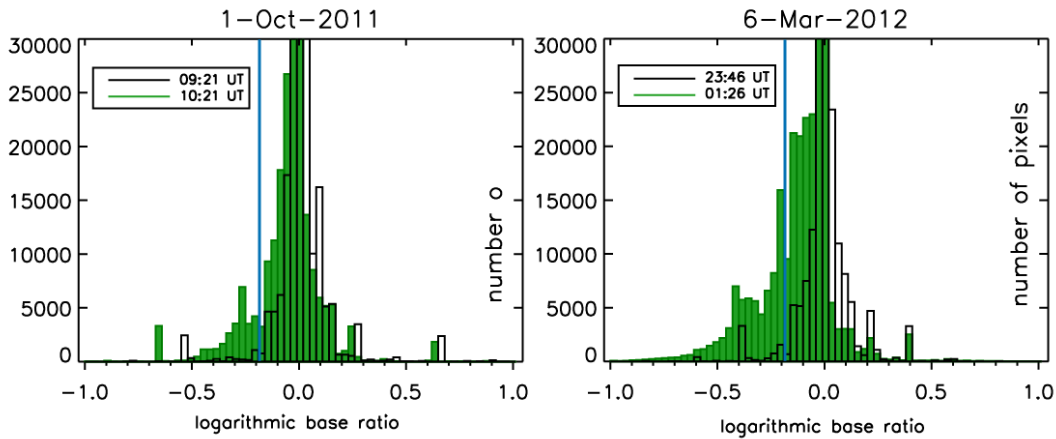


Figure 4-5: Intensity distributions of logarithmic base-ratio images for dimming events that occurred on 2011 October 1 (left) and 2012 March 6 (right). The black histogram is calculated from an image during a pre-event time step (i.e. non-dimming state), and the green histogram is from an image during the time of maximal extent of the dimming. Note the shift toward negative intensity values for the distribution during the dimming state (green). The value used for first level thresholding is shown by the blue vertical line.

In order to reduce noise and the number of misidentified pixels, morphological operators (with a kernel of  $3 \times 3$  pixels) are used to smooth the extracted regions and remove small-scale features. It also helps in situations, where gaps need to be filled in order to let seed pixels grow to more distant dimming parts. Finally, only pixels of **LBR** data, that represent direct neighbors of the seed pixels in **BD** data create the dimming region (cf. Fig. 4-6f), and are subsequently used to extract the properties (area, intensity) of the dimming regions.

In Figure 4-6, we illustrate all the major steps of the dimming detection algorithm. The top panels show the original data (a), the **BD** image (b) and the **LBR** image (c). The masks of the extracted regions for each step are shown in the bottom panels: the darkest pixels derived from the **BD** image (d), which are used as the seed pixels in the thresholded **LBR** data (e) by applying the region-growing algorithm to

form the final dimming region (f). As it can be noticed, the noise in the **LBR** data is mostly present in regions higher up in the corona and does not overlap with the noise of **BD** data in the low corona. Thus, the chosen approach combining the two types of data is effective for the dimming extraction above the solar limb.

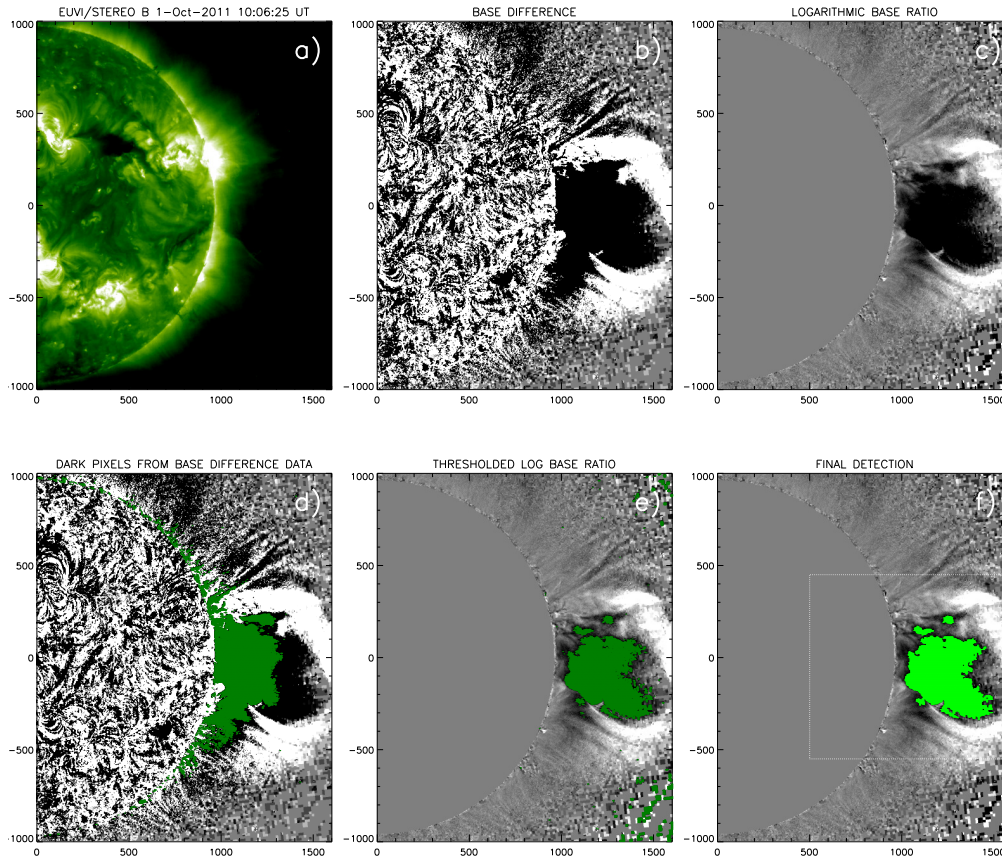


Figure 4-6: Dimming detection for the event on 2011 October 1. The top panels present original **EUVI/STEREO** 195 Å filtegrams (a) together with base-difference (b) and logarithmic base-ratio (c) data. The bottom panels highlight pixels identified during the different steps of the detection: the darkest pixels extracted from base difference data (d), logarithmic base ratio data thresholded by level -0.19 (e), the final dimming region segmented for this time step in logarithmic base ratio data (f). The coordinates are given in arcsec from Sun center.

Finally, the chosen parameters for the algorithm are: thresholding level for logarithmic base ratio data ( $thr_{LBR}$ ), thresholding level for base difference data ( $thr_{BD}$ ), the amount of darkest pixels extracted from base difference data ( $dark\_pix$ ), the size of the square for the smoothing functions for base difference and logarithmic base ratio data ( $s_{BD}$  and  $s_{LBR}$ , respectively):

$$\begin{aligned}
\text{thr}_{\text{LBR}} &= -0.19 \text{ DN}, \\
\text{thr}_{\text{BD}} &= -1.0 \text{ DN}, \\
\text{dark\_pix} &= 30\%, \\
s_{\text{LBR}} &= [3, 3], \\
s_{\text{BD}} &= [3, 3].
\end{aligned}
\tag{4.4}$$

To remove small areas from the final extracted region, e.g., distant parts not connected to this dimming, we suggest to use the `label` function from *skimage.measure* library in Python. The routine adds an index to all dimming areas that were finally extracted and deletes all areas where the number of pixels is less than, e.g., 10% of the number of pixels in the biggest region.

For illustration, we show Figure 4-7 as an example of the detection and different appearance of the dimming event that occurred on 2011 October 1, observed on-disk by SDO AIA [Dissauer et al., 2019] and off-limb by the STEREO-B satellite. We show the direct SDO AIA 211Å (top) and the STEREO-B/EUVI 195Å (bottom) images close to the time of maximal extent of the dimming, the corresponding logarithmic base-ratio images and the timing maps. The colors in the timing maps encode for each dimming pixel the time of its first detection.

### 4.3 Characteristic dimming parameters

With our developed algorithm, we can extract and analyze various parameters associated with coronal dimming regions and their temporal evolution, providing a comprehensive understanding of their physical properties. Our analysis focuses on key parameters that characterize the dynamics, morphology, and brightness of these dimming regions. In particular, we investigate both the area and brightness parameters for the BD and LBR data and their corresponding derivatives.

**Identification of dimming pixels:** At each time step, denoted by  $t_m$ , we systematically identify the dimming pixels, represented as  $p_i$ . Tracking of these pixels is critical to understanding the evolving dimming regions within the data.

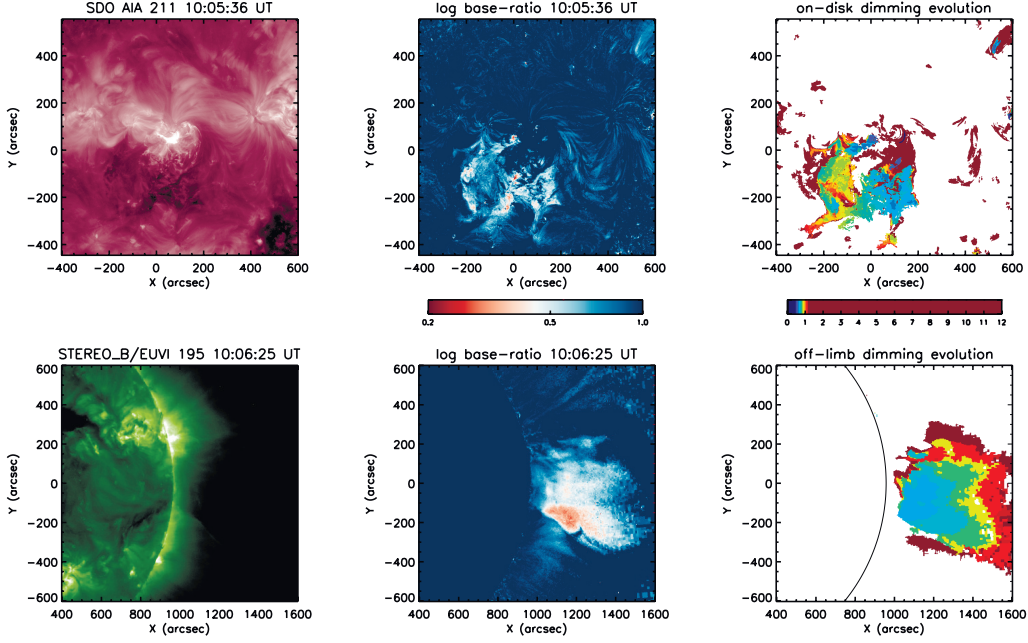


Figure 4-7: Illustration of the dimming evolution from two different viewpoints for the event of 2011 October 1. The top panels represent on-disk dimming observations: **SDO AIA 211Å** filtegram (left), logarithmic base-ratio map (middle), timing map (right), that marks when each dimming pixel was detected for the first time (presented in hours after the flare onset). The bottom panels show the same for the off-limb dimming observations by **STEREO-B/EUVI**.

**Instantaneous dimming mask:** To visualize the dimming regions at a given time  $t_m$ , we create a mask for instantaneous dimming pixels, denoted as  $S_m(p_i, t_m)$ . This mask is binary and assigns a value of 1 to pixels that are inside the dimming regions and 0 to pixels that are outside these regions. This mask represents all the dimming pixels at a given time step  $t_m$ .

**Cumulative dimming mask:** To track the evolution of dimming regions over time, we accumulate all pixels identified as dimming pixels from the initial time point to a specific time point, denoted  $t_n$ .

The cumulative dimming pixel mask  $C(p_i, t_n)$  is created over time by combining the instantaneous dimming pixel masks identified from  $t_0$  until  $t_n$ ,

$$C(p_i, t_n) = S_n(p_i, t_n) \cup S_{n-1}(p_i, t_{n-1}) \cup \dots \cup S_0(p_i, t_0). \quad (4.5)$$

$C(p_i, t_n)$  - the cumulative mask, which contains every pixel which was flagged

as dimming pixel by the time period  $[t_0, t_n]$

With the cumulative masks, we can observe the full extent of the total dimming region over time.

Cumulative masks allow us to study the full extent of the total dimming region over time. Figure 4-8 shows the evolution of the cumulative dimming masks for the example event 2011 October 1. The left and middle panels show snapshots of the original and LBR STEREO/EUVI images. The corresponding dimming cumulative masks, extracted by our algorithm, are presented in the right panels. Green pixels show the newly detected dimming regions, while gray pixels represent all pixels that were extracted as part of the dimming region during previous time steps.

### 4.3.1 Dimming area

By using the extracted masks, the evolution of coronal dimming regions is studied by the instantaneous and cumulative areas: the instantaneous area  $A_{in}(t_n)$  represents the number of pixels identified as dimming pixels at a certain time step  $t_n$ , the cumulative area  $A_{cu}(t_n)$  is determined by combining the number of all dimming pixels detected up to time  $t_n$ :

$$A_{cu}(t_n) = \sum_i C(p_i, t_n) a_i, \quad (4.6)$$

where  $a_i$  is the area of each dimming pixel  $p_i$  within the cumulative dimming pixel mask  $C(p_i, t_n)$ . In Section 4.4, we introduce the novel method to eliminate the projection effects and calculate  $a_i$  as a surface area of a sphere for every pixel, significantly improving the accuracy of the area estimation.

With this parameter, we capture the full extension of the dimming region until the time  $t_n$ . With the time evolution of both quantities, we can study the spatial and temporal morphology of the dimming region in detail.

The corresponding area growth rate  $dA/dt(t_i)$  characterizes how fast the dimming is developing; it is calculated as the corresponding time derivative of  $A_{in}(t)$  or  $A_{cu}(t)$  [see also Dissauer et al., 2018a]. The time evolution of these quantities

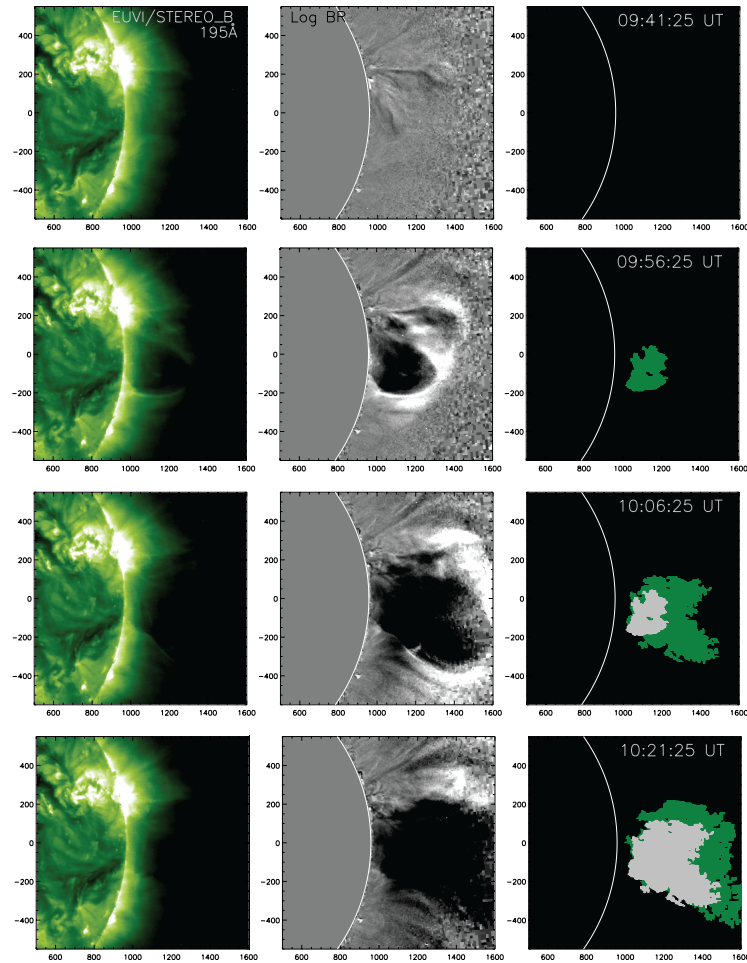


Figure 4-8: Coronal dimming evolution for the 2011 October 1 event. From left to right: direct [EUVI/STEREO-B](#) filtergrams, [LBR](#) images, and cumulative dimming pixel masks. In the right panels, the green pixels on top of the cumulative dimming pixel masks (gray regions) represent all newly detected pixels compared to the previously shown time step. The white contour indicates the solar limb.

allows us to study the dynamic evolution of the dimming region and to determine its impulsive phase.

### 4.3.2 Dimming brightness

According to [Mason et al. \[2016\]](#), it has been observed that CMEs associated with dark and large dimming regions tend to be more massive. The analysis of dimmings on-disk by [Dissauer et al. \[2019\]](#) proves this statement. Consequently, the total brightness parameter becomes a valuable tool for quantifying the extent of plasma evacuation during CME events.

It's important to note that the approach chosen for defining the dimming region significantly impacts the information we can extract from the parameter's temporal evolution.

The total instantaneous brightness  $I_{in}$  of the dimming region at time step  $t_m$ , is calculated as the sum of dimming pixels intensities at the time step  $t_m$ :

$$I_{in}(t_m) = \sum_i I(p_i, t_m) S_m(p_i, t_m), \quad (4.7)$$

where  $I(p_i, t_m)$  is the intensity at  $t_m$  for a dimming pixel  $p_i$  in the instantaneous mask  $S_m(p_i, t_m)$ . This equation quantifies the total brightness within the dimming region at a particular moment in time. It allows us to track how the brightness changes instantaneously as the dimming event progresses. Whether a maximum dimming area or minimum pixel intensity contributes to the minimum value of instantaneous brightness can be uncertain. To mitigate this uncertainty and create a parameter that solely depends on pixel intensity, we calculate the cumulative brightness:

$$I_{cu}(t_m) = \sum_i I(p_i, t_m) C(p_i, t_n), \quad (4.8)$$

where  $I(p_i, t_m)$  is the intensity at  $t_m$  for a certain dimming pixel  $p_i$  within a fixed cumulative dimming mask  $C(p_i, t_n)$ . Here, the dimming area is the same for the full-time range because it is defined as all dimming pixels that have been identified from the start  $t_0$  to time  $t_n$ . This cumulative brightness parameter is particularly valuable for tracking the overall increase or decrease in dimming intensity over the entire duration of the event, especially for investigating the recovery phase.

After defining the instantaneous and cumulative brightness, we calculate their change rates. The corresponding time derivative gives the brightness change rate:

$$\frac{dI}{dt} = \frac{I(t_m) - I(t_{m-1})}{t_m - t_{m-1}}, \quad (4.9)$$

Furthermore, for each type of total brightness, we extract the mean intensity of the dimming by dividing the total dimming brightness  $\bar{I}(t_i)$  by the area  $A(t_m)$  at the same time step for instantaneous and by the constant area  $A(t_n)$  for cumulative:

$$\bar{I}_{in}(t_m) = \frac{I_{in}(t_m)}{A(t_m)}, \bar{I}_{cu}(t_m) = \frac{I_{cu}(t_m)}{A(t_n)}. \quad (4.10)$$

### 4.3.3 Impulsive phase of the dimming

Coronal dimmings typically begin to form concurrently with the early stages of CMEs and may persist for several hours following their inception [e.g., [Dissauer et al., 2018b](#), [Vanninathan et al., 2018](#)]. Our analysis primarily focuses on the impulsive phase of coronal dimming evolution, as characterized by the area growth rate profile  $dA/dt$ .

To identify this impulsive phase, we adopt the definition established in [Dissauer et al. \[2018a\]](#) and [Dissauer et al. \[2018b\]](#). We pinpoint the start of the impulsive phase, denoted as  $t_{start}$ , as the local minimum occurring closest in time before the highest peak of  $dA/dt$ . Subsequently, we determine the end of the impulsive phase, marked as  $t_{end}$ , as the moment when the value of the area growth rate falls below 15% of its maximum, as indicated by the following equation:

$$\dot{A}(t) \leq 0.15 \cdot \dot{A}_{max}. \quad (4.11)$$

The duration of the impulsive phase for the coronal dimming event can then be estimated as the time difference between  $t_{end}$  and  $t_{start}$ :

$$t_{dur} = t_{end} - t_{start}. \quad (4.12)$$

This parameter,  $t_{dur}$ , characterizes the duration of the impulsive phase and provides crucial insights into the temporal dynamics of coronal dimming events.

### 4.3.4 Magnetic flux

When paired with observations of flare ribbons, coronal dimmings serve as a diagnostic instrument for exploring the magnetic configuration of solar eruptions. This is particularly valuable because the detailed structure and positions of dimmings can provide additional insight into the diverse flux systems involved in the eruption

process.

To comprehensively understand the magnetic properties of coronal dimmings, we use the following approach to extract the positive and negative magnetic fluxes up to time  $t_n$ :

$$\begin{aligned}\Phi_+(t_n) &= \sum_i B_+(p_i)C(p_i, t_n)a_i, \\ \Phi_-(t_n) &= \sum_i B_-(p_i)C(p_i, t_n)a_i.\end{aligned}\tag{4.13}$$

Assuming closed loops, we can calculate the total unsigned magnetic flux as the mean of the absolute values of the reconnection fluxes in both polarity regions [Tschernitz et al., 2018]:

$$\Phi(t_n) = \frac{(\Phi_+ + |\Phi_-|)}{2}.\tag{4.14}$$

This extraction process is performed from cumulative masks  $C(p_i, t_n)$  exclusively with pixels where the magnetic field density in the line of sight exceeds the SDO/HMI 720 s noise threshold ( $|B| > 10$  G). According to Couvidat et al. [2016], the HMI 720 s LOS magnetograms have a photon noise of 3 G at the solar disk center. To address the increasing noise levels toward the limb, we use a threshold of 10 G [similar to Tschernitz et al., 2018].

In addition, we calculate the time derivatives for each parameter to quantify the corresponding rates of change in magnetic flux.

Studying these magnetic properties helps us understand the amount of magnetic flux present in the dimming region and subsequently ejected into interplanetary space by the CME to determine whether it is in equilibrium and whether it originates from isolated, magnetically strong regions.

### 4.3.5 Recovery time

The recovery time of coronal dimmings refers to the duration required for the solar corona to restructure and replenish itself after the occurrence of a CME.

During a CME event, the intense energy and material ejected by the Sun can lead to the formation of dimming regions as plasma and magnetic fields are temporarily

removed or redistributed. The recovery time indicates how quickly the solar corona recovers from these perturbations and restores the typical plasma and magnetic field configurations from before the CME.

The recovery parameter can provide insights into the natural processes of solar restructuring. Depending on the research question, this metric can be defined in differently: as the time of dimming area decrease or increase of brightness; for the total dimming region or its core/secondary parts. We define and investigate this parameter further in the following chapters. As it will be seen, different metrics provide different timescales.

## 4.4 Area correction

The methods of dimming analysis described in this work strongly rely on the dimming area parameter. The images of the Sun provide only a 2D representation of the actual 3D solar surface. Projection effects lead to the different weights of each pixel; e.g., closer to the limb, the pixel area is larger than for pixels closer to the Sun center. Therefore, for an accurate definition of the area, we present a method to identify the surface area of a sphere for each pixel. All the code is publicly available on GitHub<sup>1</sup>.

The equation of the sphere is given by

$$x^2 + y^2 + z^2 = R^2. \quad (4.15)$$

Here,  $R$  is the radius of the sphere in kilometers, and  $(x, y, z)$  are the coordinates of points of a sphere. The surface of a sphere can be described as a function of two variables:

$$z = f(x, y) = \sqrt{R^2 - x^2 - y^2}. \quad (4.16)$$

The projection of the sphere onto the  $XY$  plane is a circle belonging to the  $XOY$  plane, where  $O$  is the center of the sphere. The surface area of a sphere that has the

<sup>1</sup>[https://github.com/Chigaga/area\\_calculation](https://github.com/Chigaga/area_calculation)

region  $S$  as its projection onto the  $XOY$  plane is given by [Bronshtein et al., 2007]

$$\sigma = \int_S \int \sqrt{1 + \left(\frac{\partial z}{\partial x}\right)^2 + \left(\frac{\partial z}{\partial y}\right)^2} dx dy. \quad (4.17)$$

As follows from Equation (4.16),

$$\begin{aligned} \frac{\partial z}{\partial x} &= -\frac{x}{\sqrt{R^2 - x^2 - y^2}} \\ \frac{\partial z}{\partial y} &= -\frac{y}{\sqrt{R^2 - x^2 - y^2}}. \end{aligned} \quad (4.18)$$

Therefore, using Equation (4.18), Equation (4.17) can be rewritten as

$$\sigma = R \int_S \int \frac{1}{\sqrt{R^2 - x^2 - y^2}} dx dy. \quad (4.19)$$

Further, we present how to estimate the surface area of a sphere, where projection  $S$  onto the  $XOY$  plane has a size of 1 pixel. Figure 4-9 shows the scheme of a solar image, where the outer square shows the boundaries of a solar image from a spacecraft. The marker C in the top left corner indicates the pixel with the coordinates (1,1), and  $i$  and  $j$  mark row and column numbers. The marker C' also shows the pixel with the coordinates (1,1), but in a new coordinate system with rows  $i'$  and columns  $j'$  derived from  $i$  and  $j$  in the following way:

$$\begin{aligned} i' &= i - Top \\ j' &= j - Left. \end{aligned} \quad (4.20)$$

Here, the Top/Left show the distance (in pixels) from the top/left border of the image to the beginning of the Sun.

$P$  is a pixel area which we are estimating, and  $(i'_p, j'_p)$  are the coordinates of its center. Pixel  $P$  is a square with a side  $a$ , the size of which is defined as

$$a = \frac{R}{R_P}. \quad (4.21)$$

Here,  $R$  is the radius of the Sun in kilometers,  $R_P$  is radius of the Sun in pixels.

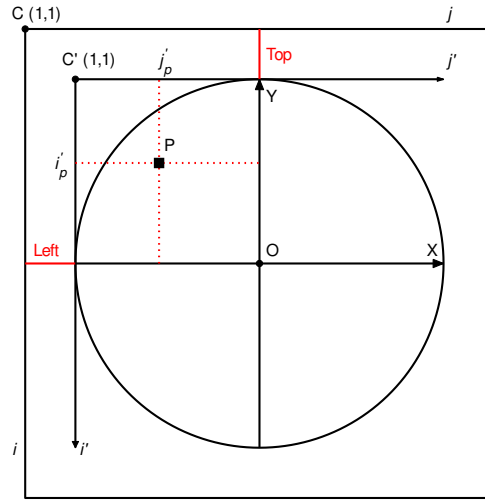


Figure 4-9: Scheme of a solar image. The outer square shows the boundaries of a solar image from a spacecraft. The marker  $C$  at the top left corner indicates the pixel with the coordinates  $(1,1)$ ,  $i$  - row number,  $j$  - column number. The marker  $C'$  also shows the pixel with the coordinates  $(1,1)$ , but in a new coordinate system with rows  $i'$  and columns  $j'$  connected to  $i$  and  $j$  via Equation (4.20). “Top”/“Left” show the distance (in pixels) from the top/left border of the image to the beginning of the Sun.  $P$  is a pixel, and  $(i'_p, j'_p)$  are the coordinates of its center.

A coordinate  $Y$  of the lower pixel boundary is defined by

$$a(R_P - i' - 0.5). \quad (4.22)$$

A coordinate  $Y$  of the upper pixel boundary is given by

$$a(R_P - i' + 0.5). \quad (4.23)$$

A coordinate  $X$  of the left pixel boundary is determined as

$$a(-R_P + j' - 0.5). \quad (4.24)$$

A coordinate  $X$  of the right pixel boundary is defined by

$$a(-R_P + j' + 0.5). \quad (4.25)$$

Taking into account Equations (4.22–4.25), and replacing the calculation of the

double integral by the successive calculation of two simple integrals, Equation (4.19) can be rewritten as

$$\sigma = R \int_{a(-R_P+j'-0.5)}^{a(-R_P+j'+0.5)} dx \int_{a(R_P-i'-0.5)}^{a(R_P-i'+0.5)} \frac{1}{\sqrt{R^2 - x^2 - y^2}} dy. \quad (4.26)$$

Further, we solve the internal integral from Equation (4.26) analytically and the external one numerically. The internal integral from Equation (4.26) can be rewritten as

$$\int_{a(R_P-i'-0.5)}^{a(R_P-i'+0.5)} \frac{1}{\sqrt{R^2 - x^2} \sqrt{1 - \frac{y^2}{R^2 - x^2}}} dy. \quad (4.27)$$

Let us use the change of variables in Equation (4.27):

$$\begin{aligned} u &= \frac{y}{\sqrt{R^2 - x^2}} \\ du &= \frac{dy}{\sqrt{R^2 - x^2}}. \end{aligned} \quad (4.28)$$

Thus, Equation (4.27) can be rewritten as

$$\int_{\frac{a(R_P-i'-0.5)}{\sqrt{R^2-x^2}}}^{\frac{a(R_P-i'+0.5)}{\sqrt{R^2-x^2}}} \frac{1}{\sqrt{1-u^2}} du. \quad (4.29)$$

The solution of the integral represented by Equation (4.29) is given by

$$\arcsin\left(\frac{a(R_P - i' + 0.5)}{\sqrt{R^2 - x^2}}\right) - \arcsin\left(\frac{a(R_P - i' - 0.5)}{\sqrt{R^2 - x^2}}\right). \quad (4.30)$$

Further, we solve the external integral of the resulting function given by Equation (4.30) using the mean rectangle method [Hughes-Hallett et al., 2017]. First, we divide the integration interval by  $N$  regions:

$$dx = a/N. \quad (4.31)$$

Here,  $N = 1000$ . Then we calculate the integral by finding a sum of the areas of  $N$  rectangles defined by

$$A_k = R \left( \arcsin\left(\frac{a(R_P - i' + 0.5)}{\sqrt{R^2 - (x_k + \frac{dx}{2})^2}}\right) - \arcsin\left(\frac{a(R_P - i' - 0.5)}{\sqrt{R^2 - (x_k + \frac{dx}{2})^2}}\right) \right) dx. \quad (4.32)$$

Here,  $k = 1, 2, \dots, N$ ;  $A_k$  is calculated at the middle of each region, and  $x_k$  takes the values within integration limits from  $a(-R_P + j' - 0.5)$  to  $a(-R_P + j' + 0.5)$  and for each  $k$  is estimated as

$$x_k = a(-R_P + j - 0.5) + (k - 1)dx. \quad (4.33)$$

The resulting area of a pixel is defined by the sum of  $x_k$ .

With this method, we calculate the area of every pixel of the solar disk and construct a correction map, where each pixel is weighted by its area (Figure 4-10). The color bar shows the ratio of each pixel area to the square pixel in the center of the solar disk. Any mask of the dimming region can be applied to this map to obtain the final dimming area. We can see that the suggested calibration creates significant changes in the area values. For this reason, we use the derived spherical projections of the pixels to derive the area parameter.

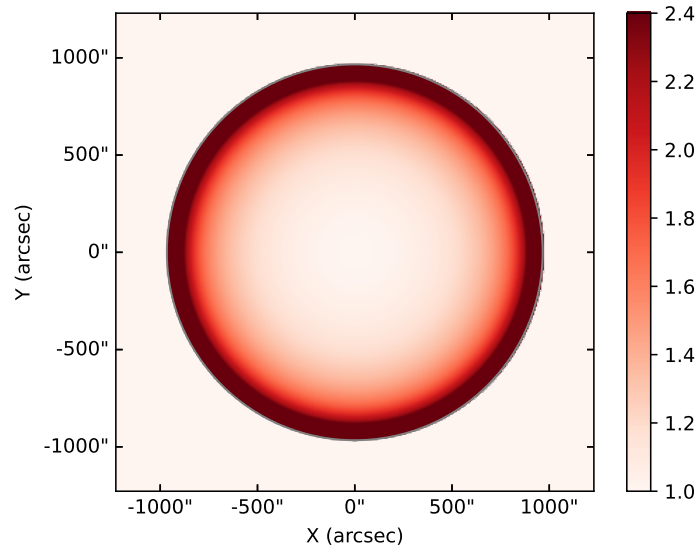


Figure 4-10: Correction area map for the full solar disk for SDO/AIA observations of 28 October 2021. The colorbar shows the ratio of every pixel area to the average pixel and increases closer to the limb.

We propose adopting this approach for a precise correction of all on-disk pixels. In particular, it will be useful for the pixels located close to the limb (beyond  $60^\circ$ ), which are disregarded in the classical correction method using a factor of  $1/\cos \alpha$  [Hagenaar, 2001]. By implementing this alternative method, we can achieve en-

hanced accuracy in the correction process for solar images.

## 4.5 Examples of dimming analysis

Here we present two published case studies as examples of the analysis of coronal dimmings as the diagnostic tool for solar eruptive events. These examples show the importance of observing coronal dimming to gain insight into the early stages of CME development and how the analysis of dimmings with other CME signatures provides various information about the event. They also highlight how the choice of parameters for dimming analysis can reveal different insights into the progression of these events. We show only the parts related to the coronal dimmings, but the studies presented here examine many more signatures and processes during these events.

### 4.5.1 International Women Day event - 8 March 2019

In [Dumbović et al. \[2021\]](#) study, we address a fascinating event that defies conventional expectations in the field of solar phenomena. In particular, we examine a C1.3 flare with a double-peaked profile that occurred on March 8, 2019, during a period of solar minimum that fittingly coincided with International Women’s Day (SOL-2019-03-08T03:07C1.3). Despite its relatively low GOES classification, this flare exhibited various features typically associated with stronger solar flares. These included coronal dimmings, the appearance of two EUV waves, type II and III bursts, and the ejection of two coronal loops that interestingly occurred in pairs.

For the dimming analysis in this research, we define a more strict thresholding level to focus on the darkest parts within the dimming region. Given the dual characteristics of the event, we analyze two distinct segments within the dimming region.

Note, that in Section 6 we show the recovery time analysis for this event, where a more shallow dimming region was segmented.

## Dimming analysis

To segment the dimming regions, we use logarithmic base ratio images created from [SDO/AIA 211 Å](#) frames with a reference image taken at 02:39 UT. For the detection algorithm we applied a logarithmic threshold of -0.38 and calculated the corresponding areas on the spherical solar surface. Our main focus was to identify the spatial distribution of these dimming regions and to follow their temporal evolution, especially with respect to the two-stage behavior of the studied flare.

Figure 4-11 shows the progression of the coronal dimming using [SDO/AIA 211 Å](#) filtergrams, log base ratio images, and detection masks. At 03:10 UT we observe two distinct dimming centers in the lower corona near the core of the active region and two more on its western edge. In particular, the northern center at about  $(x,y)=(20'',280'')$  is clearly identified as the origin of the erupting large loops. Thereafter, two dimming regions emerge: one east and one west of the AR, that coincide with the endpoints of the observed flare ribbons (Fig.2 in the associated paper).

Crucially, the evolution of the primary dimming is a distinct two-stage pattern, with the western dimming region expanding first, followed by the eastern one. This feature can also be seen in the timing map in Figure 4-12, which shows the initial rapid development phase of the dimming during the first hour of its development. Thus, we divided the dimming region within the active region into an eastern and western segment, with the division at  $x = 50''$ . We then monitored the instantaneous dimming area and brightness in each of these detected dimming regions separately, comparing their dynamics with flare flux.

## Results

Figure 4-13 shows a comparative analysis of the (a) area, (b) brightness and (c) its derivatives within two dimming regions together with (d) [GOES 1–8 Å](#) flux in soft X-ray light and time derivative of the 0.5–4 Å flux. The dimming area and brightness in the western part rapidly increase between 03:10 and 03:16 UT, coinciding with the impulsive phase of the first flare peak in [GOES](#) soft X-rays. At the same time, the eastern part also develops, but at a slower pace. Subsequently, there is a sudden increase in eastern dimming between 03:32 and 03:38 UT, coinciding with the second

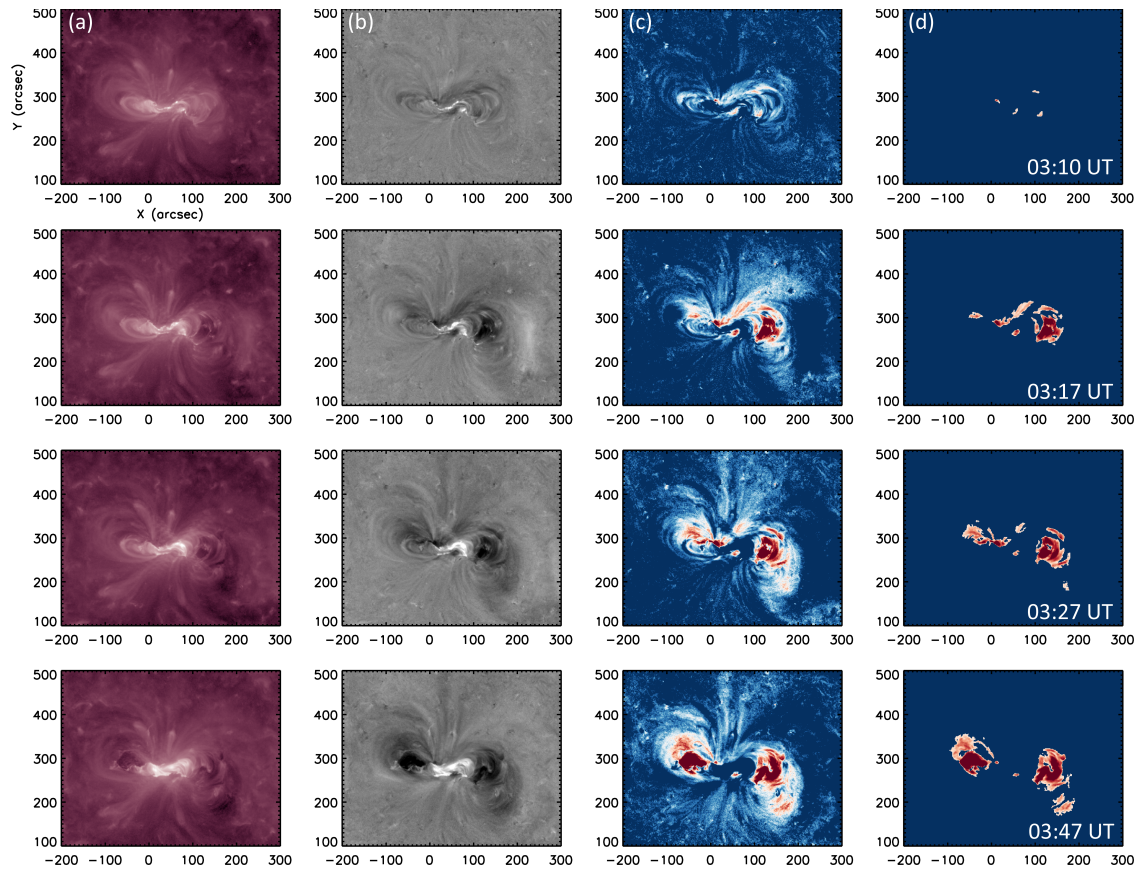


Figure 4-11: Coronal dimming evolution as observed in SDO/AIA 211 Å filtergrams: a) direct images, b) logarithmic base ratio images scaled to  $[-1, 1]$ , c) logarithmic base ratio images scaled to  $[-0.7, 0]$  to highlight the pixels that decreased in intensity, d) segmented dimming masks applying a logarithmic threshold level of  $-0.38$ . From [Dumbović et al. \[2021\]](#).

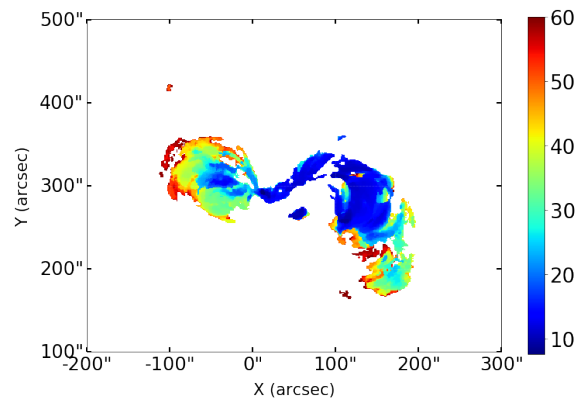


Figure 4-12: Timing map of the coronal dimming region indicating when each dimming pixel was detected for the first time. The color bar in the timing map gives the time (in minutes) after 03:00 UT. From [Dumbović et al. \[2021\]](#).

peak of the derivative of the [GOES](#) flare.

Thus, our dimming analysis decisively indicates the occurrence of two eruptions. Nevertheless, it is important to note that we cannot definitively distinguish between core and secondary dimmings for all observed dimmings. Based on the dimming analysis alone, we cannot provide a conclusive determination. Together with a comprehensive analysis of all detected CME signatures in the low corona (flare, EUV waves, coronal loops), the double nature of the event was stated.

At the same time, the coronagraph observations do not clearly confirm the existence of two distinct CMEs. Only a single entity can be observed, likely consisting of two sheared and twisted structures consistent with the two eruptions observed in the lower corona.

## Conclusion

Our detailed analysis of the 8 March 2019 event, focusing in particular on the coronal dimming, has revealed a distinct two-stage pattern indicative of two separate eruptions. The dimming regions, both east and west, exhibited dynamics that closely followed the flare flux, adding to the evidence for a double eruption.

Coronal dimmings can provide insights into the double nature of magnetic structures during their initial phases, which can help to identify and understand the initial magnetic configuration and dynamics before they evolve or combine at higher altitudes. This understanding can be crucial for modeling CME parameters and predicting their potential geoeffectiveness.

### 4.5.2 2 November 2021

In [Thalmann et al. \[2023\]](#) we investigate the magnetic dynamics of a solar eruptive event using various modeling techniques, revealing insights into its evolution from the solar source to interplanetary space, to emphasize the significance of both pre-eruptive and eruptive magnetic properties.

It is widely accepted that the acceleration of a solar flare results from magnetic reconnection, and this principle allows us to use flare ribbons as indicators to track

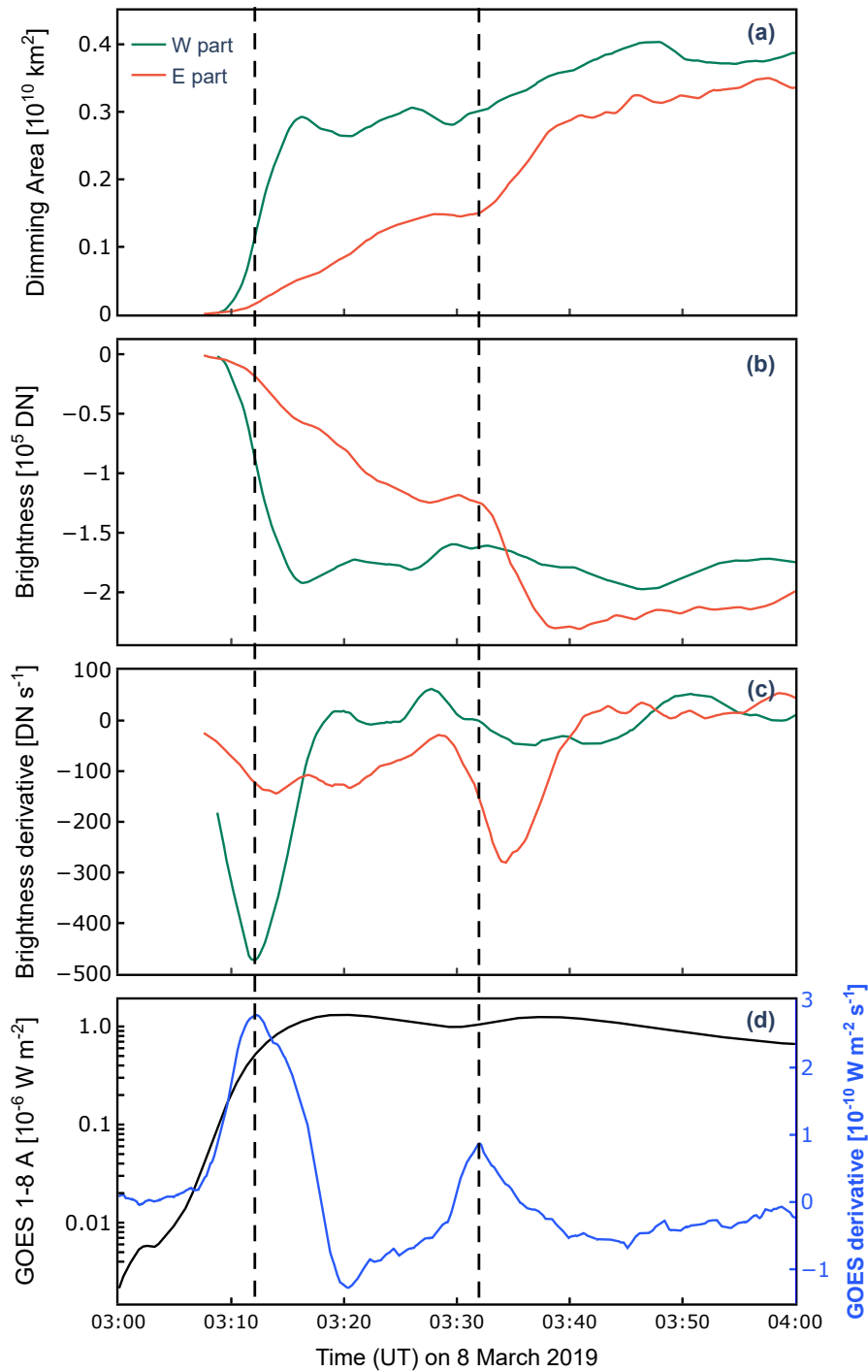


Figure 4-13: Time evolution of the derived coronal dimming parameters: a) instantaneous dimming area and b) brightness, calculated separately for the eastern (orange) and western (green) components of the dimming region. c) Time derivative of the dimming brightness plotted in panel b. d) GOES 1–8 Å soft X-ray light curve and 0.5–4 Å time derivative of the flare emission. Two vertical dashed lines mark the peaks in GOES derivative. The curves are smoothed with a forward-backward exponential smoothing method [Brown, 1963]. From Dumbović et al. [2021].

local reconnection rates and, consequently, flare reconnection flux [as discussed in [Priest and Forbes, 2002](#)]. Similarly, coronal dimmings, as demonstrated in [Thompson et al. \[1998, 2000\]](#), [Dissauer et al. \[2018a, 2019\]](#), can serve as valuable tools for estimating global reconnection rates. Dimmings reflect the evacuation of plasma in the lower corona along the magnetic field lines of an arcade originally located above a pre-existing flux rope. These field lines are then closed by magnetic reconnection following a coronal mass ejection. In this context, coronal dimmings tend to develop before magnetic reconnection occurs.

### Event description

We study a series of connected events – a confined C4.5 flare, a flare-less filament eruption, and a double-peak M-class flare – that originated in NOAA active region (AR) 12891 on late 2021 November 1 and early 2021 November 2.

Active region 12891 was the first geo-effective [AR](#) of the current solar cycle 25 when it produced a long-duration M-class flare (SOL-2021-11-02T01:20M1.7; peak time 03:01 UT; heliographic position N16W09) preceded by a smaller C-class flare (SOL-2021-11-01T23:35C4.5; peak time 23:40 UT; heliographic position N17E04). An extended filament partially erupted during successive activity.

### Dimming analysis

For the analysis of coronal dimmings, we use sequences of [AIA](#) 211 Å maps corrected for differential rotation to the reference time 1 November 23:05 UT. We extract the cumulative dimming area  $A(t)$  and its derivative  $dA/dt$  using the standard thresholding level in the detection algorithm (Sec. 4.2.5). We estimate the total cumulative dimming flux and corresponding flux change rate using [HMI](#) LOS magnetograms within the “magnetic dimming region”, i.e., where the flux density exceeds 10 G [[Dissauer et al., 2018a](#)].

To calculate the flux from the flare ribbons for comparison, we use sequences of [AIA](#) 1600 Å maps, corrected for differential rotation to the same reference time of 01 November 23:05 UT. Following [Veronig and Polanec \[2015\]](#), we segment the flare ribbons and derive the positive, negative, and total magnetic reconnection flux and

the corresponding flux change rates (time derivatives) from the derived flare ribbon masks.

Both for the dimming and flare ribbon analysis, we apply a  $\pm 5\%$  change to the threshold level and compute the mean values and corresponding standard deviation of the reconnection flux for further comparison.

## Results

Figure 4-14 shows the spatial evolution of coronal dimmings together with the flare ribbons. During the early phase of the M1.6 flare, extended flare ribbons developed after  $\sim 02:14$  UT yet lacked the signatures of an erupting structure. The latter appeared only after  $\sim 02:20$  UT and was directed toward south. At that time, pronounced X-ray sources also developed and the maximum growth rate in dimming area was reached ( $\approx 4 \times 10^7 \text{ km}^2 \text{ s}^{-1}$ ).

The mean magnetic flux in coronal dimmings (black solid curve in Figure 4-15(c)) exhibits no obvious response to the C4.5-class flare, while the strongest responses occur before the ribbon-associated fluxes, during the early impulsive phase of the M1.6 flare. From the mean cumulative flare ribbon flux (black dashed curve in Figure 4-15(b)), we estimate that a total of  $\approx 1.5 \pm 0.1 \times 10^{21} \text{ Mx}$  was liberated between 01 Nov 23:40 UT and 02 November 04:00 UT, i.e., during the course of the C4.5 and M-class flares. Similarly, from the cumulative dimming flux (black dashed curve in Figure 4-15(c)), we estimate a total of  $\approx 9.7 \pm 0.5 \times 10^{21} \text{ Mx}$ .

Comparison of the relative timing of dimming reconnection fluxes reveals a period of significant contribution to the latter during which no significant contribution is observed from flare ribbons. This can indicate that during the flare-less filament eruption and the early phase of the double-peak M-class flare, between 02 November  $\sim 01:00$ – $02:00$  UT, magnetic reconnection was taking place high in the solar corona, too weak to produce a measurable imprint onto the low solar atmosphere where the flare ribbons have been tracked (using AIA 1600 Å images). This is also supported by the fact that the flare ribbons were much more pronounced and exhibited larger spatial extents when observed in AIA 304 Å. Therefore, the ribbon-based estimate likely represents a lower limit of the total reconnection flux. As discussed

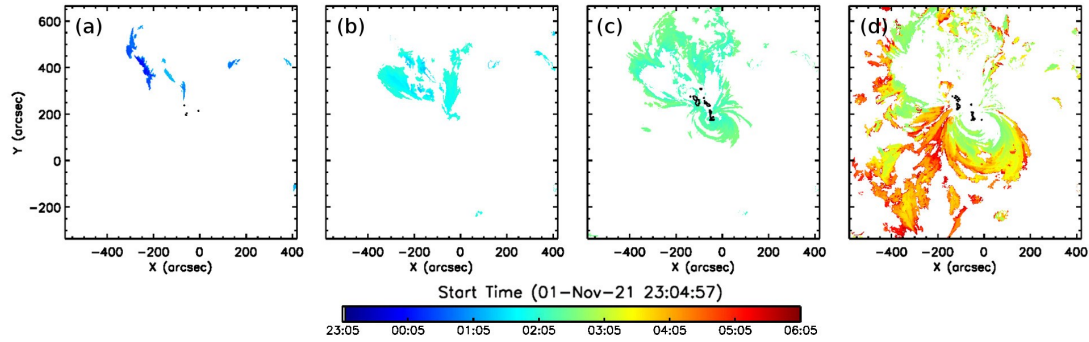


Figure 4-14: Spatial and temporal evolution of coronal dimmings and flare ribbons. Area newly occupied by coronal dimmings during individual episodes, color-coded according to time: (a) the C4.5 flare and a subsequent (flare-less) partial filament eruption (01 November 23:05 – 02 November 01:20 UT), (b) the early phase of the M1.7 flare (01:20 – 02:05 UT), (c) the impulsive phase of the M1.7 flare (02:05 – 02:40 UT), and (d) the early decay phase of the M1.7 flare (02:40 – 05:48 UT). The corresponding total area occupied by flare ribbons is outlined as a black contour. Adapted from [Thalmann et al. \[2023\]](#).

in [Forbes and Lin \[2000\]](#), [Lin et al. \[2004\]](#), when magnetic reconnection occurs at higher heights in the solar corona and does not create sufficiently energetic radiation to produce visible signatures in the near layers of the solar atmosphere, the magnetic flux enclosed by the dimming regions should be used as a more accurate estimate of the reconnection flux compared to the flux enclosed by the flare ribbons.

## Conclusion

In combination with flare ribbon observations, coronal dimmings represent an important diagnostic tool to study and understand the magnetic dynamics of solar eruptions, especially since their fine structure and position could provide additional information about the different flux systems involved in the eruption.

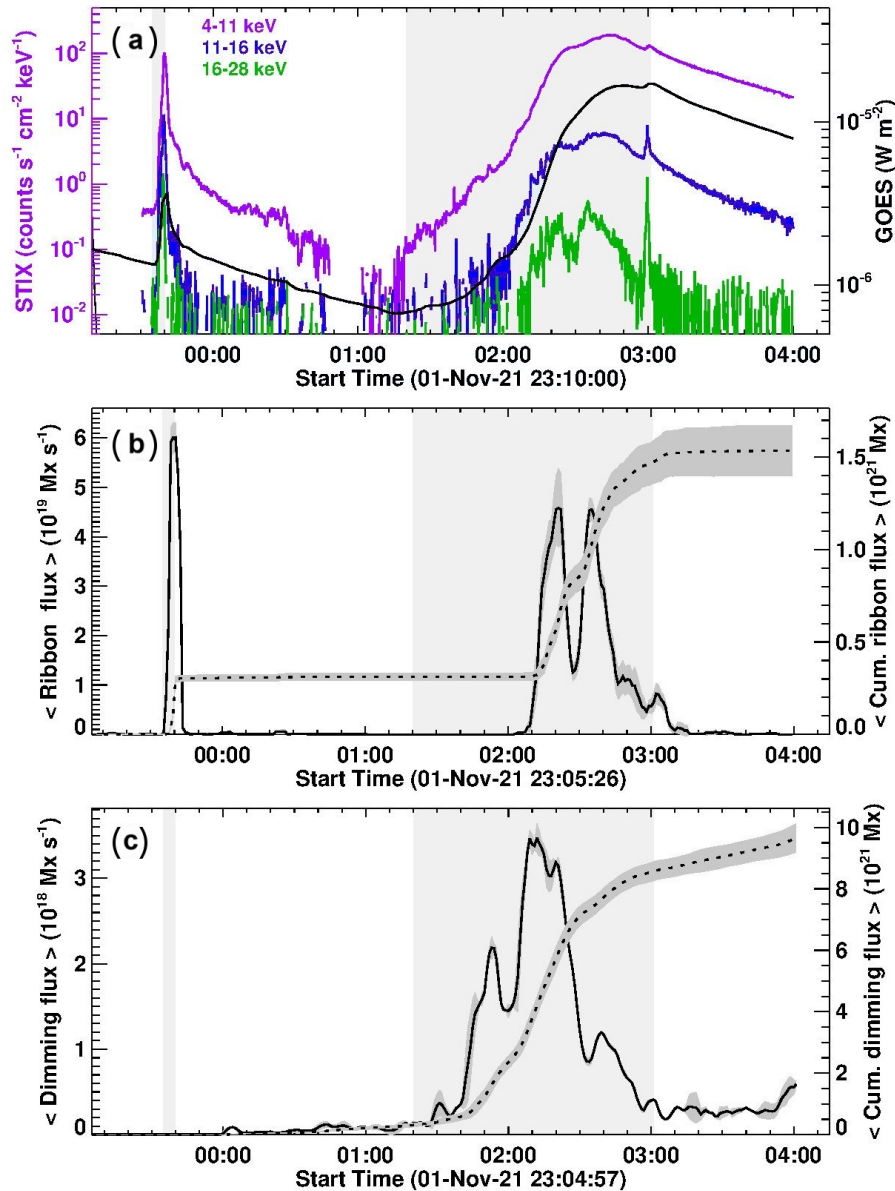


Figure 4-15: Time evolution of (a) STIX count rates at 4–11 keV (purple), 11–16 keV (blue), and 16–28 keV (green) energies together with the GOES 1–8 Å SXR flux (black). (b) Reconnection flux rate (solid) and cumulative reconnection flux (dashed) in flare ribbons. (c) Reconnection flux rate (solid) and cumulative reconnection flux (dashed) in dimmings. Gray-shaded vertical bands mark the impulsive phases of flares. The panels cover the time around the eruptive activity (01 November 23:00 UT – 02 November 04:00 UT). Adapted from [Thalmann et al. \[2023\]](#).

# Chapter 5

## Relation to the CME speed and mass

This chapter is dedicated to answering research question Q1:

*How can we use coronal dimmings detected off-limb to estimate the mass and speed of coronal mass ejections?*

### 5.1 Project summary

Although previous research has recognized the relationship between coronal dimming and CME mass/speed, there has been no holistic statistical analysis that simultaneously evaluates both off-limb and on-disk observations. In this Chapter, we present a statistical analysis of 43 coronal dimming events associated with Earth-directed CMEs that occurred during the quasi-quadrature period of the [SDO](#) and [STEREO](#) satellites. We investigated coronal dimming events observed above the limb by [STEREO/EUVI](#) and compared their properties with the mass and velocity of the associated CMEs. The unique position of the satellites allowed us to compare our results with those of [Dissauer et al. \[2018b, 2019\]](#), who studied the same events observed by [SDO/AIA](#) against the solar disk. Such statistic, including multi-viewpoint observations, is performed for the first time and confirms the relationship between coronal dimmings and CME parameters for the off-limb viewpoint. The research detailed in this Chapter has been published in *The Astrophysical Journal* [[Chikunova et al., 2020](#)].

## 5.2 Literature review

The mass-loss nature of appearance of coronal dimmings is supported by the presence of plasma outflows detected in spectroscopic observations in the EUV [e.g., Harrison and Lyons, 2000, Harra and Sterling, 2001, Tian et al., 2012, Veronig et al., 2019] and the intensity decrease observed at multiple wavelengths [Zarro et al., 1999b, Chertok and Grechnev, 2003]. Moreover, differential emission measure (DEM) diagnostics reveal impulsive drops in coronal dimming regions by up to 70% of the pre-event values [López et al., 2017, Vanninathan et al., 2018, Veronig et al., 2019].

The automated algorithms allow to process a large number of events and create a statistical basis of coronal dimmings and their associated CMEs. However, there exist only a few statistical studies of coronal dimmings [Bewsher et al., 2008, Reinard and Biesecker, 2008, Aschwanden, 2016, Mason et al., 2016, Krista and Reinard, 2017]. A thorough methodological approach and comprehensive statistical analysis of the characteristic properties of coronal dimmings, and their relation to the decisive parameters of the associated CMEs and flares has been presented in a series of papers by Dissauer et al. [2018a,b, 2019]. In these studies 62 dimming events were analyzed using multi-viewpoint observations by the SDO and STEREO satellites in quasi quadrature: coronal dimmings were observed on-disk by SDO/AIA [Lemen et al., 2012] and the related magnetic fluxes were obtained using SDO/HMI, while the kinematics and the mass of the associated CME was observed in STEREO EUVI and COR data close to the limb, minimizing projection effects. These studies revealed that the CME mass shows high correlations with the dimming area, its total brightness, and magnetic flux, whereas the maximal speed of the CME is strongly correlated with their corresponding time derivatives (i.e. area growth rate, brightness change rate, and magnetic flux rate) with correlation coefficients in the range of  $c \sim 0.6 - 0.7$  [Dissauer et al., 2018b, 2019].

## 5.3 Methodology

We study the evolution of off-limb coronal dimmings and their corresponding CMEs. We derive characteristic dimming parameters, such as its area, brightness and dura-

tion, using observations, where the coronal dimmings and the associated CME are observed off-limb by [STEREO/EUVI](#).

We study the same data set as in [Dissauer et al. \[2018b\]](#), but now extract the coronal dimming properties and their evolution from [STEREO/EUVI](#), which observes the dimmings above the limb. This approach allows us for the first time to compare the results of on-disk and off-limb observations of coronal dimmings, and also to study how the viewing position affects the derived properties.

### 5.3.1 Data and Data preprocessing

In this study, we used [STEREO/EUVI](#) filtergrams of the 195 Å passband with a cadence of 5 minutes (except for individual events where it can vary from 1.5 min to 10 min). According to [Dissauer et al. \[2018a\]](#), [Kraaikamp and Verbeeck \[2015a\]](#), coronal dimmings are best observed in wavelengths sensitive to quiet Sun coronal temperatures (e.g. 195 Å, 171 Å, 211 Å). 195 Å has the highest cadence for [STEREO/EUVI](#) and therefore we use this wavelength.

#### Event selection

We study the time range between May 2010 and September 2012 when [SDO](#) was in quasi-quadrature with the [STEREO-A](#) and [STEREO-B](#) satellites, increasing their separation angle to the Sun-Earth line during this period from  $\pm 75^\circ$  to  $\pm 125^\circ$ . We focus on 43 events in which coronal dimmings and their associated Earth-directed CMEs were observed off-limb by at least one of the two [STEREO](#) satellites. 39 of these events overlap with the event set from [Dissauer et al. \[2018b, 2019\]](#) who studied the same dimmings as observed on-disk by [AIA](#) instrument on-board [NASA's SDO](#) satellite [[Lemen et al., 2012](#)]. Four events were excluded in the [Dissauer et al. \[2018b, 2019\]](#) studies, due to filament material that partially obscured the on-disk dimming detection. This was not the case for the [STEREO](#) off-limb observations, and thus they are included in the present work. However, for 23 events of the overall data set of 62 events, the off-limb dimming extraction was not possible due to only partial visibility of the dimmings by the [STEREO](#) satellites or the activity of multiple active regions at the same time. One event (2012 July 2) was excluded from the statistics

due to its complexity (disappearance of trans-equatorial loops) revealed during the comparative analysis from the two viewpoints.

### CME kinematics

The kinematical CME parameters used for comparison with the derived dimming properties are from the STEREO/EUVI and COR measurements in Dissauer et al. [2019]. The fastest event in the data set occurred on 2012 March 6 with a maximal velocity of  $\sim 3700 \text{ km s}^{-1}$  and mass of  $1.83 \times 10^{16} \text{ g}$ . For the other events the maximal velocities of the CMEs vary from  $370 \text{ km s}^{-1}$  to  $2000 \text{ km s}^{-1}$ , and the values of CME masses lie between  $2.03 \times 10^{14} \text{ g}$  and  $1.78 \times 10^{16} \text{ g}$ .

### Data Preprocessing

For each event we analyze a series of STEREO EUVI images, which begins 30 minutes before the associated flare and lasts for 12 hours in total. All EUVI images of the data set were checked for the exposure time, prepared with standard SolarSoft routines (`secchi_prep.pro`) and corrected for differential rotation (`drot_map.pro`). Unfortunately, reliable equivalent routines for calibrating the STEREO data have not yet been developed within the Python Sunpy environment. The images were cut automatically by half (either East or West hemisphere), depending on which satellite observed the event better, STEREO-A or STEREO-B.

### Dimming detection

The detection approach that we created for this study is fully described in Section 4.2.6. We used both BD and LBR data for the thresholding algorithm based on region-growing with the same set of parameters.

## 5.3.2 Characteristic dimming parameters

The set of parameters that we derive to characterize coronal dimmings and their evolution is extracted by the same approach as described in Dissauer et al. [2018b] and in Section 4.3. We derive instantaneous  $A_{in}(t)$  and cumulative  $A_{cu}(t)$  dimming

areas from [LBR](#) data, instantaneous  $I_{in}(t)$  and cumulative brightness  $I_{cu}(t)$  from both, [BD](#) and [LBR](#) data, their derivatives and the duration of the impulsive phase of the dimming  $t_{dur}$ , i.e. the time range when most of the dimming region develops. The mean dimming brightness parameters  $\bar{I}_{in}(t)$  and  $\bar{I}_{cu}(t)$  are derived from the same time steps as the corresponding total brightness.

To estimate the uncertainty of the extracted parameter values, caused by using a specific threshold for segmenting the dimming regions, we applied a  $\pm 5\%$  change to the logarithmic threshold level of -0.19 and then calculated the mean value and the standard deviation  $\sigma$  for all the dimming parameters (see [Figure 5-1](#)).

## 5.4 Results

We study a set of 43 coronal dimming events that are observed above the limb by the [STEREO-A](#) or [STEREO-B EUVI](#) instruments in the 195 Å passband (cf. [Table 5.1](#)). These events have been observed during a period where the [STEREO](#) s/c were in quasi-quadrature with spacecraft located along the Sun-Earth line, and the same dimming events have been studied in observations against the solar disk by the [SDO/AIA](#) instrument in [Dissauer et al. \[2018b, 2019\]](#). For 37 events in our list, we have also the CME mass, and for 27 events the CME maximum velocity derived from [STEREO EUVI](#) and [COR](#) data in [Dissauer et al. \[2019\]](#). In [Sect. 5.3.2](#) we present the temporal evolution of the dimming characteristics and their distribution. In [Sect. 5.4.2](#) we relate our findings for the off-limb dimmings observed by [EUVI](#) to the results obtained for the corresponding on-disk dimming events observed by [SDO/AIA](#) from [Dissauer et al. \[2018b\]](#). In [Sect. 5.4.3](#) we study the correlations of the decisive parameters describing off-limb coronal dimmings that we derived with the speed and mass of their associated CMEs.

All the plots presented in the following sections show the mean values of the derived parameters, while the error bars represent the  $1\sigma$  standard deviation. The plots are presented in logarithmic space. The Pearson correlation coefficient  $c$  as well as the linear regression fits shown are also derived in logarithmic space, i.e.  $\log(y) = d + k \cdot \log(x)$ . The values of the obtained correlation and fit parameters are

annotated in each of the scatter plots shown. To obtain the mean and the standard deviation of  $c$  we apply a bootstrap method [Wall and Jenkins, 2012]: we select random data pairs with replacements and repeat the procedures, calculating the Pearson coefficient 10000 times. In the same way as Kazachenko et al. [2017] and Dissauer et al. [2018b] we classify the level of correlation as:  $c = [0.2, 0.4]$  - weak,  $c = [0.4, 0.6]$  - moderate,  $c = [0.6, 0.8]$  - strong,  $c = [0.8, 1.0]$  - very strong.

### 5.4.1 Evolution and distribution of the dimming parameters

Figure 5-1 shows the time evolution of the coronal dimming parameters for two example events. Panels (a-b) show the instantaneous  $A_{in}$  and the cumulative  $A_{cu}$  area (black), respectively, together with the corresponding area growth rates (green). Panel (c) shows the total cumulative brightness  $I_{br,cu}$  and its change rate (red). We note that the evolution of the total brightness is representative of the different brightness definitions, as they all are similar to each other, reaching their minimum at the same time (only six events from our data set reveal a significant difference in time of the minimum of instantaneous and cumulative brightness, one of them is the example event of 2012 March 6). The gray shadow bands represent the  $1\sigma$  range. Vertical lines indicate the start and the end time of the dimming impulsive phase (orange lines), the maximum of the area growth rate (green), the maximum of the instantaneous area and the minimum of the brightness (blue) and brightness change rate (red). In each event, the intensity decreases rapidly when the dimming area expands. The same tendency can be seen for the cumulative parameters, indicating that at this time the dimming regions become not only bigger but also darker.

Studying the time evolution of the coronal dimming characteristics we extract parameters for the statistics and comparison with the CMEs quantities. We define the dimming size  $A$  by the cumulative area at end of the impulsive phase of the dimming  $t_{end}$ . The maximum of the instantaneous area  $A_{max}$  is defined as the largest size of the dimming region during the 6 hours after the start of the impulsive phase. The area growth rate parameters are obtained by the maximum of the  $dA_{cu}(t)/dt$  and  $dA_{in}(t)/dt$  profiles, respectively.

Figure 5-2 compares the values of the parameters  $A_{max}$  and  $A$ . The black line

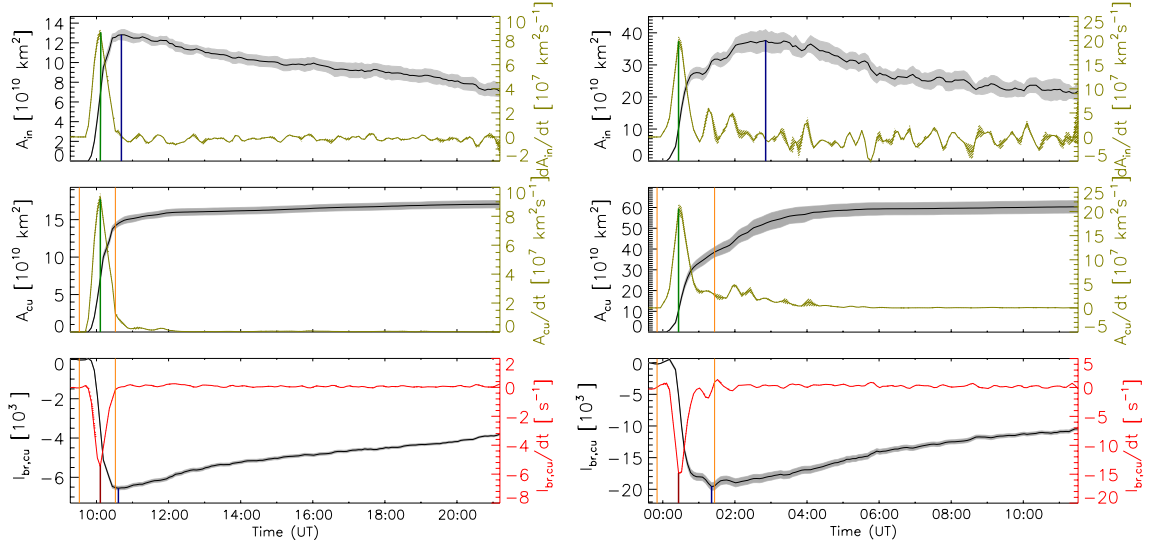


Figure 5-1: Time evolution of the dimming parameters for the events that occurred on 2011 October 1 (left) and 2012 March 6 (right): (a) instantaneous area  $A_{in}$  (black) and its growth rate (green), (b) cumulative area  $A_{cu}$  (black) and its growth rate (green); (c) cumulative brightness from LBR maps  $I_{br,cu}$  (black) and its change rates (red). The light gray bands show the uncertainty ranges for each parameter ( $1\sigma$ ). Orange boundaries represent the start and the end time of the impulsive phase, green vertical lines show the maximum of the area growth rate, blue lines show the maximum of the instantaneous area or the minimum of the brightness, and red line marks the minimum of the brightness change rate.

represents the linear regression fit to all data points. The coefficients of the fitting line are presented in the bottom-right corner ( $k = 0.97$ ,  $d = 0.41$ ). The corresponding correlation coefficient is given in the top-left corner ( $c = 0.99 \pm 0.01$ ). The high positive value of  $c$  and the slope of the fitting regression line  $k \sim 1$  illustrates that the two different approaches for identifying the dimming area provide almost identical results.

We also extract the minimum of the total brightness for base-difference (instantaneous  $I_{bd,in}$  and cumulative  $I_{bd,cu}$ ) and logarithmic base-ratio (instantaneous  $I_{br,in}$  and cumulative  $I_{br,cu}$ ) data. Because  $I(t)$  usually reaches the minimum after the dimming impulsive phase, we searched for their minimum in the time range of 6 hours after  $t_{start}$ . The mean dimming brightness parameters  $\bar{I}_{in}$  and  $\bar{I}_{cu}$  are derived from the same time steps as the corresponding total brightness. Figure 5-3 shows that the instantaneous and cumulative brightness extracted from logarithmic base ratio maps (the same is also true for base-difference data) are almost identical

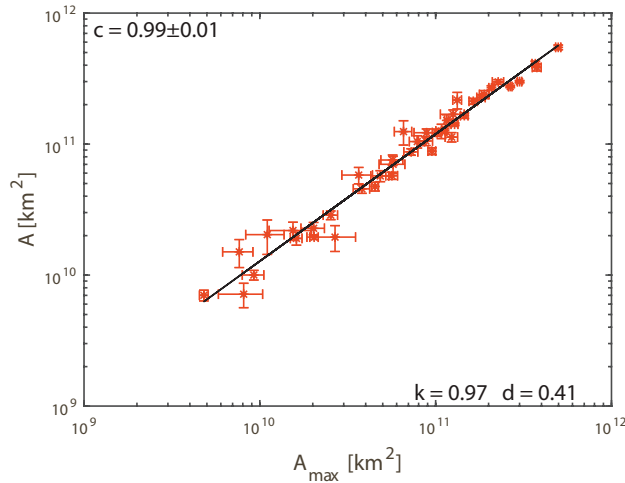


Figure 5-2: The maximum of the instantaneous dimming area  $A_{max}$  against the cumulative dimming area  $A$  at the time  $t_{end}$  of the impulsive dimming evolution in logarithmic space. The black line represents the linear regression fit to all data points. For this and subsequent correlation plots: the correlation coefficient  $c$  is given in the top left corner; the fit parameters  $k, d$  of the linear regression  $\log(y) = d + k \cdot \log(x)$  are given in the bottom right corner.

( $c = 0.99$ ;  $k = 0.98$ ,  $d = 0.10$ ). This means that we can use one approach to describe the dimming brightness for the comparative analysis.

In addition to the characteristic dimming parameters listed above, we estimated the recovery time of the dimmings. We describe the results of this analysis in the next Chapter 6.

In Table 5.1, we summarize all dimming parameters derived in our analysis. For each event we list the STEREO satellite, which was used for the analysis, and the derived dimming properties: the maximum of the instantaneous dimming area  $A_{max}$ , the cumulative area  $A$ , the maximal cumulative area growth rate  $\dot{A}$ , the total dimming brightness from logarithmic base-ratio data: cumulative  $I_{br,cu}$  and instantaneous  $I_{br,in}$ , the total dimming brightness from base-difference data: cumulative  $I_{bd,cu}$  and instantaneous  $I_{bd,in}$ , the mean instantaneous brightness  $|\bar{I}_{br,in}|$ , the brightness change rate  $\dot{I}_{br,in}$  and the duration of the impulsive phase of the dimming  $t_{dur}$ . The CME quantities such as the mass  $m_{CME}$  and the maximal speed  $v_{max}$  are listed in the last columns of the table.

Figure 5-4 shows the distributions of the main dimming parameters derived from the whole data set: the cumulative dimming area  $A$  and its growth rate  $dA/dt$ , the

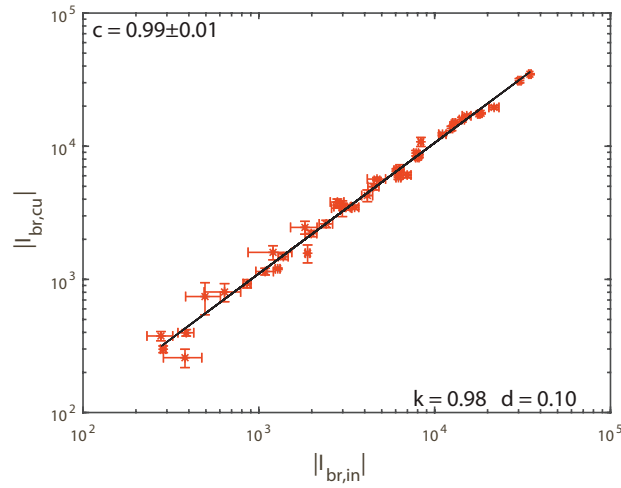


Figure 5-3: Absolute values of the cumulative total brightness  $|I_{br,cu}|$  versus absolute values of the instantaneous total brightness  $|I_{br,in}|$  of the dimming regions, calculated from logarithmic base-ratio maps. The black line represents the linear regression fit to all data points.

absolute mean intensity from logarithmic base ratio data  $\bar{I}_{br,in}$  and the duration of the impulsive phase  $t_{dur}$  (note, that panels (a-c) are shown in the logarithmic scale). The dimming areas range from  $7.0 \times 10^9 \text{ km}^2$  to  $5.5 \times 10^{11} \text{ km}^2$ , with the mean value of  $1.33 \pm 1.23 \times 10^{11} \text{ km}^2$ . The area growth rate  $dA/dt$  varies from  $2.7 \times 10^6 \text{ km}^2 \text{ s}^{-1}$  to  $2.9 \times 10^8 \text{ km}^2 \text{ s}^{-1}$ , with the mean value of  $7.41 \pm 6.96 \times 10^7 \text{ km}^2 \text{ s}^{-1}$ . The mean brightness decrease of the total dimming regions varies in the interval  $[-0.41, -0.18]$ , the mean value is  $-0.28 \pm 0.05$  (note, that values of brightness are calculated from LBR data). The duration of the impulsive dimming phase varies from 25 to 155 minutes. On average, it lasts for  $66 \pm 28$  minutes.

#	Date	Sc	$A_{\max}$ [km <sup>2</sup> ]	$A$ [km <sup>2</sup> ]	$\dot{A}$ [km <sup>2</sup> s <sup>-1</sup> ]	$I_{br, cu}$ (10 <sup>3</sup> )	$I_{br, in}$ (10 <sup>3</sup> )	$I_{bd, cu}$ [DN]	$I_{bd, in}$ [DN]	$\bar{I}_{br, in}$ [s <sup>-1</sup> ]	$\dot{I}_{br, in}$ [s <sup>-1</sup> ]	$t_{dur}$ [min]	$m_{CME}$ [g]	$v_{\max}$ [km s <sup>-1</sup> ]
			(10 <sup>10</sup> )	(10 <sup>7</sup> )	(10 <sup>3</sup> )	(10 <sup>3</sup> )	(10 <sup>5</sup> )	(10 <sup>5</sup> )	(10 <sup>5</sup> )				(10 <sup>15</sup> )	(10 <sup>3</sup> )
1	20100716	B	0.63	1.26	0.45	-0.38	-0.29	-0.57	-0.44	-0.15	-0.18	-22.46	-29.86	115
2	20100801	A	22.68	29.42	11.15	-17.02	-15.35	-5.84	-5.26	-0.29	-0.33	-9.88	-11.56	95
3	20100807	A	8.9	10.35	6.76	-4.99	-4.53	-2.09	-1.82	-0.24	-0.25	-10.05	-10.18	65
4	20110213	A	7.64	10.2	3.97	-4.27	-3.87	-4.26	-3.31	-0.21	-0.25	-20.82	-32.66	130
5	20110214	A	0.43	0.57	0.21	-0.29	-0.24	-1.16	-0.87	-0.25	-0.28	-100.65	-100.53	65
6	20110215	A	5.37	7.15	2.68	-3.54	-3.11	-3.96	-3.41	-0.25	-0.27	-27.58	-35.27	80
7	20110307	B	1.43	2.19	0.79	-0.81	-0.69	-0.79	-0.42	-0.18	-0.21	-17.86	-12.91	85
8	20110621	A	16.79	21.1	9.08	-13.64	-12.85	-14.47	-13.44	-0.32	-0.38	-34.13	-39.85	150
9	20110711	A	6.72	8.4	6.04	-4.78	-4.28	-1.68	-1.48	-0.28	-0.32	-9.95	-10.94	50
10	20110802	A	11.53	12.49	10.87	-7.59	-7.32	-3.88	-3.72	-0.3	-0.32	-15.45	-16.07	35
11	20110803	A	17.81	22.5	6.79	-12.55	-11.67	-4.04	-3.57	-0.28	-0.31	-8.94	-10.53	95
12*	20110804	A	11.74	21.22	13.35	-10.75	-8.4	-3.38	-2.65	-0.25	-0.33	-7.94	-10.64	65
13	20110906	A	25.13	26.95	23.51	-17.78	-17.35	-6.59	-6.32	-0.33	-0.34	-12.16	-12.52	55
14	20110906	A	37.23	41.24	27.62	-31.22	-30.72	-20.6	-20.3	-0.38	-0.41	-24.86	-27.14	75
15*	20110907	A	18.69	26.18	19.66	-15.31	-14.39	-12.3	-11.65	-0.29	-0.32	-23.4	-42.58	55
16	20110908	A	0.36	0.59	0.57	-0.24	-0.19	-0.43	-0.35	-0.21	-0.22	-36.05	-40.78	65
17	20110927	B	0.85	0.99	0.71	-0.4	-0.37	-1.97	-1.79	-0.2	-0.21	-99.46	-101.83	65
18	20110930	A	1.84	2.25	0.84	-1.07	-0.96	-2.53	-2.34	-0.24	-0.26	-55.97	-63.31	105
19	20111001	B	12.74	14.27	8.67	-6.59	-6.25	-3.38	-3.18	-0.23	-0.24	-11.79	-12.41	50
20	20111002	A	3.25	5.81	2.78	-2.53	-2.01	-3.07	-2.49	-0.22	-0.25	-26.28	-30.48	65
21	20111002	A	1.59	1.91	1.16	-0.92	-0.83	-1.29	-1.14	-0.24	-0.25	-33.43	-35.82	85
22	20111124	A	9.78	12.11	3.41	-6.44	-5.71	-13.28	-12.8	-0.26	-0.29	-54.59	-65.18	150
23	20111222	A	3.84	4.48	2.6	-2.22	-2.02	-1.73	-1.64	-0.25	-0.26	-19.24	-21.25	50
24	20111225	A	0.37	0.63	0.9	-1.04	-0.95	-2.45	-2.05	-0.82	-0.22	-192.13	-100.09	50

25	20111225	A	5.3	7.09	9.8	-3.49	-3.1	-3.99	-3.87	-0.24	-0.26	-28.04	-32.98	35	5.90	-
26	20111226	A	12.74	16.18	9.5	-7.86	-6.87	-3.33	-2.96	-0.24	-0.26	-10.26	-11.22	65	4.60	1.02
27*	20120119	B	26.53	29.37	18.17	-17.31	-16.74	-5.68	-5.27	-0.29	-0.31	-9.63	-9.9	95	13.55	-
28	20120123	A	12.17	16.54	11.42	-9.04	-7.94	-6.39	-5.5	-0.27	-0.3	-19.25	-21.97	60	12.45	1.99
29	20120306	B	27.66	32.57	23.62	-18.08	-16.92	-11.39	-12.33	-0.28	-0.3	-17.4	-22.19	55	18.35	3.69
30	20120309	B	7.6	8.53	8.15	-3.54	-3.27	-2.86	-2.65	-0.21	-0.21	-16.7	-18.53	55	7.02	1.25
31	20120310	A	18.92	23.71	13.18	-15.99	-14.54	-10.15	-10.91	-0.34	-0.38	-21.31	-28.54	75	10.83	1.65
32	20120314	A	5.24	5.75	4.18	-3.38	-3.24	-3.59	-3.48	-0.29	-0.31	-31.12	-33.09	65	3.41	-
33	20120317	A	1.69	1.88	2.5	-1.08	-1.01	-1.08	-0.93	-0.29	-0.3	-28.49	-27.34	45	0.20	-
34	20120405	A	9.07	15.21	10.1	-7.41	-6.04	-2.41	-1.91	-0.24	-0.28	-7.88	-8.89	50	5.95	-
35	20120511	A	2.39	2.84	0.72	-1.49	-1.34	-1.58	-1.39	-0.26	-0.28	-27.7	-29.05	120	3.37	1.16
36	20120603	B	9.3	10.6	13.28	-5.55	-5.18	-1.42	-1.25	-0.26	-0.28	-6.65	-6.67	30	3.68	-
37	20120606	A	3.4	5.6	4.53	-2.63	-2.34	-1.05	-0.92	-0.23	-0.25	-9.32	-9.73	45	3.13	0.77
38	20120614	A	10.08	12.36	7.49	-6.46	-5.73	-3.65	-3.21	-0.26	-0.28	-14.69	-15.86	65	7.76	1.44
39	20120702	A	0.3	0.41	0.12	-0.19	-0.16	-0.21	-0.14	-0.23	-0.25	-25.24	-23.4	120	4.85	0.57
40	20120712	B	47.04	54.82	28.8	-31.15	-29.66	-6.95	-6.33	-0.28	-0.31	-6.31	-6.7	110	17.80	1.27
41*	20120804	B	4.19	11.98	5.73	-3.84	-3.05	-4.66	-3.35	-0.16	-0.21	-19.38	-33.07	110	11.05	-
42	20120815	A	0.94	1.96	1.17	-0.77	-0.55	-0.38	-0.25	-0.2	-0.23	-9.62	-35.44	45	1.03	0.60
43	20120925	B	2.14	3.71	3.68	-1.35	-1.16	-0.67	-0.57	-0.18	-0.19	-8.97	-9.49	35	-	0.47
44	20120927	A	8.61	12.25	8.02	-5.72	-4.84	-3.39	-2.82	-0.23	-0.27	-13.8	-19.25	70	9.37	1.50

Table 5.1: For each event we list the STEREO satellite used for the analysis and the dimming characteristics: the dimming instantaneous area  $A_{max}$ , the cumulative area  $A$ , the maximal cumulative area growth rate  $\dot{A}$ , the total dimming brightness from LBR data: cumulative  $I_{br,cu}$  and instantaneous  $I_{br,in}$ , the total dimming brightness from BD data: cumulative  $I_{bd,cu}$  and instantaneous  $I_{bd,in}$ , the mean instantaneous brightness  $|\bar{I}_{br,in}|$ , the brightness change rate  $\dot{I}_{br,in}$  and the duration of the impulsive phase of the dimming  $t_{dur}$ . CMEs quantities: the mass  $m_{CME}$  and the maximal speed  $v_{max}$ . Events marked with \* are not studied in [Dissauer et al. 2018b, 2019].

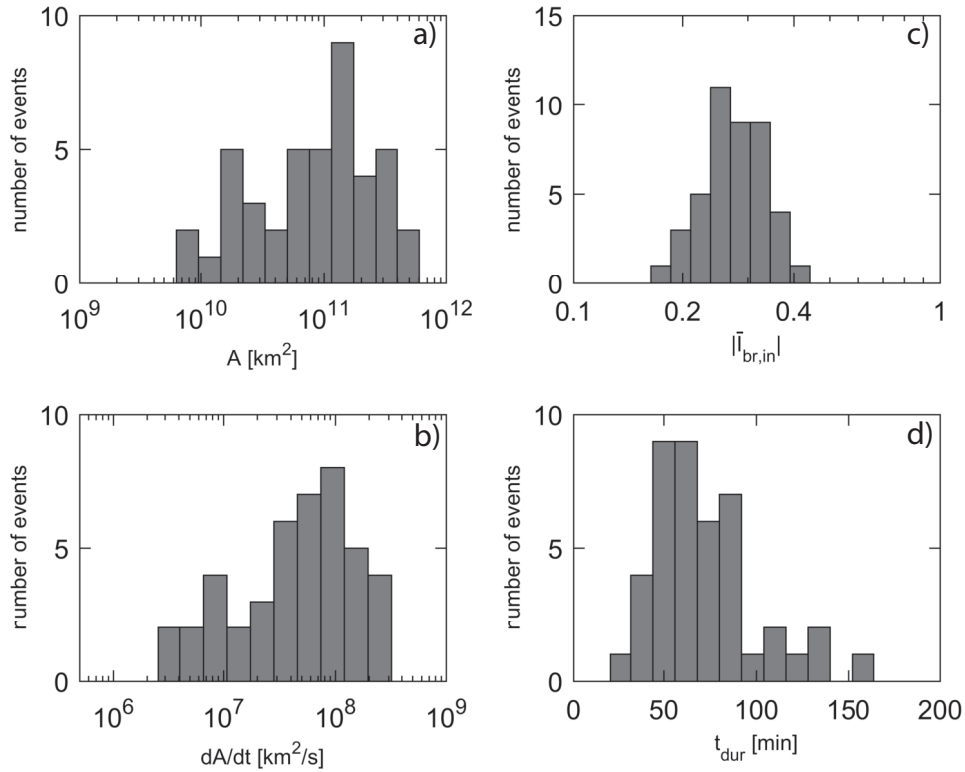


Figure 5-4: Distributions of characteristic dimming parameters: a) maximum of the cumulative dimming area  $A$ , b) maximum of the cumulative area growth rate  $dA/dt$ , c) absolute values of the mean intensity from logarithmic base ratio data  $|\bar{I}_{br,in}|$ , d) duration of the dimming impulsive phase  $t$ . Panels (a-c) are presented in logarithmic space, panel (d) in linear space.

### 5.4.2 Relation between off-limb and on-disk dimmings

We compare the dimming parameters that we obtained from the *STEREO*/*EUVI* 195 Å off-limb observations with the corresponding outcomes for the dimmings observed on-disk by *SDO*/*AIA* 211 Å in Dissauer et al. [2018b, 2019]. Figure 5-5 shows the scatter plot between the dimming areas derived from on-disk and off-limb observations, which reveal a strong correlation ( $c = 0.63 \pm 0.10$ ). For the events under study, off-limb dimmings tend to be larger than their corresponding on-disk counterpart: only 8 events reveal a smaller dimming area for the off-limb observations compared to the on-disk areas.

To investigate whether the position of the *STEREO* satellites significantly affects

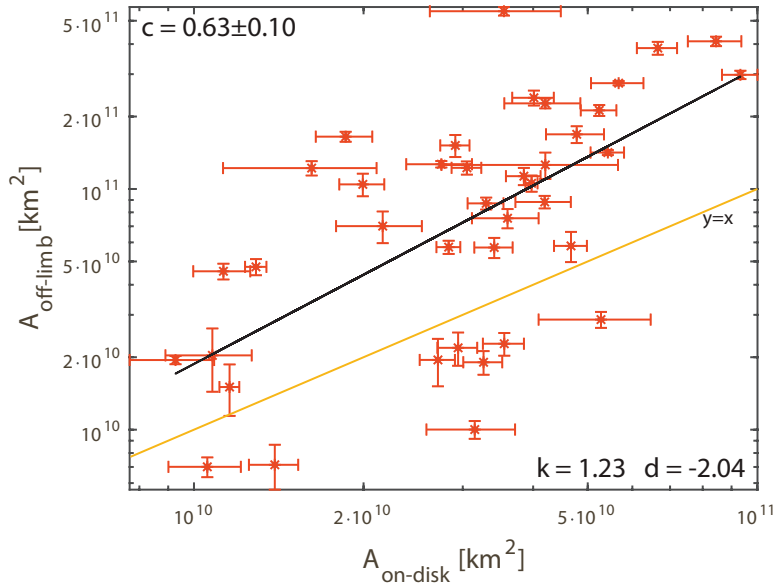


Figure 5-5: Scatter plot of the dimming areas derived off-limb by [STEREO/EUVI](#),  $A_{\text{off-limb}}$ , and on-disk by [SDO/AIA](#),  $A_{\text{on-disk}}$  in logarithmic space. The black line represents the linear regression fit to all data points. The orange line is the identity line  $y = x$ .

the derived dimming area via projection effects or by obscuring parts of the dimming region behind the limb, we studied the dimming areas as a function of source region location with respect to the observing spacecraft. Figure 5-6 shows the ratio of the off-limb area  $A_{\text{off-limb}}$  and on-disk area  $A_{\text{on-disk}}$  against the central meridian distance of the CME source region for the [STEREO](#) spacecraft. The coordinates of the dimming sources are derived from the heliographic positions of the associated flares given in [Dissauer et al. \[2018b\]](#). We can notice, that all the events were observed with a central meridian distance ( $\text{CMD}$ ) in the range  $[60^\circ, 130^\circ]$ , but there is no significant dependence of the area ratio between the off-limb and on-disk observations on the  $\text{CMD}$ . Also, there is no obvious change at a  $\text{CMD}$  of  $> 90^\circ$ , i.e. for events where for [STEREO](#) the associated flare is located behind the limb, and thus part of the dimming regions may be obscured.

Figure 5-7 shows the scatter plot of total instantaneous brightness calculated from off-limb and on-disk observations by using base-difference (left panel) and logarithmic base-ratio (right panel). The correlation coefficients result in  $c = 0.60 \pm 0.14$  and  $c = 0.77 \pm 0.09$ , respectively. The regression lines (in black) have a slope

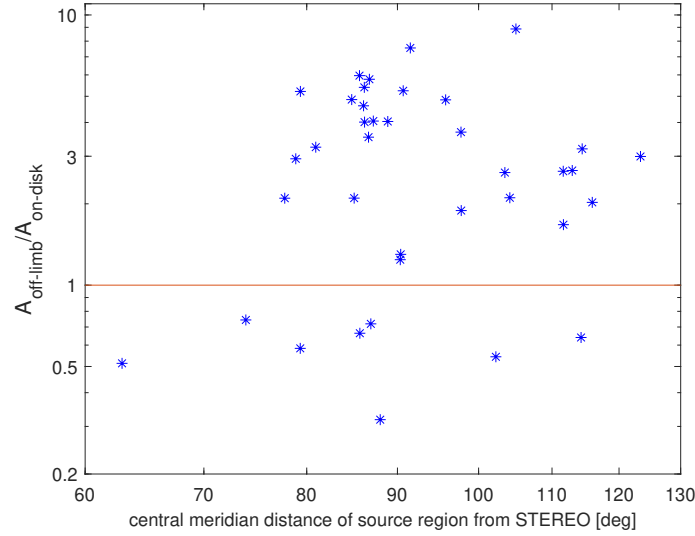


Figure 5-6: Ratio of the extracted off-limb and on-disk dimming areas versus the central meridian distance of the source region from the [STEREO](#) satellite. The orange horizontal line indicates a ratio of 1.

coefficient close to 1 ( $k = 0.98$  and  $k = 1.06$ ) and are therefore almost parallel to the 1:1 correspondence lines (orange), indicating that both parameters are linearly related.

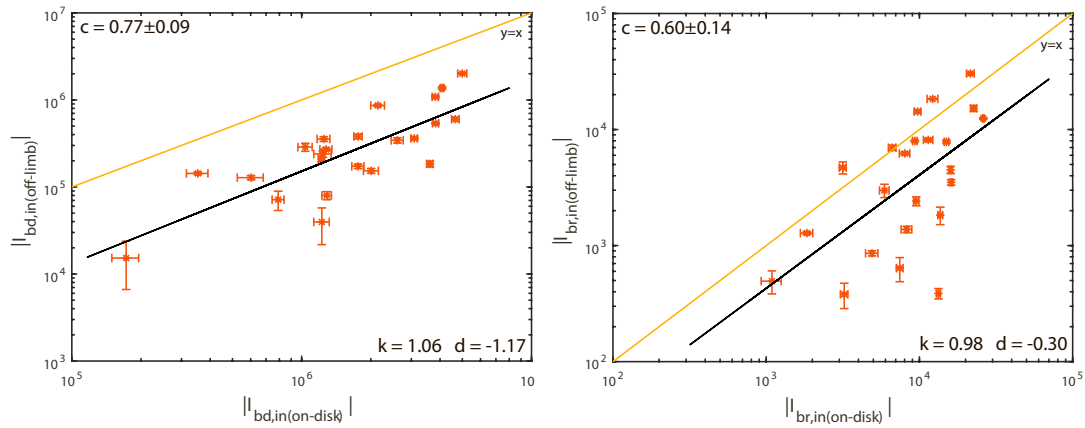


Figure 5-7: Comparison of the total instantaneous brightness from base-difference data (left panel) and from logarithmic base-ratio data (right panel) for on-disk and off-limb observations, presented in absolute values. The black line represents the linear regression fit to all data points. The orange line is the identity line  $y = x$ .

### 5.4.3 Relation between off-limb dimming and CME parameters

Figure 5-8 shows the cumulative off-limb dimming area  $A$  against the mass (left panel) and maximum speed (right panel) of the CME. We obtain a very high correlation between the dimming area and CME mass:  $c = 0.82 \pm 0.06$  (in logarithmic space), i.e. the larger the area of the dimming, the more mass the associated CME contains. This correlation provides strong support of the physical interpretation of the appearance of the dimming as a density depletion due to the evacuation of plasma. These results are in agreement with the findings for the on-disk coronal dimmings by Dissauer et al. [2019], where  $c = 0.69 \pm 0.10$ . We also find a high correlation between the area of the dimming  $A$  and the speed of the CME ( $c = 0.67 \pm 0.10$  in logarithmic space).

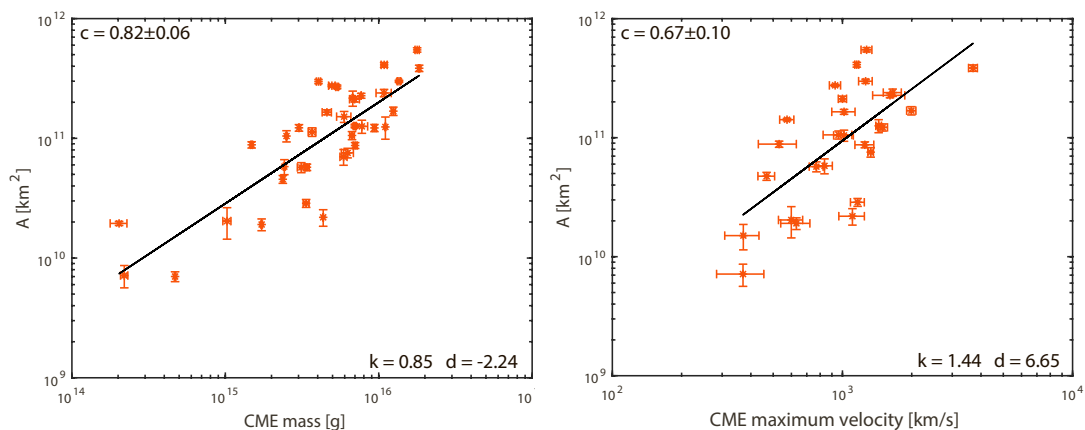


Figure 5-8: Cumulative area of the coronal dimming  $A$  against the CME mass  $m_{CME}$  (left) and the CME maximal speed  $v_{max}$  (right) in logarithmic space. The black line represents the linear regression fit to all data points.

In addition, we also investigated the relation between the dynamic evolution of the dimming, as described by the peak of its area growth rate  $dA/dt$ , and the parameters of the associated CME (Figure 5-9). The correlation coefficient in logarithmic space are  $c = 0.76 \pm 0.08$  and  $c = 0.59 \pm 0.14$ , respectively, indicating a close connection between the dimming growth rate with the mass and speed of the associated CME.

Figure 5-10 shows the correlation plots of the absolute values of total instan-

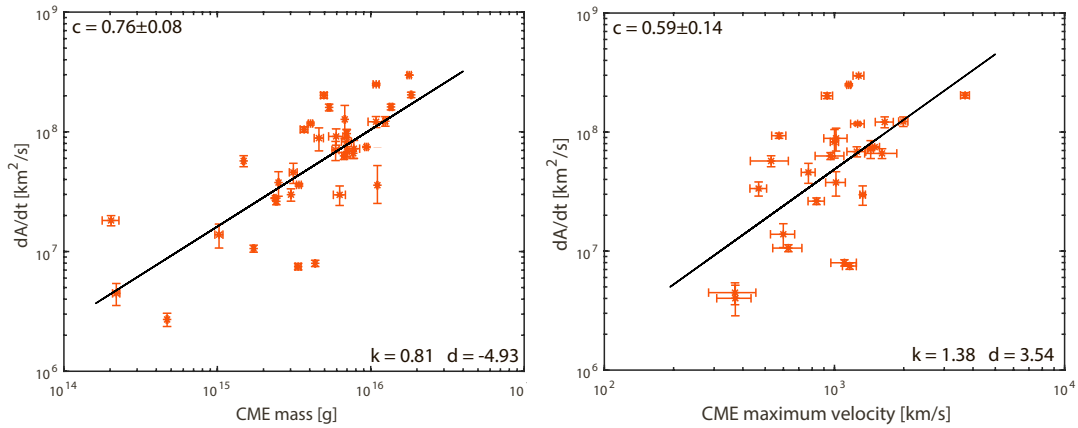


Figure 5-9: Correlation of the area growth rate  $dA/dt$  of the coronal dimming observed off-limb and the CME mass (left) and CME maximal speed (right). The black line represents the linear regression fit to all data points.

taneous dimming brightness calculated from LBR data against the CME mass (left panel) and maximal speed (right panel). The correlation coefficients are  $c = 0.75 \pm 0.08$  and  $c = 0.63 \pm 0.11$ , respectively, indicating a strong correlation. In addition, in Figure 5-11 we show the correlation between the mean instantaneous brightness  $|\bar{I}_{br,in}|$  and the CME speed ( $c = 0.48 \pm 0.14$ ).

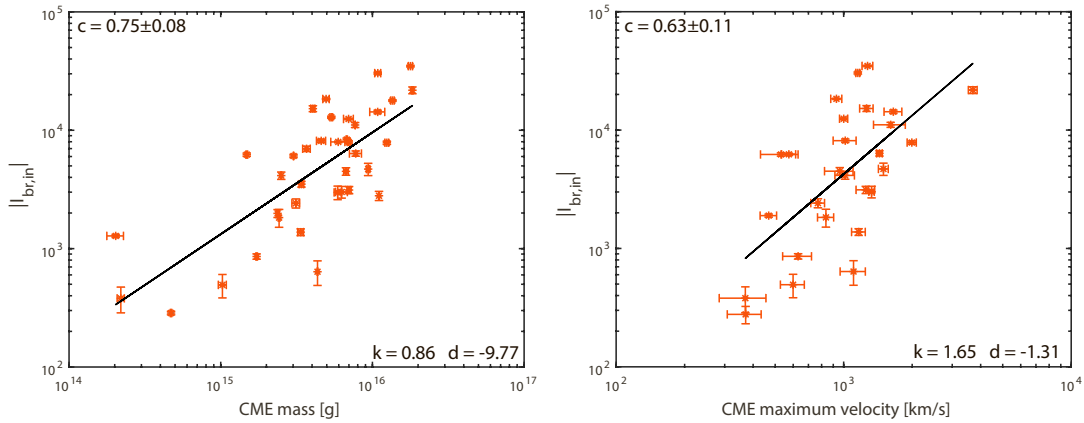


Figure 5-10: Absolute values of the total instantaneous dimming brightness  $|I_{br,in}|$  against the mass (left panel) and the maximum velocity (right panel) of the corresponding CME in logarithmic space. The brightness is calculated from LBR data. The black line represents the linear regression fit to all data points.

We also obtained a strong correlation between the dimming brightness change rate and the maximal speed of the CME: the faster the total dimming brightness is changing, the higher is the velocity of the associated CME. Figure 5-11 shows the

absolute values of the instantaneous brightness change rate calculated from **LBR** data against the CME maximal speed. The correlation coefficient is  $c = 0.61 \pm 0.12$ .

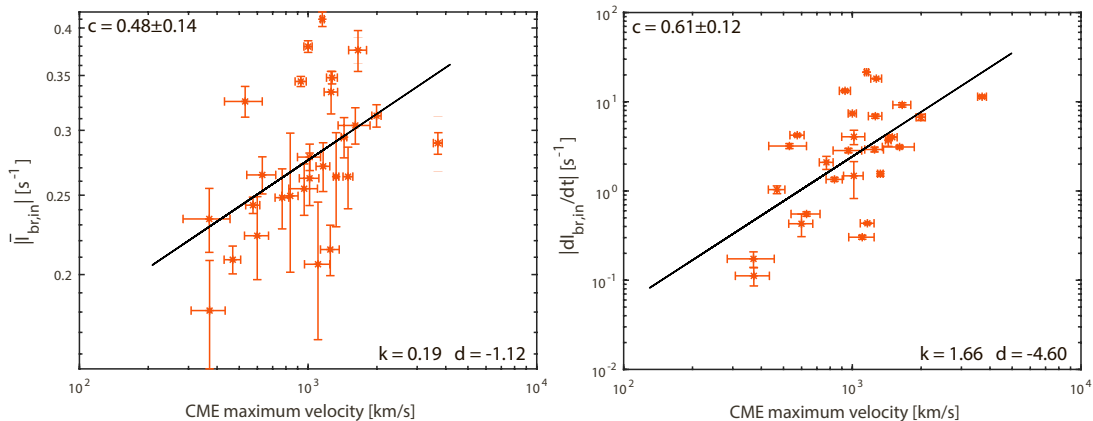


Figure 5-11: Mean instantaneous dimming brightness  $|\bar{I}_{br,in}|$  (left panel) and instantaneous brightness change rate  $|d\bar{I}_{br,in}/dt|$  (right panel), calculated from **LBR** maps, against the maximum velocity of the associated CME in logarithmic space. All parameters are presented by their absolute values. The black line represents the linear regression fit to all data points.

## 5.5 Summary and Discussion

We have developed a robust automated algorithm for the segmentation of coronal dimmings above the solar limb in **STEREO/EUVI** 195 Å images. The method is based on the combination of base-difference and logarithmic base-ratio data using a region-growing algorithm. This segmentation algorithm was applied to 43 off-limb coronal dimming events, and characteristic parameters describing their dynamic evolution, size, and brightness were derived. The events under study occurred between May 2010 and September 2012, where the two **STEREO** satellites were close to quadrature position with respect to the Sun-Earth line. This unique setting allows us to derive the properties of the coronal dimmings above the solar limb in the **STEREO/EUVI** data, and for the first time to compare them with parameters of the same dimmings observed against the solar disk by **SDO/AIA** as well as with the associated CME kinematics and mass derived above the limb (minimizing projection effects) in [Dissauer et al. \[2018b, 2019\]](#). This approach provides us with important

insight into the different projections of the coronal dimmings, and how they relate to the associated CME properties.

The off-limb dimming observations give us a line-of-sight integration across the CME from a lateral perspective. Thus, they provide us with a good view of its lateral expansion but the radial view is limited in height by the FOV of the EUVI imagers. The on-disk dimming observations are an integration of emission along the line-of-sight of the CME propagation, and thus correspond to a projection of the cross-section of the CME from a top view. However, they are affected by the “background” emission of the lower atmosphere layers, which makes it difficult to extract faint dimming regions and their effects higher up in the corona. On the other hand, on-disk dimmings provide us with the earliest insight into Earth-directed CMEs in observations from the Sun-Earth line, before the CME front reaches the FOV of white-light coronagraphs. Thus, comparing the properties of coronal dimmings observed simultaneously from different views in their on-disk/off-limb projections as well as their relation to the CME velocity and mass, allows us to assess the potential of using coronal dimmings for early CME characterization from satellites located either at L1 or L5.

Our main findings are as follows:

1. The derived off-limb dimming areas range from  $7.01 \times 10^9 \text{ km}^2$  to  $5.48 \times 10^{11} \text{ km}^2$  (Fig. 5-4). For the overlapping 39 events, which were studied also in Dissauer et al. [2018b, 2019], the mean value is  $1.24 \pm 1.23 \times 10^{11} \text{ km}^2$ , while the on-disk observations give  $3.51 \pm 0.71 \times 10^{10} \text{ km}^2$ . Only for 8 events the dimming area observed against the disk shows larger values than for the off-limb observations (see Fig. 5-5), with a correlation coefficient of  $c = 0.63 \pm 0.10$ .
2. We compared the total dimming brightness calculated from LBR and BD data with the corresponding brightness extracted against the disk (Fig. 5-7). The correlation coefficients are  $c = 0.60 \pm 0.14$  and  $c = 0.77 \pm 0.09$ , respectively, and the slopes derived from the fits in logarithmic space are close to 1. This means that the entire decrease in the intensity of the dimming region observed

on-disk and off-limb are linearly related to each other (with respect to the logarithmic space), but in most cases the on-disk dimming intensity is smaller (darker).

3. We also checked the duration of the impulsive dimming phase of 43 events obtained from off-limb observations (see panel (d) in Fig. 5-4). Although the time cadence of the STEREO data is much lower than the cadence of SDO/AIA, the duration parameter both for on-disk and off-limb observations is on average  $\sim 60 - 70$  minutes.
4. The CME mass shows the strongest correlation with the parameters, reflecting the total extent of the dimming, i.e. its area and total brightness:  $c = 0.82 \pm 0.06$  and  $c = 0.75 \pm 0.08$ , respectively (see Fig. 5-8 and Fig. 5-10). This result demonstrates that off-limb observations are able to provide a more accurate estimation of the CME mass.
5. The maximal CME speed correlates with the parameters describing the dynamics of the coronal dimmings:  $c = 0.59 \pm 0.14$  for the correlation with the area growth rate  $dA/dt$  (see Fig. 5-9),  $c = 0.61 \pm 0.12$  for the correlation with the instantaneous brightness change rate, derived from LBR data (Fig. 5-11). In addition, there is also a moderate correlation ( $c = 0.48 \pm 0.14$ ) of the CME maximal velocity and the mean brightness of the dimming (see also Fig. 5-11).

Figure 5-5 shows that for the events under study, off-limb dimmings tend to be larger than their corresponding on-disk counterparts. Due to the line-of-sight integration, the density depletion higher up in the corona may not be detected for on-disk observations due to brighter lower-lying regions. Base-ratio images, showing relative changes in intensity, allow us to detect these regions from the off-limb perspective. At the same time, the area parameters show a strong correlation ( $c \sim 0.63$ ), which may indicate that mostly large dimmings are also detected in the higher corona.

Although typically the area of the dimming observed off-limb is larger than on-disk, the absolute total brightness obtained from off-limb base-difference data is

lower than the one obtained from the on-disk data (see Fig. 5-7). Dimming regions detected higher up in the corona, show less significant intensity decrease compared to dimming regions detected close to the surface where the density of the corona is higher. The biggest area contribution of dimming regions detected off-limb results from these regions higher up, but they do not contribute much to the overall intensity decrease of the dimming region.

We found a very strong correlation between the CME mass and the dimming area, which confirms the relation of coronal dimmings and CME physical properties for the off-limb viewpoint. This is similar to the previous findings from the on-disk study [Dissauer et al., 2019]. More massive CMEs evacuate more plasma and create larger regions of EUV density depletion, which we detect from different lines of sight (see Fig. 5-8). The correlation coefficient revealed an even higher value than for on-disk results ( $c = 0.82 \pm 0.06$  for off-limb against  $c = 0.69 \pm 0.10$  for on-disk). This may be related to the fact that the CME parameters were also extracted from STEREO data. Thus, the projection effects may cause similar uncertainties for the dimming quantities and the CME parameters derived.

The maximal area of the dimming also demonstrates a high correlation coefficient with the speed of the CME ( $c = 0.67 \pm 0.10$  in logarithmic scale). This relationship supports the finding that faster CMEs are usually also more massive [Mason et al., 2016, Aschwanden, 2016, Dissauer et al., 2019] and therefore are also associated with a larger coronal dimming region. The correlation of the area growth rate with the CME speed and mass ( $c \sim 0.6-0.7$ ) supports this statement (Fig. 5-9).

According to Mason et al. [2016], CMEs that are associated with dark and large dimmings, tend to be more massive. The analysis of the dimmings on-disk by Dissauer et al. [2019] supports this statement: the correlation coefficient is  $c \sim 0.6$  for the correlation between the dimming total brightness and the CME mass. In the off-limb case the total dimming brightness  $|I_{br,in}|$  reveals an even stronger correlation with the CME mass ( $c \sim 0.75$ ). Thus, dimmings can provide a measure of the amount of plasma evacuation in the CME: darker dimmings indicate a larger density depletion.

Furthermore, we found a moderate correlation ( $c = 0.48 \pm 0.14$ ) of the mean

instantaneous brightness  $|\bar{I}_{br,in}|$  with the CME speed (Fig. 5-11). As the coronal plasma density strongly decreases with height, this correlation may indicate that faster CMEs tend to develop lower in the corona. This is consistent with studies of the CME source region characteristics and the fact that low in the corona also the magnetic field and thus the driving Lorentz force is stronger [Vršnak et al., 2007, Bein et al., 2011]. The same correlation from the on-disk observations reveals  $c = 0.68 \pm 0.08$ .

## 5.6 Conclusion

We performed a statistical analysis of 43 coronal dimming events that occurred during the time range between May 2010 and September 2012 that were observed simultaneously on-disk by SDO and off-limb by the STEREO satellites. The unique location of these satellites allowed us for the first time to look into the connection of the coronal dimmings and their associated Earth-directed CMEs statistically and to compare the results obtained from multi-viewpoint observations. Based on regression analysis, we confirm the relation of on-disk coronal dimmings and CME parameters presented in Dissauer et al. [2019] also for the off-limb viewpoint, for certain parameters providing even higher correlation coefficients than with the reported dimmings observed from on-disk by SDO AIA. Parameters describing the total dimming extent, i.e. area and the total brightness strongly correlate with the CME mass ( $c \sim 0.7-0.8$ ). The derivative of these parameters, i.e. the area growth rate and the brightness change rate show a high correlation with the CME speed ( $c \sim 0.6$ ), indicating the close relation between the CME and dimming dynamics.

In our observation range chosen (May 2010 - September 2012), the -A and -B satellites were located close to an L5/L4 configuration. The results from our study have therefore also relevant implications for the planned future L5 space weather mission, where Earth-directed CMEs, which are the most geo-effective, will be observed off-limb. The observations of coronal dimmings by solar EUV imagers may help us to obtain a better characterization of Earth-directed CMEs, which is relevant for space weather applications. The distinct statistical relations derived between dim-

ming parameters and decisive CME quantities for the different scenarios of L1 and L5 satellite locations (with correlation coefficients up to 0.8), provide a profound basis to improve early calculations of speed and mass of Earth-directed CMEs by including also the information of coronal dimmings.

# Chapter 6

## Dimming lifetime

This chapter is dedicated to answering research question Q2:

*How and when does the solar corona recover after a CME eruption?*

### 6.1 Project summary

Our first attempt to track the dimming recovery is based on use of 12-hour timeframe of the [STEREO](#) observations of the 43 dimmings events detected offlimb. We use a metric centered on a 50% reduction in the maximum dimming area. This analysis indicates a bimodal distribution of recovery times, categorized as less than or more than 6 hours, and suggesting two classes of the corona replenishment. To arrive at a definitive conclusion, we conduct a detailed study with a longer-term observation of dimming events.

In the next study, we examine four specific cases (September 6, 2011, March 7, 2012, June 14, 2012, and March 8, 2019) in which coronal dimmings are associated with flare/CMEs. Our goal is to gain insight into the long-term evolution and recovery of these coronal dimmings, and we present two different approaches to improve our understanding of the ongoing dynamics: the fixed mask approach and the area box approach.

For each of these events, we employ a unified methodology using EUV image data from both the [SDO](#) and [STEREO](#) satellites. Certain observational factors, such as artifacts and derotation, may affect the observation of dimming recovery. However,

our initial approach allows us to comprehensively track the overall evolution of dimming regions despite these challenges. Moreover, the pixel box approach not only complements existing studies, but also helps to investigate the different behavior of core and secondary dimmings. In summary, our study provides a comprehensive analysis of coronal dimming recovery in these particular cases and demonstrates the potential of the proposed approaches for future studies.

This study is presented in [Ronca et al. \[under review\]](#).

## 6.2 Literature review

The analysis of coronal dimming recovery and the study of its duration aim to understand the timing and mechanisms involved in the transition from an "open" magnetic field to a closed configuration after a solar eruption.

Two primary mechanisms govern the recovery of dimmings: either they contract in size or experience an increase in emission within their boundaries. The earliest systematic study by [Kahler and Hudson \[2001\]](#) examined dimmings in Yohkoh/SXT images and found that dimmings generally recovered through area contraction rather than increased brightness. [Attrill et al. \[2008\]](#), studying SOHO/EIT data, discovered that recovery involved both area shrinking and a progressive increase in emission. This recovery process typically featured outward-to-inward contraction and exhibited some inhomogeneity.

The difference in observations between [Kahler and Hudson \[2001\]](#) and [Attrill et al. \[2008\]](#) can be attributed to the distinct temperature sensitivities of the instruments used. SOHO/EIT captures emissions at temperatures around 1.5 MK, whereas Yohkoh/SXT primarily observes plasmas above 3 MK. This suggests that dimming recovery processes may not heat the coronal plasma sufficiently to be detected by Yohkoh/SXT.

[Reinard and Biesecker \[2008\]](#) conducted a statistical analysis of 96 dimming events observed by SOHO/EIT during 1998-2000. They found that dimming recovery typically featured a sharp rise from the minimum, followed by gradual recovery, with an average recovery time of approximately 4-5 hours. Most cases exhibited a

single linear slope in the recovery profile, while some displayed a two-step recovery with an initial steeper slope.

The recovery of dimmings can vary based on their morphological types. For instance, core dimmings may exhibit different recovery behaviors than secondary dimmings. [Vanninathan et al.](#) reconstructed Differential Emission Measure (DEM) maps and selected subfields within core and secondary dimmings separately and analyzed the density and temperature changes. It was found that in the localized core dimming regions, the density drops sharply within about 30 min and stays at these low levels for  $> 10$  hrs, whereas in the secondary dimming regions the density drop is more gradual, and the corona starts with the recovery and replenishment within 1-2 hrs. This finding was interpreted as evidence that the core dimmings are a signature of a flux rope still connected to the Sun, thus preventing the refill of coronal plasma in these regions.

Several theories exist regarding the physics behind dimming recovery. [Jin et al. \[2009\]](#) proposed a mechanism involving a mass supply from the lower transition region. [Attrill et al. \[2008\]](#) emphasized the role of interchange reconnection between open magnetic fields of the dimming region, small coronal loops, and emerging flux in facilitating dimming recovery. This process disperses open magnetic fields into the surrounding quiet Sun, ultimately restoring dimming emission.

Another plausible mechanism involves the interaction of erupting flux with itself or nearby preexisting open magnetic fields. This interaction can lead to a gradual reduction in closed flux connected to the Sun, contributing to dimming recovery.

However, it's important to note that research on dimming recovery is still limited, and observations of dimmings disappearing before the associated MCs reach 1 AU are based on only a few events. Other factors, such as global shock waves, can also affect observations and complicate interpretations.

In summary, recovery of coronal dimmings is influenced by several factors, including instrument sensitivity, morphological types, and the surrounding magnetic environment. Although several mechanisms have been proposed, further research is needed to fully understand the intricacies of dimming recovery and its implications for solar and interplanetary physics.

### 6.3 Statistical study

In the previous Chapter, we presented the statistical analysis of dimmings detected off-limb. In addition to other characteristics defined by the dimming impulsive phase, the time span of 12 hours allowed us to make the first attempts to track the dimming recovery time. It is important to highlight that for off-limb observations, it is impossible to distinguish between core and secondary dimmings.

For the presented data set of 43 events, we define a metric for the dimming recovery time  $t_{rec}$  as the difference between the time of the maximal instantaneous area  $A_{in}(t)$  ( $= A_{max}$ ) and the moment when the value of the instantaneous dimming area  $A_{in}(t)$  falls below 50% of its maximum ( $= 0.5 \cdot A_{max}$ ). For five events it was impossible to calculate the recovery time because of subsequent CME eruptions from the same active region during the dimming recovery. For 7 events of the sample, the derived recovery times are underestimated, as the drop to a value of  $0.5 \cdot A_{max}$  was not reached within the 12 hrs length of the time series that we studied for each event.

The distribution of the parameter  $t_{rec}$  for the other 38 dimming events is plotted in Figure 6-1. The recovery time varies from 0.7 hrs to 10.9 hrs. The histogram indicates a bimodal distribution with one group of fast recovery (smaller than  $\sim 6$  hrs), and another group with longer recovery times of  $> 6$  hrs.

The mean value is  $4.6 \pm 2.8$  hrs, which supports the results by Reinard and Biesecker [2008], where the mean of the recovery time  $4.8 \pm 0.3$  hrs was reported as well as with Krista and Reinard [2017] who found that the time from the area maximum to when dimming fully disappears is on average  $\sim 6$  hrs.

The dimming recovery times are suggestive of a bimodal distribution, with one group of  $t_{rec}$  values smaller than 6 hrs and another group with values of  $t_{rec} > 6$  hrs. This may indicate that there exist two different classes of dimmings as concerns the replenishment properties of the corona in the aftermath of a CME eruption. We also note that for 7 events in our sample, the recovery time defined by the decrease of the instantaneous dimming area to 50% of its peak value was not reached within the studied time range of 12 hrs, and may thus be even longer. These findings can

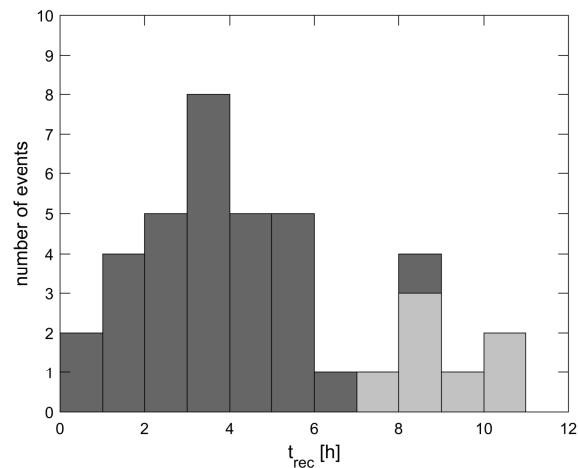


Figure 6-1: Distribution of dimming recovery times derived from **38** events of our sample. Note that for 7 events (light coloured bars), the derived recovery time gives only a lower estimate.

be set in context with the study of [Vanninathan et al. \[2018\]](#).

However, to provide a definite conclusion on that, we would need to follow the dimming events over an extended time range. However, measuring the dimming area accurately presents a challenge due to the inherent limitations of single-viewpoint observations, especially for off-limb observations.

Therefore, a novel approach is required, and we elaborate on it in this chapter.

## 6.4 Methodology

Here our analysis aims to determine, for specific events, the maximum time intervals in which we can continue to detect coronal dimming signatures associated with a CME - the dimming recovery time. This time interval provides information about the time scale of coronal renewal following a solar eruption and the extent to which a CME remains connected to the Sun through its legs.

A major challenge in the study of dimming recovery is the distortion effect that occurs when images are aligned to a reference time to compensate for differential rotation. This distortion leads to artifacts in segmenting the dimming region and tracking its parameters. It remains an obstacle due to the limitations of single-point observation.

In our project, we propose an innovative approach to mitigate the effects of image distortion in the analysis of coronal dimmings. In this approach, a fixed mask is used to track the evolution of the solar corona while extracting critical parameters such as instantaneous brightness and area. In this way, we aim to improve the accuracy and reliability of our dimming analysis.

### 6.4.1 Event selection

#### 2011 September 6

On September 6, 2011, [NOAA AR 11283](#) produced a series of significant solar events. First, at 22:20 UT there was an X2.1 class flare (N14 W18), accompanied by a halo CME of a speed  $990 \text{ km s}^{-1}$  (see [Table 6.1](#)). About a day later, at 22:38 UT, a second X1.8-class occurred with a partial halo CME (angular width of  $167^\circ$ ). On September 8, at 15:46 UT, a third M6.7-class flare originated from the same active region, associated with CME with  $37^\circ$  angular width [consortium and team](#).

The strong activity of [NOAA AR 11283](#) during the rising phase of solar cycle 24, which occurred near the center of the solar disk, attracted the attention of numerous scientists (e.g., [Jiang et al. \[2013b\]](#), [Jiang et al. \[2013a\]](#), [Romano et al. \[2015\]](#) studied this [AR](#) and the related flares/CMEs, while [Dissauer et al. \[2016\]](#), [Vanninathan et al.](#), [Prasad et al. \[2020\]](#) studied coronal dimmings).

This particular case stands out because of its position as the only one analyzed within a 48-hour period. While its proximity to the center of the Sun (see [Fig. 6-2a](#)) facilitates observation, it also leads to reprojection effects caused by differential rotation in images taken more than two days after the reference time. Therefore, the observation time was limited to a few hours after the occurrence of the third eruption to mitigate these disturbances.

#### 2012 March 7

[NOAA AR 11429](#) produced five CMEs during the first two weeks of March 2012, at the beginning of the maximum of solar cycle 24. The largest and most energetic CME occurred on March 7 [Liu et al. \[2013\]](#). Two notable flares were observed that

day: an X5.4 class flare (N18 E31) at 00:24 UT and an X1.3 class flare at 01:14 UT [Ajello et al. \[2014\]](#). The first CME has a speed of  $2680 \text{ km s}^{-1}$ ; the second CME is not visible because it closely followed the first in time.

We focus on the first X5.4 flare/CME event of March 7 to study the associated dimming. We also consider the M6.3 class flare/CME at 03:58 UT on March 9, which is also associated with a halo CME.

This active region is located in the northwest quadrant of the solar disk, near the western edge (Fig. 6-2b). The dimming associated with these events is clearly visible in the original images and represents the most prominent coronal dimming event identified by [SDO/EVE Veronig et al. \[2020\]](#).

### 2012 June 14

On June 14, 2012, a long-lasting M1.9 class flare (S17 E06), accompanied by a halo CME with speed of  $990 \text{ km s}^{-1}$  was triggered by [NOAA AR 11504](#) at 14:35 UT.

This event occurred close to the maximum of solar cycle 24 in June 2012. The active region was located in the southern hemisphere, near the central part of the solar disk (see Fig. 6-2c). This region of the Sun was quite densely populated with various active regions, and there was also a prominent coronal hole to the left of the [AR](#) of interest.

### 2019 March 8

On March 8 at 03:07 UT, a double-peaked C1.3-class flare (N09 W13) occurred (as detailed in Section 4.5.1), with the second peak occurring at 03:47 UT. The following day, on March 9 at 12:26 UT, a B6.2-class flare occurred. These solar events originated from active region [AR 12734](#). Each of these flares was associated with a corresponding CME, with angular widths of  $74^\circ$  and  $71^\circ$ , respectively. The first CME exhibited a speed of  $290 \text{ km s}^{-1}$ .

This active region was located in the upper half of the solar disk, precisely at its center (see Fig. 6-2d). These eruptions occurred during the solar minimum phase between cycles 24 and 25. Despite their relatively low [GOES](#) flux, the first flare garnered scientific attention due to its association with various distinctive solar

eruption phenomena, as discussed earlier [Dumbović et al., 2021]. The timing of the first flare can be divided into two distinct stages: one from 03:07 to 03:20 UT and another commencing after 03:20 UT.

Detailed information about all events can be found in Table 6.1, which also includes the time of the base map and the time of the fixed mask (maximum dimming).

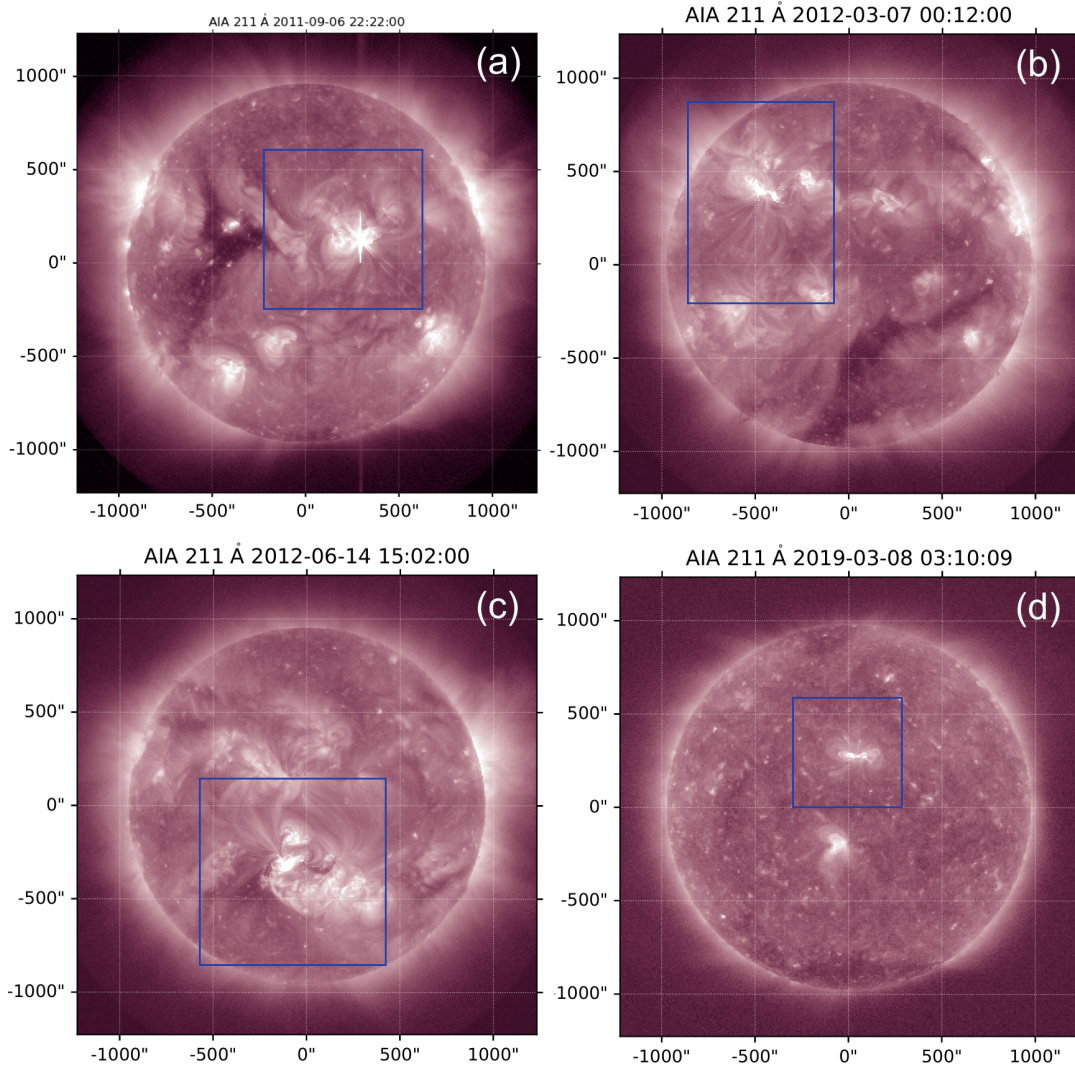


Figure 6-2: Snapshots of events under analysis: (a) September 6 2011, (b) March 7 2012, (c) June 14 2012, (d) March 8 2019. Blue rectangles show the chosen regions of interest, indicating the location of eruptions on the solar disk.

Date	NOAA AR	Flare Location	Flare Class	Time (UT)			Flare duration [min]	CME speed [km/s]
				Start	Peak	End		
2011/09/06	11283	N14 W18	X2.1	22:12	22:20	22:23	11	990
2012/03/07	11429	N18 E31	X5.4	00:02	00:24	00:40	38	2680
2012/06/14	11504	S17 E06	M1.9	12:51	14:35	15:56	185	990
2019/03/08	12734	N09 W13	C1.3	03:07	03:18	03:58	51	290

Table 6.1: Event Review: NOAA Active Region and flare location, flare class, GOES flare time interval (from start to end, including the peak time), CME speed as listed in the LASCOC catalogue ([https://cdaw.gsfc.nasa.gov/CME\\_list/](https://cdaw.gsfc.nasa.gov/CME_list/)), apart from the CME speed of 2011 September 6 event, taken from Dissauer et al. [2016].

### Time cadence

For each event, the SDO/AIA 211Å time series cover a 72-hour period, starting 30 minutes before the corresponding flare. Data are recorded at 5-minute intervals for the first 24 hours and at 30-minute intervals for the following 48 hours. The exception is the September 6, 2011 event, where a 5-minute cadence is maintained for the entire 48-hour period.

In contrast, the STEREO/EUVI 195 Å data maintain a consistent 5-minute cadence throughout the time interval.

For each event, we determine the time of onset, peak, and end of the flare associated with a CME. We also examine whether other phenomena occur within the 72-hour time window.

## 6.4.2 Data preprocessing

All the steps of data preprocessing of SDO/AIA and STEREO/EUVI are the same as described in the introduced approach in Section 4.2.5: we load and calibrate data using Python Sunpy routines, differential rotate every image to a pre-event base map at 30 minutes before the flare onset. After that, we create base difference and logarithmic base ratio images for the dimming extraction.

### 6.4.3 Dimming detection

In our approach to detecting dimming on disk, as described in Section 4.2, we identify a pixel as a dimming pixel if its intensity falls below -0.19 in the logarithmic ratio. After that we use an algorithm that uses the darkest 10% of pixels in each logarithmic base ratio (LBR) image as the seed pixel. We do not apply median filtering in this analysis to avoid inadvertently connecting artifacts in later time steps. In addition, we do not fill the holes left in the images by the algorithm, as this is more appropriate for cumulative parameters. However, in this analysis, we use instantaneous masks, and these holes could potentially represent physical variations between different regions of dimming.

For the off-limb dimming detection from STEREO/EUVI data we used the same approach and set of parameters as described in Section 4.2.5. We used the classical thresholding levels for the off-limb dimming detection from STEREO/EUVI data.

Figure 6-3 shows a snapshot of all four cases studied at a time when the main eruption dimming is close to its maximum extent. The left column shows the original SDO/AIA images followed by the corresponding LBR image at the same time. The last two columns on the right show the original STEREO/EUVI image of the Sun and the corresponding LBR image, respectively. The original SDO/AIA and STEREO/EUVI images were calibrated and de-rotated to basemap time. The color scale of the LBR images is based on the same interval, from -0.7 to 0.0 DN, to allow good visualization of the dimming. The events shown in this figure, from top to bottom, are 2011 September 6, 2012 March 7, 2012 June 14, 2019 March 8.

### 6.4.4 Calculation of coronal dimming parameters

Examining the long-term evolution is more challenging than analyzing the impulsive phase of dimming because, over the course of days, the coronal structure itself undergoes changes. This introduces uncertainty into the differential rotation correction of individual coronal pixels, resulting in noise in the BD and LBR images.

We study characteristic parameters such as instantaneous area and brightness. We identify the instantaneous dimming area  $A_{in}(t)$  as described in Sec. 4.3 and

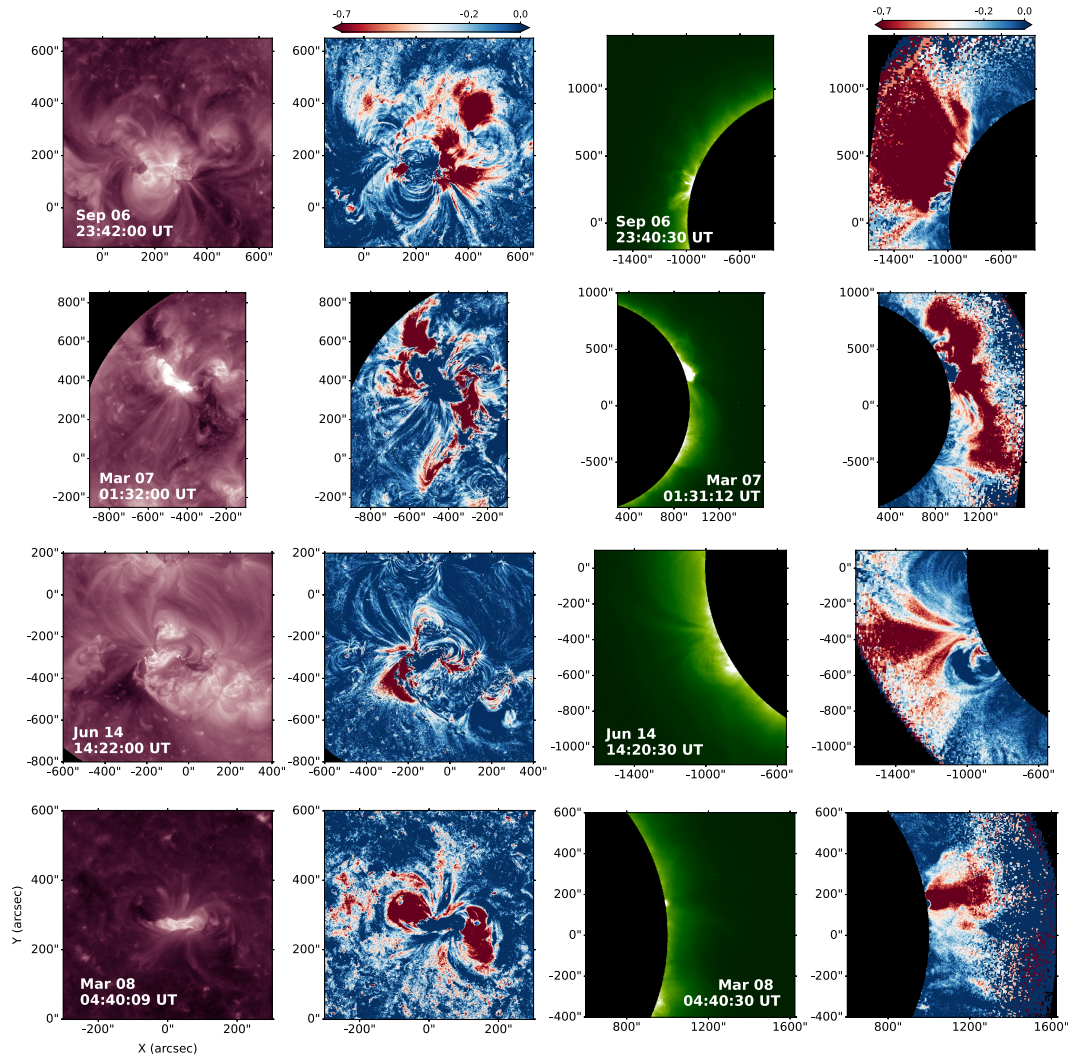


Figure 6-3: Snapshot of all the four cases under study. From top to bottom: 2011 September 6, 2012 March 7, 2012 June 14 and 2019 March 8. The shown time instant corresponds to when the dimming is close to its maximum extension. Left column: original SDO/AIA image. Middle left column: LBR image corresponding to the SDO/AIA direct image. Middle right column: original STEREO/EUVI image of the Sun. Right column: LBR image corresponding to the original STEREO/EUVI. The colorbar of both the LBR images is based on the interval from  $-0.7$  to  $0$  DN. Dimming detection procedure is based on the thresholding value of  $-0.19$ , so all pixels belonging to the dimming region stretch from white to red regions.

apply the pixels correction method (Sec. 4.4), calculating the spherical projection of the pixels.

Use of the instantaneous brightness curves  $I_{in}(t)$  (Sec. 4.3) is a conventional method for studying dimming evolution over time. However, this approach is typically used for shorter time intervals following a solar flare or CME event. In contrast, our current analysis spans an observation period of 3 days. With such a long observation period, there is a higher probability of artifacts associated with the differential rotation process that are subsequently identified as coronal dimmings by the region-growing algorithm. These artifacts are most pronounced in regions near the solar limb.

Detecting seed pixels at each moment may include pixels associated with artifacts or the expansion of dimming regions triggered by subsequent flares or CMEs occurring within the studied timeframe. Consequently, this results in a continual fluctuation in the dimming area over time, no longer linked to the recovery process.

To mitigate the impact of dimming size variations and minimize artifact influence, we have concentrated our analysis on specific sections of the cropped image. We propose two approaches for examining the duration of dimming events.

### Fixed mask

The first approach involves applying a consistent dimming mask to each map. By using an instantaneous fixed mask instead of a cumulative one, we can minimize the inclusion of flaring regions within the mask that might impact our calculations.

This fixed mask is determined as the largest instantaneous dimming mask in terms of the number of pixels among the LBR maps observed within the initial two hours from the onset of flare/CME activity. This timeframe is considered sufficient to encompass the impulsive phase of dimming, as supported by statistical data in references [Dissauer et al. \[2018b\]](#) and [Chikunova et al. \[2020\]](#). However, for the June 2012 and March 2012 events, the chosen map represents a relative maximum rather than the absolute maximum extension. In both instances, the dimming area continues to expand, especially during the prolonged flare activity that spans approximately 3 hours in the case of June 2012.

After the maximum dimming extension within the impulsive phase is identified and used as a mask on top of BD maps, the instantaneous brightness  $I_{fix}$  of each map (at time  $t_m$ ) is computed as the sum of all the pixels' intensities inside the masked region:

$$I_{fix}(t_m) = \sum I(p_i, t_m) C_{fix}(p_i, t_{max})$$

where  $I(p_i, t_m)$  is the intensity at  $t_m$  for a certain dimming pixel  $p_i$  within the fixed dimming mask  $C_{fix}(p_i, t_{max})$ . In this case, it is not considered whether a pixel is an instantaneous dimming pixel at the time  $t_m$ , but all the pixels of the fixed dimming mask contribute to the calculation.

Regarding cumulative masks, it's important to note that numerous other regions, such as those associated with flares, are included in the calculations. When studying the entirety of dimming regions, both core and secondary, this inclusion can make long-duration light curves more unclear (see examples in Fig. 6-4 and Fig. 6-5). Thus, it is better to track the maximum instantaneous mask.

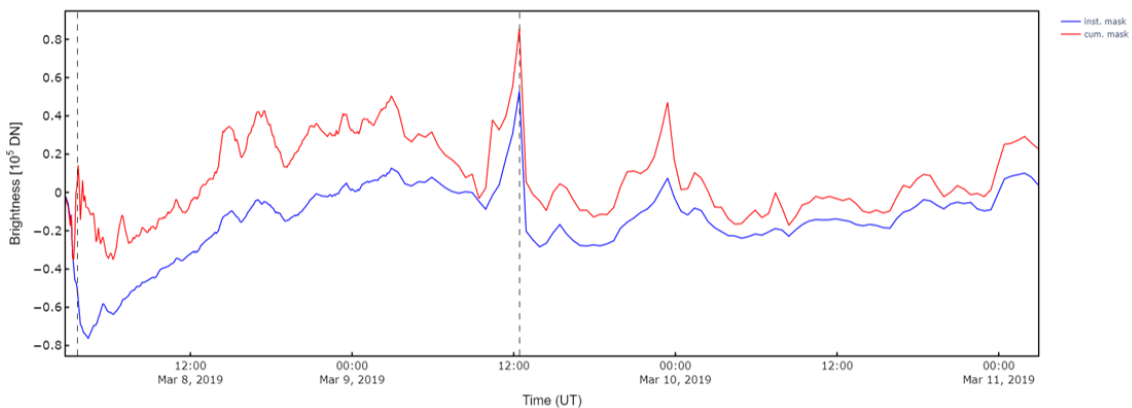


Figure 6-4: Comparison of the dimming brightness within the maximum instantaneous (blue) and maximum cumulative mask for the 8 March 2019 event.

Figures 6-6 – 6-9 illustrate the time evolution of the four studied events. In each figure, from left to right: AIA 211 Å snapshots at five different time points within the analysis time range, the corresponding LBR images, the extracted dimming pixel masks (red) on top of the LBR images. The color bar marks the LBR intensity. Pixels that fall below the detection threshold ( $-0.19$  DN) transition from white to dark red, making the progression of dimming. A blue contour in the bottom

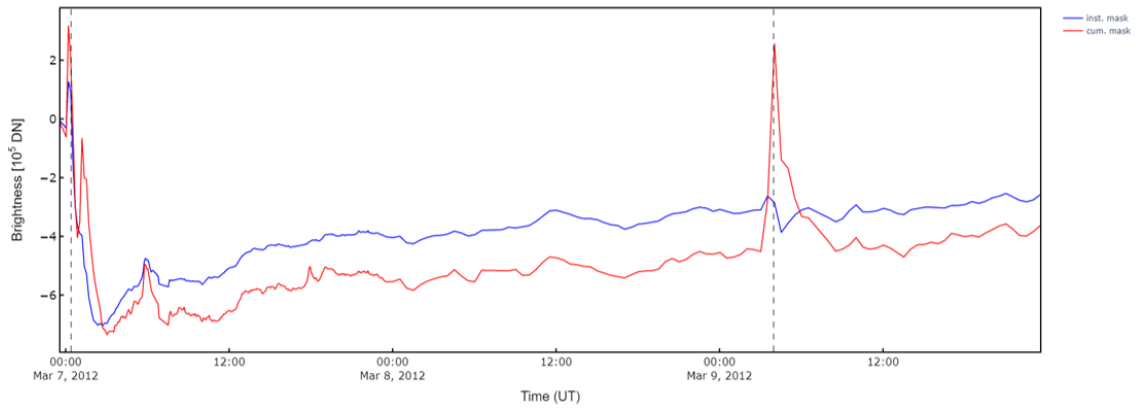


Figure 6-5: The same as Fig. 6-4 but for the 7 March 2012 event.

right panel delineates the fixed mask. These images shows the effect of de-rotation over longer observation periods, with Fig.6-7 serving as a prime example, where red zones appear towards the eastern edge. The right panel also highlights the difference between tracking the brightness within the detected dimming area and the fixed mask approach: the artifacts of de-rotation can notably influence the dimming brightness. In contrast, the fixed mask approach effectively mitigates this impact.

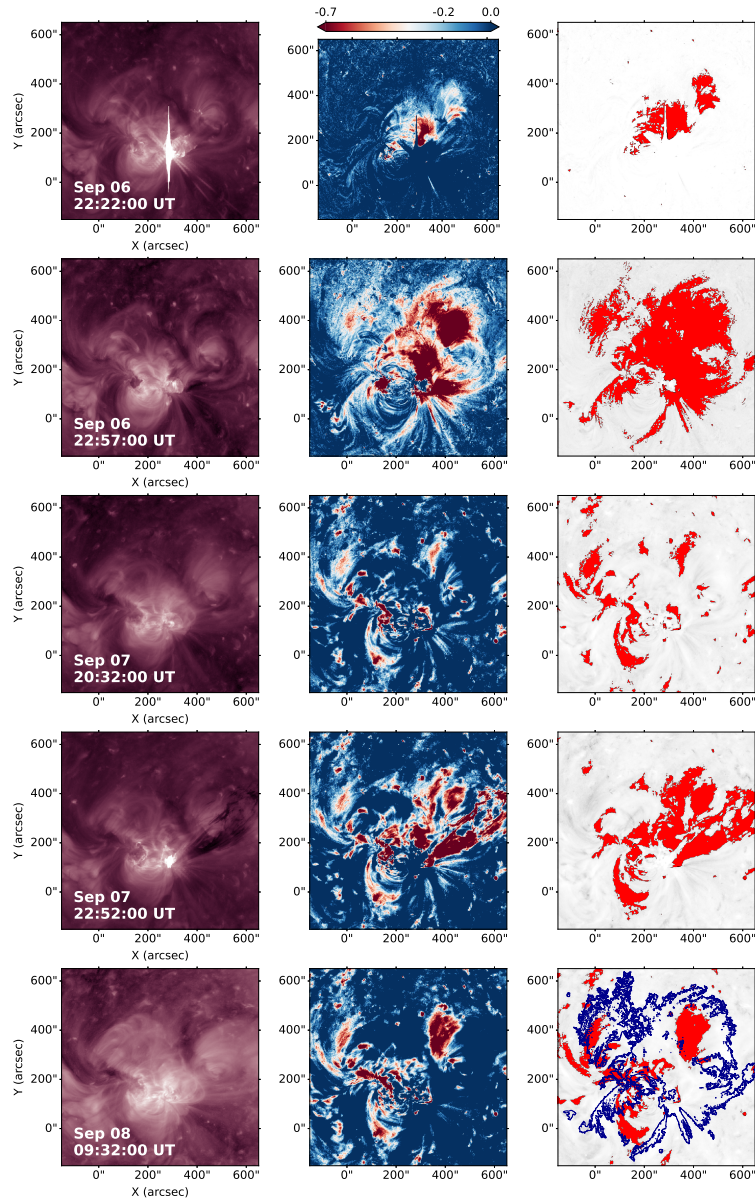


Figure 6-6: Evolution of coronal dimming region for September 6, 2011 event. Time sequence of the original SDO/AIA 211 Å images (left), LBR images (middle), and extracted dimming pixel masks on top of the LBR images. In the bottom right panel, the blue contour of the fixed dimming mask is overlaid.

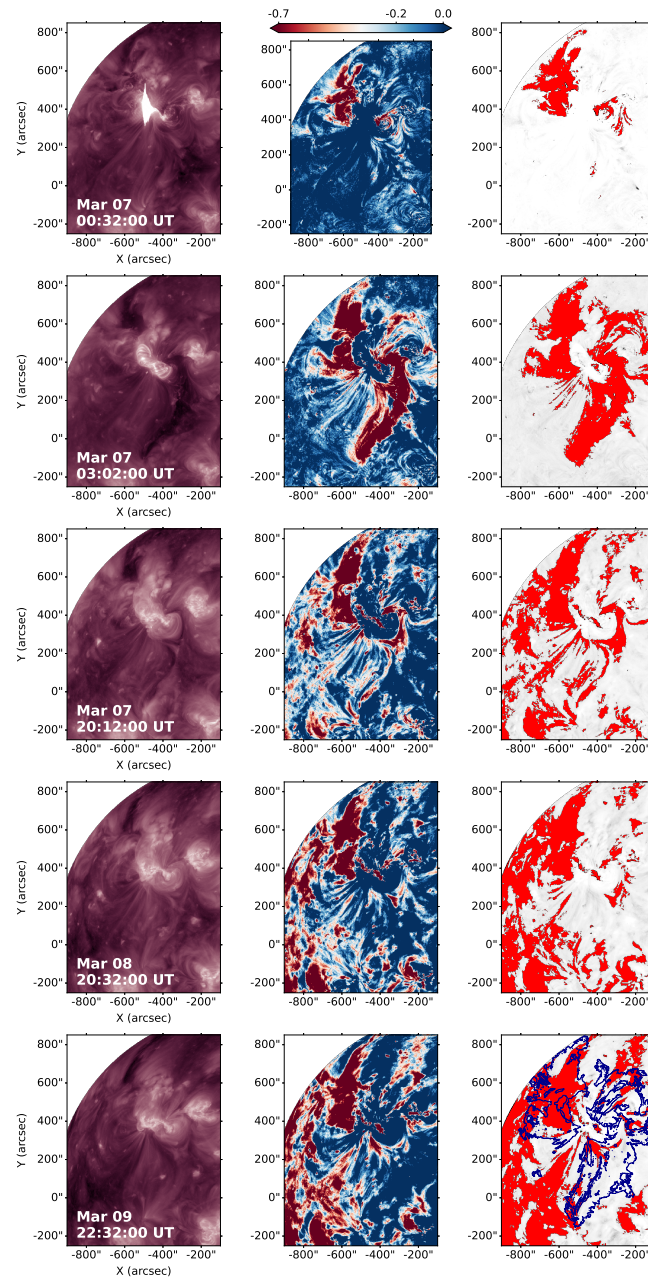


Figure 6-7: The same as Fig. 6-1 for March 7, 2012 event.

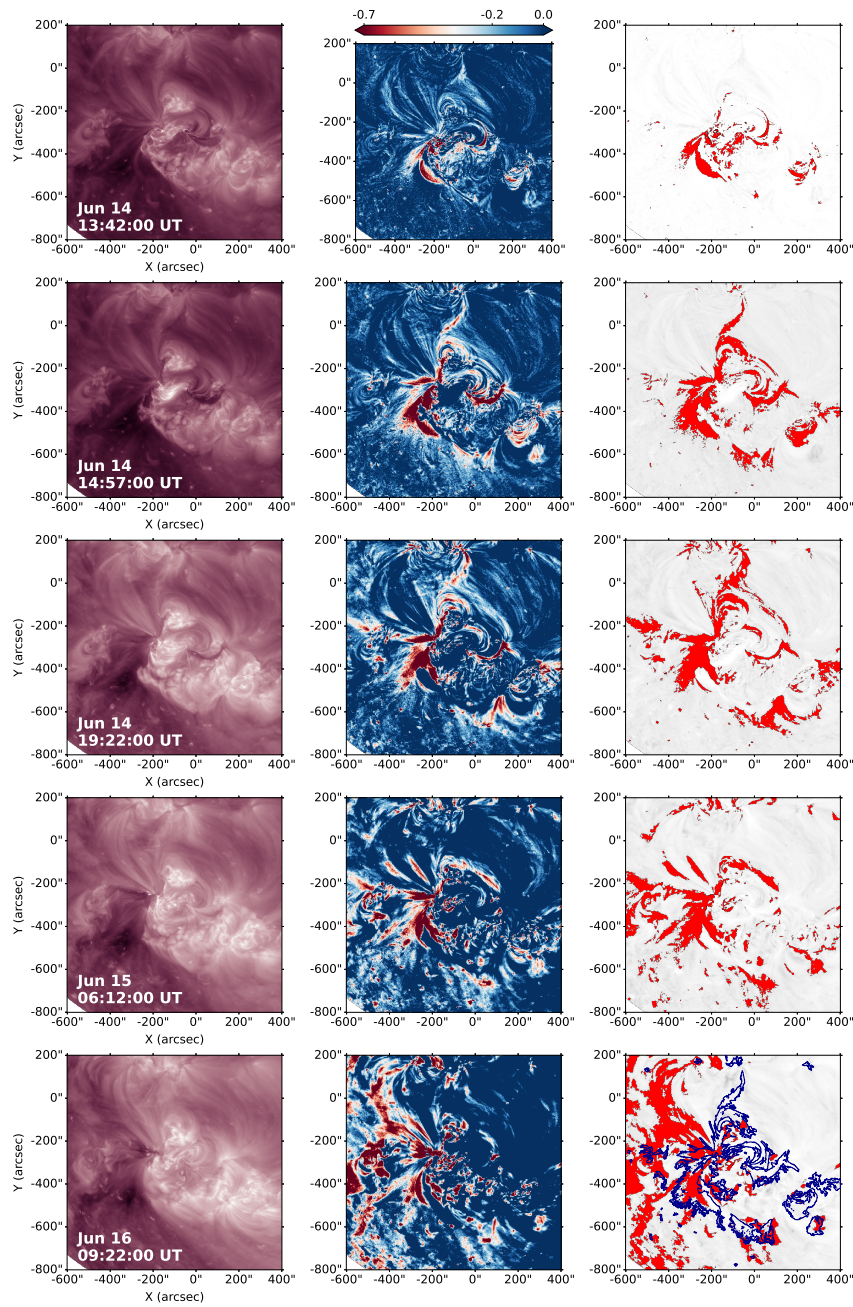


Figure 6-8: The same as Fig. 6-1 for June 14, 2012 event.

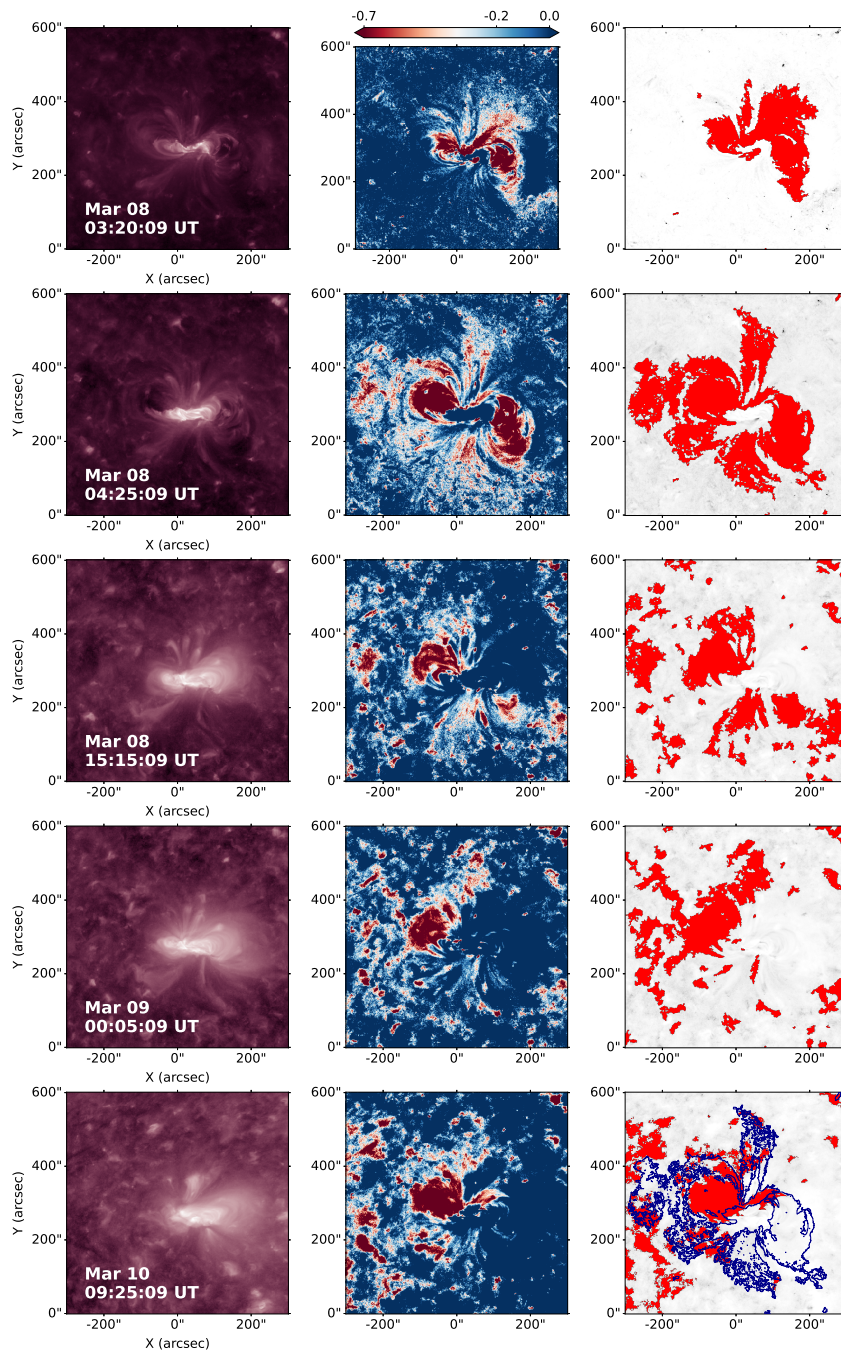


Figure 6-9: The same as Fig, 6-1 for March 8, 2019 event.

### Area boxes

The second approach involves a focused investigation within a highly localized region of the overall map. We divide this region into several  $3 \times 3$  pixel boxes using the original SDO/AIA images, BD images, and LBR images. Within each box, we compute the mean intensity value of the pixels.

To determine the position of each box, we manually select them based on visual inspection of the LBR images, where dimming regions can be easily seen, and on the dimming binary maps. These boxes can be strategically placed either close to the eruption center or further away to observe the evolution of brightness over time.

This approach offers great versatility. Its main advantage is the possibility to observe different behaviors depending on the placement of the box. In addition, it allows the study of local behavior within dimming regions that may be less affected by the overall long-term evolution and data processing.

## 6.5 Results

In the following subsections, we address a comprehensive analysis of the evolution of global dimming, focusing on both area and intensity for each of the four events examined. For the 2011 September 6 and 2019 March 8 (Women’s Day) events, we also examine area boxes within the overarching global dimming region. This investigation aims to highlight the intricate structures within these dimming regions and to contrast the long-term evolution of global dimming attributes with their localized dynamics. Finally, we provide a comparative assessment of all events by quantifying the evolution of global dimming intensity using the fixed mask method.

### 6.5.1 2011 September 6

Figure 6-10 shows the analysis outcome for the 2011 September 6 event. The four panels show the flare evolution using the GOES 1-8 Å soft X-ray flux (panel *a*), the instantaneous dimming area  $A_{inst}$  (panel *b*), the instantaneous dimming brightness  $I_{inst}$  (panel *c*) and the instantaneous brightness  $I_{fix}$  of the region within the fixed mask (panel *d*) as a function of time. These intensities are related to the observation of the event in the base-difference images. Panels *b* and *c* also compare instantaneous area and brightness between data from the SDO/AIA and STEREO/EUVI 195 Å instruments.

The GOES flux helps visualize the time of occurrence of the flares, which is generally close in time to the onset of the associated CME [Maričić et al., 2007, Bein et al., 2012]. The analysis spans 48 hours, and during this time, three flares occur, each associated with a CME. The instantaneous brightness (Fig.6-10*c*) shows a recovery, especially after the first and second flare, but never reaches a full recovery to the pre-event level. The same is true for the instantaneous area (Fig.6-10*b*). Data from EUVI aboard STEREO-A are also used and show a similar trend to the data from AIA. In particular, the steep decrease (increase) associated with the dimming brightness (area) shows similar behavior, and the peak periods are almost coincident. There is also no complete recovery of the dimming.

Figure 6-10*d* shows the behavior of instantaneous brightness within the fixed dimming mask. In this case, both dimming and non-dimming pixels are included in the identified region for the time step under consideration, so bright pixels belonging to the flares can also visibly contribute to the brightness calculation. In fact, the three flares/CMEs appear like three peaks and after the first one a sharp brightness decrease is observed, falling well below the level before the flare (corresponding to the so-called "post-flare dimmings" in full-Sun observations; see Veronig et al. [2021a]). The brightness decreases to a minimum point corresponding to the maximum extent of the dimming region.

In the hours following the first eruption, a full recovery of brightness can be observed at 14:57 UT on September 7, well before 24 hours have passed. Even when the second flare occurs on September 7 (24 hours after the first), it has no significant

effect on the intensity within the fixed dimming region identified in the first event. One reason for this could be the location of the dimming and the direction of its extension: The first dimming extended mainly toward the northwest of the eruption site, while the second extended both in that direction and toward the northeast and thus was partially outside the fixed dimming mask. The portion of the second dimming that remains within the fixed mask is smaller than the first dimming, so the overall brightness of the fixed region fluctuates around zero, with both dark dimming pixels and brighter pixels present within the fixed mask region. Finally, a smaller spike is observed on September 8, corresponding to the last flare. Dimming is very small and overlaps with parts of the previous dimming regions that have not yet disappeared.

Thanks to the brightness curve, we were able to determine that there is a recovery process. Using the original [SDO/AIA](#) images, we investigated the mechanism behind this recovery. We observed that the dimming recovers from the outer edges inward and toward the center. In particular, the region farthest from the center of the eruption is the first to recover, while some dark regions near the center of the eruption still remain. This is further investigated by specifically analyzing the recovery behavior of certain small regions using the  $3 \times 3$  pixel box approach.

Figure 6-11 shows the [LBR](#) map on 2011 September 6 during the impulsive dimming phase, with four colored diamonds marking the center of the  $3 \times 3$  pixel boxes. In particular, boxes 1 (yellow), 3 (red), and 4 (light blue) are near the eruption site, while box 2 (pink) is farther away, in the middle of a very dark dimming region, likely a secondary dimming region within a magnetic plage region. The goal of the boxes is to track the ongoing dynamics and intensity behavior in the selected regions.

Fig. 6-12 shows the evolution of the average [LBR](#) brightness of the four boxes.

It can be clearly seen that box 2 and box 3 already show a complete recovery before the second flare occurred (marked by the dashed line). However, by observing also the evolution of the original, [BD](#) and [LBR](#) images, it can be seen that there are post-flare loops that gradually extend toward the dimming region of box 3. Therefore, this recovery can be considered as a projection effect resulting from the

line-of-sight integration of these loops over the dimming region. In contrast, the recovery process of field 2 is related to the shrinkage of the overlying field. This region recovers most rapidly to its pre-event intensity and exhibits linear, gradual recovery behavior.

Box 1 shows a more complex evolution. Initially, it shows a similar recovery rate as box 3. One possible reason for this could be that the same post-event eruption loops propagate through this region, but from the opposite side. Thereafter, however, the intensity within this field decreases. The region where the field is located shrinks due to the expansion of the flare ribbons into this region, which could indicate reconnection between the overlying field and the erupting flux rope. Lastly, box 4 shows weaker intensity recovery during the first 12 h after the CME, especially compared to box 2. This result is consistent with [Attrill et al. \[2008\]](#) and therefore, it is reasonable from an observational point of view to classify this dimming area as a core dimming region. It should be noted, however, that this region may not represent the footpoints of an erupting flux rope in a classical sense. This box is located within a dimming region that likely contains field lines that opened during the eruption ([Prasad et al. \[2020\]](#)). By combining observations and data-driven MHD simulations, [Prasad et al. \[2020\]](#) found that this dimming region spatially coincides with the footpoints of the dome surface of a 3D magnetic null point. In this study, a causal relationship was inferred between the magnetic reconnections at the 3D null point and the dimming due to the transformation of field lines of the inner spine to open field lines to the outer spine.

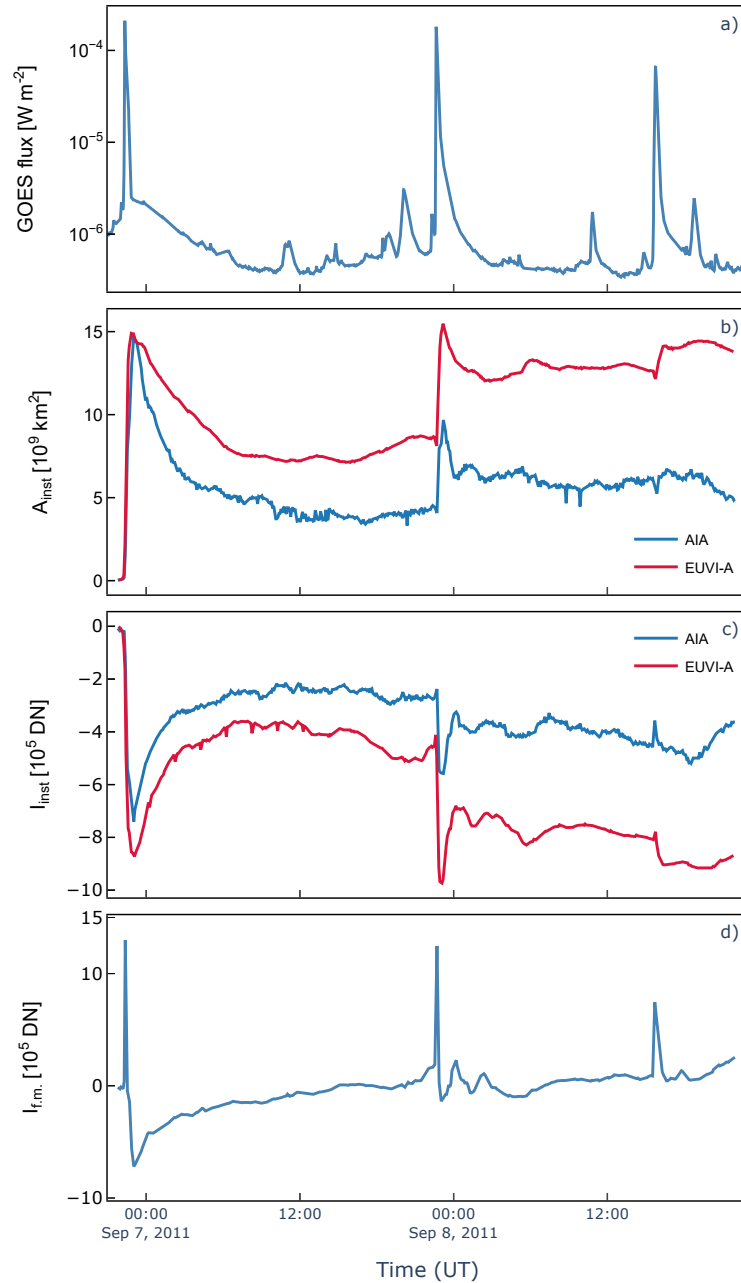


Figure 6-10: Evolution of dimming area and brightness in the 2011 September 6 event. The data from **STEREO**, having a higher cadence, are smoothed. (a) **GOES** 1-8 Å soft X-ray flux. (b) Instantaneous dimming area evolution over time. Comparison between **SDO/AIA** (blue curve) and **STEREO/EUVI-A** (red curve). (c) Instantaneous dimming brightness evolution over time. Comparison between **SDO/AIA** (blue curve) vs **STEREO/EUVI-A** (red curve). (d) Instantaneous brightness evolution within the fixed mask.

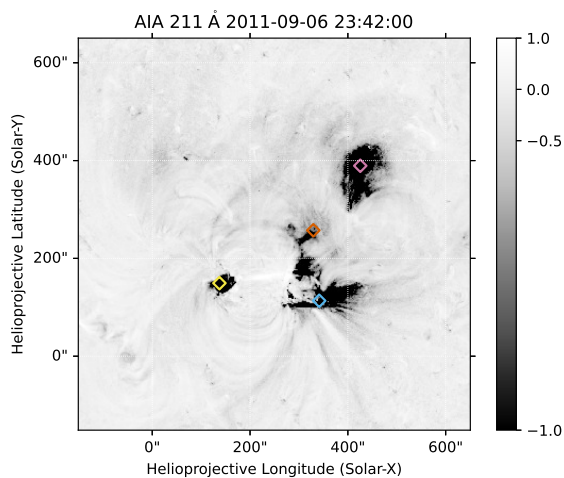


Figure 6-11: 2011 September 6 event. Four boxes of size  $3 \times 3$  pixels are located on the LBR image. Box 1: yellow marker. Box 2: pink marker. Box 3: red marker. Box 4: light blue marker.

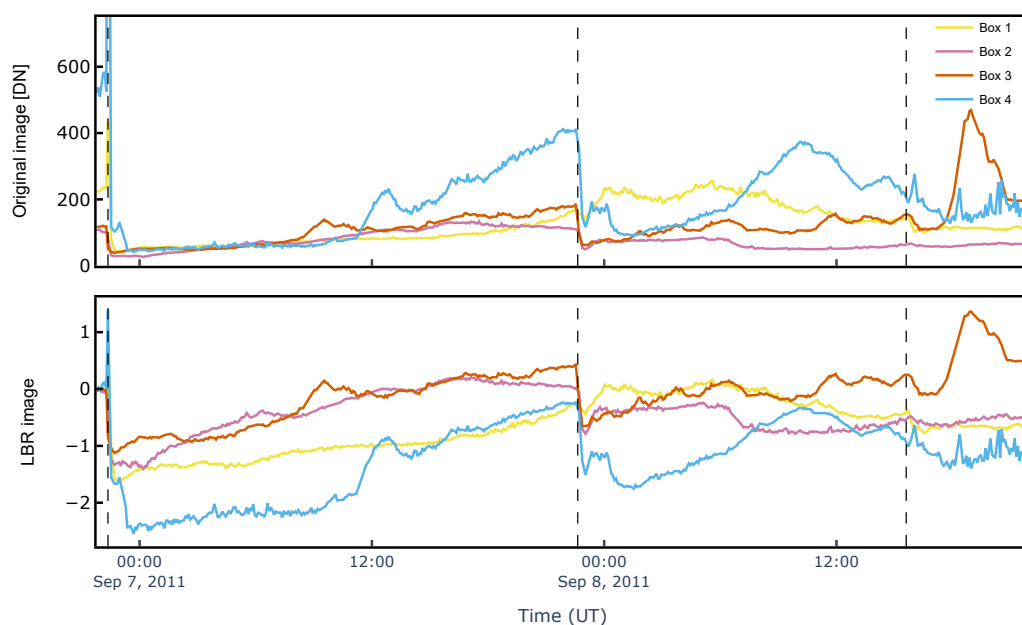


Figure 6-12: Comparison of the brightness behaviour for each of the chosen  $3 \times 3$  pixel box shown in Fig. 6-11. The dashed line indicates the peak time of the two X-class and the one M-class flare.

### 6.5.2 2012 March 7

Figure 6-14 shows the evolution of dimming brightness and area for the 2012 March 7 event. Using the curves of instantaneous dimming area and brightness in the *b* and *c* panels, one can observe a continuous growth of the dimming area with a simultaneous decrease in brightness in both the SDO/AIA and STEREO -B/EUVI data. It seems that the dimming formed after the flare/CME on March 7 does not recover after two days, but increases continuously. At the time of the March 9 flare/CME, this trend is still present. The AIA and EUVI instrument data show similar behavior, especially in the large increase (decrease) in area (brightness) and the overall decrease in instantaneous brightness. However, there is a difference between the observations of the two instruments: While the data from SDO/AIA show a continuous growth of the area and a decrease of the brightness, the data from STEREO-B/EUVI show a shrinkage of the dimming area (red line in the *b* field) accompanied by a slight recovery trend of the brightness, followed by a nearly constant value of both the instantaneous area and the brightness. This behavior is maintained until the second flare after about 52 hours, resulting in a further decrease in instantaneous intensity and an increase in area. A review of the original images and the instantaneous dimming maps shows that the dimming expands near the eastern edge and becomes larger with time. Because of the proximity of AR to the eastern limb, this behavior is interpreted as an artifact of the differential rotation procedure affecting the two regions of dimming: the northeast region closer to the edge and the southwest region. Therefore, using the fixed mask curve is more reliable for interpreting this event.

By looking at the development within the fixed dimming mask (Fig. 6-14-*d*), the brightness does not recover. The second flare does not appear as a distinct intensity peak, unlike what happens in September case (Fig. 6-10-*d*). This is partly because the majority of the dark dimming pixels are still inside the fixed mask, but also because the bright flare region is outside the fixed mask, unlike the 2011 September 6 event.

Another interesting aspect of the 2012 March 7 event is revealed when looking at the original SDO/AIA images and the dimming evolution within the fixed mask.

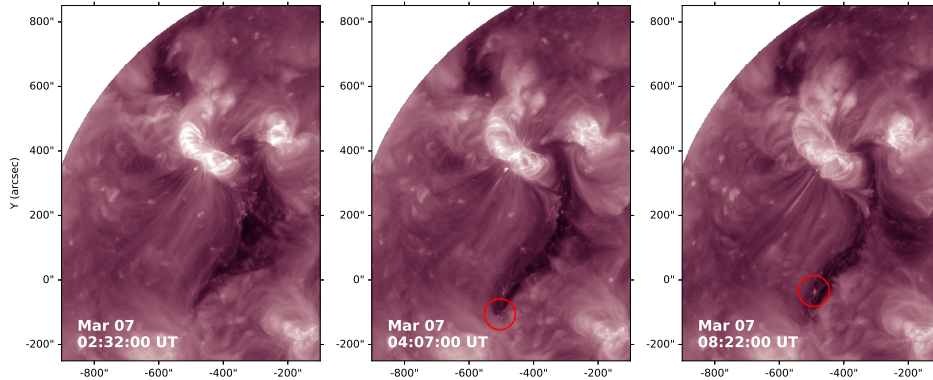


Figure 6-13: Snapshots from 2012 March 7 event at 02:32, 04:07 and 08:22 UT. The red circle marks where brightenings are observed. These brightenings are not detected in the segmentation process, meaning they are brighter than the surrounding regions. They might indicate that there is flux emergence and interchange reconnection inside the dimming region.

As mentioned earlier, this dimming is composed of two regions. While the region in the northeast does not recover within 72 hours of observation, the region in the south does. In particular, it can be observed that the recovery is not only due to the shrinking of the dimming boundaries but also that some flux from below the photosphere occurs, which helps to replenish the region: brightenings are observed at certain times within the southern part of the dimming, e.g., on 2012 March 7 at 04:07, 05:42, 08:22, or 09:17 UT. They are seen in the original [AIA](#) image, but are also not included in the dimming region by the region growing algorithm, which means that they are brighter compared to the surrounding region (i.e., the dimming): some bright pixels actually appear below the dimming. The March case is the only case in this study where the recovery is not only due to the shrinkage of the dimming regions themselves, but also to flux emergence and interchange reconnection within the regions.

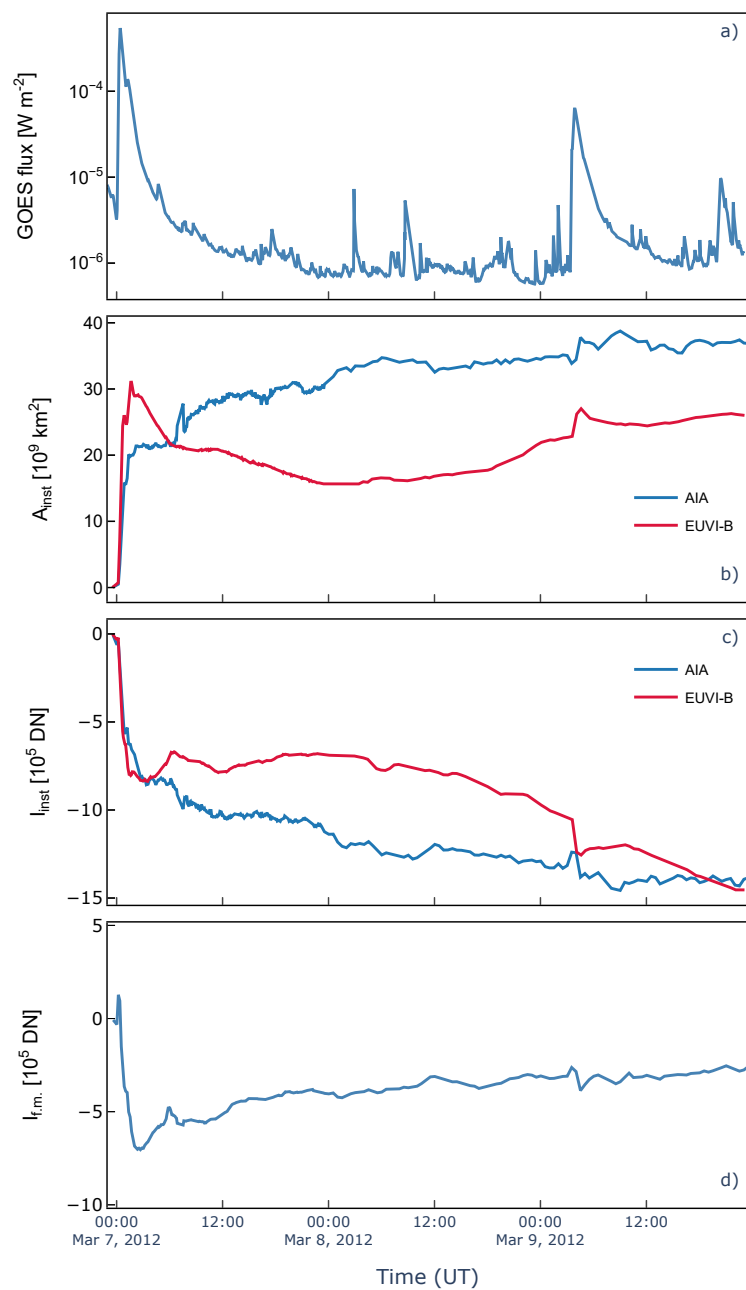


Figure 6-14: Same as in Fig. 6-10, but for event on 2012 March 7. EUVI data is from STEREO-B.

### 6.5.3 2012 June 14

The results for the 2012 June 14 case are shown in Figure 6-15. What is immediately striking is the enormous discrepancy in the behavior of the curves obtained with the instantaneous dimming masks of [SDO/AIA](#) and [STEREO-A/EUVI](#) (panels *b* and *c*). The latter shows a complete recovery, while the former shows an incessant growth of the dimming.

The 2012 June 14 event shows artifacts related to the differential rotation procedure that caused the dimming near the solar limb. By changing the observational approach, i.e., restricting the observation to the region inside the fixed mask (panel *d*), it is possible to see that the behavior of the corresponding intensity curve has a similar trend to the instantaneous brightness obtained with [STEREO-A](#). A full recovery is registered at about 03:40 UT, which is followed by an oscillating behavior of the average brightness.

Looking at the original images, one can conclude that there is some dynamic in [AR](#) and in its surroundings that make the interpretation of this event challenging. This complex dynamic could be related to ongoing reconnection activity, but to prove this would require further analysis, which is beyond the scope of this article. The oscillating behavior of the brightness evolution within the fixed mask supports this interpretation, as dimming regions form throughout the course of the full 72-hour period.

Also, the source [AR 11504](#) is very close to a coronal hole. This makes things more complicated, being partially responsible for the detection of darkening in the western part of the image, mainly because bright loops that covered the [CH](#) before the CME disappeared during the eruption, as seen in Figure 6-16. In addition, jet-like features are also observed at the edge of the [CH](#), indicating ongoing interchange reconnection.

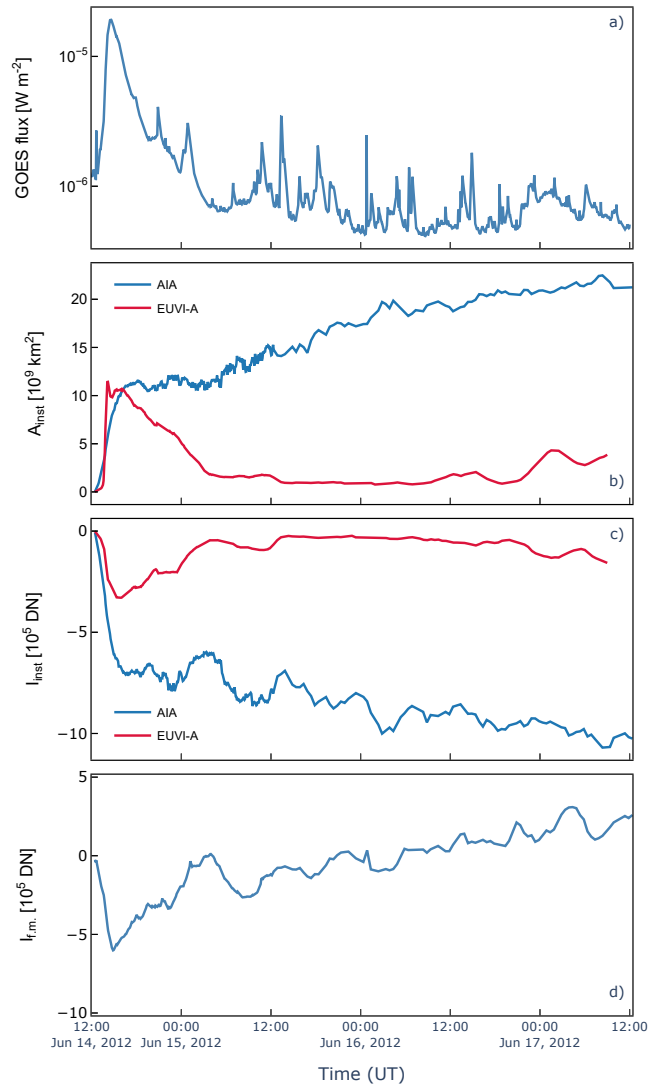


Figure 6-15: Same as in Fig. 6-10, but for event on 2012 June 14.

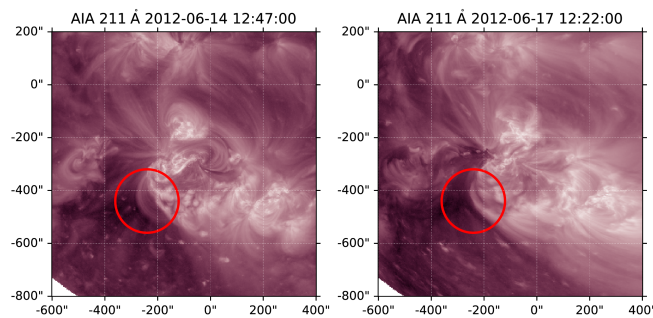


Figure 6-16: Comparison of the dimming region observations at the start and at the end of the time range (June 14 - June 17). The coronal hole can be seen after disappearing loops (in red circle), being included into the dimming detection.

### 6.5.4 2019 March 8

The results for the 2019 March 8 event are shown in Figure 6-17. Data from [STEREO-A/EUVI](#) were not available for the entire analysis duration but only for approximately 48 hours. For this case, the [GOES](#) class is low (C1), but the flare is associated with a broad range of phenomena typical for eruptive flares (see Section 4.5.1), and it occurred during a period of solar minimum.

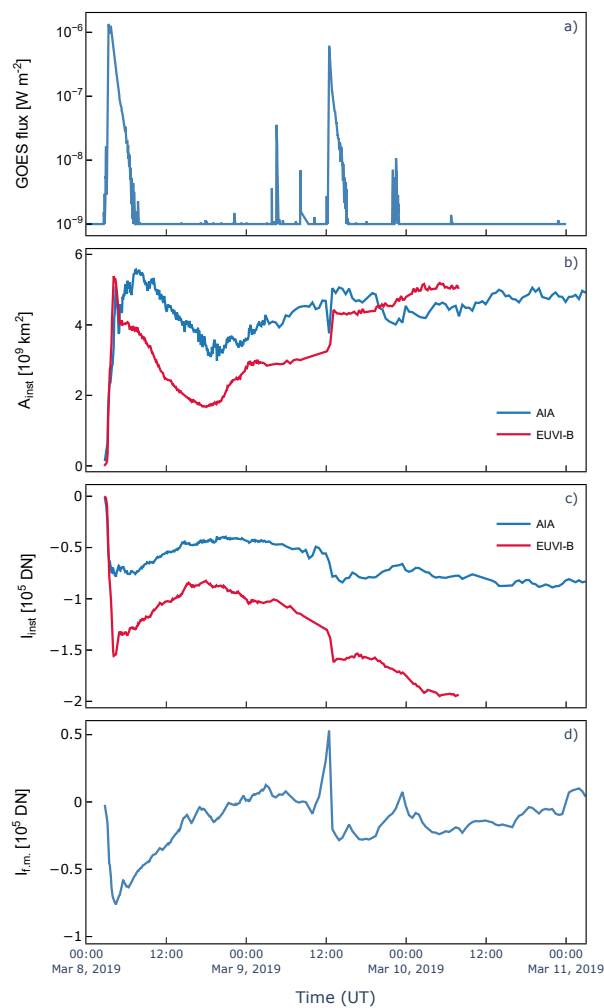


Figure 6-17: Same as in Fig. 6-10, but for event on 2019 March 8 (International Women’s Day event). For the comparison with [STEREO-A](#) data, there is no available information for the third day of the analysis.

In this case, the instantaneous brightness and area from [AIA](#) and [EUVI](#) show similar behavior and neither of them shows recovery. The situation is different with

the fixed mask brightness curve (Fig.6-17-d), where the bright emission of the second flare is followed by a decrease in the total brightness, which recovers over a short period (about 17 hours). In reviewing the original AIA images in both 211 Å and 193 Å growing loops appear to occur, especially in the western region, and it is concluded that the main recovery mechanism for these dimming regions might be simple loop refilling.

An interesting observation in this case is related to the application of the pixel boxes (see Fig. 6-18) used to study the recovery trend of the southern secondary dimming. The average brightness of pixel boxes 1, 2, 3, and 4, shown in Fig. 6-18 LBR image is plotted in Figure 6-19.

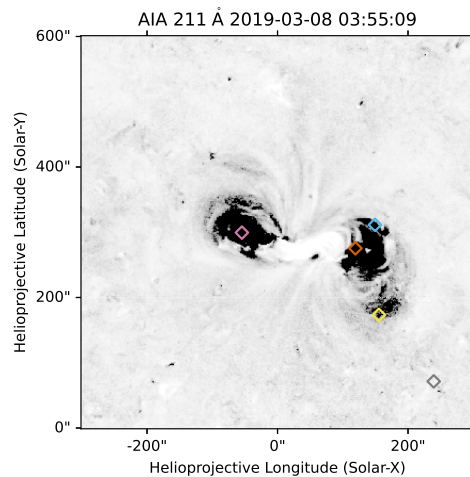


Figure 6-18: 2019 March 8, 04:25 UT. Five boxes of size 3x3 pixels are located on top of the LBR image. The colormap is in logarithmic scale to better visualize the darkest pixels. *Box 1*: yellow marker. *Box 2*: pink marker. *Box 3*: red marker. *Box 4*: light blue marker. *Reference Box*: gray marker. The reference box is located outside the dimming region, in a quieter region of the solar corona.

Box 1 shows a linear, gradual recovery, returning to pre-event intensity within about 17 hours. Box 2, on the other hand, is located in the middle of the eastern region of the dimming and shows a rapid recovery (about 8 hours) followed by a nearly stationary intensity value until the second flare occurs. These results appear to be consistent with what was suggested by Attrill et al. [2008]: It was possible to identify a long-lived part within the dimming did not recover by the end of the data set, implying that the internal recovery is slower than the process occurring

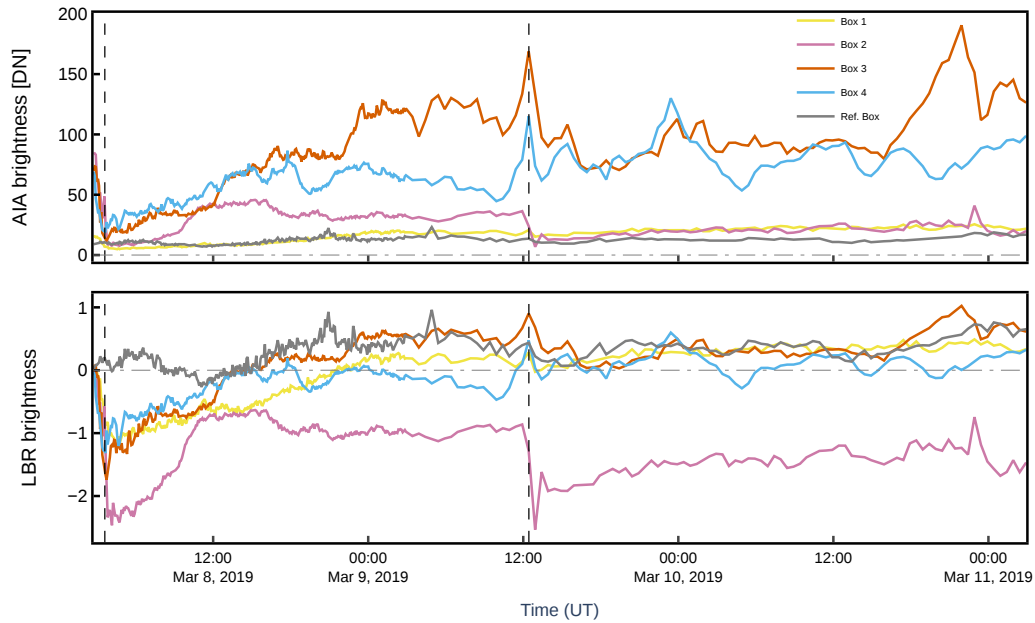


Figure 6-19: Comparison of the brightness behavior for each of the chosen  $3 \times 3$  pixel box shown in Fig.6-18. The dashed vertical lines mark the peak time of each flare. The dashed horizontal line marks the 0-brightness level. Top: intensity evolution from the original [AIA](#) images. Bottom: intensity evolution from the [LBR](#) images.

in the peripheral regions. Therefore, box 2 could be part of a core dimming, while box 1 belongs to the periphery. In addition, boxes 3 and 4 are located within the western region of the dimming and at the boundary of the dimming region with the solar corona. Box 3 shows a similar intensity decrease (maximum decrease) as the pink marker, which does not recover. In this case, the rapid recovery may be due to the flare ribbons sweeping across this dimming. The situation is similar for box 4. Finally, another box is placed on the image that is outside the dimming region and far from the coronal hole to the east and the other [AR](#) to the northeast of the region of interest. This box is used as a reference to compare the brightness inside and outside the dimming region.

### 6.5.5 Comparison of the events

The four selected events differ greatly from each other based on the intensity of the flare, their location on the solar disk, the speed of the associated CME, their

duration, and their occurrence with respect to the solar cycle. The different sequence of flares in the analyzed time interval also plays a role in the diversification of the individual cases. For example, from 2011 September 6 three flares/CMEs occur within 48 hours, while from 2012 June 14 only one long-lasting flare associated with a CME occurs. As a result of these many factors, the intensity behavior and area behavior of the coronal dimming are different for each case studied. Fig. 6-20 shows the intensity curves of the fixed mask in the left column and the instantaneous area evolution of the dimming within the fixed mask in the right column for all four events. The gray rectangles mark the flare time interval and the time shown is limited to 24 hours to focus on the behavior of the first flare/CME in each data set, without the interference from subsequent eruptions.

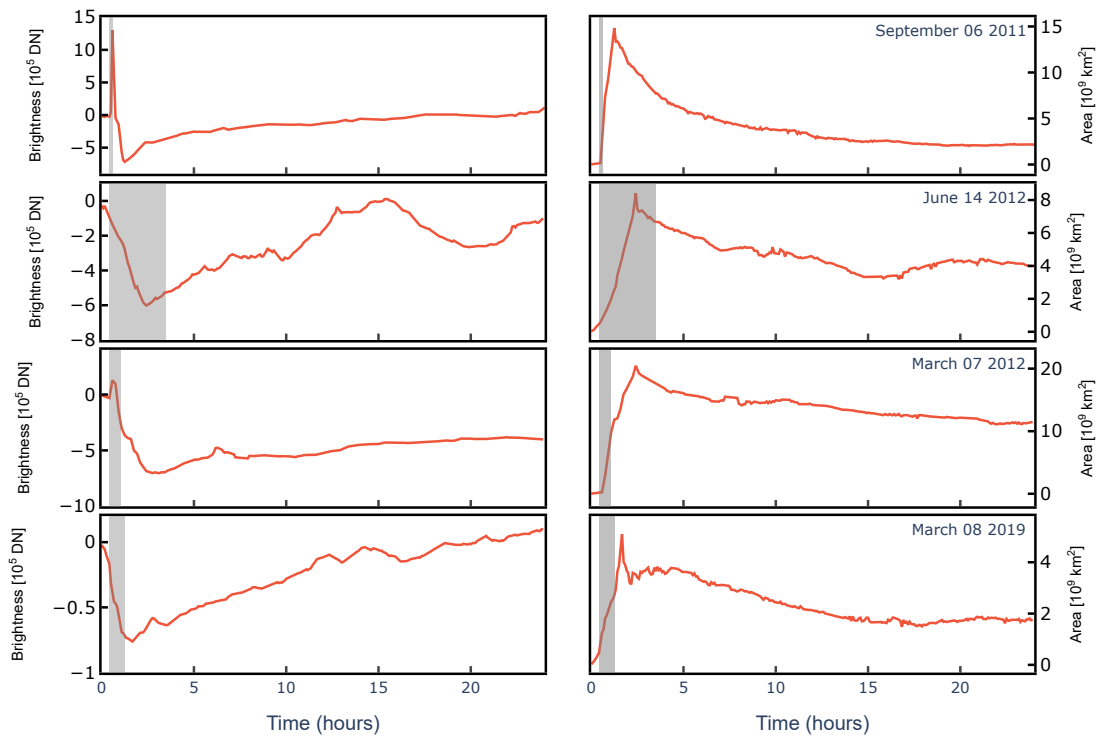


Figure 6-20: Evolution over 24h of the average brightness of the fixed mask region (left) and of the instantaneous area of the dimming contained within the fixed mask (right) for each of the events. The shaded rectangle marks the GOES flare duration.

In all four cases, the intensity decreases dramatically when the flare starts. This

decrease does not occur in the same way for all events. 2011 September 6 and 2012 March 7 events initially show an increase in brightness due to the presence of the bright flare emissions within the fixed mask regions, while 2012 June 14 and 2019 March 8 events show a slight decrease in intensity a bit earlier than the onset of the flare. After the minimum intensity value is reached, recovery begins. Reinard and Biesecker [2008] analyzed the period of increasing/decreasing area and brightness of the dimming in their statistical work. They found that about a quarter of the events showed a two-step evolution of the intensity and/or area recovery curves.

In our study, the intensity of the fixed mask shows a two-stage behavior in all four cases, with a steep initial recovery slope followed by a flatter recovery. This is particularly evident in the 2011 September 6 case, but this trend is also observed in the other three cases. As for the instantaneous dimming area within the fixed mask, this behavior is less striking, due in part to the 2019 March 8 case, where a very sharp drop in area is followed by a milder recovery trend.

Of the four cases examined, three show full recovery of both brightness and area before 24 hours have passed, while one does not return to pre-event intensity levels within the 72-hour analysis period.

## 6.6 Discussion

This project aims to build upon existing knowledge of dimming recovery mechanisms and to devise and evaluate techniques that can enhance our comprehension of the physical processes underlying dimming recovery.

Four case studies were analyzed to conduct this research. Limitations were identified in terms of observation time for events near the western or eastern limb, as they are subject to distortions and thus artifacts due to differential rotation. New approaches have been identified to limit the analysis to very specific regions, by applying the mask of maximum dimming area to the whole data set or by analyzing pixel boxes located in the regions of interest within the dimming. The results obtained show similarities to the work of Attrill et al. [2008] and Vanninathan et al., with the identification of core dimmings, which show a slow and sometimes never-

ending recovery, and the secondary dimmings, located farther from the center of the eruption, being the first regions to recover with an almost linear, gradual trend.

The first of the developed approaches is based on applying the same mask to all dataset images. The application of this mask allows us to greatly limit the effects of artifacts associated with the de-rotation of the image to correct for differential solar rotation.

In addition, by limiting the region of interest, we can partially filter out the influence of other dimmings that results from other events originating from the same AR. When different dimmings occur at similar locations but propagate in different directions, the fixed mask approach provides better discrimination of the two areas of influence. However, when additional events partially overlap with the location of the initial one, this has an impact on the intensity evolution (e.g., see 2011 September 6/7 events).

Applying this method to analyze the four cases studied, we found that in three of them (2011 September 6, 2012 June 14, 2019 March 8) the total intensity fully recovered within the fixed mask region before 24 hours passed. This result is consistent with Reinard and Biesecker [2008]. As for the mechanism behind dimming recovery, it appears that all four events studied recovered by shrinking the outer boundaries. However, in the case of the 2012 March 7 event, some brightenings were observed that could indicate a replenishment of the plasma emerging and re-connecting inside the dimming region. However, a distinction between the behavior of core dimmings and secondary dimmings is to be taken into account [Attrill et al., 2008, Vaminathan et al.] and here the second approach comes into play.

The second approach focuses on analyzing a fixed small sub-region of the entire image by selecting a small box of size 3x3 pixels. It is then possible to monitor the mean intensity evolution of specific regions and compare different parts within the same dimming region to detect local differences.

The advantage of this approach is its flexibility and the ability to distinguish and better observe core dimming regions and secondary dimming regions. Care must be taken as ongoing dynamics around the pixel box must be monitored. Indeed, recovery of mean intensity within the box may be the result of loops covering the region

of interest. Nevertheless, this approach can be integrated with recent studies and help identify core dimming regions [for example [Dumbović et al., 2021](#), , where the authors did not distinguish between core and secondary dimmings] and investigate their recovery time (in accordance to [Attrill et al. \[2008\]](#) and [Vanninathan et al.](#), where core dimming regions do not recover until the end of their analysis time interval).

In the future, a systematic statistical analysis could be useful to quantify the recovery time of coronal dimmings using the fixed mask approach, while the pixel box method could be useful to understand the dynamics of different types of dimmings, possibly by integrating the knowledge of previously analyzed events, but with a stronger focus on the recovery phase of the dimming rather than its early evolution.

## 6.7 Conclusions

We examined recovery time for four coronal dimming events using EUV data both from SDO and STEREO satellites. Three of the four cases showed complete recovery within 24 hours post-flare/CME eruption. The major mechanism for recovering appears to be shrinking from the outermost boundaries inwards. Brightness recovery exhibited a two-step trend, with an initial steeper and quicker segment followed by a slower one. Core dimmings persisted beyond the analysis period, indicating prolonged non-recovery, while peripheral regions (secondary dimmings) showed complete recovery.

The two proposed approaches have been tested and validated in this study, proving their importance for the analysis of the recovery phase of coronal dimmings. The first method allows to follow the dimming region development, mitigating the artifacts and derotation effects. The second, complementing, method offers insights into the differential behaviors of core and secondary dimmings.

# Chapter 7

## Relation to the CME direction

This chapter is dedicated to answer research question Q3:

*How is the evolution and morphology of dimmings connected to the early propagation direction of CMEs?*

### 7.1 Project summary

In this study, we investigate the relation between the spatiotemporal evolution of the dimming region and both the dominant direction of the filament eruption and CME propagation for the 28 October 2021 X1.0 flare/CME event observed from multiple viewpoints in the heliosphere by Solar Orbiter, [STEREO-A](#), [SDO](#), and [SOHO](#).

We present a method for estimating the dominant direction of the dimming development based on the evolution of the dimming area, taking into account the importance of correcting the dimming area estimation by calculating the surface area of a sphere for each pixel. To determine the propagation direction of the flux rope during early CME evolution, we performed 3D reconstructions of the white-light CME by graduated cylindrical shell modeling ([GCS](#)) and 3D tie-pointing of the eruptive filament.

This research is published in *Astronomy & Astrophysics* [[Chikunova et al., 2023](#)].

As a separate part, we also demonstrate the first version of (Dimming InfeRred Estimate of CME Direction) [DIRECD](#) method on the 1 October 2011 case study.

This method, formulated through the combination of findings from the initial study, is designed to estimate the initial direction of CME propagation by analyzing the morphology of coronal dimmings. This study was accepted for publication in *Astronomy & Astrophysics* [Jain et al., 2023].

## 7.2 Literature review

In this study, we investigate an important aspect of the dimming–CME relationship, namely the evolution of the dimming area (projected onto the 2D image plane) and how it relates to the directivity of the different parts of the erupting magnetic structure, namely the filament and the CME (both reconstructed in 3D using multi-viewpoint observations).

In recent years, numerous studies have focused on the 3D reconstruction of CMEs using dual and triple coronagraphic observations from the STEREO and SOHO spacecraft. The tie-pointing method [Mierla et al., 2008, Byrne et al., 2010, Liewer et al., 2011, Liu et al., 2010] identifies the same feature in images taken from different viewpoints and triangulation has been used to determine its position in 3D [Thompson, 2006]. Epipolar geometry [introduced by Inhester, 2006] has also been used to better constrain the tie-points to a given straight line and helps to reduce the matching problem. Another approach involves the reconstruction of an associated filament located within the CME flux rope and containing the material of the CME bright core [Illing and Hundhausen, 1986, Li and Zhang, 2013]. Liewer et al. [2009] used stereoscopic tie-pointing for the 19 May 2007 erupting filament reconstruction and compared the filament appearance prior to and after the eruption to reveal the place of magnetic reconnection. Susino et al. [2014] combined a 3D reconstruction of the erupting filament with a polarization ratio technique [Moran and Davila, 2004] for a better determination of the CME kinematics. To examine the 3D development of CMEs resulting from nonradial filament eruptions, Zhang [2021] used a cone model, placing the apex of the cone at the source region of an eruption instead of the Sun center as in the traditional cone models. A different approach is forward modeling from coronagraphic observations. Graduated cylindrical shell (GCS) mod-

eling [Thernisien et al., 2006a, Thernisien, 2011] of CMEs uses a strongly idealized flux rope structure composed of two cones, representing the legs of a CME, and a torus-like structure connecting the two cones, making a so-called “hollow croissant” shape. These and other methods of reconstructing the CME direction are described and compared in detail in Mierla et al. [2010]. All of them require the presence of at least two simultaneous observations of the CME from different vantage points and significantly depend on the presence of the STEREO satellite.

We look closer at the source region of an event and try to understand whether or not the single-point observations of the coronal dimmings can indicate the initial direction of the erupting filament and/or CME propagation. Coronal dimmings can be observed in great detail by different EUV instruments 2.5, revealing crucial information about the early configuration of the eruption and its initial parameters [e.g., case studies by Möstl et al., 2015, Temmer et al., 2017, Dissauer et al., 2018a, Heinemann et al., 2019, Dumbović et al., 2021, Thalmann et al., 2023]. The observations of dimmings provide us with various possibilities to monitor the CME low coronal signatures, increasing the chances of detecting geoeffective eruptions at a very early stage, that is, even before their front reaches the FOV of coronagraphs.

### 7.3 Data and event observation

The event under study took place on 28 October 2021 from NOAA active region (AR) 12887. The CME and filament eruption were associated with an X1.0 flare (start: 15:17 UT, peak: 15:35 UT) at heliographic position S28W01. The event also produced a globally propagating EUV wave and a ground-level enhancement (GLE), which were studied independently by different research groups [Devi et al., 2022, Hou et al., 2022, Papaioannou et al., 2022, Klein et al., 2022]. The three-dimensional velocity of the plasma outflows associated with the event was estimated in Sun-as-a-star spectroscopic observations by Xu et al. [2022] resulting in  $v \approx 600 \text{ km s}^{-1}$ . A data-driven simulation of the eruption was presented by Guo et al. [2023]. The authors discuss their finding of good agreement with observations when including the morphology of the eruption, the kinematics of the flare ribbons, EUV radiation,

and the two components of the EUV waves predicted by the magnetic stretching model.

The CME appeared as a halo in the SOHO/LASCO C2 field of view starting at 15:48 UT. Figure 7-1 shows simultaneous observations of its evolution by SOHO/LASCO C2 (left panels) and STEREO-A EUVI COR2 coronagraphs (right panels). The brightest part of the CME (yellow arrows) propagates southward for LASCO, while STEREO/COR1 shows the signatures of a three-part CME structure [Illing and Hundhausen, 1986, Low and Hundhausen, 1995, Vourlidas et al., 2013, Cheng et al., 2017, Howard et al., 2017, Veronig et al., 2018]. Around 16:36 UT, we observe a second propagating part, namely a flank of the CME (red arrows). The LASCO catalog<sup>1</sup> reports a plane-of-sky speed of the CME of about 1500 km s<sup>-1</sup>.

The EUV low coronal signatures of the CME were simultaneously observed by the SDO/AIA and STEREO-A/EUVI, separated by 37.6° in longitude at this date (see Figure 7-2). The AIA instrument provides images of the Sun in seven EUV filters with a pixel scale of 0.6 over a FOV of about 1.3R<sub>⊙</sub>. EUVI observes the Sun through four EUV passbands over a FOV up to 1.7R<sub>⊙</sub> providing images with a pixel scale of 1.6.

For our analysis of coronal dimmings, we used AIA 193 Å filtergram images with a 12s cadence. The selection of 193 Å for observing and extracting coronal dimmings is motivated by the systematic study of Dissauer et al. [2018a], demonstrating that this wavelength effectively captures both the quiet and AR coronal plasma that is expelled during CMEs. The same images effectively resolve the filament propagation and we matched them with 2.5 min cadence sequences of 195 Å EUVI data for a 3D reconstruction of the filament. Both data series were calibrated and corrected for differential rotation to a reference time of 28 October 15:05 UT using the Sunpy library [The SunPy Community et al., 2020] in Python. The detection and analysis procedures were also developed using Python.

Figure 7-3 gives an overview of the event as observed by the AIA original 193 Å filter showing direct images (left) and processed base-difference images (right). The coronal dimming, eruptive filament, and EUV wave are well observed in base

<sup>1</sup>[https://cdaw.gsfc.nasa.gov/CME\\_list/](https://cdaw.gsfc.nasa.gov/CME_list/)

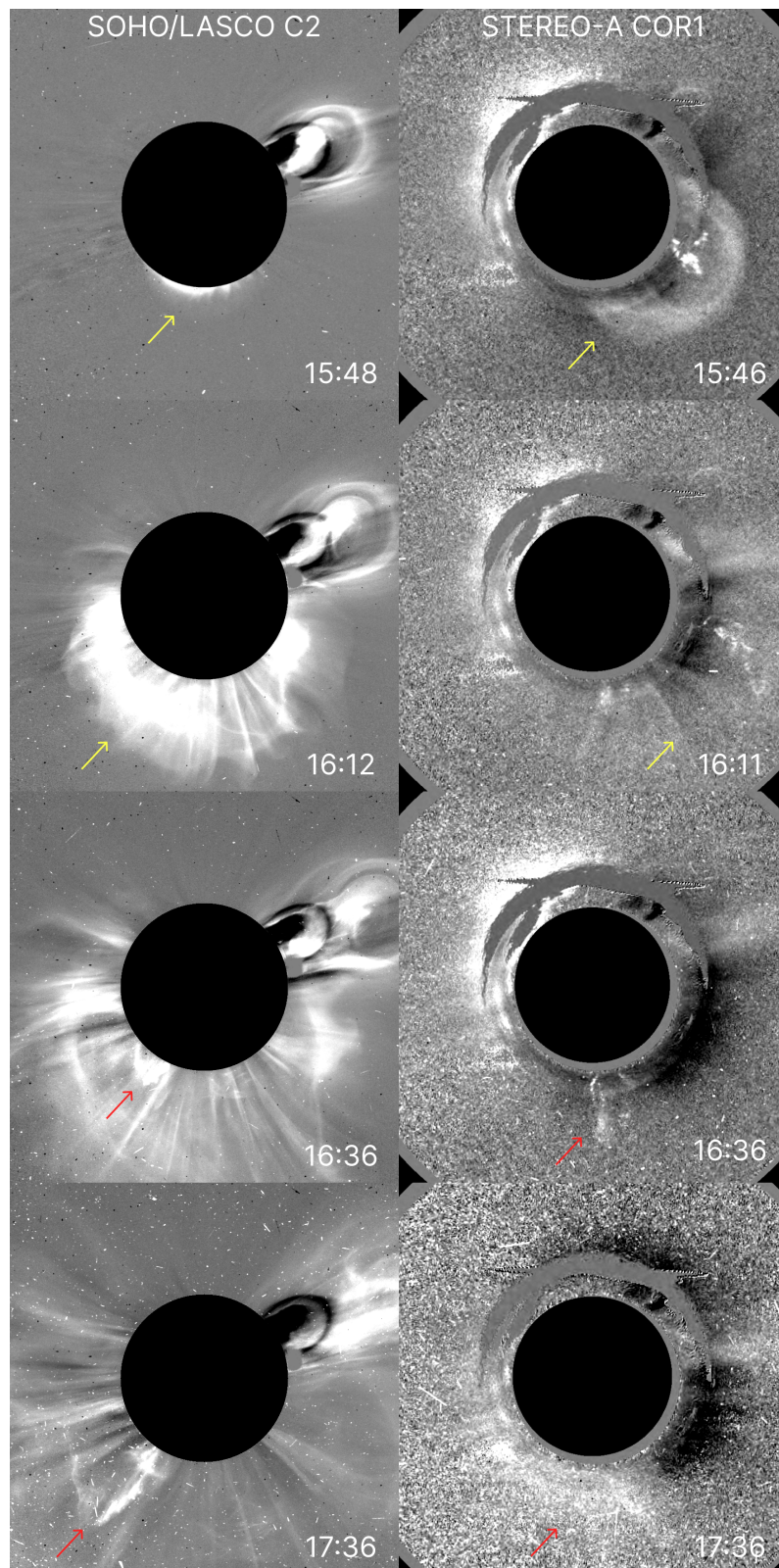


Figure 7-1: Snapshots of coronagraphic observations using JHelioviewer [Müller et al., 2017]. Left column: SOHO/LASCO C2 white-light base difference images. Right column: White-light base difference images from STEREO-A COR1. Yellow arrows indicate the CME and red arrows show the propagated leg of the filament eruption at time steps 16:36 UT and 17:36 UT, respectively.

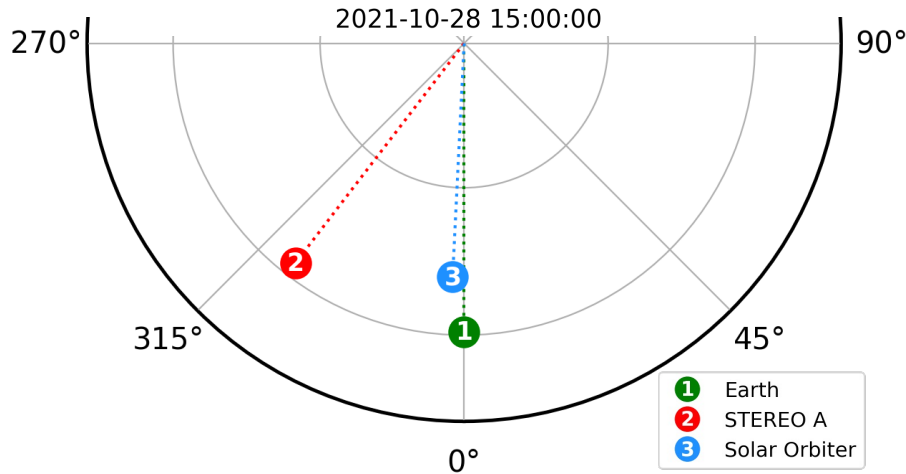


Figure 7-2: View of the ecliptic plane showing the various spacecraft positions on 28 October 2021. SDO is located along the Sun–Earth line, while the STEREO-A and Solar Orbiter spacecraft are positioned  $37.6^\circ$  and  $2.8^\circ$  to the east, respectively. The image was generated using the Solar-MACH tool [Gieseler et al., 2023].

difference data, originating at longitudes close to the disk center for the line of sight (LOS) from Earth. The dimming is detected from the earliest time steps, starting around 15:05 UT with quasi-circular propagation, which later dominates mostly to the southeast, reaching the neighboring active region. The filament eruption starts around 15:10–15:12 UT, propagating to the southeast and reaching off-limb at 15:47 UT. Another part of the filament is visible off-limb around 15:35 UT to the west. The EUV wave appears around 15:28 UT and is visible on the solar surface up to 15:50 UT, showing an initially quasi-circular propagation, with dense fronts toward the north (second and third panels, see also the accompanying movie). Devi et al. [2022] presented a full analysis of the EUV wave evolution, reporting a maximum speed of its propagation of about  $700 \text{ km s}^{-1}$ .

The associated X1.0 flare was also detected in hard X-rays (HXR) by the Spectrometer Telescope for Imaging X-rays (STIX) [Krucker et al., 2020] on board Solar Orbiter. During the 28 October 2021 event, Solar Orbiter was close to the Sun–Earth line ( $2.8^\circ$  east) at a distance of 0.80 AU from the Sun. As this was an X-class flare, STIX detected significant emission in both the thermal and nonthermal energy ranges, enabling insight into a broader range of the flare process. STIX uses a pair of grids to indirectly reconstruct images of the HXR photons by producing Moire fringes that differentially illuminate different detector pixels. STIX images (Fig-

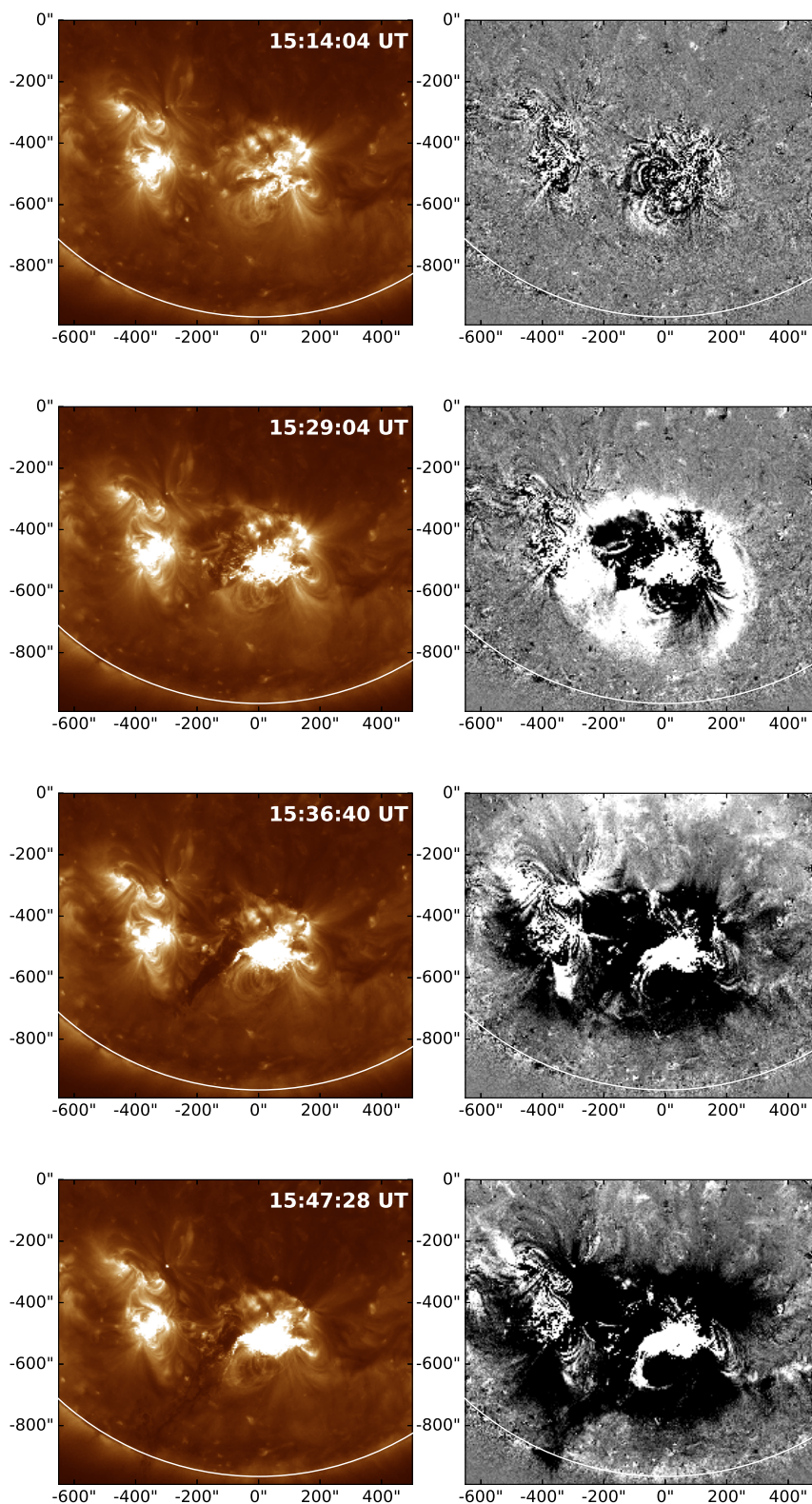


Figure 7-3: Overview of the 28 October 2021 event, showing the dimming evolution and eruption of the filament in AIA 193 Å. Left: Direct images. Right: Corresponding base-difference images. Four time steps are shown, while the full evolution of the event can be found in the accompanying movie.

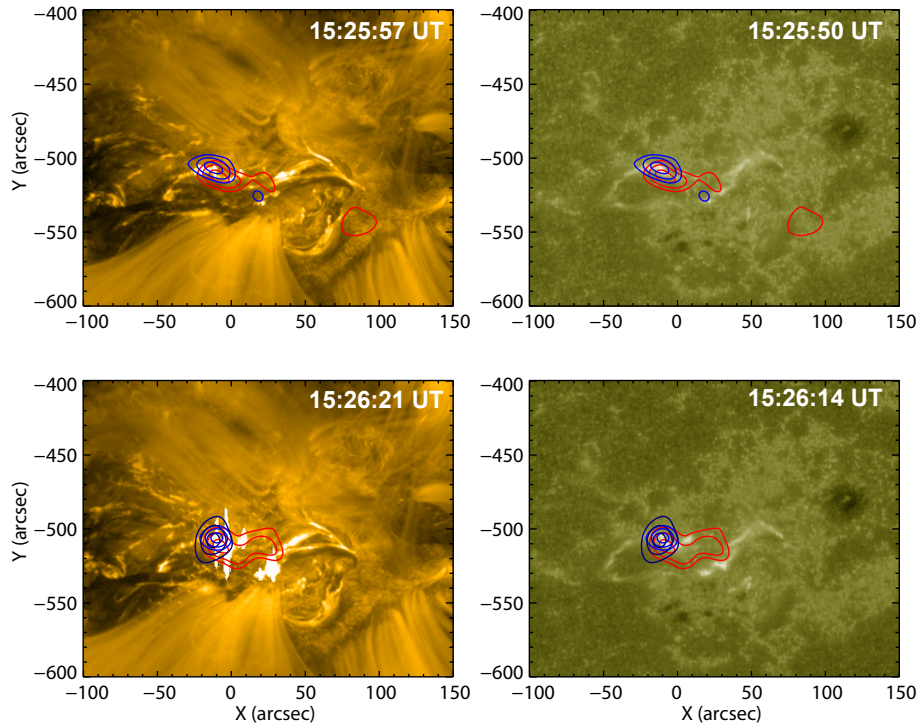


Figure 7-4: *STIX* images showing 50%, 70%, and 90% contours for energy bands 4 – 10 keV (red), 15 – 25 keV (blue), and 25 – 50 keV (dark blue). The *STIX* contours are rotated to the point of view of *SDO* and overlaid on *AIA* images. The *AIA* images are shown for two different time steps: Top row - 15:25 UT, and Bottom row - 15:26 UT; and at two different *AIA* filters: Left column - 171 Å, and Right column - 1600 Å.

ure 7-4) were produced in three energy bands: the thermally dominated 4–10 keV, the intermediate 15–25 keV, and the nonthermal 25–50 keV band. For context and comparison, these were overlaid on *SDO AIA* 171 Å and 1600 Å images after being rotated to the *SDO* point of view. In order to accurately perform the rotation of the *STIX* sources, estimates of the X-ray source heights must be made. For the nonthermal footpoints, we used the equation in [Aschwanden et al. \[2002\]](#) relating energy to height. For the thermal sources, we assumed a semi-circle connecting the two ribbons. As there was no *STIX* aspect solution for this time, we applied a small adjustment of  $[-40, 5]$  to align the *STIX* sources with the *AIA* ribbons. The *STIX* observations were corrected for the difference in light travel time (94.58 s) from the Sun to Solar Orbiter and from the Sun to Earth.

## 7.4 Methods and results

Our approach consists of three steps. First, we developed a method for estimating the dominant direction of the dimming development (Section 7.4.1). Second, to determine the direction of parts of the erupting structure and flux rope during the early CME evolution, we performed 3D reconstructions of the eruptive filament (Section 7.4.2) and a 3D CME reconstruction using GCS modeling (Section 7.4.3). Finally, we studied the relation between the dominant dimming direction, the direction of the filament eruption, and the CME (Section 7.4.4).

### 7.4.1 Coronal dimming

Here, we present the method we used to estimate the dominant direction of the dimming development, which includes the dimming segmentation (Section 7.4.1), followed by our assessment of the evolution of the dimming area with the help of a sector analysis (Section 7.4.1).

#### Dimming segmentation

For the dimming segmentation and analysis, we used a sequence of AIA 193 Å maps within the 15:00-15:57 UT time range. For the algorithm, we created base-difference images, indicating the absolute change in the intensity values with respect to the pre-eruptive coronal state. We applied an automated detection technique based on thresholding and region growing to these images (as described in Sec. 4.2.5). First, we extracted all pixels with intensity dropping below  $-30$  DN. The type of data preprocessing and the thresholding level were selected empirically by qualitatively checking images during different development stages of the dimming in order to also include distant parts (see Figure 7-3). Second, we used 30% of the darkest pixels of this set as seeds for the region-growing algorithm to connect all the separated parts of the dimming region. To minimize the noise, we used median filtering with a  $3 \times 3$  kernel.

We obtained the dimming masks for all the time steps from 15:05 to 15:57 UT and united them into one cumulative dimming mask. This mask contains all pixels

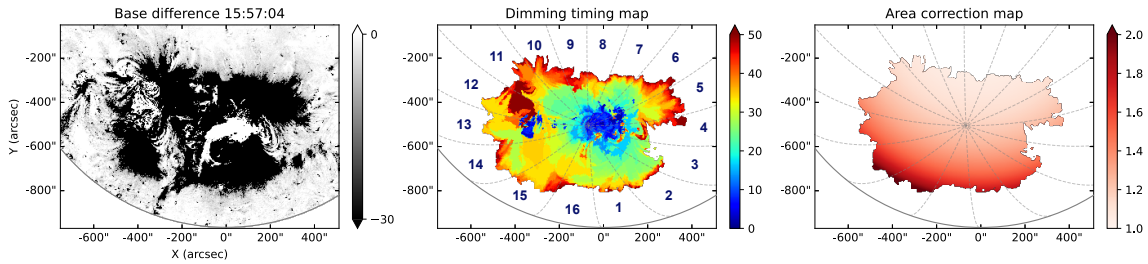


Figure 7-5: Total area of the dimming region. Left: Base-difference map at the time of maximal dimming extent at 15:57 UT. Middle: Cumulative timing map of the whole dimming extraction, color-coded in minutes from 15:05 UT. Right: Same dimming map, but each pixel shows the ratio of its area to the area of the average pixel in the center. Dashed curves and numbers represent the chosen sectors.

that have been flagged as dimming pixels during the chosen time range. However, pixels of the erupting filament also show up in the mask as they have a similar intensity level. To exclude these pixels, we used the same mask in a base-difference image at one of the last time steps (when the filament was already gone) and refined the mask by deleting all the pixels with intensity above  $-30$  DN, subsequently filling the gaps within the contour. The final cumulative dimming mask (Figure 7-5) was then used for further dimming analysis.

### Dimming sector analysis

To determine the main direction of the dimming expansion, we designed a spherical polar coordinate system centered at the source region and divided the solar surface into 16 angular sectors of  $\Delta\phi = 22.5^\circ$  width (counted counterclockwise). The source location was defined in accordance with the center of the flare emission contours from STIX (Figure 7-4). For each sector, we further calculated the surface area of all pixels (see Sec.4.4).

Figure 7-5 (left panel) shows the dimming region at the times close to its maximal extent [similar to the end of the dimming impulsive phase described in Dissauer et al., 2018b], the cumulative dimming map, where each pixel is color-coded according to the time of its first detection (middle panel) and also according to the ratio of each corrected pixel area to the average (square) pixel area in the center of the Sun (right panel) for each sector.

We define the main direction of the overall dimming development as the middle

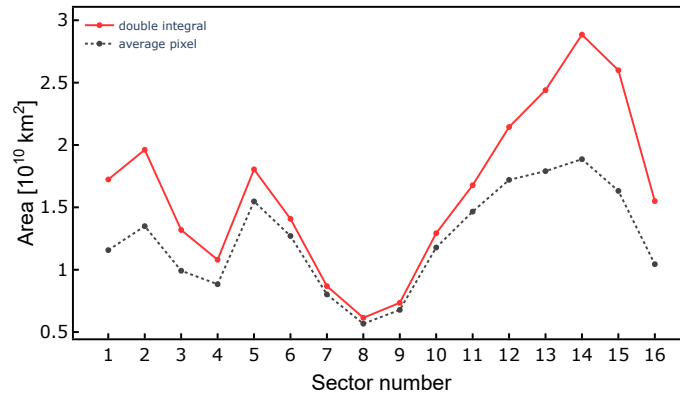


Figure 7-6: Dimming area on the plane (dashed black curve) and over the surface (red curve) calculated for each sector.

longitude of the sector with the largest area. To estimate the uncertainty in the area due to a specific threshold used for the dimming segmentation, we additionally applied a  $\pm 5\%$  change to the threshold level and computed the mean values and corresponding standard deviation of the dimming area in each sector. The resulting dimming areas for the different sectors together with the uncertainty ranges are shown in Figure 7-7.

Figure 7-6 shows the difference between calculating the area from the number of pixels and considering their spherical representation. We can see that the suggested calibration creates significant changes in the total area values. For this reason, we use the derived spherical projections of the pixels to derive the area parameter.

As can be seen, the dimming dominates in the southern sectors with the largest area in sector no. 14. Furthermore, analyzing the cumulative timing map (the middle panel in Figure 7-5), we observe a two-stage evolution of the dimming region. Initially, the dimming spreads around the source, as indicated by the presence of blue and green pixels indicating evolution until  $\approx 15:35$  UT. Subsequently, the southeastern part of the dimming region becomes more pronounced and dominates the overall expansion.

In this particular case, the use of one cumulative mask in the dimming segmentation instead of tracking the dimming region over time helps to include the dimming areas hidden by other coronal structures at different stages of their evolution; for example, those initially covered by flare loops. At the same time, we note that the sector analysis can also be successfully implemented on a sequence of dimming

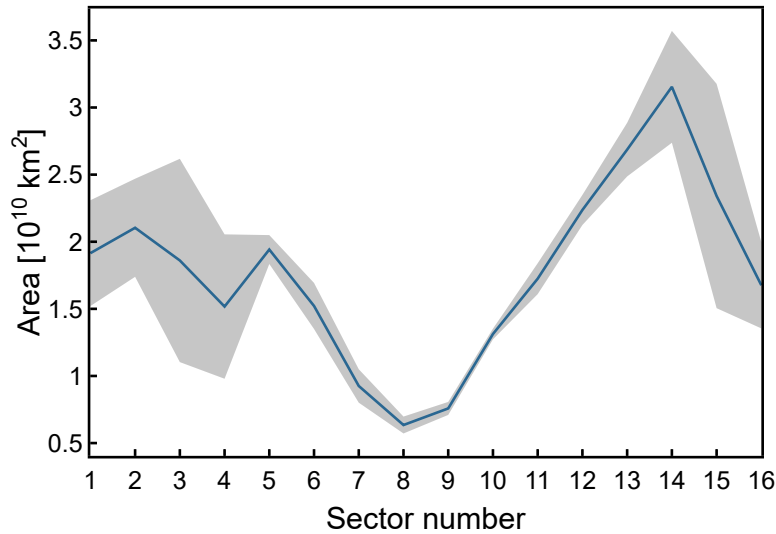


Figure 7-7: Dimming area calculated for each sector in the full cumulative map. The shaded band indicates the error estimation using different threshold levels used for the dimming segmentation. The largest dimming area is in sector no.14.

masks, which allows us to track the time evolution of characteristic dimming parameters (e.g., area/brightness/leading edge) during different parts of the dimming evolution with respect to the eruption source. The dominant direction of the dimming propagation can then be defined as the sector with the fastest dynamics; for example, with the highest area change rate for the particular time step.

## 7.4.2 Eruptive filament

Here, we present 3D reconstructions of the eruptive filament (Section 7.4.2) and study its kinematics (Section 7.4.2).

### Three-dimensional reconstruction of the erupting filament

The dense and cool filament material is usually thought to be embedded in the dips of a magnetic flux rope, where the magnetic tension force keeps it in balance against the gravitational force. Therefore, the erupting filament can be analyzed in order to locate the inner part of the erupting flux rope during the early stages of the eruption. The use of dual-point EUV observations from [SDO](#) and [STEREO-A](#) allows us to perform the 3D reconstruction of the eruptive filament using an epipolar geometry approach (see full description in [Inhester \[2006\]](#), [Podladchikova et al. \[2019\]](#)). A

point on the object and two observer positions create an epipolar plane, which, by definition, is seen as an epipolar line in each of the observer's images. At each time step, we manually identify the highest points of the filament from [SDO/AIA 193 Å](#) images and match these with the corresponding points on the epipolar lines located in [STEREO-A/EUVI 195 Å](#) data. Thus, for every point of the filament there is only one degree of freedom in placing the corresponding matching point in another image. In order to enhance the contrast of the erupting or moving features, we use base-difference images along with direct images for feature identification.

Figure 7-8 shows a sequence of [SDO/AIA 193 Å](#) (top) and [STEREO-A/EUVI 195 Å](#) (bottom) maps, where the colored markers highlight the propagation of the erupting filament based on matching the same features on both [AIA](#) (blue) and [EUVI](#) (red) images. We track the filament growth using direct images for the time steps 15:05-15:32 UT (a) and base-difference images for 15:35-15:57 UT (b). For each point of the filament, we obtain coordinates in [HEEQ](#) coordinate system, defining its position in 3D.

We then determine the orthogonal projections of the reconstructed 3D points on the solar surface—which reflect the projected direction of the filament eruption—using the following equation:

$$\begin{aligned} X_P &= \frac{R_{Sun} \cdot X}{\sqrt{X^2 + Y^2 + Z^2}}, \\ Y_P &= \frac{R_{Sun} \cdot Y}{\sqrt{X^2 + Y^2 + Z^2}}, \\ Z_P &= \frac{R_{Sun} \cdot Z}{\sqrt{X^2 + Y^2 + Z^2}}. \end{aligned} \tag{7.1}$$

Here,  $X_P$ ,  $Y_P$ , and  $Z_P$  denote the 3D cartesian coordinates of the orthogonal projection on the solar surface,  $R_{Sun}$  is the solar radius, and  $X$ ,  $Y$ , and  $Z$  are the 3D coordinates of the reconstructed points of the filament.

Figure 7-9 represents the connection of the low coronal signatures (left panels) with the CME propagation further out (right panels). The left panels show snapshots of [SDO/AIA 193 Å](#) (top, 15:49:52 UT) and [STEREO-A/EUVI 195 Å](#)

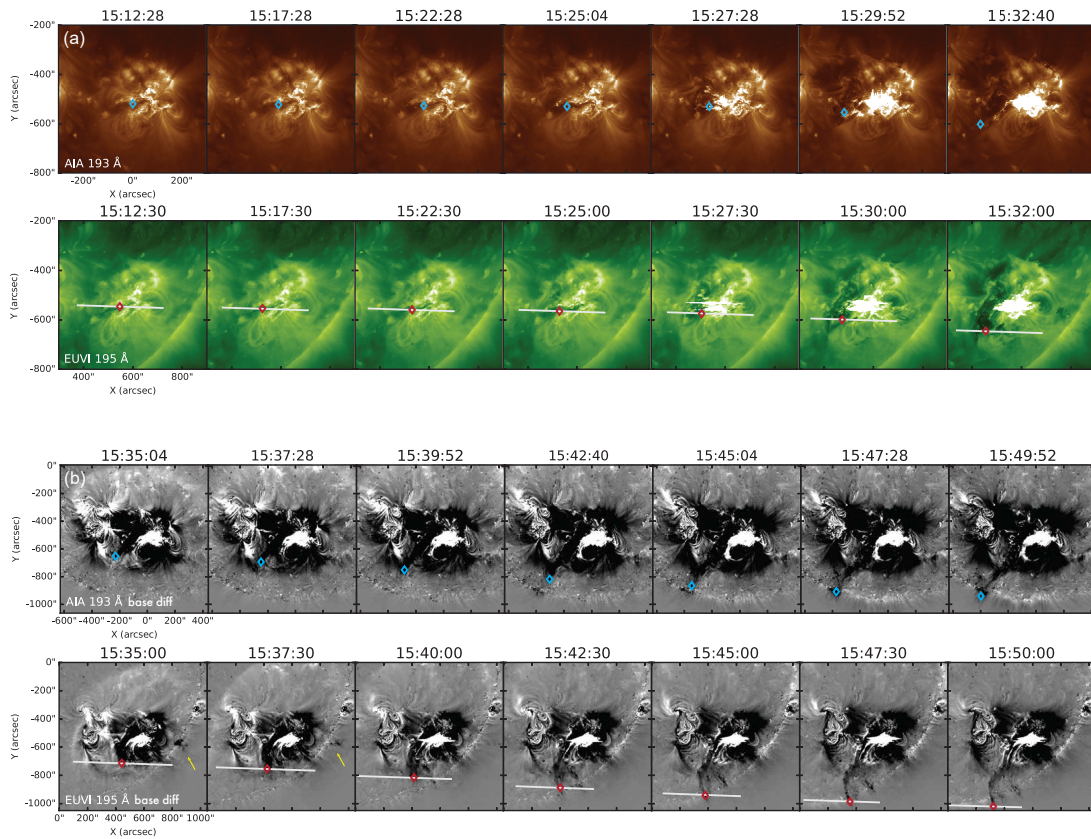


Figure 7-8: Evolution of the erupting filament between 15:12 and 15:32 UT in [SDO AIA 193 Å](#) (top) and [STEREO-A EUVI 195 Å](#) direct images (a) and between 15:35 and 15:50 UT in base difference images (b). Blue markers show the upper tip of the filament observed by [SDO AIA](#), and red markers indicate the matching points from the [STEREO-A](#) vantage point. Epipolar lines are shown in white. The yellow arrows indicate another, central part of the filament eruption. We note that the image scale of panels (a) and (b) is different. An animation of the reconstructions of panel (b) can be found in the accompanying movie.

(bottom, 15:50:00 UT) with matching points of the eruptive filament (blue and red, respectively, the same points as in Figure 7-8b) and their orthogonal projections on the surface (green for AIA and yellow for EUVI). A white grid shows the dimming sectors on the solar surface. Solar EUV images show only the filament projections along the LOS of the spacecraft, and, as can be seen from Figure 7-9 (left panels), the LOS and the orthogonal (which is independent of the viewpoint) projections of the filament are located in different sectors. At the same time, the distance between the LOS and orthogonal projections is significantly greater for STEREO-A (bottom) than for SDO (top), as STEREO-A, positioned  $37.6^\circ$  east of Earth, reveals the location of the event in the southwestern quadrant of the hemisphere, whereas SDO gives a view of the event in the southern hemisphere close to the disk center. We note that the orthogonal projections of the filament are located in the sector with the largest area of dimming (no.14).

The right panels of Figure 7-9 show later observations of the CME propagation from SOHO/LASCO C2 (top) and STEREO-A COR2 (bottom) coronagraphs. This visual representation shows that the filament trajectory appears differently from these two viewpoints. The filament propagates almost as a straight line in the view from SDO. At the same time, STEREO observations reveal that a part of the filament structure decelerates and falls back to the solar surface.

To gain a deeper understanding of the filament trajectory, we calculate its deflection from the radial direction in 3D space. To do so, we define a linear fit to the filament points constrained to the first reconstructed point with the lowest height. The angle between the linear fit and the radial direction is  $54^\circ$ . SDO/STEREO observations allowed us to reconstruct only one “leg” of the filament (the eastern one), whereas the coronagraphic observations indicate another filament part, appearing earlier. Xu et al. [2022] also revealed this double structure of the eruption and estimated the velocities of the other part. We additionally analyzed the deflection of the filament propagation from radial by splitting the angle of deflection into two components. To this end, we projected the linear fit and radial direction onto equatorial and meridional planes and calculated the 2D angles between projections in each plane. Both vectors (dark red and black lines, respectively) with their pro-

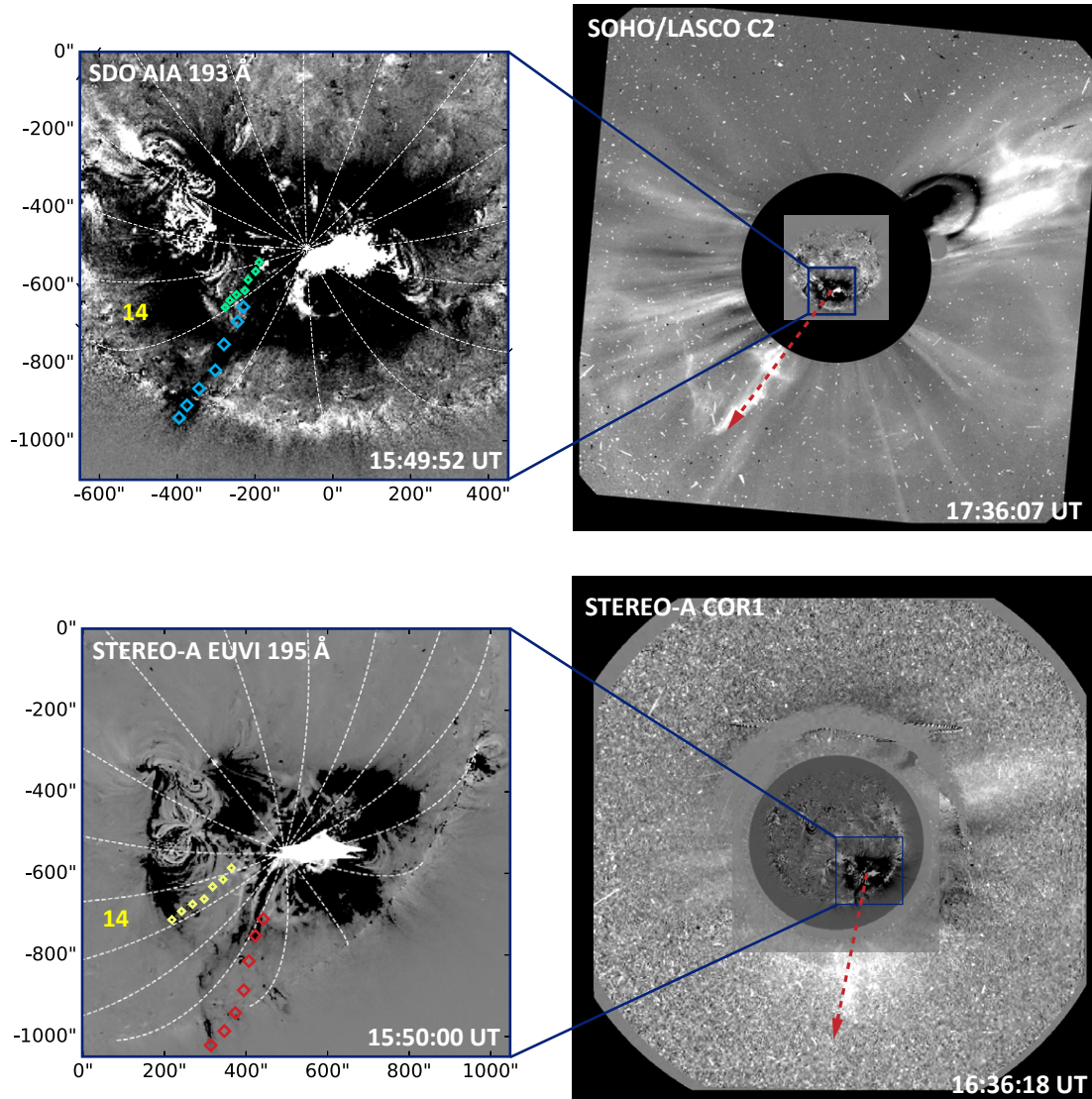


Figure 7-9: Connection of the low coronal signatures with the CME propagation further out. Left panels: **SDO AIA 193 Å** and **STEREO-A EUVI 195 Å** base-difference images with reconstructed matching points of the eruptive filament (blue and red, respectively) and their orthogonal projections on the surface (green and yellow). The sector with the largest area of dimming is marked by its number (no.14). Right panels: Propagation of the CME seen from **SOHO/LASCO C2** (top) and **STEREO-A COR2** (bottom) coronagraphs at later time steps. Red arrows indicate the filament development as the bright substructure of the CME. Coronagraphic observations were obtained using JHelioviewer [Müller et al., 2017].

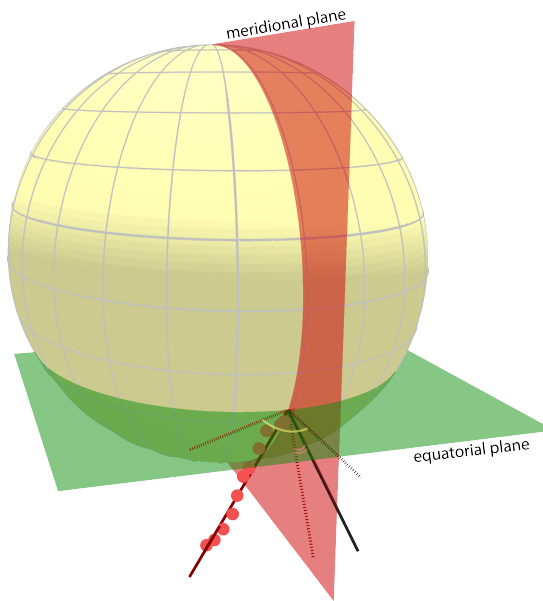


Figure 7-10: Three-dimensional model of the Sun with the reconstructed filament. Red points show the reconstructed heights of the filament. The dark red line shows a linear fit and the red dashed lines represent projections onto equatorial (green) and meridional (red) planes. The black line indicates the radial direction, and the dashed black line shows its projection onto the equatorial plane. Equatorial and meridional planes both go through the intersection of the linear fit with the solar surface (filament origin). The radial direction is located in the meridional plane by definition. For clarity, the heliocentric coordinates grid is shown in gray. The inclination angle from the radial in the equatorial plane is shown as a yellow arc, and the inclination angle in the meridional plane is shown as two red arcs, respectively.

jections (dashed lines) are presented in Figure 7-10. We derive that the linear fit to the filament points is declined from radial by  $64^\circ$  (yellow arc) to the east and  $by 38^\circ$  (two red arcs) to the south.

### Kinematics of the erupting filament

From the 3D reconstructions of the upper tip of the filament identified in each frame, we estimate its height and speed. Figure 7-11 shows the time evolution of the height (a), speed (b), and acceleration (c) of the filament in comparison to the GOES soft X-ray (SXR) flux evolution of the associated flare and its change rate (d) and the STIX hard X-ray count rates at different energies (e). In the panel (a) we show the resulting filament heights with black dots, while the error

bar represents a  $\pm 5$  pixel shift in the [AIA](#) images in finding the matching point along the epipolar line. To obtain the filament velocity and acceleration profiles, we first smooth the filament height data and obtain the first and second direct numerical derivatives. The smoothing technique which [Podladchikova et al. \[2017\]](#) present and extend to nonequidistant data optimizes between two criteria in order to find a balance between data fidelity and smoothness of the approximating curve [see also the applications in [Veronig et al., 2018](#), [Dissauer et al., 2019](#), [Gou et al., 2020](#), [Saqri et al., 2023](#)]. Using the derived acceleration profile, we then interpolate to equidistant data points (solid line in (c) panel) based on the minimization of the second derivatives and reconstruct the corresponding velocity (solid line in (b) panel) and height (solid line in the (a) panel) profiles by integration. We also obtain the errors of kinematic profiles by representing the reconstructed filament height, velocity, and acceleration as an explicit function of original errors of filament height–time data (blue shaded areas). The dots in panels (b) and (c) give the first and second time derivatives obtained directly from the height measurements. As the eruption evolves, the upper filament parts start to become fainter from around 15:40 UT. Therefore, at later stages of observation, we may not be able to accurately identify the highest points of the filament, but instead only the lower ones located further inside it. Consequently, the measured heights and velocities at these times may be underestimated. In panel (d), we calculate the change rate of the [GOES SXR](#) flux as the first-order numerical derivative and smooth by a forward-backward exponential smoothing method [[Brown, 1963](#)]. As can be seen from [Figure 7-11](#), the height of the filament increases up to  $312 \pm 5$  Mm within 37 minutes with a maximum speed of  $\approx 250 \text{ km s}^{-1}$ . The filament shows a slow rise from 15:12 until 15:25 UT, and then rapidly accelerates to  $\approx 366 \text{ m s}^{-2}$ , reaching 52 Mm at 15:28 UT with a further gradual increase in speed. The peak of acceleration is cotemporal with peaks in the high-energy [STIX](#) curve and a rapid increase in [GOES](#) flux. The overall evolution of the filament speed profile precedes the associated flare flux: the flare started at  $\approx 15:17$  UT, reached its maximum around 15:35 UT, and then entered a phase of decline.

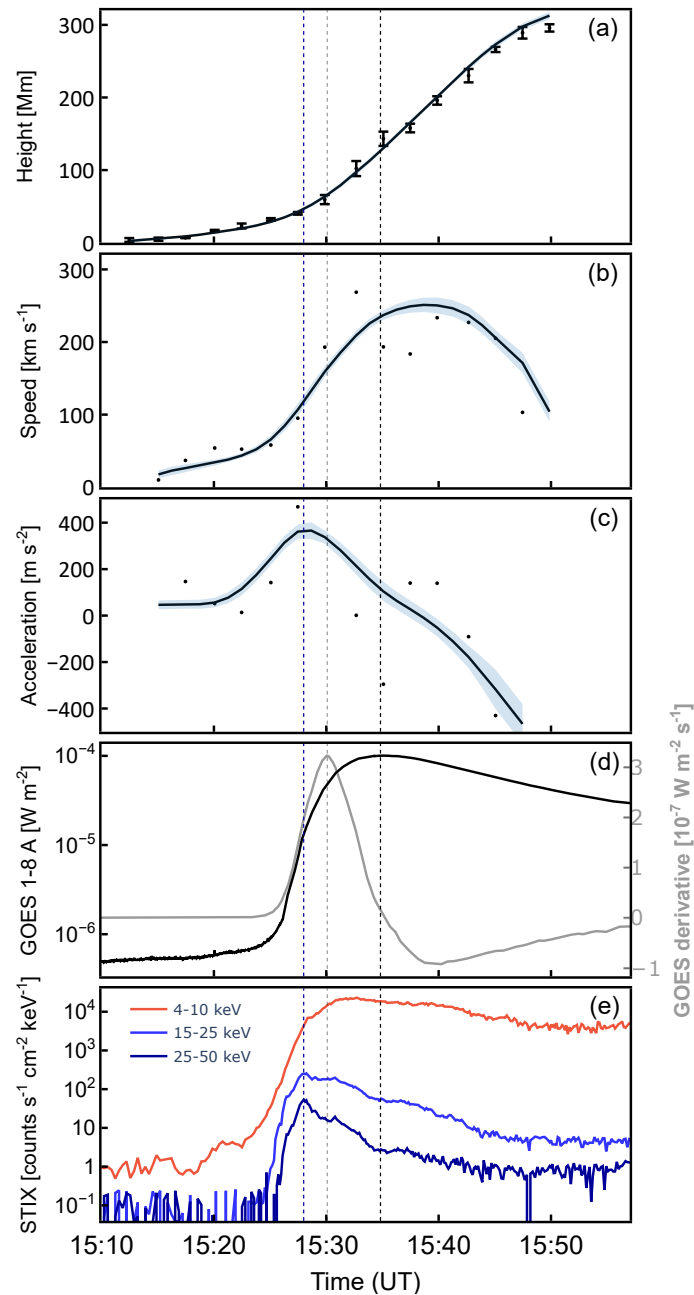


Figure 7-11: Kinematics of the erupting filament and associated flare evolution. (a) Height estimations of the filament (black markers). The error bar presents the five-pixel shift in finding the matching point along the epipolar line. The corresponding black solid line indicates the smoothed height–time profile. (b) Speed and (c) acceleration of the filament obtained by numerical differentiation of height–time data (dots) and smoothed profiles (lines). The shaded areas give the error ranges. (d) GOES 1 – 8 Å SXR light curve (black curve, left Y-axis) and the corresponding change rate (gray curve, right Y-axis). (e) STIX HXR count rates at 4–10 keV (red), 15–25 keV (blue), and 25–50 keV (dark blue) energies. The vertical dashed lines mark the peaks in the 25–50 keV HXR curve (dark blue), the GOES SXR flux (black), and its derivative (gray).

### 7.4.3 GCS reconstruction of the CME

We also analyzed the associated 3D CME structure and direction using the **GCS** model applied to the **SOHO/LASCO** C2 and **STEREO-A/COR2** coronagraph data, which have a **FOV** out to  $6R_{\odot}$  and  $15R_{\odot}$ , respectively. The top panels in Figure 7-12 show the observations of the CME by **STEREO-A COR2** (left) and **SOHO/LASCO C2** (right) coronagraphs. The bottom panels show the best fit (green mesh) resulting from the **GCS** 3D flux rope model when requiring that the boundary of the **GCS** model flux rope match the outer edge of the CME shape in **COR2** (left) and **LASCO** (right) white-light images.

We obtain the following parameters of this reconstruction: heliocentric longitude  $lon = 357^{\circ}$ , heliocentric latitude  $lat = -30^{\circ}$ , height corresponding to the apex of the croissant  $h = 6R_{\odot}$ , tilt of the croissant axis to the solar equatorial plane  $tilt = 15^{\circ}$ , half-angle measured between the apex and the central axis of a leg of the croissant  $\alpha/2 = 60^{\circ}$ , and aspect ratio  $r = 0.5$ . The footprint positions of the croissant are located at  $[299^{\circ}, -46^{\circ}]$  and  $[55^{\circ}, -14^{\circ}]$ . As can be seen from Fig.7-12, the CME according to **GCS** reconstructions propagates almost radially in the southeastern direction.

### 7.4.4 Relationship between dimming, filament, and CME directivity

Using the Python code provided in von Forstner [2021], we plotted the **GCS** structure on the 3D model of the Sun to compare it with the coronal dimming. Figure 7-13 reveals a match between the total dimming region (blue contour) and the reconstructed shape and direction of the CME, represented by the **GCS** croissant (green mesh). Notably, the dimming contour precisely aligns with the inner portion (blue mesh) located between the two footpoints of the **GCS** croissant. Our tracking of the dimming region extends from 15:00 UT up to 15:57 UT, while the CME structure was reconstructed for 16:12 UT. Assuming the CME propagates without deflection during this time span, our observations strongly suggest a spatial association between these features. To investigate this association more thoroughly, we compare

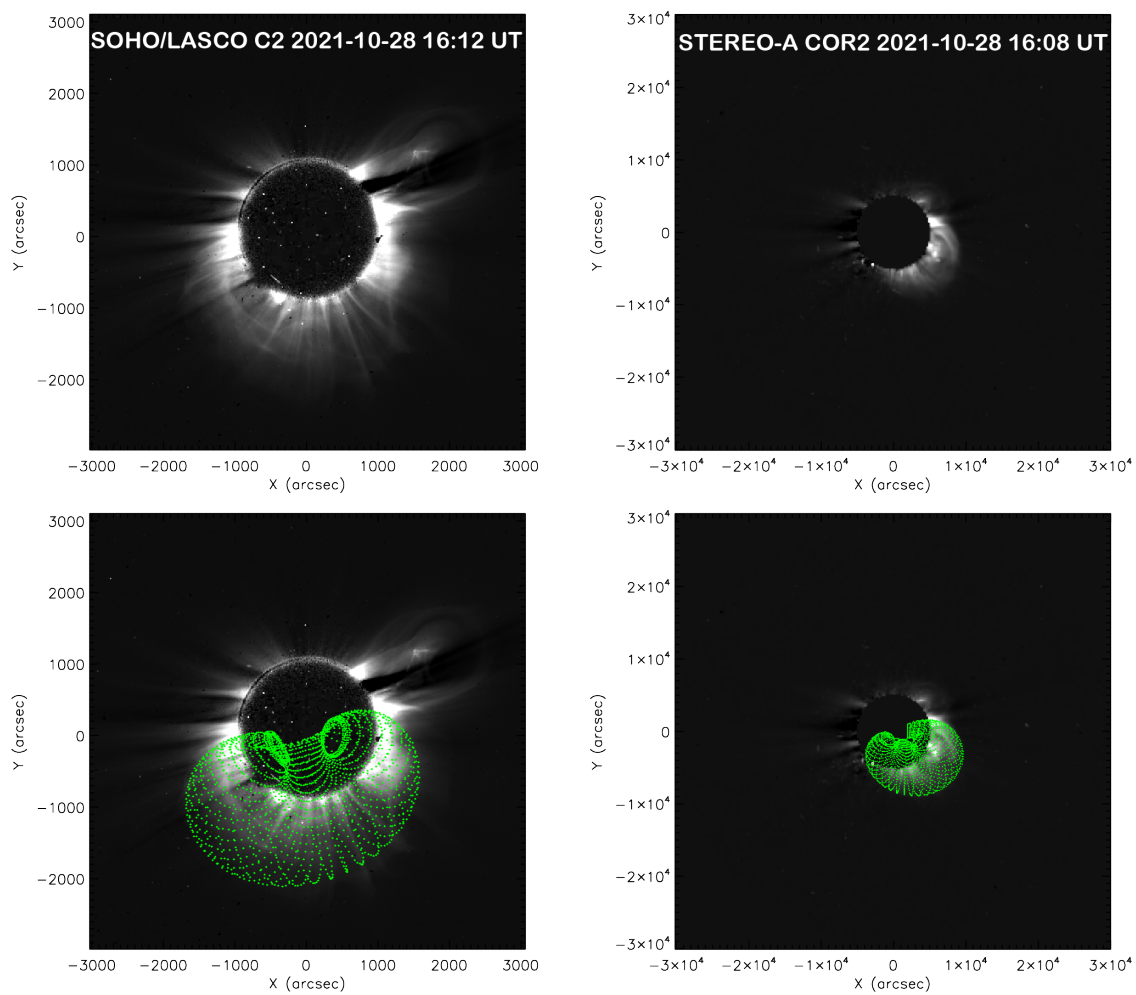


Figure 7-12: Observations of the CME by [SOHO/LASCO C2](#) (left) and [STEREO-A COR2](#) (right) coronagraphs with the [GCS](#) reconstructions (green mesh).

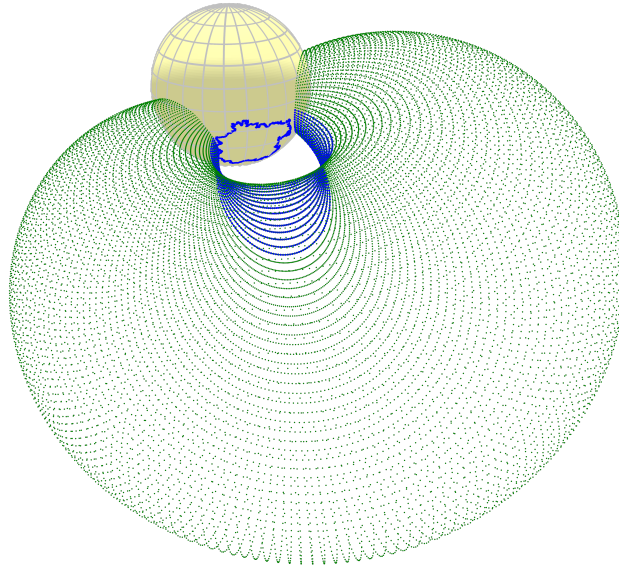


Figure 7-13: Three-dimensional model of the Sun with the **GCS** croissant (green mesh with blue inner part) and coronal dimming (blue contour).

both structures on the solar surface using the orthogonal projection of the inner part (the closest one to the solar surface) and the location of the primary axis of **GCS**.

Figure 7-14 shows an **AIA** 193 Å image with the total cumulative dimming area (blue contour) and the projected inner part of the **GCS** reconstruction (green mesh). We mark the source point of the primary axis of the **GCS** croissant with a green marker. As can be seen, the projections (green) are mainly concentrated in the center of the dimming, which allows us to link the 2D dimming with the 3D CME bubble. To explore this further, we also determined the center of mass of the dimming (red marker in Figure 7-14). For each pixel, we consider its position vector  $\mathbf{r}_i = (x_i, y_i)$  and associate it with a weight  $a_i$ , where  $i = 1, 2, \dots, n$ . The center of mass, denoted  $\mathbf{r}_{\text{cm}}$ , is then computed using the formula:

$$\mathbf{r}_{\text{cm}} = \frac{\sum_{i=1}^n a_i \mathbf{r}_i}{\sum_{i=1}^n a_i}. \quad (7.2)$$

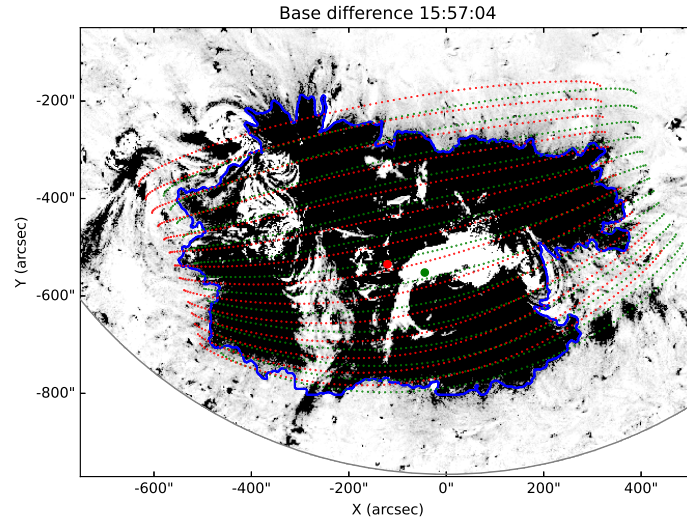


Figure 7-14: AIA 193 Å base difference image showing the dimming region (blue contour) with an overlaid orthogonal projection of the inner part of the GCS bubble (green mesh). The green marker indicates the source location derived from the GCS reconstruction, and the red marker represents the center of mass of the dimming region. The red mesh shows the orthogonal projection of the inner part of the GCS reconstruction, with the source point shifted to the location of the center of mass.

Here, the weight of each pixel corresponds to its area on the solar surface. Consequently, the larger the area, the more significant its contribution to the overall dimming morphology. By analyzing the coordinates of the center of mass, we gain insights into the propagation of the dimming relative to the eruption source (flare coordinate) and can compare it to the primary axis footpoint of the GCS croissant. The center of mass for the dimming has a heliographic longitude of  $lon_{cm} = -8^\circ$  and a heliographic latitude of  $lat_{cm} = -28.8^\circ$  and lies within the sector associated with the dominant dimming propagation. The center of mass is located  $5^\circ$  to the west and  $1.2^\circ$  to the north from the location of the primary axis of the GCS, which is within the uncertainty range of the reconstruction.

We further create a modified GCS croissant with the same parameters but with a shifted primary axis to align with the center of mass of the dimming area. The orthogonal projection of this adjusted croissant is illustrated in Figure 7-14 with red mesh. The full GCS croissant (green) with its shifted version (red) almost align in the SOHO/LASCO 16:12 UT coronagraph image (Figure 7-15). Consequently, the center of mass can serve as an additional validation measure for obtaining the CME direction.

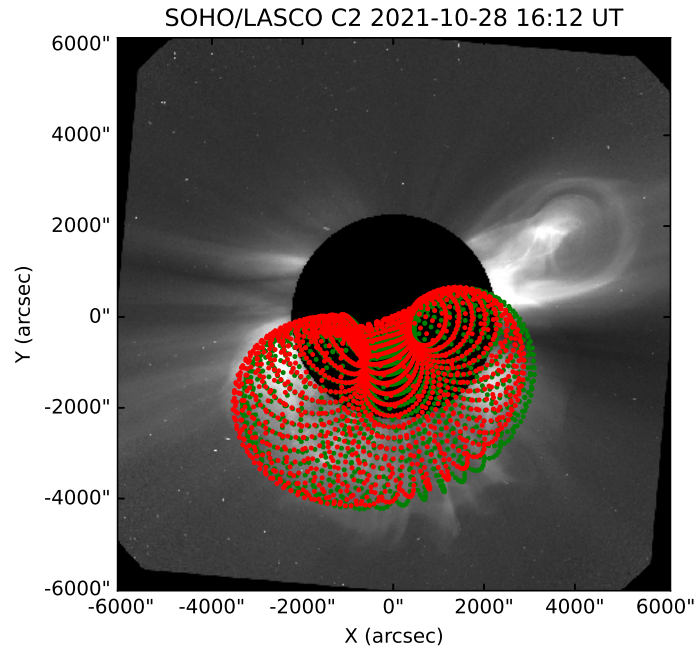


Figure 7-15: Comparison of the two versions of the [GCS](#) reconstruction on the [SOHO/LASCO C2 16:12 UT](#) image of the CME. The green mesh represents the [GCS](#) reconstruction from coronagraph observations, and the red mesh represents the same croissant with a changed location of source chosen by the dimming center of mass.

Figure 7-16 combines all results of our event analysis in one visualization of the studied eruptive features, shown from [SDO](#) and [STEREO-A](#) perspectives: the dimming region (blue contour) with the dominant dimming direction (filled sector), the reconstructed 3D filament motion (red points) with their orthogonal projections (purple points), and the modeled CME according to [GCS](#) reconstructions (the inner part of the [GCS](#) bubble is shown as blue mesh, the main axis as a green vector). The dark red line shows a linear fit to the reconstructed 3D filament points constrained to the first reconstructed point with the lowest height.

With this visual representation, for the first time we can directly compare and relate the dimming evolution, the filament eruption, and the CME propagation to one another:

- The orthogonal projections of the erupting filament, which reflect the projected motion of this structure onto the solar surface, are located in the same sector as the dominant direction of the dimming evolution. Orthogonal projections are independent of the observation point, allowing us to establish a link between

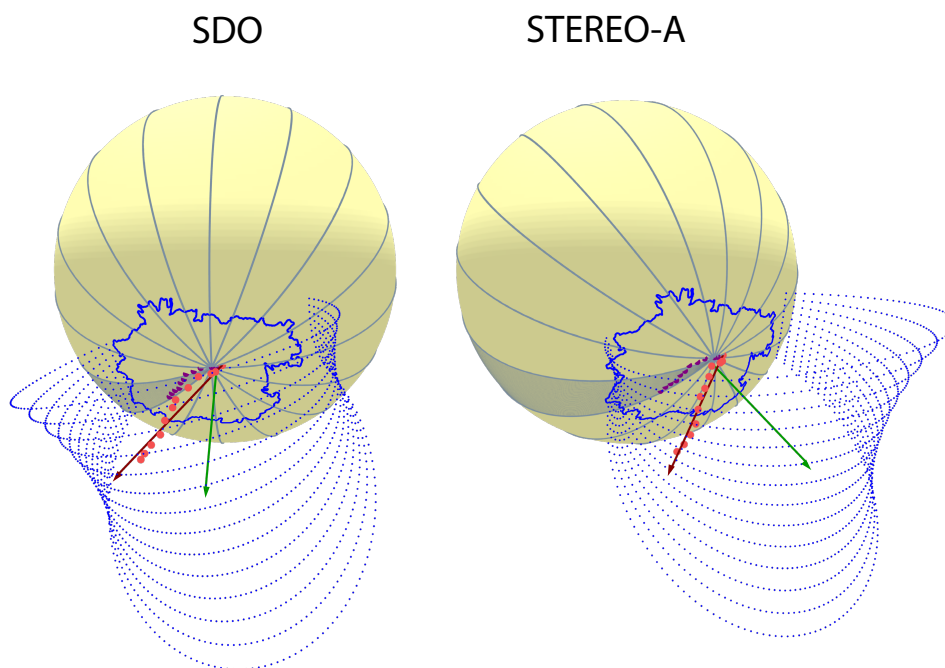


Figure 7-16: Three-dimensional model of the Sun observed from **SDO** (left) and **STEREO-A** (right). The dimming borders are shown with blue contours and the sectors are drawn as light blue lines (the filled area indicates the sector of dominant dimming propagation). Red points mark the reconstructed filament heights, and purple points are their orthogonal projections on the surface. The inner part of the **GCS** reconstruction is plotted as blue mesh. The dark red line presents the straight line fit to the reconstructed filament positions. The green line shows the axis of the CME, which is represented by the **GCS** croissant.

the 3D direction vector and the evolution of the dimming area on the solar surface. Consequently, the morphology of the coronal dimming serves as a reliable indicator of motion of the lower-lying signatures associated with the eruption of the flux rope.

- Despite the prevailing southwestern direction of the dimming propagation, it is important to consider the comprehensive dimming morphology, which also exhibits its widespread evolution around the eruption source. A compelling correspondence can be observed between the total dimming region and the reconstructed shape and direction of the CME. Specifically, the dimming contour reflects the inner part of the **GCS** croissant, indicating their spatial association.
- The angle between the fit to the reconstructed filament height evolution and the apex of the **GCS** croissant is  $50^\circ$ . This value roughly matches with the CME half-width parameter of the **GCS** reconstruction ( $\alpha/2 = 60^\circ$ ), which represents the angle between the apex and the leg of the CME croissant. This similarity suggests that the reconstructed filament can be reasonably associated with the eastern leg of the **GCS** croissant, indicating a notable correspondence between the two structures.

## 7.5 Discussion and conclusions

In this paper, we present a detailed analysis of the different features involved in the eruption of the 28 October 2021 X1.0 event, namely the erupting filament, the CME, and the coronal dimming evolution. Our research involves the reconstruction of both the low-lying filament eruption and the CME structure at a height of  $6R_\odot$  in order to determine the direction of the initial flux rope propagation in 3D space. Simultaneously, we define the dominant propagation of the dimming growth based on an assessment of the evolution of the dimming area and the sector analysis on the solar surface. To compare the directions, we calculated the orthogonal projections of the reconstructed points (both filament and **GCS**), which enabled us to track their motion projected onto the solar surface.

We developed a method to estimate the dominant direction of the dimming development based on our assessment of the evolution of the dimming area using sector analysis. Initially, the dimming expansion spreads symmetrically around the source region; subsequently, it undergoes further development toward the southeast. The sector analysis of the cumulative dimming area clearly indicates that the dominant direction of total dimming growth aligns with one of the southeastern sectors.

As we consider the dimming region on the solar sphere, we introduce a novel technique that involves identifying the surface area for each pixel. This approach effectively minimizes projection effects, as it takes into account the spherical projection of each individual pixel of the dimming area. We made the code for the calculation of the correction publicly available on GitHub.

A filament was observed both by [SDO](#) and [STEREO-A](#) up to  $\approx 312$  Mm in height, which allowed us to reconstruct its evolution in 3D. The erupting filament starts to rise at a slow speed at  $\approx 15:12$  UT, and then rapidly accelerates between  $\approx 15:25$  and  $15:30$  UT, which coincides with a phase during which the flare rises in the [GOES](#) 1–8 Å [SXR](#) flux, while the filament impulsive acceleration occurs co-temporally with the [HXR](#) high-energy hard X-ray emission at 15–25 keV and 25–50 keV (see Fig. 7-11). The maximum speed and acceleration of the erupting filament area  $\approx 250$  km s<sup>-1</sup> and  $\approx 366$  m s<sup>-2</sup>, respectively. A similar filament evolution was also reported in [Devi et al. \[2022\]](#), where the time–distance plots of the filament heights in 2D were used to derive the height and kinematics profiles. These authors also report a nonlinear acceleration at the same range, which they relate to the presence of torus instability in the eruption behavior.

The reconstructed filament heights projected to the solar surface coincide with the dominant direction of the dimming expansion. This allows us, for the first time, to make a direct comparison of the dimming and filament directions within a unified coordinate system. We find that the dimming precisely reflects the propagation of the filament eruption low in the corona.

The significant inclination between the motion of the 3D filament and the radial direction ( $64^\circ$  to the east and  $38^\circ$  to the south) reveals a double structure of the flux rope. Both filament parts are observed as the brightest and densest CME material in

the coronagraph images (Figure 7-9, right panels). By modeling the propagation of the flux rope using GCS reconstruction, we find that the CME primarily propagates radially in the southeastern direction. We obtain a deviation of  $50^\circ$  between the direction of the CME and the erupting filament. This indicates that the portion of the filament used for the 3D reconstruction, which is clearly observed, does not correspond to the apex of the CME flux rope. Instead, it is associated with one of the legs of the flux rope. In addition, the close agreement between the deviation angle value and the half-width parameter of the GCS reconstruction ( $\alpha/2 = 60^\circ$ ) further supports the correspondence between the reconstructed filament and the eastern leg of the GCS croissant.

The strongly nonradial behavior of the erupting filament obtained from the 3D reconstruction may also indicate a pronounced lateral expansion of the flux rope, which contrasts with the assumption of self-similar propagation in the GCS reconstruction of the CME. This would lead to nonradial propagation of the CME leg, even if its apex is propagating radially. Hovis-Afflerbach et al. [2023] also discussed whether the evolution of the filament in the low corona can be used as a predictor of CME direction, as observed in coronagraph data.

We observed distinct signatures of both components of the flux rope in the evolution of the dimming region. While the dominant propagation of the dimming follows a southwestern direction, reflecting the filament evolution, it is important to acknowledge the comprehensive morphology of the dimming, which shows an extensive evolution around the eruption source. Our analysis reveals a compelling relation between the total dimming region and the reconstructed shape and direction of the CME. Specifically, the dimming contour closely aligns with the inner part of the GCS croissant, while the center of mass of the dimming region is situated in close proximity to the projection of the primary axis of the GCS reconstruction, indicating a clear spatial association between the dimming and the CME.

At the same time, in our case study, we do not find the direction of the filament eruption to be directly related to the direction of the CME expansion, evidenced by a significant deviation angle between the reconstructed filament heights and the CME (GCS) axis. The filament material is lying in the lower portion of the expanding flux

rope [Cheng et al., 2014]. With that, we point out that the filament itself cannot always be used as a reliable proxy to predict the main direction of CME propagation.

These findings highlight that the evolution of the dimmings reflects both the direction of a low-lying erupting magnetic structure (filament) and the global propagation of CMEs. Further research efforts need to consider both the dominant dimming direction and the dimming morphology in order to understand the link between 2D dimming information and the initial 3D direction of the CME/flux rope and, therefore enhance our understanding of its early dynamics.

## 7.6 Development of DIRECD method

Our exploration into the relationship between dimming and CME direction paved the way for the creation of the **DIRECD** (Dimming InfeRred Estimate of CME Direction) method. This technique estimates the initial CME propagation direction by analyzing the morphology of coronal dimmings. We describe the full methodology and our first results on the CME modeling from coronal mass ejections in collaborative study [Jain et al. \[2023\]](#). Here we outline only the main aspects of our approach and encourage the reader to follow our paper and the project's future advancements. We show the 1 October 2011 event as an example of the method application.

### 7.6.1 Project summary

Initially, we simulate various CMEs in 3D using a geometric CME cone model [[Zhao et al., 2002](#), [Xie et al., 2004](#), [Mays et al., 2015](#)], adjusting parameters like width, height, source location, and deviation from the radial direction to understand their impact on the CME's projection onto the solar sphere.

Using the developed sector analysis, we identify the dominant direction of dimming evolution. Then we address an inverse challenge to recreate a variety of CME cones with diverse heights, widths, and deviations from radial movement.

Our ultimate goal is to determine which combinations of CME parameters lead to orthogonal projections onto the solar sphere that best match the geometry of the dimming at the maximum of its impulsive phase and allow us to determine the 3D direction of the CME.

### 7.6.2 Methods and Analysis

#### Dimming analysis

Our analysis focuses on dimming at the end of the impulsive phase (see [Section 4.3.3](#)), when the connections between an expanding CME, and dimming are fully established [[Dissauer et al., 2018a](#)]. We build a spherical polar coordinate system centered at the source region and split the solar sphere into 12 angular sectors of  $30^\circ$

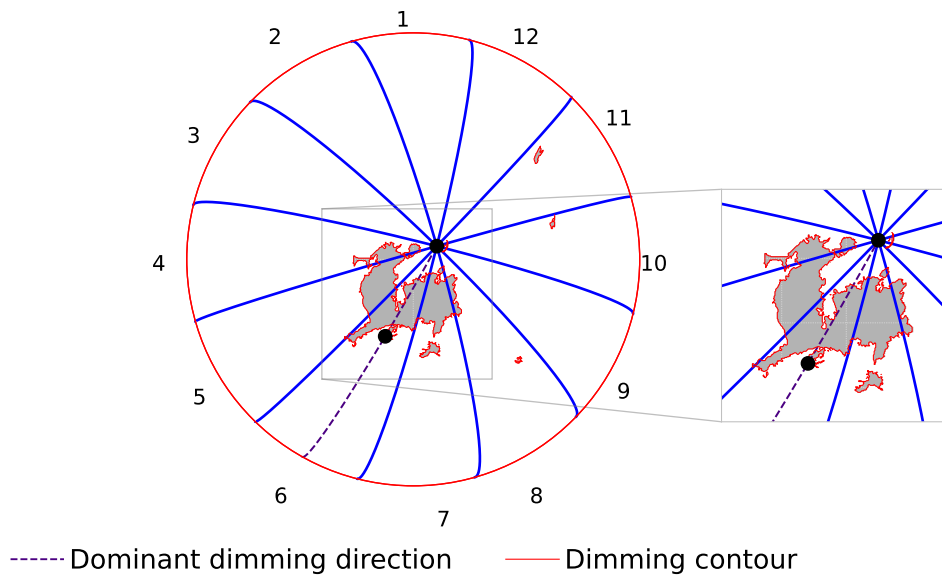


Figure 7-17: Dominant direction of dimming expansion at the end of impulsive phase for 1 October 2011. Cumulative dimming pixel mask outlined by gray with red contours. The blue lines indicate the 12 sectors: the The dashed purple line indicates the sector of dominant dimming development. The black dots show the dimming edges (one of them being the source) in the sector of dominant dimming which are used to generate the CME cones at different heights, associated widths and inclination angles.

width each and derive the dimming area values  $A$  in each sector. The sectors are numbered in counterclockwise direction with sector 1 pointing towards the North. Following sector analysis, we define the dominant dimming direction by the sector of largest cumulative dimming area extent, which is in this case sector 6 (Figure 7-17).

### Connecting the dimming and CME propagation direction

Once the dominant dimming direction is determined, we create an ensemble of CME cones that originate at the source location and extend into 3D space such that the edges of the cone's orthogonal projections remain confined within the dimming edges. We use two 3D lines: one linking the Sun's center to the source, and the other from the Sun's center to the dimming edge in the dominant direction (Figure 7-18, black lines). This approach ensures the CME cone projections fit to the dominant dimming direction, with each cone possessing unique height, width, and inclination parameters. The generated CME cones for 1 October 2011 are shown in Figure 7-19.

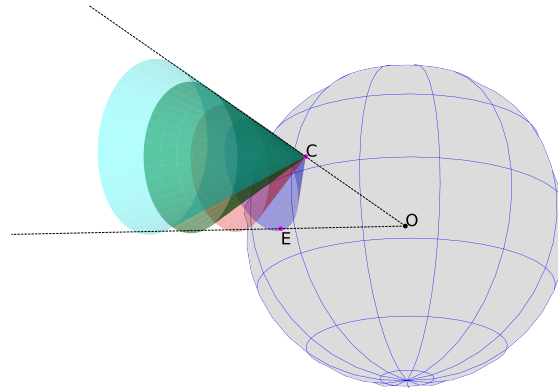


Figure 7-18: Ensemble of cones of different heights, widths and inclination angle bounded by the dimming edges C and E. The dotted lines outline the dimming edges extended into space connected through the Sun center.

Figure 7-19 shows that the cone projections shrink significantly at heights between  $0.27-1 R_{\odot}$ , with minor changes at higher heights. The dynamics of this shrinkage can be illustrated in Figure 7-20 (red line, left Y axis) by comparing the projections of cones at different heights. The optimal fit of the cone to the dimming, taking into account the shrinking in the projection area, is chosen as 5% of the peak of the red line. For the 1 October 2011 event it is a cone with the height of  $1.04 R_{\odot}$ , width of  $48.7^{\circ}$ , and  $24.3^{\circ}$  for inclination. The next criteria is evaluation of the dimming area within this projection (blue line, right Y axis). We accept only the solutions with coverage larger than 95%. The empirical thresholds will be validated in the future statistics. We note that if a CME parameter is known from other sources, we can determine the full parameter set given the unique relationship between the height, width, and inclination in our ensemble.

### 7.6.3 Resulted CME cone

We find that for the 1 October 2011 event the best fit of the CME projections to the dimming extent is a CME cone with height of  $1.04 R_{\odot}$  (a height at which the CME still remains connected to the dimming), CME width of  $48.7^{\circ}$  and inclination angle of  $24.3^{\circ}$ . By projecting the obtained 3D direction onto the meridional and equatorial planes, we obtained that the CME was directed towards the South-East ( $21^{\circ}$  South and  $12^{\circ}$  East).

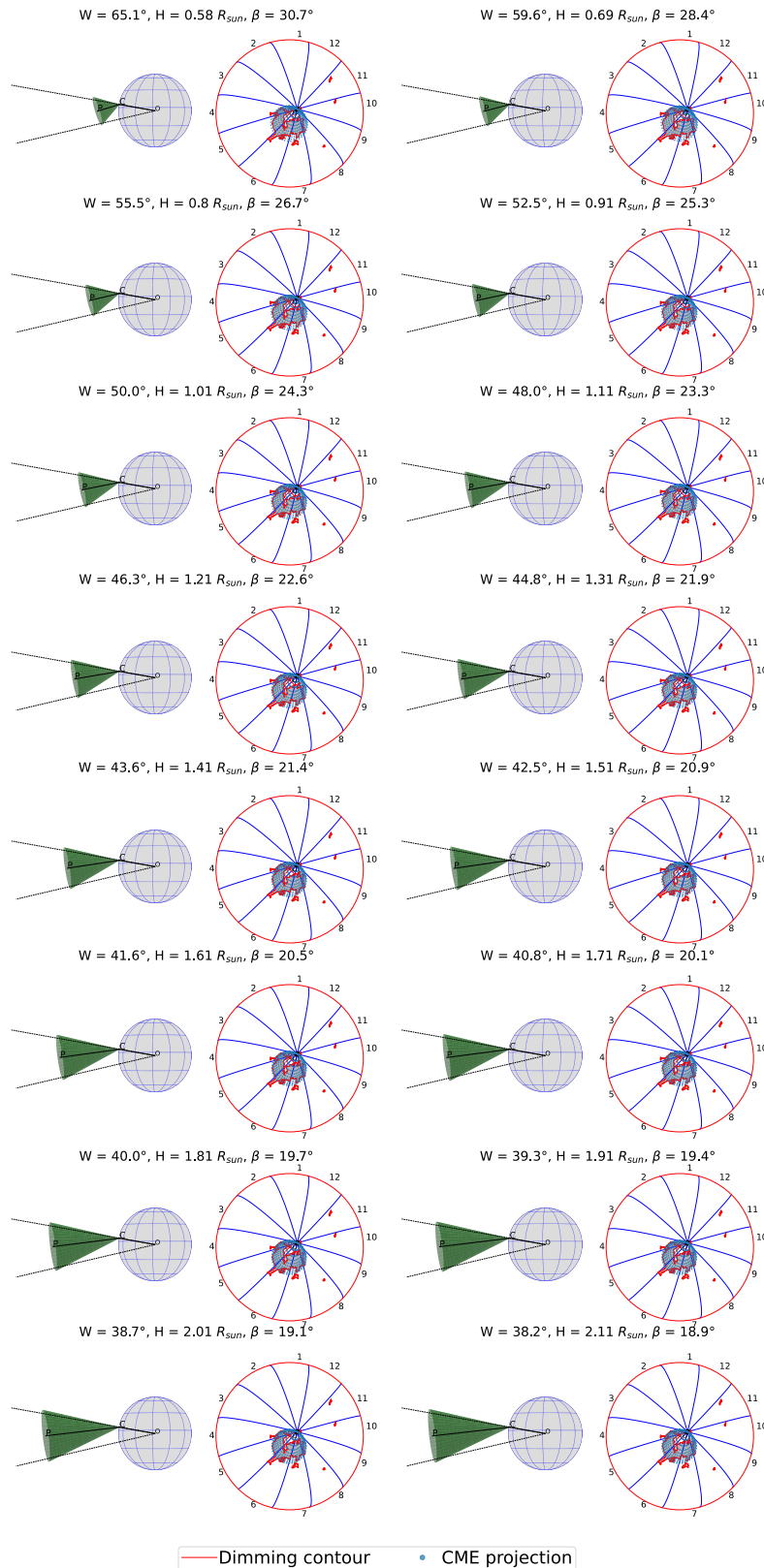


Figure 7-19: CME cones at heights of 0.58–2.11  $R_{\odot}$  for 1 October 2011 (columns 1 and 3) with associated widths and inclination angles and their orthogonal projections onto the solar sphere (columns 2 and 4) bounded by the dimming edges. Columns 1 and 3 depict the side view to better show the reconstructed cones, columns 2 and 4 show the face-on view.

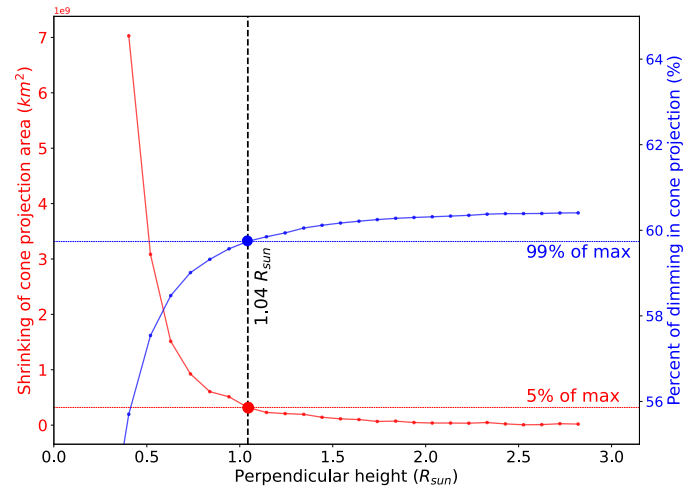


Figure 7-20: Consecutive differences in projection area of the generated cones ensemble (red, left Y-axis) and percentage of dimming area in projection to the total projection area (blue, right Y-axis) at the end of the impulsive phase. Vertical dashed line indicates the step, where consecutive differences reach 5% of the maximum of the cone projection area, which also lies within 95% of the maximum percentage of dimming area in projection.

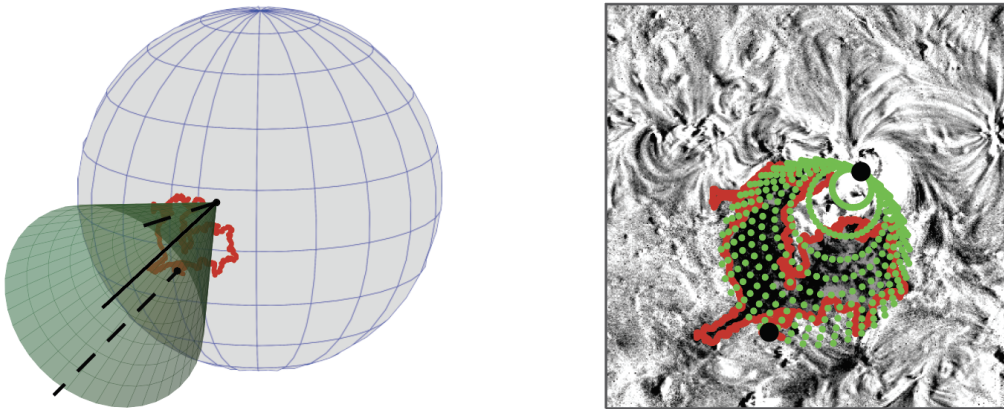


Figure 7-21: Best fit CME cone for 1 October 2011 event: 3D model (green mesh, left panel) and its projection on the solar surface (green dots, right panel). Red boundaries indicate the segmented dimming together with the source location and dimming edge along the direction of dominant dimming evolution (black dots). 3D black lines connect the solar center with the source location and the edge of the dimming along the dominant dimming direction (dashed), the main axis of the resulted CME cone (solid line).

### 7.6.4 Validation

The CME direction can be directly compared with the GCS reconstructions for the studied events. Our outcome for 1 October 2011 event is in agreement with the study by Temmer et al. [2017], where the authors used GCS reconstruction from multi viewpoint coronagraph observations of the CME, and concluded that the associated two-step filament eruption and the CME propagated towards the South-East.

In Jain et al. [2023] we also validate the resulted cone with the reconstruction of CME bubble at the similar height. We take the advantage of the multi-viewpoint by the STEREO-A and STEREO-B spacecraft for this event and identify identical features of the CME bubble from EUVI imagers onboard STEREO-A and STEREO-B and employ an algorithm of 3D reconstructions based on epipolar geometry, a similar one as we used for the filament reconstruction in Section 7.4.2.

### 7.6.5 Summary

This research proves that coronal dimmings can be proxies for the early CME propagation direction. The DIRECD method offers early CME direction estimates before it can be detected from coronagraph, operates without requiring multi-viewpoint observations, and it is particular useful for Earth-directed events. However, it's best suited for CMEs initiated below  $0.4 R_{\odot}$  and up to  $3 R_{\odot}$  above the surface since higher up no dimming footprint is detected anymore [Dissauer et al., 2019]. Further work should involve a broader CME event sample and evaluations on the accuracy and limitations of this method.

## 7.7 Conclusion

We introduced a methodology to estimate the dominant direction of dimming development and compare it with the 3D reconstructed trajectory of CME and erupting filament. This approach was applied in the case study of 28 October 2021 X1.0 flare/CME event.

The dominant propagation of the dimming growth reflects the direction of the erupting magnetic structure (filament) low in the solar atmosphere. At the same time, the overall dimming morphology aligns with the inner part of the CME reconstruction, confirming the use of dimming observations to obtain insight into the CME direction.

Building on these findings, we developed the **DIRECD** method to determine the initial direction of CME propagation early in its evolution. This method simulates a cone model from the dimming observations, considering both the dominant dimming direction and its overall morphology. The reconstructed cone for case event of 1 October 2011 was validated with 3D tie-pointing of the CME bubble and GCS reconstruction higher up in the corona. Our study demonstrates a proof of concept that coronal dimmings can be used as a proxy of the early CME propagation direction. It will allow us to gain early information about the direction of a CME even before it becomes visible in the field of view of coronagraphs. This holds practical significance for space weather forecasting and the proactive mitigation of potential adverse impacts on Earth.

# Chapter 8

## Conclusions and future work

### Conclusions

The findings and outcomes of this study can be divided into two main groups. First, we have developed a comprehensive methodology for dimming analysis in Python, from data preparation to methods that relate dimming evolution to the properties of coronal mass ejections and other eruptive signatures. Second, we have applied the developed techniques to clearly demonstrate that dimmings not only indicate the onset of the eruptive event, but also serve as a valuable diagnostic tool for coronal mass ejections to provide the early estimates of their speed and mass, initial trajectory, and the recovery of the solar corona after an eruption.

### Methods and framework

The important contribution of this study is the development of a comprehensive methodology for dimming analysis in Python. This framework is both robust, ensuring accurate dimming analysis, and flexible, allowing application to different research questions and objectives, including statistical analysis and case studies. We detailed the steps of **loading**, **calibrating**, and necessary **preprocessing** of the data using validated and adjusted routines from Python Sunpy library, rapidly developing by the work of heliophysics community.

We have outlined **methods for deriving characteristic dimming parameters** and adapting the detection and processing strategy to the specific analysis goals.

To accurately determine the dimming parameters, especially those that strongly depend on the area, we introduced a **technique that calculates the surface area** for each pixel. This method adeptly reduces projection distortion by taking into account the spherical projection of each pixel within the dimming area. We have made the code for this correction publicly available on GitHub.

A major highlight of this work is the development of an **automatic algorithm for segmenting coronal dimming** in Python that is suitable for **both on-disk and off-limb** dimming extraction. The availability of consistent, high-cadence, high-resolution imaging data from missions such as [SDO/AIA](#), [STEREO-A/EUVI](#), [GOES/SUVI](#), [Proba-2/SWAP](#), and [EUI](#) on the Solar Orbiter enables us to continuously observe and track coronal dimmings throughout the evolution of coronal mass ejections. In addition, the off-limb dimming segmentation algorithm can be applied to the observations of the next planned [ESA's L5 mission Vigil](#), where the Earth directed events will be observed off-limb.

Moreover, we introduced two methods for tracking the dimming recovery time. The first, using a **fixed mask** for all images in the dataset, effectively mitigates the artifacts of differential rotation and allows to study the general trend of the dimming region recovery. The second approach, **area box analysis**, focuses on tracking mean intensity within a fixed subregion. It provides a granular view on recovery patterns and can be quickly implemented in case studies to distinguish between core and secondary dimmings.

To link the 2D dimming morphology to to 3D propagation of the erupting filament and coronal mass ejection, we have introduced a **sector analysis method**. This approach allows us to identify the predominant direction of dimming propagation on the solar surface. By combining sector analysis and orthogonal projection of reconstructed filament heights onto the solar surface, we, for the first time, are able to compare the dominant direction of dimming propagation with the direction of eruptive filament activity in one confined system of coordinates. To compare the global morphology of the dimming region with the reconstructed CME, the **center of mass of the dimming region** can be calculated and compared with the location of the source region from the [GCS](#) reconstruction. The combination of the

dimming morphology analysis techniques and the reconstruction methods initiated the **DIRECD method** for the early estimation of the CME direction.

The framework with its multiple functionalities combines traditional knowledge with innovative techniques. By applying the described methods, different aspects of dimming evolution can be studied and related to associated CME observations, providing a more comprehensive understanding of these two phenomena. This methodology not only provides us with a solid foundation for ongoing and future solar observations, but also expands our ability to explore and understand the intricate dynamics of coronal dimming events in great detail.

### **Q1: Relation to CME speed and mass**

We conducted a statistical study on 43 coronal dimming events between May 2010 and September 2012, observed concurrently on-disk by **SDO** and off-limb by the **STEREO** satellites (Chapter 5). The unique positioning of satellites allowed us for the first time to investigate the relation between coronal dimmings and their corresponding Earth-directed CMEs statistically and to compare the results obtained from multi-viewpoint observations. Our analysis confirms the relation of coronal dimmings and CME physical properties for the off-limb viewpoint.

Dimming parameters, reflecting properties of the total dimming region at its final extent, area and total brightness, show strong correlations with CME mass, with correlation coefficients  $c \sim 0.7-0.8$ . The correlation coefficient for dimming area - CME mass relation revealed an even higher value than for on-disk results ( $c = 0.82 \pm 0.06$  for off-limb against  $c = 0.69 \pm 0.10$  for on-disk). Derivatives of these parameters, such as area growth rate and brightness change rate have shown significant correlations ( $c \sim 0.6$ ) with CME speed, indicating the close relation between the CME and dimming dynamics. For the area-mass relation there was obtained higher correlation coefficients than were reported before for dimmings observed on-disk.

Together with [Dissauer et al. \[2019\]](#) analysis, this study represents the first multi-point analysis of coronal dimmings. Comparing the properties of coronal dimmings observed simultaneously from different views in their on-disk/off-limb projections as well as their relation to the CME velocity and mass, allows us to assess the

potential of using coronal dimmings for early CME characterization from satellites located either at L1 or L5.

### **Q2: Dimming lifetime**

We tracked the dimming region to investigate the recovery of the solar corona after CME eruption for four cases (2011 September 6, 2012 March 7, 2012 June 14 and 2019 March 8) in Chapter 6. In our methodology, we take into account the progression of both complete dimming regions and their individual parts, facilitating the independent tracking of both core and secondary dimmings evolution.

In three of the four cases analyzed, full recovery occurs within less than 24 hours after the onset of the CME, consistent with the results of [Reinard and Biesecker \[2008\]](#). The primary mechanism causing this recovery appears to be a gradual shrinking that begins at the outermost edges and progresses inward. We found a distinct two-stage pattern in brightness recovery, which is characterized by an initial steep and rapid phase followed by a gradual phase.

It is noteworthy that specific segments of the dimming, possibly indicative of core dimmings, persist throughout the analysis period and do not return to their initial brightness levels within 3 days. These core dimming regions exhibit distinct recovery patterns compared to the peripheral regions - secondary dimmings, which gradually undergo a full restoration of brightness.

### **Q3: Relation of the direction**

In our study of the 28 October 2021 X1.0 event (Chapter 7), we explored the intricate relationship between the erupting filament, the CME, and the coronal dimming evolution. To determine the propagation direction of the flux rope during early CME evolution, we performed 3D reconstructions of the white-light CME by [GCS](#) and 3D tie-pointing of the eruptive filament. The sector analysis introduced for the dimming area indicated the dominant direction of dimming propagation, which was then related to the projected heights of the erupting filament on the solar surface.

For the event under study, the dominant propagation of the dimming growth precisely reflects the direction of the erupting magnetic structure (filament) low in

the corona. Also, the overall dimming morphology closely resembles the inner part of the CME reconstruction. These results highlight that the evolution of the dimmings reflects both the direction of a low-lying erupting magnetic structure and the global propagation of CMEs.

The **DIRECD** method, formulated for estimating CME direction, was tested on the observations of coronal dimmings ondisk by **SDO**. Our results prove that coronal dimmings offer preliminary estimates of CME directions even before they emerge in the field-of-view of coronagraphs, preserving the knowledge of the eruptive source region. These estimations does not rely on multi-viewpoint observations or coronagraphs, but require only one EUV instrument tracking the dimming evolution. Additionally, if there is information on any of the CME parameters from the sources, the method directly provides the full parameter set given the unique relationship between the height, width, and inclination in the ensemble on the heights up to  $\approx 3 R_{\odot}$  above the surface.

The dimming analysis is particularly advantageous for detecting events directed towards Earth, which are difficult to assess using coronagraphs positioned along the Sun-Earth line, as these primarily capture the CME expansion rather than its progression.

Examining coronal dimmings alongside other CME signatures is crucial. The dimmings provide invaluable insights into the dynamics of CME eruptions when analyzed together with their eruptive counterparts.

Coronagraph observations do not always provide clear confirmation on the complex structure of CMEs. What is typically observed is a single entity, also can be consisting of two sheared and twisted structures consistent with the two eruptions observed in the lower corona (Section 4.5.1). In this context, coronal dimmings combined with other low coronal CME manifestations (e.g., flares, EUV waves, coronal loops) are proving to be important diagnostic tools to unravel and redefine the magnetic structure of the eruptions.

Their fine structure and precise position provide additional crucial information about the different flux systems at play during the eruption process. In combination with flare ribbon analysis (Section 4.5.2), coronal dimmings are the important

diagnostic tool to study and understand the magnetic dynamics of solar eruptions

Consequently, the synergy between coronal dimmings and other CME signatures enhances our ability to explore and interpret these complex solar events on the very early stages of evolution.

## Plans and future work

### Lifetime

We plan a systematic statistical analysis to quantify the recovery time using the fixed mask approach. We also want to investigate the possibility of using the fixed mask on the merged map from multi-viewpoint observations, i.e. synchronized EUV image. Such an approach could extend the duration of dimming region observations. However, merging data from distinct satellites necessitates advanced preprocessing techniques, [e.g., as was discussed in the context of CH tracking by [Caplan et al., 2016](#)]. Given the variety of observational tools currently in different orbits, this exploration holds a significant potential. Our plan is to check the limitations and refine the methodology.

We have plans in place to conduct an area box analysis on several events currently under examination. Our primary aim is to delve deeper into the recovery phase of the dimming, shifting our focus from its early evolution.

### Development of the DIRECD method

We describe the methodology and our first results of reconstruction of the CME direction with [DIRECD](#) method in [7.6](#). Development of this method will allow us to provide information on the CME direction early on before it is derived from coronagraph observations, which is of practical importance for space weather forecasting.

Further steps need to include a larger statistical sample of CME events, which would allow investigating the accuracy and limitations of the method in detail, as well as a study of how often the early CME direction/deflection estimates using the presented method reflect the CME's behaviour further out in the heliosphere. We

also intend to test the method using alternative instruments that observe the lower solar corona in EUV.

## Potential of the dimming research

### Space Weather applications - new missions

Several upcoming solar missions promise to further our understanding of coronal dimming. As this dissertation was being drafted, the L1 mission Aditya, equipped with the Solar Ultra-Violet Imaging Telescope [SUIT; Tripathi et al., 2017], was launched. Additionally, ESA's Lagrange L5 mission, set for 2028, will focus on the Sun's western limb. This vantage point will capture Earth-directed CMEs off-limb, along with associated dimmings, making them particularly relevant for geo-effectiveness studies.

The Sun Coronal Ejection Tracker [SunCET; Mason et al., 2021] is a NASA CubeSat mission featuring an EUV imager. It's designed to study CMEs in the middle corona, a region not extensively explored in the EUV. The SunCET mission's authors suggest that coronal dimmings could offer insights into the kinematics of Earth-directed halo CMEs observed in EUV, as opposed to visible light.

### Dimmings on the other stars

Recent research has successfully identified CME-associated coronal dimmings in EUV and X-ray observations on late-type and solar-like stars. Veronig et al. [2021b] introduced a novel method, leveraging coronal dimmings as indicators of CMEs on solar-type stars. This technique broadens our capacity to delve into stellar physics. It paves the way for detecting and characterizing stellar CMEs, enabling us to understand their properties and implications for space weather and the habitability of exoplanets around these stars. Jin et al. [2022] employed a modeling approach to simulate the dimming of stars, specifically focusing on M dwarf and young Sun-like stars. While the possibility of variations in stellar dimming patterns exists, coronal dimmings seem to be a common occurrence among G-M type stars. For the stars with comparable mass, temperature, and magnetic field strength to the Sun, solar

coronal dimming events can be used as valuable references in comparative studies of stellar coronal dimmings.

In this context, planned missions focusing on stars and exoplanets in the EUV, boasting enhanced sensitivity and extensive spectral coverage, are of immense significance. The Extreme-ultraviolet Stellar Characterization for Atmospheric Physics and Evolution [ESCAPE; France et al., 2022] is an astrophysics mission concept emphasizing ultraviolet spectroscopy. Its primary objective is to probe the high-energy radiation environment in habitable zones around proximate stars. ESCAPE aims to offer an unprecedented study of the stellar EUV and the impact of coronal mass ejections on the habitability of terrestrial exoplanets.

The ongoing and forthcoming solar observations will continue to enhance our knowledge of coronal dimming events, their intricate connections with coronal mass ejections, and their relevance in advancing solar and solar-stellar connection studies.

# Bibliography

- Alicia N Aarnio, Keivan G Stassun, W Jeffrey Hughes, and Sarah L McGregor. Solar flares and coronal mass ejections: A statistically determined flare flux–cme mass correlation. *Solar Physics*, 268(1):195–212, 2011. doi:[10.1007/s11207-010-9672-7](https://doi.org/10.1007/s11207-010-9672-7).
- MH Acuña, D Curtis, JL Scheifele, CT Russell, P Schroeder, A Szabo, and JG Luhmann. The stereo/impact magnetic field experiment. *Space Science Reviews*, 136(1):203–226, 2008. doi:[10.4236/ijaa.2012.22009](https://doi.org/10.4236/ijaa.2012.22009).
- Marco Ajello, A Albert, A Allafort, Luca Baldini, Guido Barbiellini, D Bastieri, R Bellazzini, Elisabetta Bissaldi, E Bonamente, TJ Brandt, et al. Impulsive and long duration high-energy gamma-ray emission from the very bright 2012 march 7 solar flares. *The Astrophysical Journal*, 789(1):20, 2014. doi:[10.1088/0004-637X/789/1/20](https://doi.org/10.1088/0004-637X/789/1/20).
- T. Amari, J. F. Luciani, Z. Mikic, and J. Linker. A Twisted Flux Rope Model for Coronal Mass Ejections and Two-Ribbon Flares. *Astrophys. J. Lett.*, 529(1):L49–L52, January 2000. doi:[10.1086/312444](https://doi.org/10.1086/312444).
- Markus J Aschwanden. Global energetics of solar flares. iv. coronal mass ejection energetics. *The Astrophysical Journal*, 831(1):105, 2016. doi:[10.3847/0004-637X/831/1/105](https://doi.org/10.3847/0004-637X/831/1/105).
- Markus J. Aschwanden, John C. Brown, and Eduard P. Kontar. Chromospheric Height and Density Measurements in a Solar Flare Observed with RHESSI II. Data Analysis. *Solar Phys.*, 210(1):383–405, November 2002. doi:[10.1023/A:1022472319619](https://doi.org/10.1023/A:1022472319619).
- Markus J Aschwanden, Amir Caspi, Christina MS Cohen, Gordon Holman, Ju Jing, Matthieu Kretzschmar, Eduard P Kontar, James M McTiernan, Richard A Mewaldt, Aidan O’Flannagain, et al. Global energetics of solar flares. v. energy closure in flares and coronal mass ejections. *The Astrophysical Journal*, 836(1):17, 2017. doi:[10.3847/1538-4357/836/1/17](https://doi.org/10.3847/1538-4357/836/1/17).
- G Attrill and Meredith Wills-Davey. Automatic detection and extraction of coronal dimmings from sdo/aia data. *Solar Physics*, 262:461–480, 04 2009. doi:[10.1007/s11207-009-9444-4](https://doi.org/10.1007/s11207-009-9444-4).
- G Attrill, Maria Soledad Nakwacki, LK Harra, Van Driel-Gesztelyi, Cristina Hemilse Mandrini, S Dasso, J Wang, et al. Using the evolution of coronal dimming regions

- to probe the global magnetic field topology. *Solar Physics*, 238(1):117–139, 2006. doi:[10.1007/S11207-006-0167-5](https://doi.org/10.1007/S11207-006-0167-5).
- GDR Attrill, Lidia van Driel-Gesztelyi, Pascal Démoulin, AN Zhukov, K Steed, LK Harra, Cristina Hemilse Mandrini, and J Linker. The recovery of cme-related dimmings and the icme’s enduring magnetic connection to the sun. *Solar Physics*, 252(2):349–372, 2008. doi:[10.1007/s11207-008-9255-z](https://doi.org/10.1007/s11207-008-9255-z).
- Gemma Diana Ruth Attrill and Meredith J Wills-Davey. Automatic detection and extraction of coronal dimmings from sdo/aia data. *Solar Physics*, 262(2):461–480, 2010. doi:[10.1007/s11207-008-9255-z](https://doi.org/10.1007/s11207-008-9255-z).
- Eugene H Avrett. The solar temperature minimum and chromosphere. In *Current Theoretical Models and Future High Resolution Solar Observations: Preparing for ATST*, volume 286, page 419, 2003. URL <https://ui.adsabs.harvard.edu/abs/2003ASPC..286.....P>.
- Jacques M Beckers and Paul E Tallant. Chromospheric inhomogeneities in sunspot umbrae. *Solar Physics*, 7(3):351–365, 1969. doi:[10.1007/BF00146140](https://doi.org/10.1007/BF00146140).
- BM Bein, Sigrid Berkebile-Stoiser, AM Veronig, Manuela Temmer, Nicole Muhr, Ines Kienreich, Dominik Utz, and Bojan Vršnak. Impulsive acceleration of coronal mass ejections. i. statistics and coronal mass ejection source region characteristics. *The Astrophysical Journal*, 738(2):191, 2011. doi:[10.1088/0004-637X/738/2/191](https://doi.org/10.1088/0004-637X/738/2/191).
- BM Bein, S Berkebile-Stoiser, AM Veronig, M Temmer, and B Vršnak. Impulsive acceleration of coronal mass ejections. ii. relation to soft x-ray flares and filament eruptions. *The Astrophysical Journal*, 755(1):44, 2012. doi:[10.1088/0004-637X/755/1/44](https://doi.org/10.1088/0004-637X/755/1/44).
- A Bemporad. Stereoscopic reconstruction from stereo/euv imagers data of the three-dimensional shape and expansion of an erupting prominence. *The Astrophysical Journal*, 701(1):298, 2009. doi:[10.1088/0004-637X/701/1/298](https://doi.org/10.1088/0004-637X/701/1/298).
- Bernard Benson, W. David Pan, Avijeet Prasad, G. Allen Gary, and Qiang Hu. Forecasting solar cycle 25 using deep neural networks. *Solar Physics*, 295:1–15, 2020. URL <https://api.semanticscholar.org/CorpusID:218889585>.
- D. Berghmans, J. F. Hochedez, J. M. Defise, J. H. Lecat, B. Nicula, V. Slemzin, G. Lawrence, A. C. Katsyiannis, R. van der Linden, A. Zhukov, F. Clette, P. Rochus, E. Mazy, T. Thibert, P. Nicolosi, M. G. Pelizzo, and U. Schühle. SWAP onboard PROBA 2, a new EUV imager for solar monitoring. *Advances in Space Research*, 38(8):1807–1811, January 2006. doi:[10.1016/j.asr.2005.03.070](https://doi.org/10.1016/j.asr.2005.03.070).
- Danielle Bewsher, RA Harrison, and Daniel Stephen Brown. The relationship between euv dimming and coronal mass ejections-i. statistical study and probability model. *Astronomy & Astrophysics*, 478(3):897–906, 2008. doi:[10.1051/0004-6361:20078615](https://doi.org/10.1051/0004-6361:20078615).

- DE Billings. A guide to the solar corona, acad. *Press: New York and London*, 1966. doi:10.1063/1.3034941.
- Monica G Bobra, Stuart J Mumford, Russell J Hewett, Steven D Christe, Kevin Reardon, Sabrina Savage, Jack Ireland, Tiago Pereira, Bin Chen, and David Pérez-Suárez. A survey of computational tools in solar physics. *Solar Physics*, 295(4): 1–15, 2020. doi:10.1007/s11207-020-01622-2.
- Jean-Louis Bougeret, K Goetz, ML Kaiser, SD Bale, PJ Kellogg, M Maksimovic, N Monge, SJ Monson, PL Astier, S Davy, et al. S/waves: The radio and plasma wave investigation on the stereo mission. *Space Science Reviews*, 136(1):487–528, 2008. doi:10.1007/s11214-007-9298-8.
- Yannick Boursier, Philippe Lamy, Antoine Llebaria, François Goudail, and Sebastien Robelus. The artemis catalog of lasco coronal mass ejections. *Solar Physics*, 257:125–147, 2009. URL <https://api.semanticscholar.org/CorpusID:118337588>.
- K. Bronarska, M. S. Wheatland, N. Gopalswamy, and G. Michalek. Very narrow coronal mass ejections producing solar energetic particles. *Astron. Astrophys.*, 619:A34, November 2018. doi:10.1051/0004-6361/201833237.
- I. N. Bronshtein, K. A. Semendyayev, G. Musiol, and H. Muehlig. *Handbook of Mathematics*. Springer Berlin, Heidelberg, 2007. doi:10.1007/978-3-662-46221-8.
- R. G. Brown. *Smoothing forecasting and prediction in discrete time series*. Prentice Hall, New Jersey, 1963. doi:10.2307/2283122.
- GE Brueckner, RA Howard, MJ Koomen, CM Korendyke, DJ Michels, JD Moses, DG Socker, KP Dere, PL Lamy, A Llebaria, et al. The large angle spectroscopic coronagraph (lasco). In *The SOHO Mission*, pages 357–402. Springer, 1995. doi:10.1007/BF00733434.
- D Burgess, MG Kivelson, and CT Russell. Introduction to space physics. *by*, 1995. doi:10.1017/9781139878296.
- J. T. Burkepile, A. J. Hundhausen, A. L. Stanger, O. C. St. Cyr, and J. A. Seiden. Role of projection effects on solar coronal mass ejection properties: 1. A study of CMEs associated with limb activity. *Journal of Geophysical Research (Space Physics)*, 109(A3):A03103, March 2004. doi:10.1029/2003JA010149.
- JT Burkepile, AJ Hundhausen, AL Stanger, OC St. Cyr, and JA Seiden. Role of projection effects on solar coronal mass ejection properties: 1. a study of cmes associated with limb activity. *Journal of Geophysical Research: Space Physics*, 109(A3), 2004. doi:10.1029/2003JA010149.
- J. P. Byrne, H. Morgan, D. B. Seaton, H. M. Bain, and S. R. Habbal. Bridging EUV and White-Light Observations to Inspect the Initiation Phase of a “Two-Stage” Solar Eruptive Event. *Solar Phys.*, 289(12):4545–4562, December 2014. doi:10.1007/s11207-014-0585-8.

- Jason P. Byrne. Investigating the kinematics of coronal mass ejections with the automated CORIMP catalog. *Journal of Space Weather and Space Climate*, 5: A19, July 2015. doi:[10.1051/swsc/2015020](https://doi.org/10.1051/swsc/2015020).
- Jason P Byrne, Shane A Maloney, RT James McAteer, Jose M Refojo, and Peter T Gallagher. Propagation of an earth-directed coronal mass ejection in three dimensions. *Nature Communications*, 1(1):74, 2010. doi:[10.1038/ncomms1077](https://doi.org/10.1038/ncomms1077).
- R. M. Caplan, C. Downs, and J. A. Linker. Synchronic Coronal Hole Mapping Using Multi-instrument EUV Images: Data Preparation and Detection Method. *Astrophys. J.*, 823(1):53, May 2016. doi:[10.3847/0004-637X/823/1/53](https://doi.org/10.3847/0004-637X/823/1/53).
- PF Chen. Coronal mass ejections: models and their observational basis. *Living Reviews in Solar Physics*, 8(1):1, 2011. doi:[10.1007/s41116-011-0007-6](https://doi.org/10.1007/s41116-011-0007-6).
- JX Cheng and Jiong Qiu. The nature of cme-flare-associated coronal dimming. *The Astrophysical Journal*, 825(1):37, 2016. doi:[10.1086/525269](https://doi.org/10.1086/525269).
- X. Cheng, M. D. Ding, Y. Guo, J. Zhang, A. Vourlidas, Y. D. Liu, O. Olmedo, J. Q. Sun, and C. Li. Tracking the Evolution of a Coherent Magnetic Flux Rope Continuously from the Inner to the Outer Corona. *Astrophys. J.*, 780(1):28, January 2014. doi:[10.1088/0004-637X/780/1/28](https://doi.org/10.1088/0004-637X/780/1/28).
- Xin Cheng, Yang Guo, and MingDe Ding. Origin and Structures of Solar Eruptions I: Magnetic Flux Rope. *Science China Earth Sciences*, 60:1383–1407, August 2017. doi:[10.1007/s11430-017-9074-6](https://doi.org/10.1007/s11430-017-9074-6).
- I. M. Chertok, V. V. Grechnev, A. V. Belov, and A. A. Abunin. Magnetic Flux of EUV Arcade and Dimming Regions as a Relevant Parameter for Early Diagnostics of Solar Eruptions - Sources of Non-recurrent Geomagnetic Storms and Forbush Decreases. *Solar Phys.*, 282(1):175–199, January 2013. doi:[10.1007/s11207-012-0127-1](https://doi.org/10.1007/s11207-012-0127-1).
- IM Chertok and VV Grechnev. Large-scale dimmings produced by solar coronal mass ejections according to soho/eit data in four euv lines. *Astronomy Reports*, 47(11):934–945, 2003. doi:[10.1134/1.1626196](https://doi.org/10.1134/1.1626196).
- G. Chikunova, K. Dissauer, T. Podladchikova, and A. M. Veronig. Coronal Dimmings Associated with Coronal Mass Ejections on the Solar Limb. *Astrophys. J.*, 896(1):17, June 2020. doi:[10.3847/1538-4357/ab9105](https://doi.org/10.3847/1538-4357/ab9105).
- G. Chikunova, T. Podladchikova, K. Dissauer, A. M. Veronig, M. Dumbović, M. Temmer, and E. Dickson. Three-dimensional relation between coronal dimming, filament eruption, and CME - a case study of the 28 October 2021 X1.0 event. *Astron. Astrophys.*, 678:A166, October 2023. doi:[10.1051/0004-6361/202347011](https://doi.org/10.1051/0004-6361/202347011).
- L. P. Chitta, A. N. Zhukov, D. Berghmans, H. Peter, S. Parenti, S. Mandal, R. Aznar Cuadrado, U. Schühle, L. Teriaca, F. Auchère, K. Barczynski, É. Buchlin, L. Harra, E. Kraaikamp, D. M. Long, L. Rodriguez, C. Schwanitz, P. J. Smith,

- C. Verbeek, and D. B. Seaton. Picoflare jets power the solar wind emerging from a coronal hole on the Sun. *arXiv e-prints*, art. arXiv:2308.13044, August 2023. doi:10.48550/arXiv.2308.13044.
- Consuelo Cid, Hebe Cremades, Angels Aran, Cristina Mandrini, Blai Sanahuja, Brigitte Schmieder, Michel Menvielle, Luciano Rodriguez, Elena Saiz, Yolanda Cerrato, et al. Can a halo cme from the limb be geoeffective? *Journal of Geophysical Research: Space Physics*, 117(A11), 2012. doi:10.1029/2012JA017536.
- Frédéric Clette, Leif Svalgaard, José M Vaquero, and Edward W Cliver. Revisiting the sunspot number. *Space Science Reviews*, 186(1-4):35–103, 2014. doi:10.1007/s11214-014-0074-2.
- Edward W Cliver. History of research on solar energetic particle (sep) events: the evolving paradigm. *Proceedings of the International Astronomical Union*, 4(S257):401–412, 2008. doi:10.1017/S1743921309029639.
- NASA LASCO/EIT consortium and SOHO team. Soho lasco cme catalog. [https://cdaw.gsfc.nasa.gov/CME\\_list/](https://cdaw.gsfc.nasa.gov/CME_list/). Accessed: 2022-11-25.
- S. Couvidat, J. Schou, J. T. Hoeksema, R. S. Bogart, R. I. Bush, T. L. Duvall, Y. Liu, A. A. Norton, and P. H. Scherrer. Observables Processing for the Helioseismic and Magnetic Imager Instrument on the Solar Dynamics Observatory. *Solar Phys.*, 291(7):1887–1938, August 2016. doi:10.1007/s11207-016-0957-3.
- H. Cremades, V. Bothmer, and D. Tripathi. Properties of structured coronal mass ejections in solar cycle 23. *Advances in Space Research*, 38(3):461–465, January 2006. doi:10.1016/j.asr.2005.01.095.
- NU Crooker. Solar and heliospheric geoeffective disturbances. *Journal of Atmospheric and Solar-Terrestrial Physics*, 62(12):1071–1085, 2000. doi:10.1016/S1364-6826(00)00098-5.
- Jonathan M Darnel, Daniel B Seaton, Christian Bethge, Laurel Rachmeler, Alison Jarvis, Steven M Hill, Courtney L Peck, J Marcus Hughes, Jason Shapiro, Allyssa Riley, et al. The goes-r solar ultraviolet imager. *Space Weather*, 20(4):e2022SW003044, 2022. doi:10.1029/2022SW003044.
- P. Démoulin, C. H. Mandrini, L. van Driel-Gesztelyi, B. J. Thompson, S. Plunkett, Zs. Kovári, G. Aulanier, and A. Young. What is the source of the magnetic helicity shed by CMEs? The long-term helicity budget of AR 7978. *Astron. Astrophys.*, 382:650–665, February 2002. doi:10.1051/0004-6361:20011634.
- Pooja Devi, Ramesh Chandra, Arun Kumar Awasthi, Brigitte Schmieder, and Reetika Joshi. Extreme-Ultraviolet Wave and Accompanying Loop Oscillations. *Solar Phys.*, 297(12):153, December 2022. doi:10.1007/s11207-022-02082-6.
- Karin Dissauer, Manuela Temmer, Astrid M Veronig, Kamalam Vanninathan, and Jasmina Magdalenic. Projection effects in coronal dimmings and associated euv wave event. *The Astrophysical Journal*, 830(2):92, 2016. doi:10.3847/0004-637X/830/2/92.

- Karin Dissauer, Astrid M Veronig, Manuela Temmer, Tatiana Podladchikova, and Kamalam Vanninathan. On the detection of coronal dimmings and the extraction of their characteristic properties. *The Astrophysical Journal*, 855(2):137, 2018a. doi:10.3847/1538-4357/aaaf1f.
- Karin Dissauer, Astrid M Veronig, Manuela Temmer, Tatiana Podladchikova, and Kamalam Vanninathan. Statistics of coronal dimmings associated with coronal mass ejections. i. characteristic dimming properties and flare association. *The Astrophysical Journal*, 863(2):169, 2018b. doi:10.3847/1538-4357/aad2e9.
- Karin Dissauer, Astrid M Veronig, Manuela Temmer, and Tatiana Podladchikova. Statistics of coronal dimmings associated with coronal mass ejections. ii. relationship between coronal dimmings and their associated cmes. *The Astrophysical Journal*, 874(2):123, 2019. doi:10.3847/1538-4357/ab0d8c.
- V. Domingo, B. Fleck, and A. I. Poland. The SOHO Mission: an Overview. *Solar Phys.*, 162(1-2):1–37, December 1995. doi:10.1007/BF00733425.
- Cooper Downs, Ilia I Roussev, Bart van der Holst, Noé Lugaz, and Igor V Sokolov. Understanding sdo/aia observations of the 2010 june 13 euv wave event: Direct insight from a global thermodynamic mhd simulation. *The Astrophysical Journal*, 750(2):134, 2012. doi:10.1088/0004-637X/750/2/134.
- N. Dresing, L. Rodríguez-García, I. C. Jebaraj, A. Warmuth, S. Wallace, L. Balmaceda, T. Podladchikova, R. D. Strauss, A. Kouloumvakos, C. Palmroos, V. Krupar, J. Gieseler, Z. Xu, J. G. Mitchell, C. M. S. Cohen, G. A. de Nolfo, E. Palmerio, F. Carcaboso, E. K. J. Kilpua, D. Trotta, U. Auster, E. Asvestari, D. da Silva, W. Dröge, T. Getachew, R. Gómez-Herrero, M. Grande, D. Heyner, M. Holmström, J. Huovelin, Y. Kartavykh, M. Laurenza, C. O. Lee, G. Mason, M. Maksimovic, J. Mieth, G. Murakami, P. Oleynik, M. Pinto, M. Pulupa, I. Richter, J. Rodríguez-Pacheco, B. Sánchez-Cano, F. Schuller, H. Ueno, R. Vainio, A. Vecchio, A. M. Veronig, and N. Wijsen. The 17 April 2021 widespread solar energetic particle event. *Astron. Astrophys.*, 674:A105, June 2023. doi:10.1051/0004-6361/202345938.
- Nina Dresing, Raúl Gómez-Herrero, Andreas Klassen, Bernd Heber, Yulia Kartavykh, and Wolfgang Dröge. The large longitudinal spread of solar energetic particles during the 17 january 2010 solar event. *Solar Physics*, 281:281–300, 2012. doi:10.1007/s11207-012-0049-y.
- M. Dumbović, A. M. Veronig, T. Podladchikova, J. K. Thalmann, G. Chikunova, K. Dissauer, J. Magdalenic, M. Temmer, J. Guo, and E. Samara. 2019 International Women’s Day event. Two-step solar flare with multiple eruptive signatures and low Earth impact. *Astron. Astrophys.*, 652:A159, August 2021. doi:10.1051/0004-6361/202140752.
- M Dumbović, AM Veronig, Tatiana Podladchikova, Julia K Thalmann, Galina Chikunova, Karin Dissauer, J Magdalenic, Manuela Temmer, Jingnan Guo, and Evangelia Samara. 2019 international women’s day event-two-step solar flare with

- multiple eruptive signatures and low earth impact. *Astron. Astrophys.*, 652:A159, 2021.
- Mateja Dumbović, Jingnan Guo, Manuela Temmer, M Leila Mays, Astrid Veronig, Stephan G Heinemann, Karin Dissauer, Stefan Hofmeister, Jasper Halekas, Christian Möstl, et al. Unusual plasma and particle signatures at mars and stereo-a related to cme–cme interaction. *The Astrophysical Journal*, 880(1):18, 2019. doi:[10.3847/1538-4357/ab27ca](https://doi.org/10.3847/1538-4357/ab27ca).
- AG Emslie, H Kucharek, BR Dennis, N Gopalswamy, GD Holman, GH Share, A Vourlidas, TG Forbes, PT Gallagher, GM Mason, et al. Energy partition in two solar flare/cme events. *Journal of Geophysical Research: Space Physics*, 109(A10), 2004. doi:[10.1029/2004JA010571](https://doi.org/10.1029/2004JA010571).
- R. Erdélyi and I. Ballai. Heating of the solar and stellar coronae: a review. *Astronomische Nachrichten*, 328:726–733, October 2007. doi:[10.1002/asna.200710803](https://doi.org/10.1002/asna.200710803).
- CJ Eyles, RA Harrison, Chris J Davis, NR Waltham, BM Shaughnessy, HCA Mapson-Menard, Danielle Bewsher, SR Crothers, JA Davies, GM Simnett, et al. The heliospheric imagers onboard the stereo mission. *Solar Physics*, 254(2):387–445, 2009. doi:[10.1007/s11207-008-9299-0](https://doi.org/10.1007/s11207-008-9299-0).
- Joan Feynman and SB Gabriel. On space weather consequences and predictions. *Journal of Geophysical Research: Space Physics*, 105(A5):10543–10564, 2000. doi:[10.1029/2000JA000005](https://doi.org/10.1029/2000JA000005).
- T. G. Forbes and P. A. Isenberg. A Catastrophe Mechanism for Coronal Mass Ejections. *Astrophys. J.*, 373:294, May 1991. doi:[10.1086/170051](https://doi.org/10.1086/170051).
- T. G. Forbes and J. Lin. What can we learn about reconnection from coronal mass ejections? *Journal of Atmospheric and Solar-Terrestrial Physics*, 62(16):1499–1507, November 2000. doi:[10.1016/S1364-6826\(00\)00083-3](https://doi.org/10.1016/S1364-6826(00)00083-3).
- T. G. Forbes, J. A. Linker, J. Chen, C. Cid, J. Kóta, M. A. Lee, G. Mann, Z. Mikić, M. S. Potgieter, J. M. Schmidt, G. L. Siscoe, R. Vainio, S. K. Antiochos, and P. Riley. CME Theory and Models. *Space Sci. Rev.*, 123(1-3):251–302, March 2006. doi:[10.1007/s11214-006-9019-8](https://doi.org/10.1007/s11214-006-9019-8).
- Scott E Forbush. Three unusual cosmic-ray increases possibly due to charged particles from the sun. *Physical Review*, 70(9-10):771, 1946. doi:[10.1103/PhysRev.70.771](https://doi.org/10.1103/PhysRev.70.771).
- Kevin France, Brian Fleming, Allison Youngblood, James Mason, Jeremy J. Drake, Ute V. Amerstorfer, Martin Barstow, Vincent Bourrier, Patrick Champey, Luca Fossati, Cynthia S. Froning, James C. Green, Fabien Gris , Guillaume Gronoff, Timothy Hellickson, Meng Jin, Tommi T. Koskinen, Adam F. Kowalski, Nicholas Kruczek, Jeffrey L. Linsky, Sarah J. Lipsky, Randall L. McEntaffer, David E. McKenzie, Drew M. Miles, Tom Patton, Sabrina Savage, Oswald Siegmund, Constance Spittler, Bryce W. Unruh, and M aire Volz. Extreme-ultraviolet Stellar

- Characterization for Atmospheric Physics and Evolution mission: motivation and overview. *Journal of Astronomical Telescopes, Instruments, and Systems*, 8:014006, January 2022. doi:[10.1117/1.JATIS.8.1.014006](https://doi.org/10.1117/1.JATIS.8.1.014006).
- K Galsgaard and AW Longbottom. Formation of solar prominences by flux convergence. *The Astrophysical Journal*, 510(1):444, 1999. doi:[10.1086/306559](https://doi.org/10.1086/306559).
- Antoinette B Galvin, Lynn M Kistler, Mark A Popecki, Charlie J Farrugia, Kristin DC Simunac, Lorna Ellis, E Möbius, Martin A Lee, M Boehm, J Carroll, et al. The plasma and suprathermal ion composition (plastic) investigation on the stereo observatories. *Space Science Reviews*, 136(1):437–486, 2008. doi:[10.1007/s11214-007-9296-x](https://doi.org/10.1007/s11214-007-9296-x).
- Jan Gieseler, Nina Dresing, Christian Palmroos, Johan L. Freiherr von Forstner, Daniel J. Price, Rami Vainio, Athanasios Kouloumvakos, Laura Rodríguez-García, Domenico Trotta, Vincent Génot, Arnaud Masson, Markus Roth, and Astrid Veronig. Solar-MACH: An open-source tool to analyze solar magnetic connection configurations. *Frontiers in Astronomy and Space Sciences*, 9:384, February 2023. doi:[10.3389/fspas.2022.1058810](https://doi.org/10.3389/fspas.2022.1058810).
- Peter A Gilman. Magnetohydrodynamic “shallow water” equations for the solar tachocline. *The Astrophysical Journal Letters*, 544(1):L79, 2000. doi:[10.1086/317291](https://doi.org/10.1086/317291).
- Laurent Gizon. Helioseismology of time-varying flows through the solar cycle. *Solar Physics*, 224(1):217–228, Oct 2004. ISSN 1573-093X. doi:[10.1007/s11207-005-4983-9](https://doi.org/10.1007/s11207-005-4983-9). URL <https://doi.org/10.1007/s11207-005-4983-9>.
- Lindsay Glesener, Säm Krucker, Hazel M. Bain, and Robert P. Lin. Observation of Heating by Flare-accelerated Electrons in a Solar Coronal Mass Ejection. *Astrophys. J. Lett.*, 779(2):L29, December 2013. doi:[10.1088/2041-8205/779/2/L29](https://doi.org/10.1088/2041-8205/779/2/L29).
- R. Gómez-Herrero, N. Dresing, A. Klassen, B. Heber, D. Lario, N. Agueda, O. E. Malandraki, J. J. Blanco, J. Rodríguez-Pacheco, and S. Banjac. Circumsolar Energetic Particle Distribution on 2011 November 3. *Astrophys. J.*, 799(1):55, January 2015. doi:[10.1088/0004-637X/799/1/55](https://doi.org/10.1088/0004-637X/799/1/55).
- N Gopalswamy, S Nunes, S Yashiro, and RA Howard. Variability of solar eruptions during cycle 23. *Advances in Space Research*, 34(2):391–396, 2004. doi:[10.1016/j.asr.2003.02.046](https://doi.org/10.1016/j.asr.2003.02.046).
- N. Gopalswamy, S. Yashiro, G. Michalek, G. Stenborg, A. Vourlidas, S. Freeland, and R. Howard. The SOHO/LASCO CME Catalog. *Earth Moon and Planets*, 104(1-4):295–313, April 2009. doi:[10.1007/s11038-008-9282-7](https://doi.org/10.1007/s11038-008-9282-7).
- N Gopalswamy, S Yashiro, G Michalek, G Stenborg, A Vourlidas, S Freeland, and R Howard. The soho/lasco cme catalog. *Earth, Moon, and Planets*, 104(1-4): 295–313, 2009. doi:[10.1007/s11038-008-9282-7](https://doi.org/10.1007/s11038-008-9282-7).

- Nat Gopalswamy, A Lara, RP Lepping, ML Kaiser, D Berdichevsky, and OC St. Cyr. Interplanetary acceleration of coronal mass ejections. *Geophysical research letters*, 27(2):145–148, 2000. doi:[10.1029/1999GL003639](https://doi.org/10.1029/1999GL003639).
- John T Gosling. The solar flare myth. *Journal of Geophysical Research: Space Physics*, 98(A11):18937–18949, 1993. doi:[10.1029/1999JA900449](https://doi.org/10.1029/1999JA900449).
- Tingyu Gou, Astrid M. Veronig, Rui Liu, Bin Zhuang, Mateja Dumbović, Tatiana Podladchikova, Hamish A. S. Reid, Manuela Temmer, Karin Dissauer, Bojan Vršnak, and Yuming Wang. Solar Flare-CME Coupling throughout Two Acceleration Phases of a Fast CME. *Astrophys. J. Lett.*, 897(2):L36, July 2020. doi:[10.3847/2041-8213/ab9ec5](https://doi.org/10.3847/2041-8213/ab9ec5).
- Tingyu Gou, Rui Liu, Astrid M. Veronig, Bin Zhuang, Ting Li, Wensi Wang, Mengjiao Xu, and Yuming Wang. Complete replacement of magnetic flux in a flux rope during a coronal mass ejection. *Nature Astronomy*, 7:815–824, July 2023. doi:[10.1038/s41550-023-01966-2](https://doi.org/10.1038/s41550-023-01966-2).
- JH Guo, YW Ni, Ze Zhong, Yang Guo, Chun Xia, HT Li, Stefaan Poedts, Brigitte Schmieder, and PF Chen. Thermodynamic and magnetic topology evolution of the x1.0 flare on 2021 october 28 simulated by a data-driven radiative magnetohydrodynamic model. *The Astrophysical Journal Supplement Series*, 266(1):3, 2023. doi:[10.3847/1538-4365/acc797](https://doi.org/10.3847/1538-4365/acc797).
- Jingnan Guo, Mateja Dumbović, Robert F. Wimmer-Schweingruber, Manuela Temmer, Henning Lohf, Yuming Wang, Astrid Veronig, Donald M. Hassler, Leila M. Mays, Cary Zeitlin, Bent Ehresmann, Olivier Witasse, Johan L. Freiherr von Forstner, Bernd Heber, Mats Holmström, and Arik Posner. Modeling the Evolution and Propagation of 10 September 2017 CMEs and SEPs Arriving at Mars Constrained by Remote Sensing and In Situ Measurement. *Space Weather*, 16(8):1156–1169, August 2018. doi:[10.1029/2018SW001973](https://doi.org/10.1029/2018SW001973).
- Hermance J Hagenaar. Ephemeral regions on a sequence of full-disk michelson doppler imager magnetograms. *The Astrophysical Journal*, 555(1):448, 2001. doi:[10.1086/321448](https://doi.org/10.1086/321448).
- George E Hale. On the probable existence of a magnetic field in sun-spots. *The astrophysical journal*, 28:315, 1908. doi:[10.1086/141602](https://doi.org/10.1086/141602).
- Louise K Harra and Alphonse C Sterling. Material outflows from coronal intensity “dimming regions” during coronal mass ejection onset. *The Astrophysical Journal Letters*, 561(2):L215, 2001. doi:[10.1086/324767](https://doi.org/10.1086/324767).
- R. A. Harrison and M. Lyons. A spectroscopic study of coronal dimming associated with a coronal mass ejection. *Astron. Astrophys.*, 358:1097–1108, June 2000. URL <https://ui.adsabs.harvard.edu/abs/2000A&A...358.1097H>.
- RA Harrison. The nature of solar flares associated with coronal mass ejection. *Astronomy and Astrophysics*, 304:585, 1995. doi:[10.1007/BF00658624](https://doi.org/10.1007/BF00658624).

- RA Harrison, E Hildner, AJ Hundhausen, DG Sime, and GM Simnett. The launch of solar coronal mass ejections: Results from the coronal mass ejection onset program. *Journal of Geophysical Research: Space Physics*, 95(A2):917–937, 1990. doi:[10.1029/JA095iA02p00917](https://doi.org/10.1029/JA095iA02p00917).
- RA Harrison, P Bryans, GM Simnett, and M Lyons. Coronal dimming and the coronal mass ejection onset. *Astronomy & Astrophysics*, 400(3):1071–1083, 2003. doi:[10.1051/0004-6361:20030088](https://doi.org/10.1051/0004-6361:20030088).
- Karen L. Harvey and Frank Recely. Polar Coronal Holes During Cycles 22 and 23. *Solar Phys.*, 211(1):31–52, December 2002. doi:[10.1023/A:1022469023581](https://doi.org/10.1023/A:1022469023581).
- David H. Hathaway. The Solar Cycle. *Living Reviews in Solar Physics*, 7(1):1, December 2010. doi:[10.12942/lrsp-2010-1](https://doi.org/10.12942/lrsp-2010-1).
- David H Hathaway. The solar cycle. *Living reviews in solar physics*, 12:1–87, 2015. doi:[10.1007/lrsp-2015-4](https://doi.org/10.1007/lrsp-2015-4).
- Stephan G. Heinemann, Manuela Temmer, Charles J. Farrugia, Karin Dissauer, Christina Kay, Thomas Wiegmann, Mateja Dumbović, Astrid M. Veronig, Tatiana Podladchikova, Stefan J. Hofmeister, Noé Lugaz, and Fernando Carcaboso. CME-HSS Interaction and Characteristics Tracked from Sun to Earth. *Solar Phys.*, 294(9):121, September 2019. doi:[10.1007/s11207-019-1515-6](https://doi.org/10.1007/s11207-019-1515-6).
- Zhenyong Hou, Hui Tian, Jing-Song Wang, Xiaoxin Zhang, Qiao Song, Ruisheng Zheng, Hechao Chen, Bo Chen, Xianyong Bai, Yajie Chen, et al. Three-dimensional propagation of the global extreme-ultraviolet wave associated with a solar eruption on 2021 october 28. *The Astrophysical Journal*, 928(2):98, 2022. doi:[10.3847/1538-4357/ac590d](https://doi.org/10.3847/1538-4357/ac590d).
- B. A. Hovis-Afflerbach, B. J. Thompson, and E. I. Mason. Partially erupted prominence material as a diagnostic of coronal mass ejection trajectory. *Space Weather*, 21(8):e2022SW003256, 2023. doi:<https://doi.org/10.1029/2022SW003256>. URL <https://agupubs.onlinelibrary.wiley.com/doi/abs/10.1029/2022SW003256>. e2022SW003256 2022SW003256.
- R. F. Howard, J. W. Harvey, and S. Forgach. Solar Surface Velocity Fields Determined from Small Magnetic Features. *Solar Phys.*, 130(1-2):295–311, December 1990. doi:[10.1007/BF00156795](https://doi.org/10.1007/BF00156795).
- Russell A Howard, JD Moses, Angelos Vourlidas, JS Newmark, Dennis G Socker, Simon P Plunkett, Clarence M Korendyke, JW Cook, A Hurley, JM Davila, et al. Sun earth connection coronal and heliospheric investigation (secchi). *Space Science Reviews*, 136(1):67–115, 2008. doi:[10.1007/s11214-008-9341-4](https://doi.org/10.1007/s11214-008-9341-4).
- T. A. Howard, C. E. DeForest, U. G. Schneck, and C. R. Alden. Challenging Some Contemporary Views of Coronal Mass Ejections. II. The Case for Absent Filaments. *Astrophys. J.*, 834(1):86, January 2017. doi:[10.3847/1538-4357/834/1/86](https://doi.org/10.3847/1538-4357/834/1/86).

- Douglas V. Hoyt and Kenneth H. Schatten. Group Sunspot Numbers: A New Solar Activity Reconstruction. *Solar Physics*, v. 181, Issue 2, p. 491-512 (1998)., August 1998. URL <https://ui.adsabs.harvard.edu/abs/1998SoPh..181..491H>.
- Douglas V Hoyt and Kenneth H Schatten. Group sunspot numbers: A new solar activity reconstruction. *Solar physics*, 179(1):189–219, 1998. doi:10.1023/A:1005007527816.
- H. S. Hudson. Implosions in Coronal Transients. *Astrophys. J. Lett.*, 531(1):L75–L77, March 2000. doi:10.1086/312516.
- H. S. Hudson, L. W. Acton, and S. L. Freeland. A Long-Duration Solar Flare with Mass Ejection and Global Consequences. *Astrophys. J.*, 470:629, October 1996. doi:10.1086/177894.
- HS Hudson and EW Cliver. Observing coronal mass ejections without coronagraphs. *Journal of Geophysical Research: Space Physics*, 106(A11):25199–25213, 2001. doi:10.1029/2000JA000005.
- HS Hudson, LW Acton, D Alexander, SL Freeland, JR Lemen, and KL Harvey. Yohkoh/sxt soft x-ray observations of sudden mass loss from the solar corona. In *AIP Conference Proceedings*, volume 382, pages 88–91. AIP, 1996a. doi:10.1063/1.51424.
- HS Hudson, LW Acton, and SL Freeland. A long-duration solar flare with mass ejection and global consequences. *The Astrophysical Journal*, 470:629, 1996b. doi:10.1086/177889.
- D. Hughes-Hallett, W. G. McCallum, A. M. Gleason, E. Connally, D. E. Flath, S. Kalaycioglu, B. Lahme, P. F. Lock, D. O. Lomen, D. Lovelock, G. I. Lozano, J. Morris, D. Mumford, B. G. Osgood, C. L. Patterson, D. Quinney, K. R. Rhea, A. A Sahin, A. H. Spiegler, J. Tecosky-Feldman, T. W. Tucker, A. D. Wootton, and E. J. Marks. *Handbook of Mathematics*. Springer Berlin, Heidelberg, 2017. doi:10.1007/978-3-662-46221-8.
- A. Hundhausen. *Coronal Mass Ejections*, pages 143–200. Springer New York, New York, NY, 1999. ISBN 978-1-4612-1442-7. doi:10.1007/978-1-4612-1442-7\_5. URL [https://doi.org/10.1007/978-1-4612-1442-7\\_5](https://doi.org/10.1007/978-1-4612-1442-7_5).
- N. Hurlburt, S. L. Freeland, S. Timothy, P. Shirts, and G. Slater. The Future Of SolarSoft. In *American Astronomical Society Meeting Abstracts*, volume 53 of *American Astronomical Society Meeting Abstracts*, page 213.01, June 2021. URL <https://ui.adsabs.harvard.edu/abs/2021AAS...23821301H>.
- R. M. E. Illing and A. J. Hundhausen. Disruption of a coronal streamer by an eruptive prominence and coronal mass ejection. *J. Geophys. Res.*, 91(A10):10951–10960, October 1986. doi:10.1029/JA091iA10p10951.
- RME Illing and AJ Hundhausen. Observation of a coronal transient from 1.2 to 6 solar radii. *Journal of Geophysical Research: Space Physics*, 90(A1):275–282, 1985. doi:10.1029/JA090iA01p00275.

- B. Inhester. Stereoscopy basics for the STEREO mission. *ArXiv Astrophysics e-prints*, December 2006. doi:[10.48550/arXiv.astro-ph/0612649](https://doi.org/10.48550/arXiv.astro-ph/0612649).
- S. Jain, T. Podladchikova, G. Chikunova, K. Dissauer, and A. M. Veronig. Coronal dimmings as indicators of early CME propagation direction. *Astron. Astrophys.*, 2023. doi:[10.48550/arXiv.2311.13942](https://doi.org/10.48550/arXiv.2311.13942).
- Chaowei Jiang, Xueshang Feng, ST Wu, and Qiang Hu. Magnetohydrodynamic simulation of a sigmoid eruption of active region 11283. *The Astrophysical Journal Letters*, 771(2):L30, 2013a. doi:[10.1088/2041-8205/771/2/L30](https://doi.org/10.1088/2041-8205/771/2/L30).
- Chaowei Jiang, ST Wu, Xueshang Feng, and Qiang Hu. Formation and eruption of an active region sigmoid. i. a study by nonlinear force-free field modeling. *The Astrophysical Journal*, 780(1):55, 2013b. doi:[10.1088/0004-637X/780/1/55](https://doi.org/10.1088/0004-637X/780/1/55).
- Yunchun Jiang, Liheng Yang, Kejun Li, and Dongbai Ren. Coronal and chromospheric dimmings during a halo-type cme event. *The Astrophysical Journal Letters*, 662(2):L131, 2007. doi:[10.1086/519490](https://doi.org/10.1086/519490).
- M. Jin, M. D. Ding, P. F. Chen, C. Fang, and S. Imada. Coronal Mass Ejection Induced Outflows Observed with Hinode/EIS. *Astrophys. J.*, 702(1):27–38, Sep 2009. doi:[10.1088/0004-637X/702/1/27](https://doi.org/10.1088/0004-637X/702/1/27).
- Meng Jin, Mark C. M. Cheung, Marc L. DeRosa, Nariaki V. Nitta, and Carolus J. Schrijver. Coronal Mass Ejections and Dimmings: A Comparative Study Using MHD Simulations and SDO Observations. *Astrophys. J.*, 928(2):154, April 2022. doi:[10.3847/1538-4357/ac589b](https://doi.org/10.3847/1538-4357/ac589b).
- Reetika Joshi. Study of Solar Jets and Related Flares. *arXiv e-prints*, art. arXiv:2206.02478, June 2022. doi:[10.48550/arXiv.2206.02478](https://doi.org/10.48550/arXiv.2206.02478).
- S. W. Kahler and H. S. Hudson. Origin and development of transient coronal holes. *J. Geophys. Res.*, 106:29239–29248, December 2001. doi:[10.1029/2001JA000127](https://doi.org/10.1029/2001JA000127).
- M. L. Kaiser, T. A. Kucera, J. M. Davila, O. C. St. Cyr, M. Guhathakurta, and E. Christian. The STEREO Mission: An Introduction. *Space Sci. Rev.*, 136: 5–16, April 2008. doi:[10.1007/s11214-007-9277-0](https://doi.org/10.1007/s11214-007-9277-0).
- Michael L Kaiser, TA Kucera, JM Davila, OC St Cyr, Madhulika Guhathakurta, and Eric Christian. The stereo mission: An introduction. *Space Science Reviews*, 136(1):5–16, 2008. doi:[10.1007/s11214-007-9277-0](https://doi.org/10.1007/s11214-007-9277-0).
- Ryuho Kataoka, Daikou Shiota, Hitoshi Fujiwara, Hidekatsu Jin, Chihiro Tao, Hiroyuki Shinagawa, and Yasunobu Miyoshi. Unexpected space weather causing the reentry of 38 Starlink satellites in February 2022. *Journal of Space Weather and Space Climate*, 12:41, October 2022. doi:[10.1051/swsc/2022034](https://doi.org/10.1051/swsc/2022034).
- Maria D Kazachenko, Benjamin J Lynch, Brian T Welsch, and Xudong Sun. A database of flare ribbon properties from the solar dynamics observatory. i. reconnection flux. *The Astrophysical Journal*, 845(1):49, 2017. doi:[10.3847/1538-4357/aa7ed6](https://doi.org/10.3847/1538-4357/aa7ed6).

- Maria D. Kazachenko, Marcel F. Albelo-Corchado, Cole A. Tamburri, and Brian T. Welsch. Invited Review: Short-term Variability with the Observations from the Helioseismic and Magnetic Imager (HMI) Onboard the Solar Dynamics Observatory (SDO): Insights into Flare Magnetism. *Solar Phys.*, 297(5):59, May 2022. doi:[10.1007/s11207-022-01987-6](https://doi.org/10.1007/s11207-022-01987-6).
- George V Khazanov. *Space Weather Fundamentals*. CRC Press, 2016. doi:[10.1201/9781315368474](https://doi.org/10.1201/9781315368474).
- I. W. Kienreich, M. Temmer, and A. M. Veronig. STEREO Quadrature Observations of the Three-Dimensional Structure and Driver of a Global Coronal Wave. *Astrophys. J. Lett.*, 703(2):L118–L122, October 2009. doi:[10.1088/0004-637X/703/2/L118](https://doi.org/10.1088/0004-637X/703/2/L118).
- Karl-Ludwig Klein, Sophie Musset, Nicole Vilmer, Carine Briand, Säm Krucker, Andrea Francesco Battaglia, Nina Dresing, Christian Palmroos, and Dale E. Gary. The relativistic solar particle event on 28 October 2021: Evidence of particle acceleration within and escape from the solar corona. *Astron. Astrophys.*, 663: A173, July 2022. doi:[10.1051/0004-6361/202243903](https://doi.org/10.1051/0004-6361/202243903).
- B. Kliem, J. Lin, T. G. Forbes, E. R. Priest, and T. Török. Catastrophe versus Instability for the Eruption of a Toroidal Solar Magnetic Flux Rope. *Astrophys. J.*, 789(1):46, July 2014. doi:[10.1088/0004-637X/789/1/46](https://doi.org/10.1088/0004-637X/789/1/46).
- James A Klimchuk. Key aspects of coronal heating. *Philosophical Transactions of the Royal Society A: Mathematical, Physical and Engineering Sciences*, 373(2042): 20140256, 2015. doi:[10.1098/rsta.2014.0256](https://doi.org/10.1098/rsta.2014.0256).
- MJ Koomen, CR Detwiler, GE Brueckner, HW Cooper, and R Tousey. White light coronagraph in oso-7. *Applied Optics*, 14(3):743–751, 1975. doi:[10.1364/AO.14.000743](https://doi.org/10.1364/AO.14.000743).
- Hannu E. J. Koskinen, Daniel N. Baker, André Balogh, Tamas Gombosi, Astrid Veronig, and Rudolf von Steiger. Achievements and Challenges in the Science of Space Weather. *Space Sci. Rev.*, 212(3-4):1137–1157, November 2017. doi:[10.1007/s11214-017-0390-4](https://doi.org/10.1007/s11214-017-0390-4).
- Hannu EJ Koskinen, Daniel N Baker, André Balogh, Tamas Gombosi, Astrid Veronig, and Rudolf von Steiger. Achievements and challenges in the science of space weather. *Space Science Reviews*, 212(3-4):1137–1157, 2017. doi:[10.1007/978-94-024-1588-9\\_1](https://doi.org/10.1007/978-94-024-1588-9_1).
- Takeo Kosugi, Taro Sakao, Satoshi Masuda, Kazuo Makishima, Mika Inada, Toshio Murakami, Yoshiaki Ogawara, Kentaro Yaji, and Kyoko Matsushita. The hard x-ray telescope (hxt) onboard yohkoh-its performance and some initial results. *Publications of the Astronomical Society of Japan*, 44:L45–L49, 1992. URL <https://ui.adsabs.harvard.edu/abs/1992PASJ...44L..45K>.

- Athanasios Kouloumvakos, Laura Rodríguez-García, Jan Gieseler, Daniel J. Price, Angelos Vourlidas, and Rami Vainio. PyThea: An open-source software package to perform 3D reconstruction of coronal mass ejections and shock waves. *Frontiers in Astronomy and Space Sciences*, 9:974137, September 2022. doi:10.3389/fspas.2022.974137.
- Kraaikamp and Verbeeck. Solar demon - an approach to detecting flares, dimmings, and euv waves on sdo/aia images. *J. Space Weather Space Clim.*, 5:A18, 2015a. doi:10.1051/swsc/2015019. URL <https://doi.org/10.1051/swsc/2015019>.
- Emil Kraaikamp and Cis Verbeeck. Solar Demon - an approach to detecting flares, dimmings, and EUV waves on SDO/AIA images. *Journal of Space Weather and Space Climate*, 5:A18, June 2015b. doi:10.1051/swsc/2015019.
- Larisza D Krista and Alysha A Reinard. Statistical study of solar dimmings using codit. *The Astrophysical Journal*, 839(1):50, 2017. doi:10.3847/1538-4357/aa6626.
- Larisza D Krista, Peter T Gallagher, and D Shaun Bloomfield. Short-term evolution of coronal hole boundaries. *The Astrophysical Journal Letters*, 731(2):L26, 2011. doi:10.1088/2041-8205/731/2/L26.
- Säm Krucker, G. J. Hurford, O. Grimm, S. Kögl, H. P. Gröbelbauer, L. Etesi, D. Casadei, A. Csillaghy, A. O. Benz, N. G. Arnold, F. Molendini, P. Orleanski, D. Schori, H. Xiao, M. Kuhar, N. Hochmuth, S. Felix, F. Schramka, S. Marcin, S. Kobler, L. Iseli, M. Dreier, H. J. Wiehl, L. Kleint, M. Battaglia, E. Lastufka, H. Sathiapal, K. Lapadula, M. Bednarzik, G. Birrer, St. Stutz, Ch. Wild, F. Marone, K. R. Skup, A. Cichocki, K. Ber, K. Rutkowski, W. Bujwan, G. Juchnikowski, M. Winkler, M. Darmetko, M. Michalska, K. Seweryn, A. Białek, P. Osica, J. Sylwester, M. Kowalinski, D. Ścisłowski, M. Siarkowski, M. Stęślicki, T. Mrozek, P. Podgórski, A. Meuris, O. Limousin, O. Gevin, I. Le Mer, S. Brun, A. Strugarek, N. Vilmer, S. Musset, M. Maksimović, F. Fárnik, Z. Kozáček, J. Kašparová, G. Mann, H. Önel, A. Warmuth, J. Rendtel, J. Anderson, S. Bauer, F. Dionies, J. Paschke, D. Plüschke, M. Woche, F. Schuller, A. M. Veronig, E. C. M. Dickson, P. T. Gallagher, S. A. Maloney, D. S. Bloomfield, M. Piana, A. M. Massone, F. Benvenuto, P. Massa, R. A. Schwartz, B. R. Dennis, H. F. van Beek, J. Rodríguez-Pacheco, and R. P. Lin. The Spectrometer/Telescope for Imaging X-rays (STIX). *Astron. Astrophys.*, 642:A15, October 2020. doi:10.1051/0004-6361/201937362.
- Ryun-Young Kwon and Angelos Vourlidas. Investigating the Wave Nature of the Outer Envelope of Halo Coronal Mass Ejections. *Astrophys. J.*, 836(2):246, February 2017. doi:10.3847/1538-4357/aa5b92.
- Ryun-Young Kwon and Angelos Vourlidas. The density compression ratio of shock fronts associated with coronal mass ejections. *Journal of Space Weather and Space Climate*, 8:A08, February 2018. doi:10.1051/swsc/2017045.
- Ryun-Young Kwon, Jie Zhang, and Angelos Vourlidas. Are Halo-like Solar Coronal Mass Ejections Merely a Matter of Geometric Projection Effects? *Astrophys. J. Lett.*, 799(2):L29, January 2015. doi:10.1088/2041-8205/799/2/L29.

- Philippe Lamy and Hugo Gilardy. The State of the White-Light Corona over the Minimum and Ascending Phases of Solar Cycle 25 - Comparison with Past Cycles. *Solar Phys.*, 297(10):140, October 2022. doi:[10.1007/s11207-022-02057-7](https://doi.org/10.1007/s11207-022-02057-7).
- Philippe Lamy, Olivier Floyd, Brice Boclet, Julien Wojak, Hugo Gilardy, and Tatiana Barlyaeva. Coronal mass ejections over solar cycles 23 and 24. *Space Science Reviews*, 215, 2019. URL <https://api.semanticscholar.org/CorpusID:198459301>.
- LJ Lanzerotti. Engineering issues in space weather. *Modern Radio Science 1999*, pages 25–50, 1999. doi:[10.1029/GM125p0011](https://doi.org/10.1029/GM125p0011).
- D. Lario, R. Y. Kwon, A. Vourlidas, N. E. Raouafi, D. K. Haggerty, G. C. Ho, B. J. Anderson, A. Papaioannou, R. Gómez-Herrero, N. Dresing, and P. Riley. Longitudinal Properties of a Widespread Solar Energetic Particle Event on 2014 February 25: Evolution of the Associated CME Shock. *Astrophys. J.*, 819(1):72, March 2016. doi:[10.3847/0004-637X/819/1/72](https://doi.org/10.3847/0004-637X/819/1/72).
- James R Lemen, David J Akin, Paul F Boerner, Catherine Chou, Jerry F Drake, Dexter W Duncan, Christopher G Edwards, Frank M Friedlaender, Gary F Heyman, Neal E Hurlburt, et al. The atmospheric imaging assembly (aia) on the solar dynamics observatory (sdo). In *The Solar Dynamics Observatory*, pages 17–40. Springer, 2011. doi:[10.1007/s11207-008-9255-z](https://doi.org/10.1007/s11207-008-9255-z).
- James R. Lemen, Alan M. Title, David J. Akin, Paul F. Boerner, Catherine Chou, Jerry F. Drake, Dexter W. Duncan, Christopher G. Edwards, Frank M. Friedlaender, Gary F. Heyman, Neal E. Hurlburt, Noah L. Katz, Gary D. Kushner, Michael Levay, Russell W. Lindgren, Dnyanesh P. Mathur, Edward L. McFeaters, Sarah Mitchell, Roger A. Rehse, Carolus J. Schrijver, Larry A. Springer, Robert A. Stern, Theodore D. Tarbell, Jean-Pierre Wuelser, C. Jacob Wolfson, Carl Yanari, Jay A. Bookbinder, Peter N. Cheimets, David Caldwell, Edward E. Deluca, Richard Gates, Leon Golub, Sang Park, William A. Podgorski, Rock I. Bush, Philip H. Scherrer, Mark A. Gummin, Peter Smith, Gary Auken, Paul Jerram, Peter Pool, Regina Soufli, David L. Windt, Sarah Beardsley, Matthew Clapp, James Lang, and Nicholas Waltham. The Atmospheric Imaging Assembly (AIA) on the Solar Dynamics Observatory (SDO). *Solar Phys.*, 275(1-2):17–40, Jan 2012. doi:[10.1007/s11207-011-9776-8](https://doi.org/10.1007/s11207-011-9776-8).
- D. J. Lewis and G. M. Simnett. Bulk flow velocities in the solar corona at solar maximum. *Mon. Not. Roy. Astron. Soc.*, 333(4):969–976, July 2002. doi:[10.1046/j.1365-8711.2002.05483.x](https://doi.org/10.1046/j.1365-8711.2002.05483.x).
- K.J. Li, Wen Feng, and Fei Li. Predicting the maximum amplitude of solar cycle 25 and its timing. *Journal of Atmospheric and Solar-Terrestrial Physics*, 135:72–76, 2015. URL <https://api.semanticscholar.org/CorpusID:124557941>.
- Qiang Li, Miao Wan, Shuguang Zeng, Sheng Zheng, and Linhua Deng. Predicting the 25th solar cycle using deep learning methods based on sunspot area data. *Research in Astronomy and Astrophysics*, 21, 2021. URL <https://api.semanticscholar.org/CorpusID:233992857>.

- Ting Li and Jun Zhang. Fine-scale structures of flux ropes tracked by erupting material. *The Astrophysical Journal Letters*, 770(2):L25, 2013. doi:[10.1088/2041-8205/770/2/L25](https://doi.org/10.1088/2041-8205/770/2/L25).
- P. C. Liewer, E. M. de Jong, J. R. Hall, R. A. Howard, W. T. Thompson, J. L. Culhane, L. Bone, and L. van Driel-Gesztelyi. Stereoscopic Analysis of the 19 May 2007 Erupting Filament. *Solar Phys.*, 256(1-2):57–72, May 2009. doi:[10.1007/s11207-009-9363-4](https://doi.org/10.1007/s11207-009-9363-4).
- P. C. Liewer, J. R. Hall, R. A. Howard, E. M. De Jong, W. T. Thompson, and A. Thernisien. Stereoscopic analysis of STEREO/SECCHI data for CME trajectory determination. *Journal of Atmospheric and Solar-Terrestrial Physics*, 73(10):1173–1186, June 2011. doi:[10.1016/j.jastp.2010.09.004](https://doi.org/10.1016/j.jastp.2010.09.004).
- J. Lin, J. C. Raymond, and A. A. van Ballegooijen. The Role of Magnetic Reconnection in the Observable Features of Solar Eruptions. *Astrophys. J.*, 602(1):422–435, February 2004. doi:[10.1086/380900](https://doi.org/10.1086/380900).
- Ying Liu, Arnaud Thernisien, Janet G. Luhmann, Angelos Vourlidas, Jackie A. Davies, Robert P. Lin, and Stuart D. Bale. Reconstructing Coronal Mass Ejections with Coordinated Imaging and in Situ Observations: Global Structure, Kinematics, and Implications for Space Weather Forecasting. *Astrophys. J.*, 722(2):1762–1777, October 2010. doi:[10.1088/0004-637X/722/2/1762](https://doi.org/10.1088/0004-637X/722/2/1762).
- Ying Liu, Arnaud Thernisien, Janet G. Luhmann, Angelos Vourlidas, Jackie A. Davies, Robert P. Lin, and Stuart D. Bale. Reconstructing coronal mass ejections with coordinated imaging and in situ observations: Global structure, kinematics, and implications for space weather forecasting. *The Astrophysical Journal*, 722(2):1762, 2010. doi:[10.1088/0004-637X/722/2/1762](https://doi.org/10.1088/0004-637X/722/2/1762).
- Ying D. Liu, Janet G. Luhmann, Noé Lugaz, Christian Möstl, Jackie A. Davies, Stuart D. Bale, and Robert P. Lin. On sun-to-earth propagation of coronal mass ejections. *The astrophysical journal*, 769(1):45, 2013. doi:[10.1088/0004-637X/769/1/45](https://doi.org/10.1088/0004-637X/769/1/45).
- Fernando M. López, M. Hebe Cremades, Federico A. Nuevo, Laura A. Balmaceda, and Alberto M. Vásquez. Mass-loss evolution in the EUV low corona from SDO/AIA data. *Solar Physics*, 292(1):6, 2017. doi:[10.1007/s11207-016-1031-x](https://doi.org/10.1007/s11207-016-1031-x).
- FM. López, H. Cremades, Laura Antonia Balmaceda, Federico Alberto Nuevo, and AM. Vásquez. Estimating the mass of CMEs from the analysis of EUV dimmings. *Astronomy & Astrophysics*, 627:A8, 2019. doi:[10.1051/0004-6361/201834163](https://doi.org/10.1051/0004-6361/201834163).
- B. C. Low and J. R. Hundhausen. Magnetostatic Structures of the Solar Corona. II. The Magnetic Topology of Quiescent Prominences. *Astrophys. J.*, 443:818, April 1995. doi:[10.1086/175572](https://doi.org/10.1086/175572).
- D. H. Mackay, J. T. Karpen, J. L. Ballester, B. Schmieder, and G. Aulanier. Physics of Solar Prominences: II—Magnetic Structure and Dynamics. *Space Sci. Rev.*, 151(4):333–399, April 2010. doi:[10.1007/s11214-010-9628-0](https://doi.org/10.1007/s11214-010-9628-0).

- Cristina Hemilse Mandrini, Maria Soledad Nakwacki, G Attrill, Lidia van Driel-Gesztelyi, Pascal Démoulin, S Dasso, and H Elliott. Are cme-related dimmings always a simple signature of interplanetary magnetic cloud footpoints? *Solar Physics*, 244(1-2):25–43, 2007. doi:[10.1007/s11207-007-9020-8](https://doi.org/10.1007/s11207-007-9020-8).
- Darije Maričić, Bojan Vršnak, Andrew L Stanger, Astrid M Veronig, Manuela Temmer, and Dragan Roša. Acceleration phase of coronal mass ejections: II. synchronization of the energy release in the associated flare. *Solar Physics*, 241:99–112, 2007. doi:[10.1007/s11207-006-0290-3](https://doi.org/10.1007/s11207-006-0290-3).
- Sara F. Martin. Conditions for the Formation and Maintenance of Filaments (Invited Review). *Solar Phys.*, 182(1):107–137, September 1998. doi:[10.1023/A:1005026814076](https://doi.org/10.1023/A:1005026814076).
- James Paul Mason, Thomas N Woods, Amir Caspi, Barbara J Thompson, and Rachel A Hock. Mechanisms and observations of coronal dimming for the 2010 august 7 event. *The Astrophysical Journal*, 789(1):61, 2014. doi:[10.1088/0004-637X/789/1/61](https://doi.org/10.1088/0004-637X/789/1/61).
- James Paul Mason, Thomas N Woods, David F Webb, Barbara J Thompson, Robin C Colaninno, and Angelos Vourlidas. Relationship of euv irradiance coronal dimming slope and depth to coronal mass ejection speed and mass. *The Astrophysical Journal*, 830(1):20, 2016. doi:[10.3847/0004-637X/830/1/20](https://doi.org/10.3847/0004-637X/830/1/20).
- James Paul Mason, Phillip C. Chamberlin, Daniel Seaton, Joan Burkepile, Robin Colaninno, Karin Dissauer, Francis G. Eparvier, Yuhong Fan, Sarah Gibson, Andrew R. Jones, Christina Kay, Michael Kirk, Richard Kohnert, W. Dean Pesnell, Barbara J. Thompson, Astrid M. Veronig, Matthew J. West, David Windt, and Thomas N. Woods. SunCET: The Sun Coronal Ejection Tracker Concept. *Journal of Space Weather and Space Climate*, 11:20, January 2021. doi:[10.1051/swsc/2021004](https://doi.org/10.1051/swsc/2021004).
- M. L. Mays, A. Taktakishvili, A. Pulkkinen, P. J. MacNeice, L. Rastätter, D. Odstrcil, L. K. Jian, I. G. Richardson, J. A. LaSota, Y. Zheng, and M. M. Kuznetsova. Ensemble Modeling of CMEs Using the WSA-ENLIL+Cone Model. *Solar Phys.*, 290(6):1775–1814, June 2015. doi:[10.1007/s11207-015-0692-1](https://doi.org/10.1007/s11207-015-0692-1).
- Scott W McIntosh, Robert J Leamon, and Ricky Egeland. Deciphering solar magnetic activity: The (solar) hale cycle terminator of 2021. *Frontiers in Astronomy and Space Sciences*, 10:16, 2023.
- G. Michalek, N. Gopalswamy, S. Yashiro, and K. Bronarska. Dynamics of CMEs in the LASCO Field of View. *Solar Phys.*, 290(3):903–917, March 2015. doi:[10.1007/s11207-015-0653-8](https://doi.org/10.1007/s11207-015-0653-8).
- M. Mierla, J. Davila, W. Thompson, B. Inhester, N. Srivastava, M. Kramar, O. C. St. Cyr, G. Stenborg, and R. A. Howard. A Quick Method for Estimating the Propagation Direction of Coronal Mass Ejections Using STEREO-COR1 Images. *Solar Phys.*, 252(2):385–396, November 2008. doi:[10.1007/s11207-008-9267-8](https://doi.org/10.1007/s11207-008-9267-8).

- M. Mierla, B. Inhester, A. Antunes, Y. Boursier, J. P. Byrne, R. Colaninno, J. Davila, C. A. de Koning, P. T. Gallagher, S. Gissot, R. A. Howard, T. A. Howard, M. Kramar, P. Lamy, P. C. Liewer, S. Maloney, C. Marqué, R. T. J. McAteer, T. Moran, L. Rodriguez, N. Srivastava, O. C. St. Cyr, G. Stenborg, M. Temmer, A. Thernisien, A. Vourlidas, M. J. West, B. E. Wood, and A. N. Zhukov. On the 3-D reconstruction of Coronal Mass Ejections using coronagraph data. *Annales Geophysicae*, 28(1):203–215, January 2010. doi:[10.5194/angeo-28-203-2010](https://doi.org/10.5194/angeo-28-203-2010).
- M. Mierla, D. B. Seaton, D. Berghmans, I. Chifu, A. De Groof, B. Inhester, L. Rodriguez, G. Stenborg, and A. N. Zhukov. Study of a Prominence Eruption using PROBA2/SWAP and STEREO/EUVI Data. *Solar Phys.*, 286(1):241–253, August 2013. doi:[10.1007/s11207-012-9965-0](https://doi.org/10.1007/s11207-012-9965-0).
- M. Mierla, A. N. Zhukov, D. Berghmans, S. Parenti, F. Auchère, P. Heinzel, D. B. Seaton, E. Palmerio, S. Ježič, J. Janssens, E. Kraaikamp, B. Nicula, D. M. Long, L. A. Hayes, I. C. Jebaraj, D. C. Talpeanu, E. D’Huys, L. Dolla, S. Gissot, J. Magdalenic, L. Rodriguez, S. Shestov, K. Stegen, C. Verbeeck, C. Sasso, M. Romoli, and V. Andretta. Prominence eruption observed in He II 304 Å up to  $>6 R_{\odot}$  by EUI/FSI aboard Solar Orbiter. *Astron. Astrophys.*, 662:L5, June 2022. doi:[10.1051/0004-6361/202244020](https://doi.org/10.1051/0004-6361/202244020).
- Mark Moldwin. *An introduction to space weather*. Cambridge University Press, 2008. doi:[doi.org/10.1017/CBO9780511801365](https://doi.org/10.1017/CBO9780511801365).
- Ronald L. Moore, Alphonse C. Sterling, Hugh S. Hudson, and James R. Lemen. Onset of the Magnetic Explosion in Solar Flares and Coronal Mass Ejections. *Astrophys. J.*, 552(2):833–848, May 2001. doi:[10.1086/320559](https://doi.org/10.1086/320559).
- Thomas G. Moran and Joseph M. Davila. Three-Dimensional Polarimetric Imaging of Coronal Mass Ejections. *Science*, 305(5680):66–71, July 2004. doi:[10.1126/science.1098937](https://doi.org/10.1126/science.1098937).
- Christian Möstl, Tanja Rollett, Rudy A. Frahm, Ying D. Liu, David M. Long, Robin C. Colaninno, Martin A. Reiss, Manuela Temmer, Charles J. Farrugia, Arik Posner, Mateja Dumbović, Miho Janvier, Pascal Démoulin, Peter Boakes, Andy Devos, Emil Kraaikamp, Mona L. Mays, and Bojan Vršnak. Strong coronal channelling and interplanetary evolution of a solar storm up to Earth and Mars. *Nature Communications*, 6:7135, May 2015. doi:[10.1038/ncomms8135](https://doi.org/10.1038/ncomms8135).
- Nicole Muhr, Astrid Maria Veronig, Ines Waltraud Kienreich, Bojan Vršnak, Manuela Temmer, and Bianca Maria Bein. Statistical analysis of large-scale euv waves observed by stereo/euvi. *Solar physics*, 289(12):4563–4588, 2014. doi:[10.1007/s11207-014-0563-6](https://doi.org/10.1007/s11207-014-0563-6).
- D. Müller, B. Nicula, S. Felix, F. Verstringe, B. Bourgoignie, A. Csillaghy, D. Berghmans, P. Jiggins, J. P. García-Ortiz, J. Ireland, S. Zahniy, and B. Fleck. JHelioviewer. Time-dependent 3D visualisation of solar and heliospheric data. *Astron. Astrophys.*, 606:A10, September 2017. doi:[10.1051/0004-6361/201730893](https://doi.org/10.1051/0004-6361/201730893).

- D. Müller, O. C. St. Cyr, I. Zouganelis, H. R. Gilbert, R. Marsden, T. Nieves-Chinchilla, E. Antonucci, F. Auchère, D. Berghmans, T. S. Horbury, R. A. Howard, S. Krucker, M. Maksimovic, C. J. Owen, P. Rochus, J. Rodriguez-Pacheco, M. Romoli, S. K. Solanki, R. Bruno, M. Carlsson, A. Fludra, L. Harra, D. M. Hassler, S. Livi, P. Louarn, H. Peter, U. Schühle, L. Teriaca, J. C. del Toro Iniesta, R. F. Wimmer-Schweingruber, E. Marsch, M. Velli, A. De Groof, A. Walsh, and D. Williams. The Solar Orbiter mission. Science overview. *Astron. Astrophys.*, 642:A1, October 2020. doi:[10.1051/0004-6361/202038467](https://doi.org/10.1051/0004-6361/202038467).
- Andrés Muñoz-Jaramillo, Dibyendu Nandy, and Petrus CH Martens. Helioseismic data inclusion in solar dynamo models. *The Astrophysical Journal*, 698(1):461, 2009. doi:[10.1088/0004-637X/698/1/461](https://doi.org/10.1088/0004-637X/698/1/461).
- Nariaki V Nitta, Carolus J Schrijver, Wei Liu, et al. Large-scale coronal propagating fronts in solar eruptions as observed by the atmospheric imaging assembly on board the solar dynamics observatory—an ensemble study. *The Astrophysical Journal*, 776(1):58, 2013. doi:[10.1088/0004-637X/776/1/58](https://doi.org/10.1088/0004-637X/776/1/58).
- Jennifer P. O’Hara, Marilena Mierla, Olena Podladchikova, Elke D’Huys, and Matthew J. West. Exceptional Extended Field-of-view Observations by PROBA2/SWAP on 2017 April 1 and 3. *Astrophys. J.*, 883(1):59, September 2019. doi:[10.3847/1538-4357/ab3b08](https://doi.org/10.3847/1538-4357/ab3b08).
- O. Olmedo, J. Zhang, H. Wechsler, A. Poland, and K. Borne. Automatic Detection and Tracking of Coronal Mass Ejections in Coronagraph Time Series. *Solar Phys.*, 248(2):485–499, April 2008. doi:[10.1007/s11207-007-9104-5](https://doi.org/10.1007/s11207-007-9104-5).
- Veronica Ontiveros and Angelos Vourlidas. Quantitative measurements of coronal mass ejection-driven shocks from lasco observations. *The Astrophysical Journal*, 693(1):267, 2009. doi:[10.1088/0004-637X/693/1/267](https://doi.org/10.1088/0004-637X/693/1/267).
- Mathew J. Owens and Robert J. Forsyth. The heliospheric magnetic field. *Living Reviews in Solar Physics*, 10(1):5, Nov 2013. ISSN 1614-4961. doi:[10.12942/lrsp-2013-5](https://doi.org/10.12942/lrsp-2013-5). URL <https://doi.org/10.12942/lrsp-2013-5>.
- Massimo Palomba and Juha-Pekka Luntama. Vigil: ESA Space Weather Mission in L5. In *44th COSPAR Scientific Assembly. Held 16-24 July*, volume 44, page 3544, July 2022. URL <https://ui.adsabs.harvard.edu/abs/2022cosp...44.3544P>.
- A. Papaioannou, A. Kouloumvakos, A. Mishev, R. Vainio, I. Usoskin, K. Herbst, A. P. Rouillard, A. Anastasiadis, J. Gieseler, R. Wimmer-Schweingruber, and P. Kühl. The first ground-level enhancement of solar cycle 25 on 28 October 2021. *Astron. Astrophys.*, 660:L5, April 2022. doi:[10.1051/0004-6361/202142855](https://doi.org/10.1051/0004-6361/202142855).
- Eugene N Parker. The formation of sunspots from the solar toroidal field. *The astrophysical journal*, 121:491, 1955. doi:[10.1086/146010](https://doi.org/10.1086/146010).
- Jay M. Pasachoff, Christian Lockwood, Erin Meadors, Ross Yu, Cielo Perez, Marcos A. Peñaloza-Murillo, Daniel B. Seaton, Aris Voulgaris, Ron Dantowitz, Vojtech Rušin, and Thanasis Economou. Images and Spectra of the 2017 Total

- Solar Eclipse Corona From Our Oregon Site. *Frontiers in Astronomy and Space Sciences*, 5:37, October 2018. doi:[10.3389/fspas.2018.00037](https://doi.org/10.3389/fspas.2018.00037).
- Spiros Patsourakos and Angelos Vourlidas. On the nature and genesis of euv waves: a synthesis of observations from soho, stereo, sdo, and hinode (invited review). *Solar Physics*, 281(1):187–222, 2012. doi:[10.1007/s11207-012-9988-6](https://doi.org/10.1007/s11207-012-9988-6).
- W. Dean Pesnell. Solar Cycle Predictions (Invited Review). *Solar Phys.*, 281(1): 507–532, November 2012. doi:[10.1007/s11207-012-9997-5](https://doi.org/10.1007/s11207-012-9997-5).
- W. Dean Pesnell. Lessons learned from predictions of Solar Cycle 24. *Journal of Space Weather and Space Climate*, 10:60, October 2020. doi:[10.1051/swsc/2020060](https://doi.org/10.1051/swsc/2020060).
- W Dean Pesnell, B J Thompson, and PC Chamberlin. The solar dynamics observatory (sdo). In *The solar dynamics observatory*, pages 3–15. Springer, 2011. doi:[10.1007/978-3-319-02847-7\\_16-1](https://doi.org/10.1007/978-3-319-02847-7_16-1).
- H Peter. Composition of the solar chromosphere and transition region. *Advances in Space Research*, 30:13–22, 12 2002. doi:[10.1016/S0273-1177\(02\)00171-0](https://doi.org/10.1016/S0273-1177(02)00171-0).
- Kristóf Petrovay. Solar cycle prediction. *Living Reviews in Solar Physics*, 17(1):2, March 2020. doi:[10.1007/s41116-020-0022-z](https://doi.org/10.1007/s41116-020-0022-z).
- A. A. Petrukovich, H. V. Malova, V. Yu. Popov, E. V. Maiewski, V. V. Izmodenov, O. A. Katushkina, A. A. Vinogradov, M. O. Riazantseva, L. S. Rakhmanova, T. V. Podladchikova, G. N. Zastenker, Yu. I. Yermolaev, I. G. Lodkina, and L. S. Chesalin. Modern view of the solar wind from micro to macro scales. *Physics Uspekhi*, 63(8):801–811, November 2020. doi:[10.3367/UFNe.2019.06.038677](https://doi.org/10.3367/UFNe.2019.06.038677).
- Olena Podladchikova and David Berghmans. Automated detection of eit waves and dimmings. *Solar Physics*, 228(1-2):265–284, 2005. doi:[10.1007/S11207-005-5373-Z](https://doi.org/10.1007/S11207-005-5373-Z).
- Tatiana Podladchikova, Ronald Van der Linden, and Astrid M Veronig. Sunspot number second differences as a precursor of the following 11-year sunspot cycle. *The Astrophysical Journal*, 850(1):81, 2017. doi:[10.3847/1538-4357/aa93ef](https://doi.org/10.3847/1538-4357/aa93ef).
- Tatiana Podladchikova, Astrid M. Veronig, Karin Dissauer, Manuela Temmer, and Olena Podladchikova. Three-dimensional Reconstructions of Extreme-ultraviolet Wave Front Heights and Their Influence on Wave Kinematics. *Astrophys. J.*, 877(2):68, June 2019. doi:[10.3847/1538-4357/ab1b3a](https://doi.org/10.3847/1538-4357/ab1b3a).
- Tatiana Podladchikova, Astrid M Veronig, Karin Dissauer, Manuela Temmer, and Olena Podladchikova. Three-dimensional reconstructions of extreme-ultraviolet wave front heights and their influence on wave kinematics. *The Astrophysical Journal*, 877(2):68, 2019a.
- Tatiana Podladchikova, Astrid M Veronig, Karin Dissauer, Manuela Temmer, et al. 3d reconstructions of euv wave front heights and their influence on wave kinematics. *The Astrophysical Journal*, 2019b. doi:[10.3847/1538-4357/ab1b3a](https://doi.org/10.3847/1538-4357/ab1b3a).

- Avijeet Prasad, Karin Dissauer, Qiang Hu, R Bhattacharyya, Astrid M Veronig, Sanjay Kumar, and Bhuwan Joshi. Magnetohydrodynamic simulation of magnetic null-point reconnections and coronal dimmings during the x2. 1 flare in noaa ar 11283. *The Astrophysical Journal*, 903(2):129, 2020. doi:[10.3847/1538-4357/abb8d2](https://doi.org/10.3847/1538-4357/abb8d2).
- E. R. Priest and T. G. Forbes. The magnetic nature of solar flares. *Astron. Astrophys. Rev.*, 10(4):313–377, January 2002. doi:[10.1007/s001590100013](https://doi.org/10.1007/s001590100013).
- Antti Pulkkinen, Sture Lindahl, Ari Viljanen, and Risto Pirjola. Geomagnetic storm of 29-31 October 2003: Geomagnetically induced currents and their relation to problems in the Swedish high-voltage power transmission system. *Space Weather*, 3(8):S08C03, August 2005. doi:[10.1029/2004SW000123](https://doi.org/10.1029/2004SW000123).
- Tuija Pulkkinen. Space Weather: Terrestrial Perspective. *Living Reviews in Solar Physics*, 4(1):1, May 2007. doi:[10.12942/lrsp-2007-1](https://doi.org/10.12942/lrsp-2007-1).
- Jiong Qiu and Jianxia Cheng. Gradual solar coronal dimming and evolution of coronal mass ejection in the early phase. *The Astrophysical Journal Letters*, 838(1):L6, 2017. doi:[10.3847/2041-8213/aa6798](https://doi.org/10.3847/2041-8213/aa6798).
- N. E. Raouafi, L. Matteini, J. Squire, S. T. Badman, M. Velli, K. G. Klein, C. H. K. Chen, W. H. Matthaeus, A. Szabo, M. Linton, R. C. Allen, J. R. Szalay, R. Bruno, R. B. Decker, M. Akhavan-Tafti, O. V. Agapitov, S. D. Bale, R. Bandyopadhyay, K. Battams, L. Berčič, S. Bourouaine, T. A. Bowen, C. Cattell, B. D. G. Chandran, R. Chhiber, C. M. S. Cohen, R. D’Amicis, J. Giacalone, P. Hess, R. A. Howard, T. S. Horbury, V. K. Jagarlamudi, C. J. Joyce, J. C. Kasper, J. Kinnison, R. Laker, P. Liewer, D. M. Malaspina, I. Mann, D. J. McComas, T. Niembro-Hernandez, T. Nieves-Chinchilla, O. Panasenco, P. Pokorný, A. Puschak, M. Pulupa, J. C. Perez, P. Riley, A. P. Rouillard, C. Shi, G. Stenborg, A. Tenerani, J. L. Verniero, N. Viall, A. Vourlidas, B. E. Wood, L. D. Woodham, and T. Woolley. Parker Solar Probe: Four Years of Discoveries at Solar Cycle Minimum. *Space Sci. Rev.*, 219(1):8, February 2023. doi:[10.1007/s11214-023-00952-4](https://doi.org/10.1007/s11214-023-00952-4).
- AA Reinard and DA Biesecker. Coronal mass ejection-associated coronal dimmings. *The Astrophysical Journal*, 674(1):576, 2008. doi:[10.1086/525269](https://doi.org/10.1086/525269).
- I. G. Richardson, T. T. von Rosenvinge, and H. V. Cane. The Properties of Solar Energetic Particle Event-Associated Coronal Mass Ejections Reported in Different CME Catalogs. *Solar Phys.*, 290(6):1741–1759, June 2015. doi:[10.1007/s11207-015-0701-4](https://doi.org/10.1007/s11207-015-0701-4).
- Thomas R. Rimmele, Mark Warner, Stephen L. Keil, Philip R. Goode, Michael Knölker, Jeffrey R. Kuhn, Robert R. Rosner, Joseph P. McMullin, Roberto Casini, Haosheng Lin, Friedrich Wöger, Oskar von der Lühe, Alexandra Tritschler, Alisdair Davey, Alfred de Wijn, David F. Elmore, André Fehlmann, David M. Harrington, Sarah A. Jaeggli, Mark P. Rast, Thomas A. Schad, Wolfgang Schmidt, Mihalis Mathioudakis, Donald L. Mickey, Tetsu Anan, Christian Beck, Heather K.

- Marshall, Paul F. Jeffers, Jacobus M. Oschmann, Andrew Beard, David C. Berst, Bruce A. Cowan, Simon C. Craig, Eric Cross, Bryan K. Cummings, Colleen Donnelly, Jean-Benoit de Vanssay, Arthur D. Eigenbrot, Andrew Ferayorni, Christopher Foster, Chriselle Ann Galapon, Christopher Gedrites, Kerry Gonzales, Bret D. Goodrich, Brian S. Gregory, Stephanie S. Guzman, Stephen Guzzo, Steve Hegwer, Robert P. Hubbard, John R. Hubbard, Erik M. Johansson, Luke C. Johnson, Chen Liang, Mary Liang, Isaac McQuillen, Christopher Mayer, Karl Newman, Brialyn Onodera, LeEllen Phelps, Myles M. Puentes, Christopher Richards, Lukas M. Rimmele, Predrag Sekulic, Stephan R. Shimko, Brett E. Simison, Brett Smith, Erik Starman, Stacey R. Sueoka, Richard T. Summers, Aimee Szabo, Louis Szabo, Stephen B. Wampler, Timothy R. Williams, and Charles White. The Daniel K. Inouye Solar Telescope - Observatory Overview. *Solar Phys.*, 295(12):172, December 2020. doi:[10.1007/s11207-020-01736-7](https://doi.org/10.1007/s11207-020-01736-7).
- E. Robbrecht, D. Berghmans, and R. A. M. Van der Linden. Automated LASCO CME Catalog for Solar Cycle 23: Are CMEs Scale Invariant? *Astrophys. J.*, 691(2):1222–1234, February 2009. doi:[10.1088/0004-637X/691/2/1222](https://doi.org/10.1088/0004-637X/691/2/1222).
- P. Rochus, F. Auchère, D. Berghmans, L. Harra, W. Schmutz, U. Schühle, P. Addison, T. Appourchaux, R. Aznar Cuadrado, D. Baker, J. Barbay, D. Bates, A. Ben-Moussa, M. Bergmann, C. Beurthe, B. Borgo, K. Bonte, M. Bouzit, L. Bradley, V. Büchel, E. Buchlin, J. Büchner, F. Cabé, L. Cadiergues, M. Chaigneau, B. Chares, C. Choque Cortez, P. Coker, M. Condamin, S. Coumar, W. Curdt, J. Cutler, D. Davies, G. Davison, J. M. Defise, G. Del Zanna, F. Delmotte, V. Delouille, L. Dolla, C. Dumesnil, F. Dürig, R. Enge, S. François, J. J. Fourmond, J. M. Gillis, B. Giordanengo, S. Gissot, L. M. Green, N. Guerreiro, A. Guilbaud, M. Gyo, M. Haberreiter, A. Hafiz, M. Hailey, J. P. Halain, J. Hansotte, C. Hecquet, K. Heerlein, M. L. Hellin, S. Hemsley, A. Hermans, V. Hervier, J. F. Hochedez, Y. Houbrechts, K. Ihsan, L. Jacques, A. Jérôme, J. Jones, M. Kahle, T. Kennedy, M. Klaproth, M. Kolleck, S. Koller, E. Kotsialos, E. Kraaikamp, P. Langer, A. Lawrenson, J. C. Le Clech', C. Lenaerts, S. Liebecq, D. Linder, D. M. Long, B. Mampaey, D. Markiewicz-Innes, B. Marquet, E. Marsch, S. Matthews, E. Mazy, A. Mazzoli, S. Meining, E. Meltchakov, R. Mercier, S. Meyer, M. Monnecke, F. Monfort, G. Morinaud, F. Moron, L. Mountney, R. Müller, B. Nicula, S. Parenti, H. Peter, D. Pfiffner, A. Philippon, I. Phillips, J. Y. Plessier, E. Pyllyser, F. Rabecki, M. F. Ravet-Krill, J. Rebellato, E. Renotte, L. Rodriguez, S. Roose, J. Rosin, L. Rossi, P. Roth, F. Rouesnel, M. Roulliay, A. Rousseau, K. Ruane, J. Scanlan, P. Schlatter, D. B. Seaton, K. Silliman, S. Smit, P. J. Smith, S. K. Solanki, M. Spescha, A. Spencer, K. Stegen, Y. Stockman, N. Szvec, C. Tamiatto, J. Tandy, L. Teriaca, C. Theobald, I. Tychon, L. van Driel-Gesztelyi, C. Verbeeck, J. C. Vial, S. Werner, M. J. West, D. Westwood, T. Wiegmann, G. Willis, B. Winter, A. Zerr, X. Zhang, and A. N. Zhukov. The Solar Orbiter EUV instrument: The Extreme Ultraviolet Imager. *Astron. Astrophys.*, 642:A8, October 2020. doi:[10.1051/0004-6361/201936663](https://doi.org/10.1051/0004-6361/201936663).
- Paolo Romano, Francesca Zuccarello, SL Guglielmino, F Berrilli, Roberto Bruno, V Carbone, Giuseppe Consolini, M De Lauretis, D Del Moro, A Elmhamdi, et al.

- Recurrent flares in active region noaa 11283. *Astronomy & Astrophysics*, 582:A55, 2015. doi:[10.1051/0004-6361/201525887](https://doi.org/10.1051/0004-6361/201525887).
- G. Ronca, G. Chikunova, T. Podladchikova, K. Dissauer, and A. Veronig. Recovery of the coronal dimmings. *Astron. Astrophys.*, under review.
- Iliia I. Roussev, Noé Lugaz, and Igor V. Sokolov. New Physical Insight on the Changes in Magnetic Topology during Coronal Mass Ejections: Case Studies for the 2002 April 21 and August 24 Events. *Astrophys. J. Lett.*, 668(1):L87–L90, October 2007. doi:[10.1086/522588](https://doi.org/10.1086/522588).
- Christopher Thomas Russell, JG Luhmann, and LK Jian. How unprecedented a solar minimum? *Reviews of Geophysics*, 48(2), 2010. doi:[10.1029/2009RG000316](https://doi.org/10.1029/2009RG000316).
- David M Rust. Coronal disturbances and their terrestrial effects. *Space Science Reviews*, 34(1):21–36, 1983. doi:[10.1007/978-94-009-7096-0\\_1](https://doi.org/10.1007/978-94-009-7096-0_1).
- S. Santandrea, K. Gantois, K. Strauch, F. Teston, Proba2 Project Team, E. Tilmans, C. Baijot, D. Gerrits, Proba2 Industry Team, A. de Groof, G. Schwehm, and J. Zender. PROBA2: Mission and Spacecraft Overview. *Solar Phys.*, 286(1): 5–19, August 2013. doi:[10.1007/s11207-013-0289-5](https://doi.org/10.1007/s11207-013-0289-5).
- Jonas Saqri, Astrid M. Veronig, Ewan C. M. Dickson, Tatiana Podladchikova, Alexander Warmuth, Hualin Xiao, Dale E. Gary, Andrea Francesco Battaglia, and Säm Krucker. Multi-point study of the energy release and impulsive CME dynamics in an eruptive C7 flare. *Astron. Astrophys.*, 672:A23, April 2023. doi:[10.1051/0004-6361/202245079](https://doi.org/10.1051/0004-6361/202245079).
- P. H. Scherrer, J. Schou, R. I. Bush, A. G. Kosovichev, R. S. Bogart, J. T. Hoeksema, Y. Liu, T. L. Duvall, J. Zhao, A. M. Title, C. J. Schrijver, T. D. Tarbell, and S. Tomczyk. The Helioseismic and Magnetic Imager (HMI) Investigation for the Solar Dynamics Observatory (SDO). *Solar Phys.*, 275(1-2):207–227, January 2012. doi:[10.1007/s11207-011-9834-2](https://doi.org/10.1007/s11207-011-9834-2).
- Philip Hanby Scherrer, Jesper Schou, RI Bush, AG Kosovichev, RS Bogart, JT Hoeksema, Y Liu, TL Duvall, J Zhao, CJ Schrijver, et al. The helioseismic and magnetic imager (hmi) investigation for the solar dynamics observatory (sdo). *Solar Physics*, 275(1):207–227, 2012. doi:[10.1007/s11207-011-9834-2](https://doi.org/10.1007/s11207-011-9834-2).
- Rainer Schwenn. Space weather: The solar perspective. *Living Reviews in Solar Physics*, 3(1):2, Aug 2006. ISSN 1614-4961. doi:[10.12942/lrsp-2006-2](https://doi.org/10.12942/lrsp-2006-2). URL <https://doi.org/10.12942/lrsp-2006-2>.
- Yulia Shugay, Vladimir Kalegaev, Ksenia Kaportseva, Vladimir Slemzin, Denis Rodkin, and Valeriy Eremeev. Modeling of Solar Wind Disturbances Associated with Coronal Mass Ejections and Verification of the Forecast Results. *Universe*, 8(11): 565, October 2022. doi:[10.3390/universe8110565](https://doi.org/10.3390/universe8110565).
- P. J. A. Simões and E. P. Kontar. Implications for electron acceleration and transport from non-thermal electron rates at looptop and footpoint sources in solar flares. *Astron. Astrophys.*, 551:A135, March 2013. doi:[10.1051/0004-6361/201220304](https://doi.org/10.1051/0004-6361/201220304).

- HQ Song, ZJ Zhou, LP Li, X Cheng, J Zhang, Y Chen, CX Chen, XW Ma, B Wang, and RS Zheng. The reversal of a solar prominence rotation about its ascending direction during a failed eruption. *The Astrophysical Journal Letters*, 864(2):L37, 2018. doi:[10.3847/2041-8213/aade49](https://doi.org/10.3847/2041-8213/aade49).
- EA Spiegel and NO Weiss. Magnetic activity and variations in solar luminosity. *Nature*, 287(5783):616, 1980. doi:[10.1038/287616A0](https://doi.org/10.1038/287616A0).
- A. C. Sterling and H. S. Hudson. Yohkoh SXT Observations of X-Ray “Dimming” Associated with a Halo Coronal Mass Ejection. *Astrophys. J. Lett.*, 491:L55–L58, December 1997. doi:[10.1086/311043](https://doi.org/10.1086/311043).
- Alphonse C Sterling and Hugh S Hudson. Yohkoh sxt observations of x-ray “dimming” associated with a halo coronal mass ejection. *The Astrophysical Journal Letters*, 491(1):L55, 1997. doi:[10.1086/311043](https://doi.org/10.1086/311043).
- Roberto Susino, Alessandro Bemporad, and Sergio Dolei. Three-dimensional Stereoscopic Analysis of a Coronal Mass Ejection and Comparison with UV Spectroscopic Data. *Astrophys. J.*, 790(1):25, July 2014. doi:[10.1088/0004-637X/790/1/25](https://doi.org/10.1088/0004-637X/790/1/25).
- M. Temmer, A. M. Veronig, N. Gopalswamy, and S. Yashiro. Relation Between the 3D-Geometry of the Coronal Wave and Associated CME During the 26 April 2008 Event. *Solar Phys.*, 273(2):421–432, November 2011. doi:[10.1007/s11207-011-9746-1](https://doi.org/10.1007/s11207-011-9746-1).
- M Temmer, AM Veronig, N Gopalswamy, and S Yashiro. Relation between the 3d-geometry of the coronal wave and associated cme during the 26 april 2008 event. In *Energy Storage and Release through the Solar Activity Cycle*, pages 115–126. Springer, 2011. doi:[10.1007/s11207-011-9746-1](https://doi.org/10.1007/s11207-011-9746-1).
- Manuela Temmer. Space weather: the solar perspective. *Living Reviews in Solar Physics*, 18(1):4, December 2021. doi:[10.1007/s41116-021-00030-3](https://doi.org/10.1007/s41116-021-00030-3).
- Manuela Temmer, AM Veronig, Bojan Vršnak, Jan Rybák, Peter Gömöry, Sigrid Stoiser, and Darije Maričić. Acceleration in fast halo cmes and synchronized flare hxr bursts. *The Astrophysical Journal Letters*, 673(1):L95, 2008. doi:[10.1086/527414](https://doi.org/10.1086/527414).
- Manuela Temmer, AM Veronig, EP Kontar, Säm Krucker, and B Vršnak. Combined stereo/rhessi study of coronal mass ejection acceleration and particle acceleration in solar flares. *The Astrophysical Journal*, 712(2):1410, 2010. doi:[10.1088/0004-637X/712/2/1410](https://doi.org/10.1088/0004-637X/712/2/1410).
- Manuela Temmer, Julia K. Thalmann, Karin Dissauer, Astrid M. Veronig, Johannes Tschernitz, Jürgen Hinterreiter, and Luciano Rodriguez. On Flare-CME Characteristics from Sun to Earth Combining Remote-Sensing Image Data with In Situ Measurements Supported by Modeling. *Solar Phys.*, 292(7):93, July 2017. doi:[10.1007/s11207-017-1112-5](https://doi.org/10.1007/s11207-017-1112-5).

- J. K. Thalmann, M. Dumbović, K. Dissauer, T. Podladchikova, G. Chikunova, M. Temmer, E. Dickson, and A. M. Veronig. Tracking magnetic flux and helicity from the Sun to Earth. Multi-spacecraft analysis of a magnetic cloud and its solar source. *Astron. Astrophys.*, 669:A72, January 2023. doi:10.1051/0004-6361/202244248.
- The SunPy Community, Will T. Barnes, Monica G. Bobra, Steven D. Christe, Nabil Freij, Laura A. Hayes, Jack Ireland, Stuart Mumford, David Perez-Suarez, Daniel F. Ryan, Albert Y. Shih, Prateek Chanda, Kolja Glogowski, Russell Hewett, V. Keith Hughitt, Andrew Hill, Kaustubh Hiware, Andrew Inglis, Michael S. F. Kirk, Sudarshan Konge, James Paul Mason, Shane Anthony Maloney, Sophie A. Murray, Asish Panda, Jongyeob Park, Tiago M. D. Pereira, Kevin Reardon, Sabrina Savage, Brigitta M. Sipőcz, David Stansby, Yash Jain, Garrison Taylor, Tannmay Yadav, Rajul, and Trung Kien Dang. The sunpy project: Open source development and status of the version 1.0 core package. *The Astrophysical Journal*, 890:68–, 2020. doi:10.3847/1538-4357/ab4f7a. URL <https://iopscience.iop.org/article/10.3847/1538-4357/ab4f7a>.
- A Thernisien. Implementation of the graduated cylindrical shell model for the three-dimensional reconstruction of coronal mass ejections. *The Astrophysical Journal Supplement Series*, 194(2):33, 2011. doi:10.1088/0067-0049/194/2/33.
- A Thernisien, A Vourlidas, and RA Howard. Forward modeling of coronal mass ejections using stereo/secchi data. *Solar Physics*, 256:111–130, 2009. doi:10.1007/S11207-009-9346-5.
- A Thernisien, A Vourlidas, and RA Howard. Cme reconstruction: Pre-stereo and stereo era. *Journal of Atmospheric and Solar-Terrestrial Physics*, 73(10):1156–1165, 2011. doi:10.1016/j.jastp.2011.03.015.
- A. F. R. Thernisien, R. A. Howard, and A. Vourlidas. Modeling of Flux Rope Coronal Mass Ejections. *Astrophys. J.*, 652(1):763–773, November 2006a. doi:10.1086/508254.
- A. F. R. Thernisien, R. A. Howard, and A. Vourlidas. Modeling of Flux Rope Coronal Mass Ejections. *Astrophys. J.*, 652(1):763–773, November 2006b. doi:10.1086/508254.
- B. J. Thompson, S. P. Plunkett, J. B. Gurman, J. S. Newmark, O. C. St. Cyr, and D. J. Michels. SOHO/EIT observations of an Earth-directed coronal mass ejection on May 12, 1997. *Geophys. Res. Lett.*, 25:2465–2468, 1998. doi:10.1029/98GL50429.
- B. J. Thompson, E. W. Cliver, N. Nitta, C. Delannée, and J.-P. Delaboudinière. Coronal dimmings and energetic CMEs in April-May 1998. *Geophys. Res. Lett.*, 27:1431–1434, May 2000. doi:10.1029/1999GL003668.
- BJ Thompson and DC Myers. A catalog of coronal “eit wave” transients. *The Astrophysical Journal Supplement Series*, 183(2):225, 2009. doi:10.1088/0067-0049/183/2/225.

- BJ Thompson, SP Plunkett, JB Gurman, JS Newmark, OC St. Cyr, and DJz Michels. Soho/eit observations of an earth-directed coronal mass ejection on may 12, 1997. *Geophysical Research Letters*, 25(14):2465–2468, 1998. doi:10.1029/98GL50429.
- BJ Thompson, EW Cliver, N Nitta, C Delannée, and J-P Delaboudiniere. Coronal dimmings and energetic cmes in april-may 1998. *Geophysical research letters*, 27(10):1431–1434, 2000. doi:10.1029/1999GL003668.
- William T. Thompson, Joseph M. Davila, Richard R. Fisher, Larry E. Orwig, John E. Mentzell, Samuel E. Hetherington, Rebecca J. Derro, Robert E. Federline, David C. Clark, Philip T. C. Chen, June L. Tveekrem, Anthony J. Martino, Joseph Novello, Richard P. Wesenberg, Orville C. StCyr, Nelson L. Reginald, Russell A. Howard, Kimberly I. Mehalick, Michael J. Hersh, Miles D. Newman, Debbie L. Thomas, Gregory L. Card, and David F. Elmore. COR1 inner coronagraph for STEREO-SECCHI. In Stephen L. Keil and Sergey V. Avakyan, editors, *Innovative Telescopes and Instrumentation for Solar Astrophysics*, volume 4853 of *Society of Photo-Optical Instrumentation Engineers (SPIE) Conference Series*, pages 1–11, February 2003. doi:10.1117/12.460267.
- William T Thompson, Joseph M Davila, Richard R Fisher, Larry E Orwig, John Eric Mentzell, Samuel E Hetherington, Rebecca J Derro, Robert E Federline, David C Clark, Philip TC Chen, et al. The cor1 inner coronagraph for stereo-secchi. In *Innovative Telescopes and Instrumentation for Solar Astrophysics*, volume 4853, pages 1–11. SPIE, 2003. doi:10.1117/12.460267.
- WT Thompson. Coordinate systems for solar image data. *Astronomy & Astrophysics*, 449(2):791–803, 2006. doi:10.1051/0004-6361:20054262.
- H. Tian, S. W. McIntosh, L. Xia, J. He, and X. Wang. What can We Learn about Solar Coronal Mass Ejections, Coronal Dimmings, and Extreme-ultraviolet Jets through Spectroscopic Observations? *Astrophys. J.*, 748:106, April 2012. doi:10.1088/0004-637X/748/2/106.
- V. S. Titov and P. Démoulin. Basic topology of twisted magnetic configurations in solar flares. *Astron. Astrophys.*, 351:707–720, November 1999. URL <https://ui.adsabs.harvard.edu/abs/1999A&A...351..707T>.
- V. S. Titov, Z. Mikic, J. A. Linker, and R. Lionello. 1997 May 12 Coronal Mass Ejection Event. I. A Simplified Model of the Preeruptive Magnetic Structure. *Astrophys. J.*, 675(2):1614–1628, March 2008. doi:10.1086/527280.
- T. Török and B. Kliem. Confined and Ejective Eruptions of Kink-unstable Flux Ropes. *Astrophys. J. Lett.*, 630(1):L97–L100, September 2005. doi:10.1086/462412.
- Durgesh Tripathi, A. N. Ramaprakash, Aafaque Khan, Avyarthana Ghosh, Subhamoy Chatterjee, Dipankar Banerjee, Pravin Chordia, Achim Gandorfer, Natalie Krivova, Dibyendu Nandy, Chaitanya Rajarshi, and Sami K. Solanki. The Solar

- Ultraviolet Imaging Telescope on-board Aditya-L1. *Current Science*, 113(4):616, August 2017. doi:[10.18520/cs/v113/i04/616-619](https://doi.org/10.18520/cs/v113/i04/616-619).
- Johannes Tschernitz, Astrid M Veronig, Julia K Thalmann, Jürgen Hinterreiter, and Werner Pötzi. Reconnection fluxes in eruptive and confined flares and implications for superflares on the sun. *The Astrophysical Journal*, 853(1):41, 2018. doi:[10.3847/1538-4357/aaa199](https://doi.org/10.3847/1538-4357/aaa199).
- K. Vanninathan, A. M. Veronig, K. Dissauer, and M. Temmer. Plasma Diagnostics of Coronal Dimming Events. *Astrophys. J.*, 857:62, April 2018. doi:[10.3847/1538-4357/aab09a](https://doi.org/10.3847/1538-4357/aab09a).
- Kamalam Vanninathan, Astrid M Veronig, Karin Dissauer, and Manuela Temmer. Plasma diagnostics of coronal dimming events. *The Astrophysical Journal*. doi:[10.3847/1538-4357/aad3c6](https://doi.org/10.3847/1538-4357/aad3c6).
- A. M. Veronig and W. Polanec. Magnetic Reconnection Rates and Energy Release in a Confined X-class Flare. *Solar Phys.*, 290(10):2923–2942, October 2015. doi:[10.1007/s11207-015-0789-6](https://doi.org/10.1007/s11207-015-0789-6).
- A. M. Veronig, N. Muhr, I. W. Kienreich, M. Temmer, and B. Vršnak. First Observations of a Dome-shaped Large-scale Coronal Extreme-ultraviolet Wave. *Astrophys. J. Lett.*, 716(1):L57–L62, June 2010. doi:[10.1088/2041-8205/716/1/L57](https://doi.org/10.1088/2041-8205/716/1/L57).
- A. M. Veronig, P. Gömöry, K. Dissauer, M. Temmer, and K. Vanninathan. Spectroscopy and Differential Emission Measure Diagnostics of a Coronal Dimming Associated with a Fast Halo CME. *Astrophys. J.*, 879:85, July 2019. doi:[10.3847/1538-4357/ab2712](https://doi.org/10.3847/1538-4357/ab2712).
- Astrid Veronig, Petra Odert, Martin Leitzinger, Karin Dissauer, Nikolaus Fleck, and Hugh Hudson. First detections of stellar coronal mass ejections through coronal dimmings. 2020. doi:[10.21203/rs.3.rs-114151/v1](https://doi.org/10.21203/rs.3.rs-114151/v1).
- Astrid Veronig, Petra Odert, Martin Leitzinger, Karin Dissauer, Nikolaus Fleck, and Hugh Hudson. Detection of stellar cmes through post-flare coronal dimmings. In *AGU Fall Meeting Abstracts*, volume 2021, pages U43B–07, 2021a. URL <https://ui.adsabs.harvard.edu/abs/2021AGUFM.U43B..07V>.
- Astrid M Veronig, Tatiana Podladchikova, Karin Dissauer, Manuela Temmer, Daniel B Seaton, David Long, Jingnan Guo, Bojan Vršnak, Louise Harra, and Bernhard Kliem. Genesis and impulsive evolution of the 2017 september 10 coronal mass ejection. *The Astrophysical Journal*, 868(2):107, 2018. doi:[10.3847/1538-4357/aaeac5](https://doi.org/10.3847/1538-4357/aaeac5).
- Astrid M. Veronig, Tatiana Podladchikova, Karin Dissauer, Manuela Temmer, Daniel B. Seaton, David Long, Jingnan Guo, Bojan Vršnak, Louise Harra, and Bernhard Kliem. Genesis and Impulsive Evolution of the 2017 September 10 Coronal Mass Ejection. *Astrophys. J.*, 868(2):107, December 2018. doi:[10.3847/1538-4357/aaeac5](https://doi.org/10.3847/1538-4357/aaeac5).

- Astrid M Veronig, Petra Odert, Martin Leitzinger, Karin Dissauer, Nikolaus C Fleck, and Hugh S Hudson. Indications of stellar coronal mass ejections through coronal dimmings. *Nature Astronomy*, 5(7):697–706, 2021b. doi:10.1038/s41550-021-01345-9.
- Claudio Vita-Finzi. *Inside the Sun*, pages 25–42. Springer Netherlands, Dordrecht, 2008. ISBN 978-1-4020-6881-2. doi:10.1007/978-1-4020-6881-2\_2. URL [https://doi.org/10.1007/978-1-4020-6881-2\\_2](https://doi.org/10.1007/978-1-4020-6881-2_2).
- Johan L. Freiherr von Forstner. johan12345/gcs\_python: Release 0.2.2, July 2021. URL <https://doi.org/10.5281/zenodo.5084818>.
- A Vourlidas, R Colaninno, T Nieves-Chinchilla, and G Stenborg. The first observation of a rapidly rotating coronal mass ejection in the middle corona. *The Astrophysical Journal Letters*, 733(2):L23, 2011a. doi:10.1088/2041-8205/733/2/L23.
- A Vourlidas, RA Howard, E Esfandiari, S Patsourakos, S Yashiro, and G Michalek. Erratum:“comprehensive analysis of coronal mass ejection mass and energy properties over a full solar cycle”(2010, apj, 722, 1522). *The Astrophysical Journal*, 730(1):59, 2011b. doi:10.1088/0004-637X/730/1/59.
- A. Vourlidas, B. J. Lynch, R. A. Howard, and Y. Li. How many cmes have flux ropes? deciphering the signatures of shocks, flux ropes, and prominences in coronagraph observations of cmes. *Solar Physics*, 284(1):179–201, May 2013. ISSN 1573-093X. doi:10.1007/s11207-012-0084-8. URL <https://doi.org/10.1007/s11207-012-0084-8>.
- Angelos Vourlidas, Russ A Howard, Ed Esfandiari, Spiros Patsourakos, Seiji Yashiro, and Gregorz Michalek. Comprehensive analysis of coronal mass ejection mass and energy properties over a full solar cycle. *The Astrophysical Journal*, 722(2):1522, 2010. doi:10.1088/0004-637X/722/2/1522.
- Angelos Vourlidas, B. J. Lynch, Russell A. Howard, and Yan Li. How many cmes have flux ropes? deciphering the signatures of shocks, flux ropes, and prominences in coronagraph observations of cmes. *Solar Physics*, 284:179–201, 2012. URL <https://api.semanticscholar.org/CorpusID:118425835>.
- Bojan Vršnak and Tomislav Žic. Transit times of interplanetary coronal mass ejections and the solar wind speed. *Astronomy & Astrophysics*, 472(3):937–943, 2007. doi:10.1051/0004-6361:20077499.
- Bojan Vršnak, Davor Sudar, and Domagoj Ruždjak. The cme-flare relationship: Are there really two types of cmes? *Astronomy & Astrophysics*, 435(3):1149–1157, 2005. doi:10.1051/0004-6361:20042166.
- Bojan Vršnak, Darije Maričić, Andrew L Stanger, Astrid M Veronig, Manuela Temmer, and Dragan Roša. Acceleration phase of coronal mass ejections: I. temporal and spatial scales. *Solar Physics*, 241(1):85–98, 2007. doi:10.1007/s11207-006-0290-3.

- Jasper Vivian Wall and Charles R Jenkins. *Practical statistics for astronomers*. Cambridge University Press, 2012. doi:[10.1017/CBO9781139031998](https://doi.org/10.1017/CBO9781139031998).
- Yuming Wang and Jie Zhang. A Comparative Study between Eruptive X-Class Flares Associated with Coronal Mass Ejections and Confined X-Class Flares. *Astrophys. J.*, 665(2):1428–1438, August 2007. doi:[10.1086/519765](https://doi.org/10.1086/519765).
- D. F. Webb, R. P. Lepping, L. F. Burlaga, C. E. DeForest, D. E. Larson, S. F. Martin, S. P. Plunkett, and D. M. Rust. The origin and development of the May 1997 magnetic cloud. *J. Geophys. Res.*, 105:27251–27260, December 2000. doi:[10.1029/2000JA000021](https://doi.org/10.1029/2000JA000021).
- David F. Webb and Russell A. Howard. The solar cycle variation of coronal mass ejections and the solar wind mass flux. *J. Geophys. Res.*, 99(A3):4201–4220, March 1994. doi:[10.1029/93JA02742](https://doi.org/10.1029/93JA02742).
- David F. Webb and Timothy A. Howard. Coronal mass ejections: Observations. *Living Reviews in Solar Physics*, 9(1):3, Jun 2012. ISSN 1614-4961. doi:[10.12942/lrsp-2012-3](https://doi.org/10.12942/lrsp-2012-3). URL <https://doi.org/10.12942/lrsp-2012-3>.
- DF Webb and AJ Hundhausen. Activity associated with the solar origin of coronal mass ejections. *Solar physics*, 108(2):383–401, 1987. doi:[10.1007/BF00214170](https://doi.org/10.1007/BF00214170).
- DF Webb, RP Lepping, LF Burlaga, CE DeForest, DE Larson, SF Martin, SP Plunkett, and DM Rust. The origin and development of the may 1997 magnetic cloud. *Journal of Geophysical Research: Space Physics*, 105(A12):27251–27259, 2000. doi:[10.1029/2000JA000021](https://doi.org/10.1029/2000JA000021).
- DF Webb, DR Mizuno, and BV Jackson. Cmes observed in the heliosphere by the solar mass ejection imager (smei). *Eos Trans. AGU*, 85:5, 2004. URL <https://ui.adsabs.harvard.edu/abs/2004AGUFMSH11A..03W>.
- Meredith Wills-Davey and G. D. R. Attrill. Automated Detection and Extraction of Coronal Dimmings from SDO/AIA Data. In *AAS/Solar Physics Division Meeting #40*, volume 40 of *AAS/Solar Physics Division Meeting*, page 17.08, May 2009. doi:[10.1007/S11207-009-9444-4](https://doi.org/10.1007/S11207-009-9444-4).
- R. Wolf. Abstract of his latest Results. *Mon. Not. Roy. Astron. Soc.*, 21:77, January 1861. doi:[10.1093/mnras/21.3.77](https://doi.org/10.1093/mnras/21.3.77).
- Rudolf Wolf. Astronomische Mittheilungen XLII. *Astronomische Mittheilungen der Eidgenössischen Sternwarte Zurich*, 5:29–60, January 1877. URL <https://api.semanticscholar.org/CorpusID:222465371>.
- T. N. Woods, F. G. Eparvier, R. Hock, A. R. Jones, D. Woodraska, D. Judge, L. Didkovsky, J. Lean, J. Mariska, H. Warren, D. McMullin, P. Chamberlin, G. Berthiaume, S. Bailey, T. Fuller-Rowell, J. Sojka, W. K. Tobiska, and R. Viereck. Extreme Ultraviolet Variability Experiment (EVE) on the Solar Dynamics Observatory (SDO): Overview of Science Objectives, Instrument Design, Data Products, and Model Developments. *Solar Phys.*, 275(1-2):115–143, January 2012. doi:[10.1007/s11207-009-9487-6](https://doi.org/10.1007/s11207-009-9487-6).

- Jean-Pierre Wuelser, James R. Lemen, Theodore D. Tarbell, C. J. Wolfson, Joseph C. Cannon, Brock A. Carpenter, Dexter W. Duncan, Glenn S. Gradwohl, Syndie B. Meyer, Augustus S. Moore, Rosemarie L. Navarro, J. D. Pearson, George R. Rossi, Larry A. Springer, Russell A. Howard, John D. Moses, Jeffrey S. Newmark, Jean-Pierre Delaboudiniere, Guy E. Artzner, Frederic Auchere, Marie Bougnet, Philippe Bouyries, Françoise Bridou, Jean-Yves Clotaire, Gerard Colas, Franck Delmotte, Arnaud Jerome, Michel Lamare, Raymond Mercier, Michel Mullot, Marie-Françoise Ravet, Xueyan Song, Volker Bothmer, and Werner Deutsch. EUVI: the STEREO-SECCHI extreme ultraviolet imager. In Silvano Fineschi and Mark A. Gummin, editors, *Telescopes and Instrumentation for Solar Astrophysics*, volume 5171 of *Society of Photo-Optical Instrumentation Engineers (SPIE) Conference Series*, pages 111–122, February 2004. doi:10.1117/12.506877.
- Hong Xie, Leon Ofman, and Gareth Lawrence. Cone model for halo CMEs: Application to space weather forecasting. *Journal of Geophysical Research (Space Physics)*, 109(A3):A03109, March 2004. doi:10.1029/2003JA010226.
- Yu Xu, Hui Tian, Zhenyong Hou, Zihao Yang, Yuhang Gao, and Xianyong Bai. Sun-as-a-star Spectroscopic Observations of the Line-of-sight Velocity of a Solar Eruption on 2021 October 28. *Astrophys. J.*, 931(2):76, June 2022. doi:10.3847/1538-4357/ac69d5.
- Dabin Xue, Jian Yang, Zhizhao Liu, and Shiwei Yu. Examining the economic costs of the 2003 halloween storm effects on the north hemisphere aviation using flight data in 2019. *Space Weather*, 21(3), March 2023. ISSN 1542-7390. doi:10.1029/2022SW003381.
- Youwei Yan, David C. Stenning, Vinay L. Kashyap, and Yaming Yu. Forecasting solar cycle 25 with a principled bayesian two-stage statistical model. *Research Notes of the AAS*, 5, 2021. URL <https://api.semanticscholar.org/CorpusID:237237864>.
- S Yashiro, N Gopalswamy, G Michalek, and RA Howard. Properties of narrow coronal mass ejections observed with lasco. *Advances in Space Research*, 32(12):2631–2635, 2003. doi:10.1016/s0273-1177(03)90442-x.
- S. Yashiro, N. Gopalswamy, G. Michalek, O. C. St. Cyr, S. P. Plunkett, N. B. Rich, and R. A. Howard. A catalog of white light coronal mass ejections observed by the SOHO spacecraft. *Journal of Geophysical Research (Space Physics)*, 109(A7):A07105, July 2004. doi:10.1029/2003JA010282.
- S. Yashiro, S. Akiyama, N. Gopalswamy, and R. A. Howard. Different Power-Law Indices in the Frequency Distributions of Flares with and without Coronal Mass Ejections. *Astrophys. J. Lett.*, 650(2):L143–L146, October 2006. doi:10.1086/508876.
- D. M. Zarro, A. C. Sterling, B. J. Thompson, H. S. Hudson, and N. Nitta. SOHO EIT Observations of Extreme-Ultraviolet “Dimming” Associated with a Halo Coronal Mass Ejection. *Astrophys. J. Lett.*, 520:L139–L142, August 1999a. doi:10.1086/312150.

- D. M. Zarro, A. C. Sterling, B. J. Thompson, H. S. Hudson, and N. Nitta. SOHO EIT Observations of Extreme-Ultraviolet “Dimming” Associated with a Halo Coronal Mass Ejection. *Astrophys. J. Lett.*, 520:L139–L142, August 1999b. doi:[10.1086/312150](https://doi.org/10.1086/312150).
- Jie Zhang, Manuela Temmer, Nat Gopalswamy, Olga Malandraki, Nariaki V. Nitta, Spiros Patsourakos, Fang Shen, Bojan Vršnak, Yuming Wang, David Webb, Mihir I. Desai, Karin Dissauer, Nina Dresing, Mateja Dumbović, Xueshang Feng, Stephan G. Heinemann, Monica Laurenza, Noé Lugaz, and Bin Zhuang. Earth-affecting solar transients: a review of progresses in solar cycle 24. *Progress in Earth and Planetary Science*, 8(1):56, December 2021. doi:[10.1186/s40645-021-00426-7](https://doi.org/10.1186/s40645-021-00426-7).
- Q. M. Zhang. A revised cone model and its application to non-radial prominence eruptions. *Astron. Astrophys.*, 653:L2, September 2021. doi:[10.1051/0004-6361/202141982](https://doi.org/10.1051/0004-6361/202141982).
- X. P. Zhao, S. P. Plunkett, and W. Liu. Determination of geometrical and kinematical properties of halo coronal mass ejections using the cone model. *Journal of Geophysical Research (Space Physics)*, 107(A8):1223, August 2002. doi:[10.1029/2001JA009143](https://doi.org/10.1029/2001JA009143).
- AN Zhukov and F Auchère. On the nature of eit waves, euv dimmings and their link to cmes. *Astronomy & Astrophysics*, 427(2):705–716, 2004. doi:[10.1051/0004-6361:20040351](https://doi.org/10.1051/0004-6361:20040351).